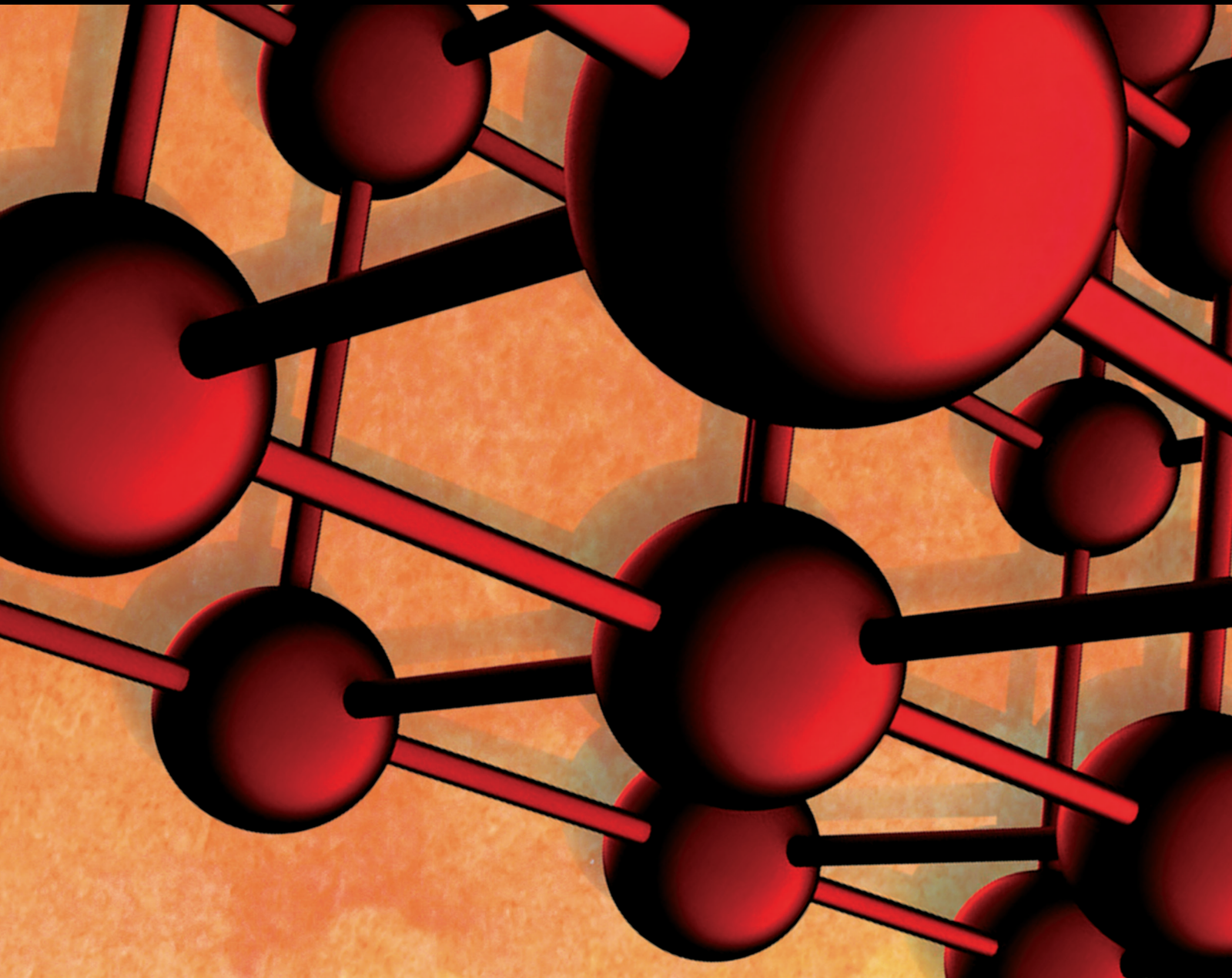


Advances in Materials Science and Engineering

# Cold Techniques and Materials for Sustainable Pavement Construction and Rehabilitation

Lead Guest Editor: Andrea Grilli

Guest Editors: Andrea Graziani, Alan Carter, and Jian Ouyang





---

# **Cold Techniques and Materials for Sustainable Pavement Construction and Rehabilitation**



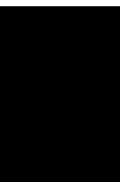
Advances in Materials Science and Engineering

---

**Cold Techniques and Materials for  
Sustainable Pavement Construction and  
Rehabilitation**

Lead Guest Editor: Andrea Grilli

Guest Editors: Andrea Graziani, Alan Carter, and  
Jian Ouyang




---

Copyright © 2020 Hindawi Limited. All rights reserved.

This is a special issue published in "Advances in Materials Science and Engineering." All articles are open access articles distributed under the Creative Commons Attribution License, which permits unrestricted use, distribution, and reproduction in any medium, provided the original work is properly cited.

# Chief Editor












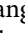






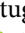
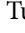


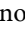




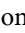



Amit Bandyopadhyay , USA

## Associate Editors

Vamsi Balla , India  
Mitun Das , USA  
Sandip Harimkar, USA  
Ravi Kumar , India  
Peter Majewski , Australia  
Enzo Martinelli , Italy  
Luigi Nicolais , Italy  
Carlos R. Rambo , Brazil  
Michael J. Schütze , Germany  
Kohji Tashiro , Japan  
Zhonghua Yao , China  
Dongdong Yuan , China  
Wei Zhou , China

## Academic Editors

Antonio Abate , Germany  
Hany Abdo , Saudi Arabia  
H.P.S. Abdul Khalil , Malaysia  
Ismael Alejandro Aguayo Villarreal , Mexico  
Sheraz Ahmad , Pakistan  
Michael Aizenshtein, Israel  
Jarir Aktaa, Germany  
Bandar AlMangour, Saudi Arabia  
Huaming An, China  
Alicia Esther Ares , Argentina  
Siva Avudaiappan , Chile  
Habib Awais , Pakistan  
NEERAJ KUMAR BHOI, India  
Enrico Babilio , Italy  
Renal Backov, France  
M Bahubalendruni , India  
Sudharsan Balasubramanian , India  
Markus Bambach, Germany  
Irene Bavasso , Italy  
Stefano Bellucci , Italy  
Brahim Benmokrane, Canada  
Jean-Michel Bergheau , France  
Guillaume Bernard-Granger, France  
Giovanni Berselli, Italy  
Patrice Berthod , France  
Michele Bianchi , Italy  
Hugo C. Biscaia , Portugal

Antonio Boccaccio, Italy  
Mohamed Bououdina , Saudi Arabia  
Gianlorenzo Bussetti , Italy  
Antonio Caggiano , Germany  
Marco Cannas , Italy  
Qi Cao, China  
Gianfranco Carotenuto , Italy  
Paolo Andrea Carraro , Italy  
Jose Cesar de Sa , Portugal  
Wen-Shao Chang , United Kingdom  
Qian Chen , China  
Francisco Chinesta , France  
Er-Yuan Chuang , Taiwan  
Francesco Colangelo, Italy  
María Criado , Spain  
Enrique Cuan-Urquizo , Mexico  
Lucas Da Silva , Portugal  
Angela De Bonis , Italy  
Abílio De Jesus , Portugal  
José António Fonseca De Oliveira  
Correia , Portugal  
Ismail Demir , Turkey  
Luigi Di Benedetto , Italy  
Maria Laura Di Lorenzo, Italy  
Marisa Di Sabatino, Norway  
Luigi Di Sarno, Italy  
Ana María Díez-Pascual , Spain  
Guru P. Dinda , USA  
Hongbiao Dong, China  
Mingdong Dong , Denmark  
Frederic Dumur , France  
Stanislaw Dymek, Poland  
Kaveh Edalati , Japan  
Philip Eisenlohr , USA  
Luis Evangelista , Norway  
Michele Fedel , Italy  
Francisco Javier Fernández Fernández , Spain  
Spain  
Isabel J. Ferrer , Spain  
Massimo Fresta, Italy  
Samia Gad , Egypt  
Pasquale Gallo , Finland  
Sharanabasava Ganachari, India  
Santiago Garcia-Granda , Spain  
Carlos Garcia-Mateo , Spain

Achraf Ghorbal , Tunisia  
Georgios I. Giannopoulos , Greece  
Ivan Giorgio , Italy  
Andrea Grilli , Italy  
Vincenzo Guarino , Italy  
Daniel Guay, Canada  
Jenő Gubicza , Hungary  
Xuchun Gui , China  
Benoit Guiffard , France  
Zhixing Guo, China  
Ivan Gutierrez-Urrutia , Japan  
Weiwei Han , Republic of Korea  
Simo-Pekka Hannula, Finland  
A. M. Hassan , Egypt  
Akbar Heidarzadeh, Iran  
Yi Huang , United Kingdom  
Joshua Ighalo, Nigeria  
Saliha Ilican , Turkey  
Md Mainul Islam , Australia  
Ilia Ivanov , USA  
Jijo James , India  
Hafsa Jamshaid , Pakistan  
Hom Kandel , USA  
Kenji Kaneko, Japan  
Rajesh Kannan A , Democratic People's  
Republic of Korea  
Mehran Khan , Hong Kong  
Akihiko Kimura, Japan  
Ling B. Kong , Singapore  
Pramod Koshy, Australia  
Hongchao Kou , China  
Alexander Kromka, Czech Republic  
Abhinay Kumar, India  
Avvaru Praveen Kumar , Ethiopia  
Sachin Kumar, India  
Paweł Kłosowski , Poland  
Wing-Fu Lai , Hong Kong  
Luciano Lamberti, Italy  
Fulvio Lavecchia , Italy  
Laurent Lebrun , France  
Joon-Hyung Lee , Republic of Korea  
Cristina Leonelli, Italy  
Chenggao Li , China  
Rongrong Li , China  
Yuanshi Li, Canada

Guang-xing Liang , China  
Barbara Liguori , Italy  
Jun Liu , China  
Yunqi Liu, China  
Rong Lu, China  
Zhiping Luo , USA  
Fernando Lusquiños , Spain  
Himadri Majumder , India  
Dimitrios E. Manolakos , Greece  
Necmettin Maraşlı , Turkey  
Alessandro Martucci , Italy  
Roshan Mayadunne , Australia  
Mamoun Medraj , Canada  
Shazim A. Memon , Kazakhstan  
Pratima Meshram , India  
Mohsen Mhadhbi , Tunisia  
Philippe Miele, France  
Andrey E. Miroshnichenko, Australia  
Ajay Kumar Mishra , South Africa  
Hossein Moayedi , Vietnam  
Dhanesh G. Mohan , United Kingdom  
Sakar Mohan , India  
Namdev More, USA  
Tahir Muhmood , China  
Faisal Mukhtar , Pakistan  
Dr. Tauseef Munawar , Pakistan  
Roger Narayan , USA  
Saleem Nasir , Pakistan  
Elango Natarajan, Malaysia  
Rufino M. Navarro, Spain  
Miguel Navarro-Cia , United Kingdom  
Behzad Nematollahi , Australia  
Peter Niemz, Switzerland  
Hiroschi Noguchi, Japan  
Dariusz Oleszak , Poland  
Laurent Orgéas , France  
Togay Ozbakkaloglu, United Kingdom  
Marián Palcut , Slovakia  
Davide Palumbo , Italy  
Gianfranco Palumbo , Italy  
Murlidhar Patel, India  
Zbyšek Pavlík , Czech Republic  
Alessandro Pegoretti , Italy  
Gianluca Percoco , Italy  
Andrea Petrella, Italy






Claudio Pettinari , Italy  
Giorgio Pia , Italy  
Candido Fabrizio Pirri, Italy  
Marinos Pitsikalis , Greece  
Alain Portavoce , France  
Simon C. Potter, Canada  
Ulrich Prah, Germany  
Veena Ragupathi , India  
Kawaljit Singh Randhawa , India  
Baskaran Rangasamy , Zambia  
Paulo Reis , Portugal  
Hilda E. Reynel-Avila , Mexico  
Yuri Ribakov , Israel  
Aniello Riccio , Italy  
Anna Richelli , Italy  
Antonio Riveiro , Spain  
Marco Rossi , Italy  
Fernando Rubio-Marcos , Spain  
Francesco Ruffino , Italy  
Giuseppe Ruta , Italy  
Sachin Salunkhe , India  
P Sangeetha , India  
Carlo Santulli, Italy  
Fabrizio Sarasini , Italy  
Senthil Kumaran Selvaraj , India  
Raffaele Sepe , Italy  
Aabid H Shalla, India  
Poorva Sharma , China  
Mercedes Solla, Spain  
Tushar Sonar , Russia  
Donato Sorgente , Italy  
Charles C. Sorrell , Australia  
Damien Soulat , France  
Adolfo Speghini , Italy  
Antonino Squillace , Italy  
Koichi Sugimoto, Japan  
Jirapornchai Suksaeree , Thailand  
Baozhong Sun, China  
Sam-Shajing Sun , USA  
Xiaolong Sun, China  
Yongding Tian , China  
Hao Tong, China  
Achim Trampert, Germany  
Tomasz Trzepieciński , Poland  
Kavimani V , India


Matjaz Valant , Slovenia  
Mostafa Vamegh, Iran  
Lijing Wang , Australia  
Jörg M. K. Wiezorek , USA  
Guosong Wu, China  
Junhui Xiao , China  
Guoqiang Xie , China  
YASHPAL YASHPAL, India  
Anil Singh Yadav , India  
Yee-wen Yen, Taiwan  
Hao Yi , China  
Wenbin Yi, China  
Tetsu Yonezawa, Japan  
Hiroshi Yoshihara , Japan  
Bin Yu , China  
Rahadian Zainul , Indonesia  
Lenka Zaji#c#kova# , Czech Republic  
Zhigang Zang , China  
Michele Zappalorto , Italy  
Gang Zhang, Singapore  
Jinghuai Zhang, China  
Zengping Zhang, China  
You Zhou , Japan  
Robert Černý , Czech Republic

# Contents


## **Adhesion Improvement between RAP and Emulsified Asphalt by Modifying the Surface Characteristics of RAP**

Zhenjun Wang , Pei Wang, Haoyan Guo, Xiaofeng Wang , and Gang Li   
Research Article (10 pages), Article ID 4545971, Volume 2020 (2020)

## **Cold Recycled Asphalt Mixture using 100% RAP with Emulsified Asphalt-Recycling Agent as a New Pavement Base Course**

Wilson Unger Filho , Luis Miguel Gutiérrez Klinsky, Rosângela Motta, and Liedi Légi Bariani Bernucci  
Research Article (11 pages), Article ID 5863458, Volume 2020 (2020)


## **Laboratory Evaluation and Construction of Fully Recycled Low-Temperature Asphalt for Low-Volume Roads**

Christiane Raab  and Manfred N. Partl  
Research Article (12 pages), Article ID 4904056, Volume 2020 (2020)





## **Investigation of the Effects of Evaporation Methods on the High-Temperature Rheological and Fatigue Performances of Emulsified Asphalt Residues**

Yang Sun, Jin-Chao Yue , Ri-Ran Wang, Rui-Xia Li, and De-Cai Wang   
Research Article (12 pages), Article ID 4672413, Volume 2020 (2020)


## **Delivering Sustainable Solutions through Improved Mix and Structural Design Functions for Bitumen Stabilised Materials**

K. J. Jenkins , C. E. Rudman, and C. R. Bierman  
Research Article (10 pages), Article ID 7460174, Volume 2020 (2020)




## **On the Recent Trends in Expansive Soil Stabilization Using Calcium-Based Stabilizer Materials (CSMs): A Comprehensive Review**

Fazal E. Jalal , Yongfu Xu , Babak Jamhiri , and Shazim Ali Memon   
Review Article (23 pages), Article ID 1510969, Volume 2020 (2020)


## **Property Improvement of Cement Emulsified Asphalt Paste Modified by Graphene Oxide**

Yu-wei Ma, Hong-yan Zhao, Gang Li , Zhen-jun Wang, Hua Tang, and Ai-qin Wang  
Research Article (11 pages), Article ID 3462342, Volume 2020 (2020)

## **Rheological Properties Comparing Hot and Cold Bituminous Mastics Containing Jet Grouting Waste**

Rosa Veropalumbo , Francesca Russo , Nunzio Viscione, and Salvatore A. Biancardo   
Research Article (16 pages), Article ID 8078527, Volume 2020 (2020)


## **Macroscopic and Microscopic Characterization of the Effect of “Activation” Process on the Performance of Buton Rock Asphalt-Modified Asphalt**

Yafei Li, Meng Guo , and Xu Liu  
Research Article (6 pages), Article ID 8148930, Volume 2020 (2020)







## **Mechanical Characterization and Chemical Identification of Clear Binders for Road Surface Courses**

Andrea Grilli , Maurizio Bocci, Amedeo Virgili, and Carla Conti  
Research Article (9 pages), Article ID 4930646, Volume 2020 (2020)



**Effect of Superplasticizer and Wetting Agent on Volumetric and Mechanical Properties of Cold Recycled Mixture with Asphalt Emulsion**

Wenting Yang, Jian Ouyang , Yan Meng, Taixiong Tang, Jijiang Chen, and Baoguo Han  
Research Article (11 pages), Article ID 6251653, Volume 2020 (2020)

**Material and Structural Properties of Fiber-Reinforced Resin Composites as Thin Overlay for Steel Bridge Deck Pavement**

Hui Zhang , Chengqi Zhou , Kuan Li , Peiwei Gao , Youqiang Pan , and Zhixiang Zhang   
Research Article (13 pages), Article ID 9840502, Volume 2019 (2019)

**Investigation of the Performance of the Ecofriendly Fiber-Reinforced Asphalt Mixture as a Sustainable Pavement Material**

Bowen Guan , Jianan Liu , Jiayu Wu, Jingyi Liu, Haitao Tian, Tengbin Huang, Chengcheng Liu, and Tao Ren  
Research Article (11 pages), Article ID 6361032, Volume 2019 (2019)

## Research Article

# Adhesion Improvement between RAP and Emulsified Asphalt by Modifying the Surface Characteristics of RAP

Zhenjun Wang <sup>1,2</sup>, Pei Wang,<sup>1</sup> Haoyan Guo,<sup>1</sup> Xiaofeng Wang <sup>3</sup> and Gang Li <sup>4</sup>

<sup>1</sup>School of Materials Science and Engineering, Chang'an University, Xi'an 710061, China

<sup>2</sup>State Key Lab High Performance Civil Engineering Materials, Nanjing 211103, China

<sup>3</sup>Henan Provincial Communications Planning & Design Institute, Zhengzhou 450052, China

<sup>4</sup>College of Water Conservancy and Architectural Engineering, Shihezi University, Shihezi 832000, China

Correspondence should be addressed to Zhenjun Wang; zjwang@chd.edu.cn and Xiaofeng Wang; wangxf0351@sina.com

Received 27 December 2019; Revised 8 February 2020; Accepted 2 March 2020; Published 22 April 2020

Guest Editor: Andrea Graziani

Copyright © 2020 Zhenjun Wang et al. This is an open access article distributed under the Creative Commons Attribution License, which permits unrestricted use, distribution, and reproduction in any medium, provided the original work is properly cited.

Recycled asphalt pavement (RAP) can be used in highway engineering again by cold recycled technology. Due to the aged asphalt on the surface of RAP, some problems such as poor adhesion between emulsified asphalt and RAP and the low properties of emulsified asphalt recycling mixture are easy to occur. This work aims at analyzing the aging degree of asphalt from RAP surface and improving the poor adhesion between RAP and emulsified asphalt by modifying the surface characteristics of RAP. In this work, a new device was designed to delaminate off the asphalt on the surface of RAP. The aging degree of asphalt at different layers was studied then by physical properties and molecular weight distribution. Slurry of hydrated lime ( $\text{Ca}(\text{OH})_2$ ) (S-Ca) and slurry of silane coupling agent (SCA) modified  $\text{Ca}(\text{OH})_2$  (S-Si-Ca) were used to modify the asphalt on the surface of RAP, respectively. The adhesion between emulsified asphalt and RAP was studied by contact angle and boiling method. Results show that the asphalt on the RAP surface can be successfully stripped into four layers through the self-designed RAP delaminating and stripping device. The aging degree of asphalt wrapped around the surface of the RAP showed a tendency to be gradually severe from outside to inside. However, asphalt at the innermost layer (L4) shows abnormal situation due to the fact that the light components are absorbed by the aggregate. In addition, reasonable dosage of SCA is determined as 3.0% in  $\text{Ca}(\text{OH})_2$  powder mass. Both S-Ca and S-Si-Ca can effectively reduce the contact angle and thus improve the adhesion between emulsified asphalt and RAP. Moreover, S-Si-Ca possesses the most obvious modification effect attributed to the formation of asphalt-SCA- $\text{Ca}(\text{OH})_2$  structure.

## 1. Introduction

During the service of asphalt pavement, aging can inevitably occur due to the combined effects of heat, oxygen, sunlight, and water. The utilization of recycled asphalt pavement (RAP) in the cold recycling process of asphalt pavement possesses the dual benefits of saving energy and protecting the environment [1, 2]. However, the application of RAP in asphalt mixture is highly limited due to the presence of the aged asphalt on the RAP surface [3, 4], which can reduce the properties of cold recycled asphalt mixture.

The surface aging degree of RAP is usually different from that of the RAP internal [5–7]. It was found that there was a big difference between the recycled asphalt and the asphalt

because the mineral powder can absorb certain components in the asphalt [8]. The penetration and ductility of the extracted aged asphalt decreased while the softening point increased with the increase of the service life of RAP [9]. Although the aging behavior of asphalt on the RAP surface has been confirmed, the aging degree of different layers of asphalt has not been distinguished.

The poor adhesion of the RAP-new asphalt interface has been an important factor restricting the development of high-performance cold recycled mixture [10]. Some modification methods have been used for improving the properties of cold recycled mixture [11–14]. It is effective to modify asphalt mixture with a reactive powder [15–17]. Hydrated lime can significantly reduce the polarity



difference between asphalt and aggregate and improve the surface free energy of asphalt and the adhesion between asphalt and aggregate [18]. The addition of fly ash can improve the mechanical property and durability of cold recycled asphalt mixture [19]. Cement can improve the early strength and water damage resistance of asphalt emulsion mixture [20]. In addition, the adhesion between asphalt and aggregate depends largely on conditions of aggregate minerals [21];  $\text{SiO}_2$  in aggregate can improve the adhesion between asphalt and aggregate due to physical adsorption [22]. For other modifiers, silane and amine can improve the RAP aggregate-new asphalt interface property [23]. Bio-oil can improve the high-temperature performance of RAP mixture in a humid environment [24].

However, most of the above studies are qualitative evaluation and there are few methods to evaluate quantitatively the modification effect of asphalt on the RAP surface, and the modification effect of aged asphalt on the RAP surface is still poor. Therefore, it is of great value to put forward one technique to improve the surface properties of RAP and its adhesion to emulsified asphalt. In this work, the characteristics analyses of aged asphalt on the RAP surface were conducted before utilizing RAP to determine the aging degree and select three appropriate modifiers to improve the surface characteristics of aged asphalt, which is expected to obtain the best RAP-new asphalt adhesion and optimize various properties of recycled asphalt mixtures.

## 2. Materials and Experimental

**2.1. Materials.** The physical and chemical properties of the asphalt selected in this paper are shown in Table 1. Emulsified asphalt was prepared using a cationic emulsifier and its properties are shown in Table 2. The main properties of the selected modifiers ( $\text{Ca}(\text{OH})_2$  and KH-550 SCA) are shown in Table 3 and Table 4, respectively. The properties of the solvent trichloroethylene (TCE) are shown in Table 5.

**2.2. Stripping of Asphalt at Different Layers of RAP Surface.** In order to evaluate the performance of asphalt at different layers of RAP, a kind of self-designed device was developed in this work, based on the Abson method (T 0726-2011) in the *Standard Test Methods of Bitumen and Bituminous Mixtures for Highway Engineering in China (JTG E20-2011)*, whose specific steps can be consulted from reference [25]. The device can effectively strip asphalt on the surface of RAP. In view of the rapid dissolving properties of asphalt in TCE, TCE was used as a solvent in this work to wash down the asphalt on the RAP surface layer by layer. As shown in Figure 1, the asphalt on the RAP surface was divided into four layers from outside to inside and labeled as layer 1, L1; layer 2, L2; layer 3, L3; and layer 4, L4, respectively.

The schematic diagram of the device for stripping asphalt is shown in Figure 2. 100 g of RAP with a particle size of 13.2 mm–19 mm was selected and rinsed with water to remove surface dust and sand as much as possible firstly. The washed RAP was placed into the device shown in Figure 2 after drying naturally. The RAP was then rinsed with a fixed

volume of TCE. After the TCE completely flowed out, the dissolved asphalt solution was collected, impurities such as mineral powder were removed, and asphalt sample was finally obtained after evaporation of TCE. The obtained asphalt samples were marked and labeled as L1, L2, L3, and L4, respectively (as shown in Figure 3).

**2.3. Preparation of Modified Slurries.** In this work, SCA solution (S-Si), S-Ca, and S-Si-Ca were used to improve the surface characteristics of RAP and increase its adhesion to emulsified asphalt. The three modifiers were prepared as follows:

- (1) In order to accelerate the ionization and dispersion of SCA in the solution, a certain concentration of the solution was prepared firstly and the formulation ratio of the solution is shown in Table 6. The pH value of the solution was adjusted to 4 by acetic acid. After the SCA was hydrolyzed in the solution at room temperature for 20 min, SCA solution (S-Si) was obtained.
- (2) The hydrated lime powder and water were prepared in a mass ratio of 0.3 : 100 and placed in a beaker, and then, the beaker was placed on a magnetic stirrer and stirred for 30 minutes at 30°C. Finally, slurry of hydrated lime (S-Ca) was obtained.
- (3) The hydrated lime possesses highly polar property and it is difficult to adhere to asphalt under normal temperature conditions. Therefore,  $\text{Ca}(\text{OH})_2$  was modified in this work. After the prepared S-Si was mixed with S-Ca, the slurry was stirred at 30°C for 20 min to obtain slurry of silane coupling agent modified  $\text{Ca}(\text{OH})_2$  (S-Si-Ca). In this work, 1%, 2%, 3%, 4%, and 5% SCA ( $\text{Ca}(\text{OH})_2$  powder weight) were used to prepare S-Si-Ca.

## 2.4. Experiment Methods

**2.4.1. Physical Property Tests.** The physical properties of asphalt at different layers were tested according to the *Standard Test Methods of Bitumen and Bituminous Mixtures for Highway Engineering in China (JTG E20-2011)*, which includes softening point, penetration at 25°C, and ductility at 25°C. To ensure the reliability of the test data, three samples were prepared and tested for each of the three tests and the average value was finally adopted as the test result.

**2.4.2. Gel Permeation Chromatography (GPC).** GPC is a very accurate and efficient method for classifying polymers according to the molecular weight. In this work, polystyrene with known relative molecular mass was used as a mono-disperse standard for direct correction; a standard curve was established and different layers of asphalt were measured and analyzed according to the standard curve. The temperature of the column was set to 25°C; the mobile phase was tetrahydrofuran; the flow rate was 1.0 mL/min; and the concentration of the sample solution was 2.0 mg/ml. A

TABLE 1: Physical and chemical properties of original asphalt.

Properties	Test results	Specification values
Softening point (°C)	48.0	≥46
Penetration (25°C, 100g, 5s) (0.1 mm)	71.2	60–80
Ductility (15°C, 5°cm/min) (cm)	≥100	≥100
Density (15°C) (g/m <sup>3</sup> )	1.029	—
Mass loss (%)	0.24	–0.8–0.8
RTFOT, penetration ratio (25°C) (%)	65.9	≥61
Ductility (15°C, 5 cm/min) (cm)	23.9	≥15

TABLE 2: Properties of emulsified asphalt.

Properties	Test results	Specification values
Residue content (%)	60.1	≥55
Evaporation residue Penetration (25°C, 100 g, 5 s) (0.1 mm)	77.1	50–300
Ductility (15°C, 5 cm/min) (cm)	49.8	≥40
Storage stability (% , 25°C) 1 d	0.4	<1.0
5 d	4.5	<5.0

TABLE 3: Composition of hydrated lime.

Composition (%)	Ca(OH) <sub>2</sub>	Chloride	Sulfate	Magnesium salt	Iron element
Mass fraction (%)	≥95.05	0.01	0.2	0.2	0.01

TABLE 4: Properties of silane coupling agent.

Properties	Chromatographic purity (%)	Density (25°C) (g/cm <sup>3</sup> )	Refractive index (25°C) (m/s)
Test results	98.1	0.944	1.419

TABLE 5: Properties of trichloroethylene (TCE).

Properties	Exterior	Density (g/cm <sup>3</sup> )	Boiling point (°C)	Melting point (°C)	Molecular weight
Test results	Colorless	1.460	87.4	–87.0	131.39

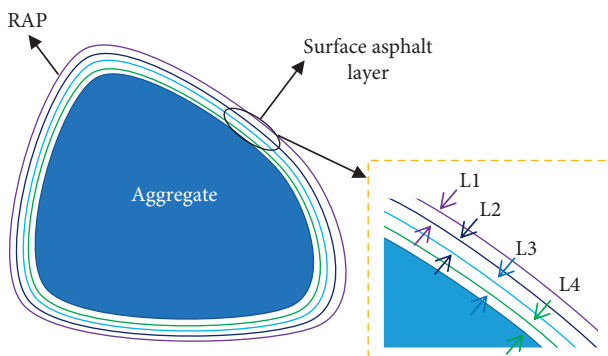


FIGURE 1: Schematic diagram of asphalt layers on the RAP surface.

normal GPC curve of the asphalt sample is shown in Figure 4.

Asphalt aging is the aggregation of small molecules to macromolecules. The higher the LMC, the more severe the aging of asphalt. The aging degree of asphalt at each layer can

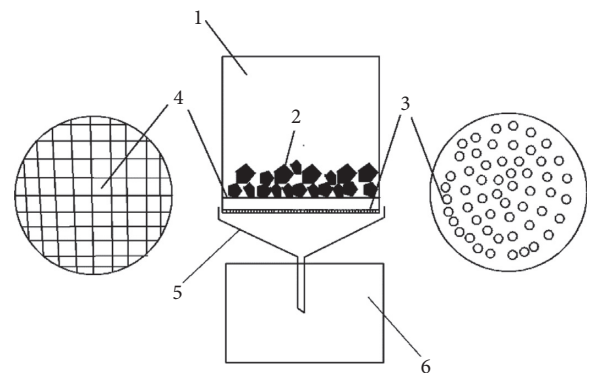


FIGURE 2: Schematic diagram of the device for stripping asphalt. (1) Container; (2) RAP; (3) chassis; (4) net-shaped support; (5) receiving funnel; (6) solution collecting device.

be evaluated by quantitatively calculating the ratio of large molecular content (LMC). The ratio of LMC to the entire molecular weight is used to quantitatively evaluate the aging degree of asphalt [25]. The LMC can be calculated according to the following equation:

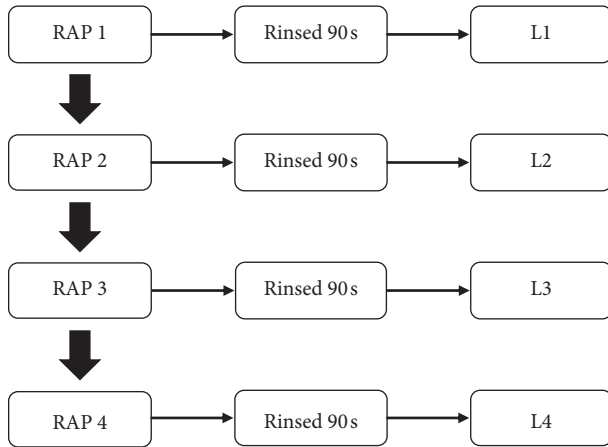


FIGURE 3: Schematic diagram of the RAP rinsing process.

TABLE 6: Formulation ratio of SCA solution.

Composition	KH-550	Ethanol	Water
Mass fraction (%)	17.8	63.5	18.7

$$LMC = \frac{AF_{5/13}C}{TAC} \times 100\%, \quad (1)$$

where  $AF_{5/13}C$  is the area of the first 5/13 of chromatogram and TAC is the total area beneath chromatogram.

**2.4.3. Asphaltene Content Tests.** The content of asphaltene at different layers was tested according to the *Standard Test Methods of Bitumen and Bituminous Mixtures for Highway Engineering in China (JTG E20-2011)*. In this work, n-heptane and toluene were used to extract asphaltene. The insoluble was further extracted after the asphalt was extracted with n-heptane, and then the soluble was extracted by toluene to obtain asphaltenes. The asphaltene content was calculated from the weight ratio of asphaltene to asphalt sample.

**2.4.4. Contact Angle Test between Emulsified Asphalt and RAP.** The contact angle measuring instrument, as a commonly used device in the research of surface free energy, is mainly used to measure the wettability of liquid to solid. The adhesion work of the system can be calculated by measuring the contact angle of emulsified asphalt on the surface of the mineral. The JGW-360BL contact angle measuring instrument was adopted in this work, which mainly includes four parts: sample test bench, lighting equipment, microsyringe, and image analysis software.

The contact angle test process is as follows: the L1 layer asphalt was heated and melted and then adhered on a  $76 \times 26$  mm glass slide to form an asphalt film. After cooling, the slide was immersed in distilled water, S-Si, S-Ca, and S-Si-Ca, respectively. In order to prevent the precipitation of solid particles during the soaking process, the slurry needed to be constantly stirred. The temperature of the solution was controlled at  $30^\circ\text{C}$  and the soaking time was 30 min. After the

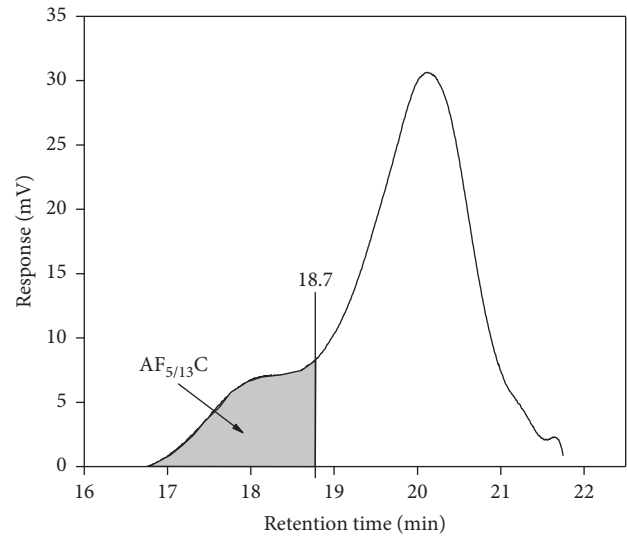


FIGURE 4: GPC analysis diagram of asphalt.

soaking, asphalt sample was left to dry. Finally, the contact angle between the treated sample and emulsified asphalt was tested.

**2.4.5. Adhesion Test between Emulsified Asphalt and RAP.** The improved boiling test was used to evaluate the adhesion of emulsified asphalt to RAP in this work according to the *Standard Test Methods of Bitumen and Bituminous Mixtures for Highway Engineering in China (JTG E20-2011)*. Since the adhesion of emulsified asphalt was not as strong as that of hot asphalt, relevant improvements were made referring to the original adhesion test. Some 13.2 mm–19 mm RAP with a shape close to cubic were selected and treated with distilled water, S-Si, S-Ca, and S-Si-Ca, respectively (the process is the same as that for asphalt in Section 2.4.3).

After treatment, the sample was rinsed with distilled water and dried naturally. Then, the treated RAP was immersed in emulsified asphalt for 1 min, and after being taken out, RAP was hung at room temperature for 24 h. Then the RAP adhered with emulsified asphalt was placed in a  $60^\circ\text{C}$  water bath for 3 min, and the area percentage of asphalt peeling from the aggregate surface was carefully observed to determine the adhesion grade. Visual observations were made immediately once the sample boiling process was finished. Examination of the sample was conducted under light and with low magnification in the visual observation of retained coating. Any thin, brownish, translucent areas were to be considered fully coated.

### 3. Results and Discussion

**3.1. Physical Properties of Asphalt at Different Layers of RAP.** The aging degree of asphalt wrapped in different layers on the surface of RAP is different. In order to study the physical properties of asphalt at different layers, the penetration, softening point, and ductility of asphalt samples were tested. The test results are shown in Figure 5. In Figure 5, the softening point of asphalt gradually decreases, while the

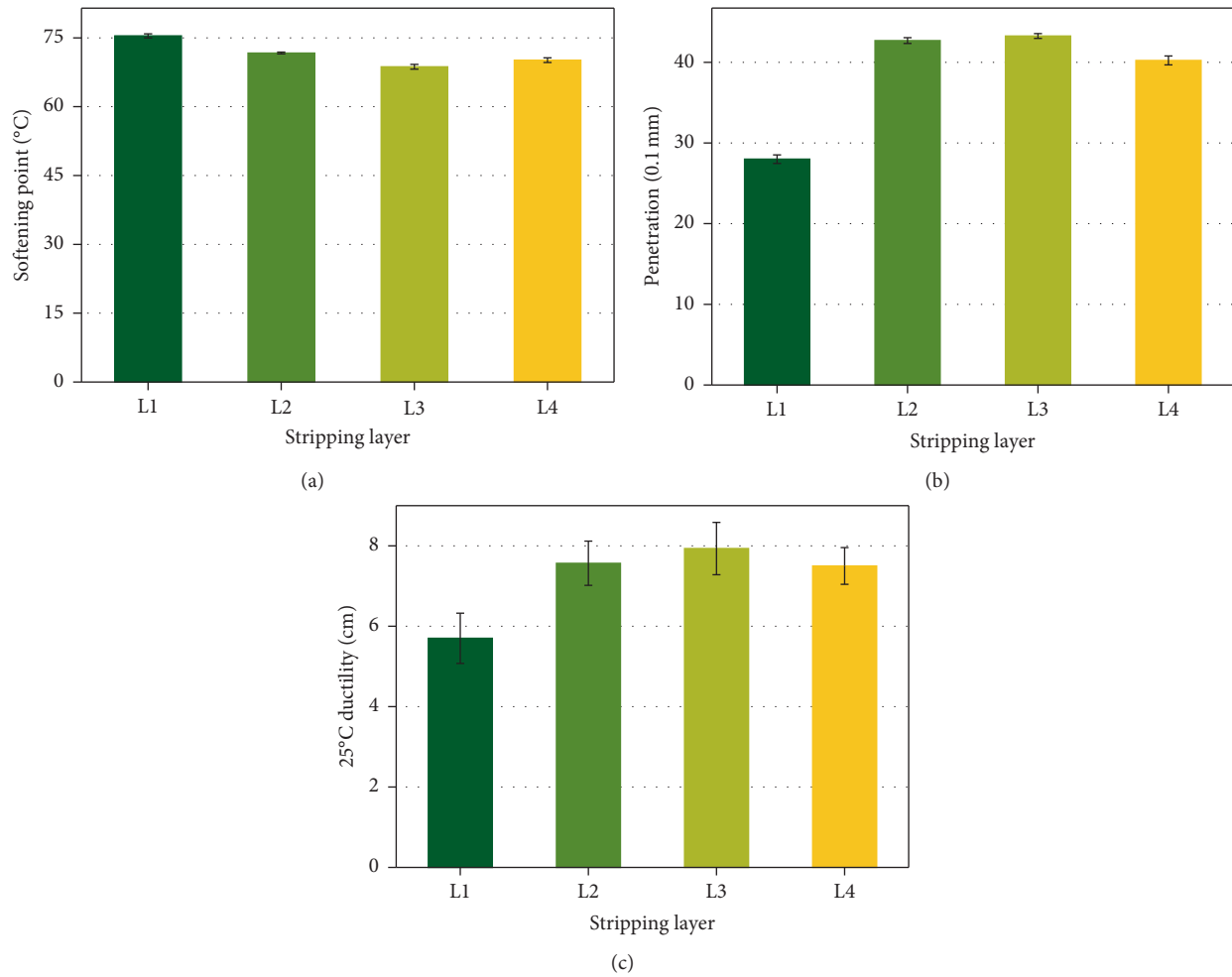


FIGURE 5: Physical properties of asphalt at different layers: (a) softening point, (b) penetration, and (c) ductility.

penetration and the ductility increase from the outside to the inside of the aggregate. However, the fourth layer of asphalt which is in close contact with aggregate shows an increase in softening point and a decrease in penetration and ductility compared with the third layer of asphalt. It is mainly due to the different aging degree of different layers of asphalt.

The outermost layer asphalt (L1) on the RAP surface suffers from the most severe aging degree due to more contact with the external environment such as air, water, and acid. At the same time, the outer layer of asphalt has a protective effect on the inner asphalt, which can slow down the aging of the inner asphalt. As the aging degree deepens, the dosage of light components in asphalt gradually decreases, and the dosage of heavy components gradually increases. Among the asphalt components, the heavy components determine the temperature sensitivity, hardness, and other characteristics of asphalt. Therefore, the higher the aging degree of asphalt, the harder the asphalt and the worse its physical properties. The main reason for the deterioration of the physical properties of L4 asphalt is that the internal aggregate absorbs the oil content of the asphalt, which reduces the dosage of light components in asphalt and thus increases the dosage of heavy components in asphalt.

**3.2. Molecular Weight Analysis of Asphalt at Different Layers.** The polymerization reaction can occur between the molecules during aging of asphalt, resulting in the change of molecular weight. GPC can sensitively capture the change of molecular weight and thus reflect the aging degree of asphalt [26, 27]. Figure 6 shows the GPC spectrum of asphalt at different layers. In Figure 6, the time when the asphalt molecules at different layers begin to flow out is different. The peak positions of asphalt at different layers are also different. The asphalt peak gradually shifts to the left as the aging degree deepens; that is, the proportion of macromolecules in the asphalt sample gradually increases [25].

According to equation (1), the LMC of asphalt at different layers was calculated and the results are shown in Figure 7. In Figure 7, the macromolecule content in L1 is the highest, which can reach 15.7%, as well as followed by L2 and L4, which are 14.7% and 14.2%, and the lowest macromolecule content is L3, which can reach 12.9%. The outermost layer asphalt of RAP suffers from the most aging due to the contact with the external environment. As a result of the absorption of the light components in the asphalt by aggregate, the heavy component dosage of the L4 layer asphalt is increased, so the proportion of macromolecules is



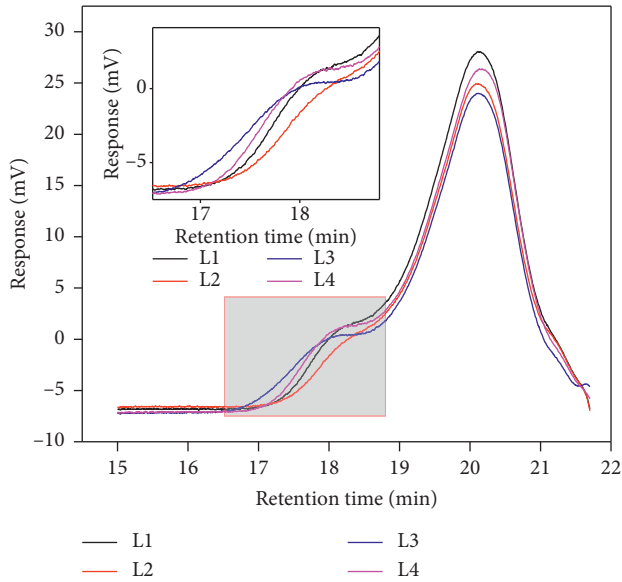


FIGURE 6: GPC curves of asphalt at different layers.

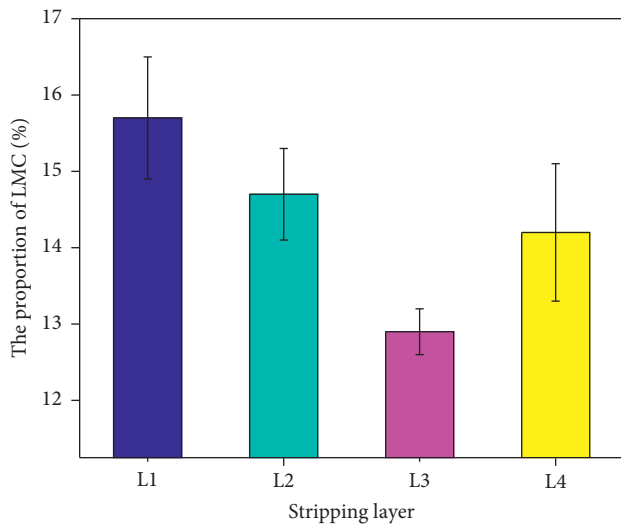


FIGURE 7: The LMC of asphalt at different layers.

enhanced. The aging of L2 and L3 is lighter due to the less affection by environmental erosion or aggregate absorption, so the proportion of macromolecules is relatively small.

From the physical performance results, the softening point, penetration, and ductility of the L1-L3 layers all maintained a certain law, but abnormalities occurred in the L4 layer. It can attribute to the absorption of lightweight components by the aggregate. This is because the molecular weight of asphalt is closely related to the physical properties of asphalt. Small molecules can promote the sliding of molecular chains. The higher the proportion of small molecules in the asphalt, the easier the molecular chain movement. On the other hand, the higher the proportion of macromolecules, the stronger the entanglement of molecular chains with each other, and the more difficult the molecular chain movement is, and thus the aged asphalt with

higher LMC gradually hardens and its physical properties decrease. This can also explain why the physical properties of L4 asphalt have inflection points.

### 3.3. Change of Asphaltene Content at Different Layers.

The chemical composition of asphalt is closely related to its physical properties. The higher the content of asphaltene, the more serious the aging of asphalt and the higher the content of macromolecule in asphalt. The asphaltene was extracted according to the characteristics of asphaltene that can be insoluble in n-heptane. Figure 8 shows the asphaltene content of asphalt peeling from different layers on the RAP surface.

It can be seen from Figure 8 that the asphaltene content in L1 is the highest, indicating the L1 asphalt suffered from the most serious aging. Under the impact of light and heat, the light components of asphalt gradually change to asphaltene, resulting in the highest asphaltene content in the L1. Moreover, the aging degree of inner asphalt is smaller due to the most external asphalt coating. The content of asphaltene kept a decrease from L1 to L3. However, L4 asphaltene content increased compared with L3, which can be mainly due to the mineral absorption of light components rather than the aging condition. L4 is far from the external atmosphere, so the possibility of L4 being affected by the external environment and aging is much lower than the other three layers.

### 3.4. Effects of RAP Modification on Contact Angle.

In contrast to ordinary aggregate, the surface of RAP has different adhesion characteristics with emulsified asphalt due to the existence of asphalt aging film. The surface energy between asphalt and RAP is directly related to the adhesion characteristics between them from the perspective of thermodynamics, so the free energy theory can be used to evaluate the adhesion performance of RAP and predict the adhesion force between modified RAP and emulsified asphalt [10].

When liquid comes in contact with solid, the liquid can have a wetting or adsorption effect on the solid surface due to the difference in surface energy between them. The contact of emulsified asphalt with RAP can be equivalent to the wetting process of emulsified asphalt and RAP. The contact angle between emulsified asphalt and RAP can change as the surface energy of the two changes. According to Young's equation, as shown in equation (2), the adhesion force between the liquid and the solid can be calculated as long as the surface tension  $\gamma_l$  of the liquid and the contact angle  $\theta$  between them are measured. The surface tension of the same test liquid is the same. Therefore, the smaller the contact angle, the greater the adhesion force between the solid and the liquid.

$$W_a = \gamma_l (\cos \theta + 1), \quad (2)$$

where  $W_a$  is the adhesion of the two substances,  $\gamma_l$  is the surface tension of the liquid, and  $\theta$  is the contact angle between the liquid and the solid.

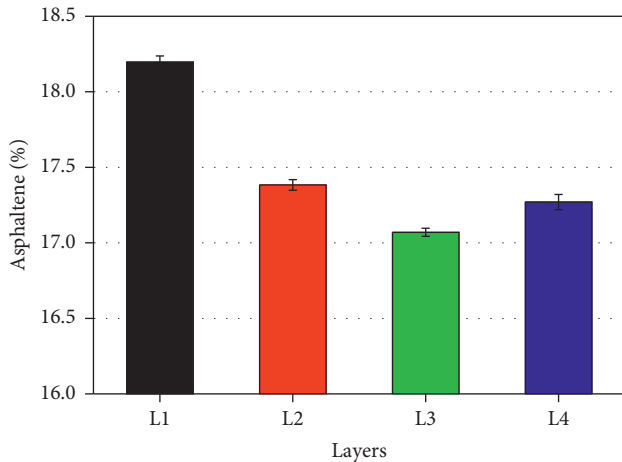


FIGURE 8: The asphaltene dosage of asphalt at different layers.

Figure 9 shows the effect of SCA dosage on the modification effect of S-Ca. The contact angle between emulsified asphalt and RAP gradually decreased with the increase of SCA dosage (0–3%), indicating that the effect of SCA on the surface modification effect of asphalt has gradually been improved. However, the contact angle of emulsified asphalt to RAP gradually increases when the dosage of SCA exceeds a certain proportion (3%). This is because suitable SCA can adhere  $\text{Ca}(\text{OH})_2$  solid particles to asphalt surface. However, the solid particles of  $\text{Ca}(\text{OH})_2$  can be completely covered by the SCA when the dosage of SCA exceeds a certain limit. This is not conducive to the adsorption of  $\text{Ca}(\text{OH})_2$  solid particles on emulsified asphalt particles, so the contact angle gradually increases. The 3% SCA dosage was selected as a precondition to the formulation of the three modifiers, S-Si, S-Si-Ca, and S-Ca. After the asphalt was treated by the three modifiers, the contact angle was tested.

The contact angle test results after different modification treatments are shown in Figure 10. In Figure 10, the contact angle between aging asphalt and emulsified asphalt is  $57.8^\circ$ . The contact angle with emulsified asphalt particles after the S-Si treatment did not decrease, but increased by  $1.7^\circ$ . However, the contact angles of emulsified asphalt particles on asphalt surface after S-Ca and S-Si-Ca treatment decreased by  $3.5^\circ$  and  $10.5^\circ$ , respectively. It shows that the adhesion between RAP and emulsified asphalt is improved after S-Ca and S-Si-Ca treatment. After the S-Ca was modified with SCA, the contact angle between emulsified asphalt and RAP is evidently decreased, which indicates that the adhesion between RAP treated with S-Si-Ca and emulsified asphalt is the highest.

### 3.5. Adhesion between Emulsified Asphalt and Modified RAP.

The adhesion of RAP treated by different modifiers to emulsified asphalt is shown in Figure 11. It can be seen from Figure 11 that the stripping amount of untreated RAP surface asphalt after boiling test is the most, and the stripping amount of RAP surface asphalt after S-Si and S-Ca treatment decreases. However, the overall stripping area is more than 30%; therefore, the adhesion grade was

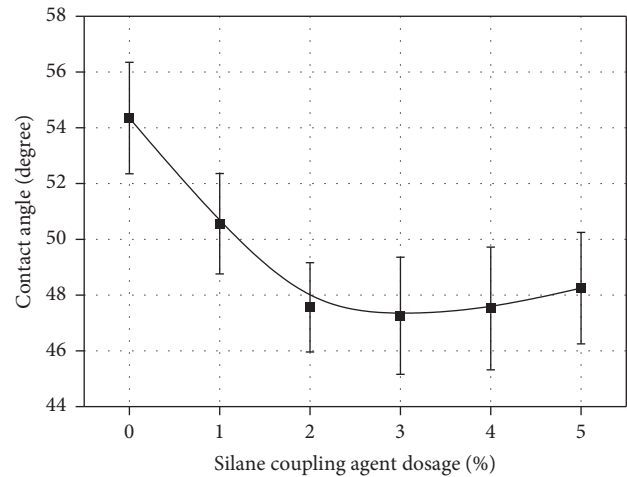


FIGURE 9: Effect of SCA dosage on the contact angle.

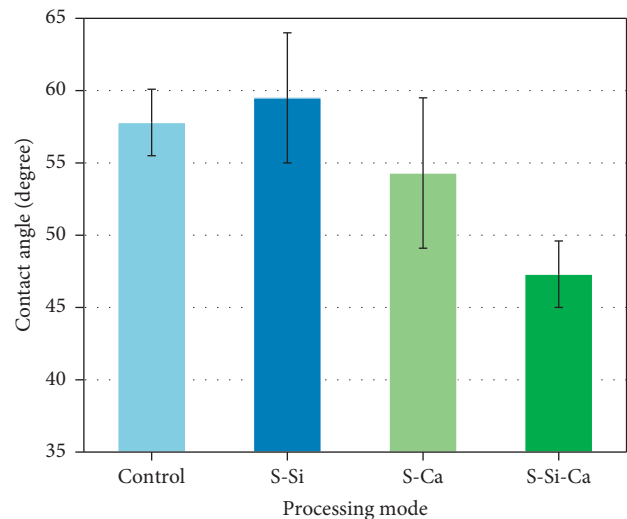


FIGURE 10: Contact angles between emulsified asphalt and RAP with different treatments.

determined as grade II. However, after S-Si-Ca treatment of RAP, the stripping amount of RAP surface asphalt significantly reduced, and the total stripping amount is between 10% and 30%, so the adhesion grade was determined as grade III.

The adhesion of RAP to emulsified asphalt is shown in Table 7. In Table 7, the adhesion grade of emulsified asphalt and RAP without treatment and treated with S-Si and S-Ca keeps the same. However, the adhesion grade of emulsified asphalt and RAP is improved to grade III after treated with S-Si-Ca. The main reason is that the SCA and  $\text{Ca}(\text{OH})_2$  can improve the wetting ability of emulsified asphalt to RAP, so the adhesion of RAP and emulsified asphalt is significantly improved.

3.6. Mechanism of Adhesion Changes between Emulsified Asphalt and RAP. The effect diagram of the modifier on RAP is shown in Figure 12. In the cold mixing process of asphalt,

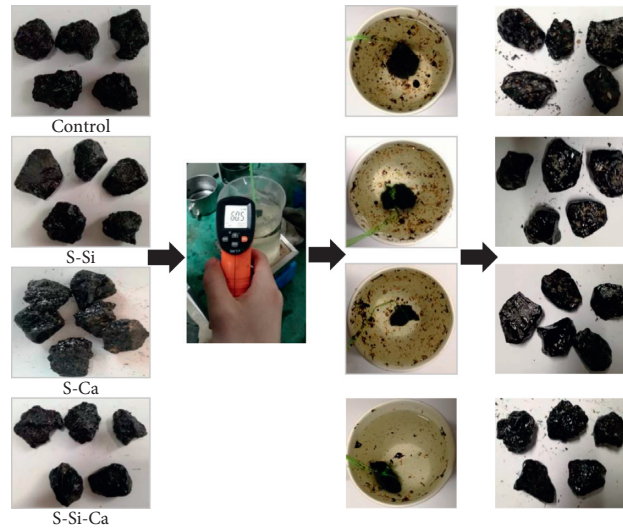


FIGURE 11: The adhesion grade test for emulsified asphalt and RAP.

TABLE 7: Adhesion results of emulsified asphalt and RAP.

Treated methods	RAP surface condition	Adhesion grade
Control	Most of the asphalt film is desorbed, and the percentage of stripping area is more than 30%	II
S-Si		II
S-Ca		II
S-Si-Ca	Asphalt film is obviously desorbed, but the percentage of stripping area is less than 30%	III

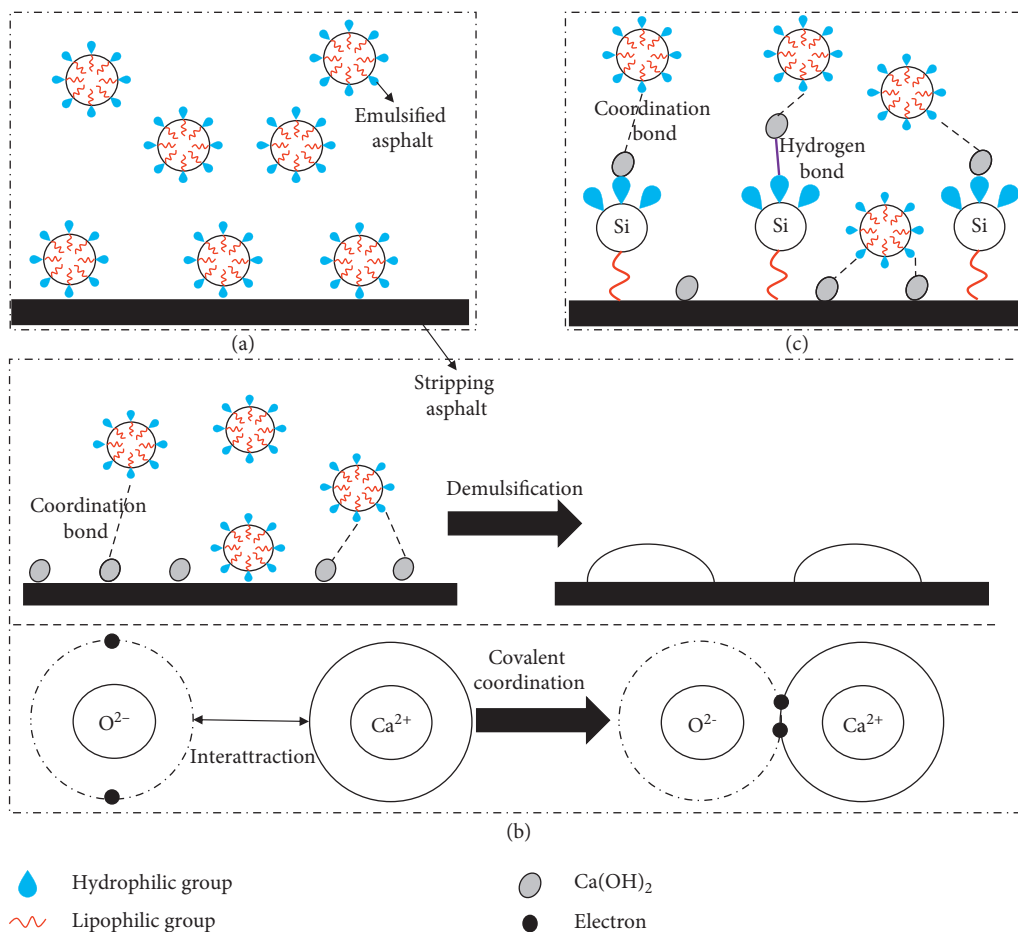


FIGURE 12: Diagram of adhesion between emulsified asphalt and RAP: (a) control, (b) S-Ca, and (c) S-Si-Ca.

emulsifier molecules can be adsorbed with inorganic materials such as aggregate and cement, which can result in the demulsification of emulsified asphalt. The droplets of asphalt would demulsify and form asphalt film on the surface of aggregate. However, as shown in Figure 12(a), the hydrophilic groups on the surface of emulsified asphalt have poor compatibility with the lipophilic group on RAP surface asphalt, which hinders emulsified asphalt particles to spread on the asphalt surface.

As can be seen from Figure 12(b), S-Ca is used as an intermediate in this paper to tightly connect the aged asphalt on the RAP surface with emulsified asphalt. At the interface between aged asphalt and  $\text{Ca}(\text{OH})_2$ , the key point is the acid-base reaction.  $\text{Ca}(\text{OH})_2$  has strong alkalinity and can react with the acidic substances in the asphalt to form calcium salts. These organic calcium salts have strong polarity and can form stronger bonds than organic acids or anhydrides [28]. Moreover, the asphalt containing calcium ion on the RAP surface can promote the adsorption and demulsification of emulsified asphalt and can also enhance the adhesion between emulsified asphalt and RAP. Calcium exists in S-Ca in the form of  $\text{Ca}^{2+}$ . The arrangement of extranuclear electrons of calcium atom is  $1s^2 2s^2 2p^6 3s^2 3p^6 4s^2$ , and that of  $\text{Ca}^{2+}$  is  $1s^2 2s^2 2p^6 3s^2 3p^6$ . It can be seen from the arrangement of extranuclear electrons that  $\text{Ca}^{2+}$  loses two electrons in the 4s orbit, so  $\text{Ca}^{2+}$  has an empty orbit without electrons. According to the formation conditions of covalent coordination bond, the 4s orbital of  $\text{Ca}^{2+}$  will receive two lone electrons contained in oxygen atom of emulsifier to form covalent coordination bond when emulsified asphalt is in contact with S-Ca. Therefore, the adhesion between aged asphalt modified by S-Ca and emulsified asphalt increases.

Due to the aging behavior of asphalt, the acidity of the RAP surface asphalt can be reduced, for the acidic substances in the asphalt can be decreased by environmental erosion [29], which can weaken the reaction between aged asphalt and S-Ca and hinder the formation of calcium salts and thus can influence the effect of the S-Ca modification. The adhesion between emulsified asphalt and RAP was further increased after RAP was treated by S-Si-Ca. On the one hand, as shown in Figure 12(c), the hydrophilic group of SCA can adsorb and form hydrogen bond with inorganic particles  $\text{Ca}(\text{OH})_2$ . On the other hand, the lipophilic group of SCA can react with organic substance on the surface of asphalt to form a chemical bond, which can well adsorb on the asphalt surface to form the structure of aged asphalt-SCA- $\text{Ca}(\text{OH})_2$ -emulsified asphalt so that aged asphalt and emulsified asphalt can be firmly combined.

#### 4. Conclusions

In this work, a self-designed RAP delamination and stripping device was applied to separate the asphalt on the RAP surface. The properties of asphalt at different stripping layers, such as penetration, softening point, 25°C ductility, and molecular weight were studied. In addition, different modification methods were used to modify the asphalt on the RAP surface and the modification effect was determined through contact angle and boiling test. Finally, the mechanism of different

modification methods was analyzed. The following conclusions are drawn:

- (a) The asphalt on the RAP surface was successfully stripped into four layers through the self-designed RAP delaminating and stripping device. The asphalt wrapped around the surface of the RAP showed a tendency to be gradually hardened from outside to inside. However, asphalt at the innermost layer (L4) being close contact with aggregate is slightly harder than that at L3 due to the fact that the light components are absorbed by the aggregate.
- (b) The proportion of macromolecules in L1 layer asphalt is the highest, which is followed by L4, L2, and L3 layers. This further proves that the aging degree of asphalt at different stripping layers is different, which maintains the same as the results of physical properties. In general, the aging degree of asphalt on the RAP surface is  $L1 > L4 > L2 > L3$ . In addition, the change rule of asphaltene is consistent with that of macromolecules.
- (c) The modification effect is improved at first but then worsened with the increase of the dosage of SCA. The reasonable dosage of SCA is determined as 3.0% in  $\text{Ca}(\text{OH})_2$  powder mass. The modification effect of the three different treatment methods gradually worsens from S-Si-Ca, S-Ca to S-Si.
- (d) The reason behind the best modification effect for S-Si-Ca RAP is that the SCA can react with organic substance on the asphalt surface to produce chemical bonds. Meanwhile, SCA can bring  $\text{Ca}(\text{OH})_2$  particles to the asphalt surface to form asphalt-SCA- $\text{Ca}(\text{OH})_2$  structure.

#### Data Availability

The data used to support the findings of this study are included within the article.

#### Conflicts of Interest

The authors declare that they have no conflicts of interest.

#### Acknowledgments

This work was supported by the National Natural Science Foundation of China (no. 51978067), Science and Technology Development Project of Xinjiang Production and Construction Corps (no. 2019AB013), the State Key Laboratory of High Performance Civil Engineering Materials (no. 2018CEM010), Henan Transportation Science and Technology Plan Project (no. 2019J1), and the Fundamental Research Funds for the Central Universities of China (no. 300102310501).

#### References

- [1] A. Sultan Saud and Z. Guo, "Evaluating the performance of sustainable perpetual pavements using recycled asphalt pavement in China," *International Journal of Transportation Science and Technology*, vol. 5, no. 3, pp. 200–209, 2017.



- [2] J. Ouyang, J. Zhao, and Y. Tan, "Modeling mechanical properties of cement asphalt emulsion mortar with different asphalt to cement ratios and temperatures," *Journal of Materials in Civil Engineering*, vol. 30, no. 10, Article ID 04018263, 2018.
- [3] W. Fedrigo, W. P. Núñez, T. R. Kleinert, M. F. Matuella, and J. A. P. Ceratti, "Strength, shrinkage, erodibility and capillary flow characteristics of cement-treated recycled pavement materials," *International Journal of Pavement Research and Technology*, vol. 10, no. 5, pp. 393–402, 2017.
- [4] H. Majidifard, N. Tabatabaee, and W. Buttlar, "Investigating short-term and long-term binder performance of high-RAP mixtures containing waste cooking oil," *Journal of Traffic and Transportation Engineering (English Edition)*, vol. 6, no. 4, pp. 396–406, 2019.
- [5] M. Ali, Z. Hassan, M. R. M. Aliha, and Y. Saghafi, "Laboratory study of the effect of oil-based recycling agents on high RAP asphalt mixtures," *International Journal of Pavement Engineering*, vol. 224, pp. 89–98, 2019.
- [6] H. Ziari, A. Moniri, and N. Norouzi, "The effect of nanoclay as bitumen modifier on rutting performance of asphalt mixtures containing high content of rejuvenated reclaimed asphalt pavement," *Petroleum Science And Technology*, vol. 37, no. 17, pp. 1946–1951, 2019.
- [7] Y. Xu, Z. Chou, Y. Li, J. Ji, and S.-F. Xu, "Effect of blending degree between virgin and aged binder on pavement performance of recycled asphalt mixture with high RAP content," *Advances in Materials Science and Engineering*, vol. 2019, p. 5741642, 2019.
- [8] Y. Ding, B. Huang, and X. Shu, "Blending efficiency evaluation of plant asphalt mixtures using fluorescence microscopy," *Construction and Building Materials*, vol. 161, no. 10, pp. 461–467, 2018.
- [9] B. Mohamadtaqi and H. Ali, "Rheological and chemical characteristics of asphalt binders recycled using different recycling agents," *Construction and Building Materials*, vol. 228, pp. 1–14, 2019.
- [10] Pi YuHui, Li Yan, Y.X. Pi, X.Y. Tan, and M.M. He, "Wetting model of asphalt on the aggregate surface and its effect factors," *Advances in Materials Science and Engineering*, vol. 2019, p. 4126464, 2019.
- [11] Z. Wang, D. Nan, X. Wang, J. Zhang, and H. Guo, "Laboratory investigation on effects of microwave heating on early strength of cement bitumen emulsion mixture," *Construction and Building Materials*, vol. 236, pp. 1–13, 2020.
- [12] W. Yang, J. Ouyang, M. Yan, T. Tang, J. Chen, and B. Han, "Effect of superplasticizer and wetting agent on volumetric and mechanical properties of cold recycled mixture with asphalt emulsion," *Advances in Materials Science and Engineering*, vol. 2020, pp. 6251653–11, 2020.
- [13] Li Jin, M. Yu, X. Cui, and W. Wang, "Properties and components of recycled engine oil bottom rejuvenated asphalt and its grey relationship analysis," *Advances in Materials Science and Engineering*, vol. 2019, Article ID 2462487, 11 pages, 2019.
- [14] M. Yu, Li Jin, X. Cui, D. Guo, and X. Li, "Antiageing performance evaluation of recycled engine oil bottom used in asphalt rejuvenation," *Advances in Materials Science and Engineering*, vol. 2019, Article ID 2947170, 8 pages, 2019.
- [15] F. Haghshenas Hamzeh, R. Rea, B. Dale, D. F. Haghshenas, R. Gerald, and Z. Martins, "Asphalt binder laboratory short-term aging: effective parameters and new protocol for testing," *Journal of Materials in Civil Engineering*, vol. 32, no. 1, Article ID 04019327, 2020.
- [16] X. Li, J. Shen, P. Shi, and H. Zhu, "Nonlinear modeling of nanoscaled properties of asphalt binders recovered from weathered asphalt mixtures," *Journal of Materials in Civil Engineering*, vol. 32, no. 1, Article ID 04019340, 2020.
- [17] D. Zhang, B. Birgisson, X. Luo, and I. Onifade, "A new long-term aging model for asphalt pavements using morphology-kinetics based approach," *Construction and Building Materials*, vol. 229, Article ID 117032, 2019.
- [18] E. Kim Robin, S. Kang, F. Spencer Billie, Ozer Hasan, and L. Al-Qadi Imad, "Stochastic analysis of energy dissipation of a half-car model on nondeformable rough pavement," *Journal of Transportation Engineering Part B Pavements*, vol. 143, no. 4, Article ID 04017016, 2017.
- [19] D. Wang, H. Zhang, and H. Zhang, "Shearing property and permanent deformation prediction model of cold recycled mixture with emulsified asphalt," *Journal of Jiangsu University. Natural Science Edition*, vol. 38, no. 2, pp. 204–210, 2017.
- [20] Z. Wang, X. Shu, T. Rutherford, B. Huang, and D. Clarke, "Effects of asphalt emulsion on properties of fresh cement emulsified asphalt mortar," *Construction and Building Materials*, vol. 75, pp. 25–30, 2015.
- [21] G. Xu and H. Wang, "Study of cohesion and adhesion properties of asphalt concrete with molecular dynamics simulation," *Computational Materials Science*, vol. 112, pp. 161–169, 2016.
- [22] X. Lv, W. Fan, J. Wang et al., "Study on adhesion of asphalt using AFM tip modified with mineral particles," *Construction and Building Materials*, vol. 207, pp. 422–430, 2019.
- [23] O. Xu, Z. Wang, and R. Wang, "Effects of aggregate gradations and binder contents on engineering properties of cement emulsified asphalt mixtures," *Construction & Building Materials*, vol. 135, pp. 632–640, 2016.
- [24] G. Shashibhushan and D. Singh, "Effects of bio-oil on performance characteristics of base and recycled asphalt pavement binders," *Construction and Building Materials*, vol. 227, pp. 1–13, 2019.
- [25] X. Wang, H. Guo, B. Yang, X. Chang, C. Wan, and Z. Wang, "Aging characteristics of bitumen from different bituminous pavement structures in service," *Materials*, vol. 12, no. 3, p. 530, 2019.
- [26] X. Xie, S. Tong, Y. Ding, H. Liu, and L. Liang, "Effect of the amount of mineral powder on the ultraviolet aging properties of asphalt," *Advances in Materials Science and Engineering*, vol. 2016, Article ID 5207391, 9 pages, 2016.
- [27] M. Zhang, P. Hao, S. Dong, Y. Li, and G. Yuan, "Asphalt binder micro-characterization and testing approaches: a review," *Measurement*, vol. 151, p. 107255, 2020.
- [28] S. Han, S. Dong, M. Liu, X. Han, and Y. Liu, "Study on improvement of asphalt adhesion by hydrated lime based on surface free energy method," *Construction and Building Materials*, vol. 227, p. 116794, 2019.
- [29] X. Zhang, *Influence of Aqueous Solution on Properties of Asphalt and Asphalt Concrete*, Wuhan University of Technology, Wuhan, China, 2018.

## Research Article

# Cold Recycled Asphalt Mixture using 100% RAP with Emulsified Asphalt-Recycling Agent as a New Pavement Base Course

Wilson Unger Filho <sup>1,2</sup>, Luis Miguel Gutiérrez Klinsky,<sup>2</sup> Rosângela Motta,<sup>1</sup> and Liedi Légi Bariani Bernucci<sup>1</sup>

<sup>1</sup>Transportation Engineering Department, Escola Politécnica, University of São Paulo, São Paulo, Brazil

<sup>2</sup>CCR Highway Research Center, Grupo CCR, São Paulo, Brazil

Correspondence should be addressed to Wilson Unger Filho; [wunger87@gmail.com](mailto:wunger87@gmail.com)

Received 27 December 2019; Accepted 27 February 2020; Published 4 April 2020

Guest Editor: Andrea Grilli

Copyright © 2020 Wilson Unger Filho et al. This is an open access article distributed under the Creative Commons Attribution License, which permits unrestricted use, distribution, and reproduction in any medium, provided the original work is properly cited.

The rehabilitation process of asphalt pavements using the technique of milling and filling can cause several environmental problems due to either the disposal of the milled asphalt mix or the exploration of natural resources. One alternative to mitigate these impacts is to reuse this milled material, known as reclaimed asphalt pavement (RAP), in the construction of new pavement layers. Within the several available techniques to reuse the RAP, cold recycling using an emulsified asphalt-recycling agent has shown great potential. The aim of this study is to evaluate the application of a cold recycled asphalt mix using 100% RAP with an emulsified asphalt-recycling agent as a new pavement base course. A trial section was built employing this material as a pavement base course in a heavy traffic highway in Brazil, and its structural behavior was monitored for 12 months using a Falling Weight Deflectometer (FWD) to assess its performance over time. Furthermore, a laboratory-testing program was performed to evaluate the recycled mixture stiffness and strength through resilient modulus and indirect tensile strength tests. These tests were used to investigate the influence of the storage interval (7, 14, and 28 days) considering the time between mixing and compaction of the mixture. The effect of the curing time after compaction (1, 3, 7, 26, and 56 days) was also assessed. It was verified in laboratory and in the trial section that the stiffness increases with curing time. Furthermore, the backcalculated elastic resilient moduli indicated values in the same order of magnitude to those obtained in the laboratory tests. In addition to the laboratory test findings, it was also observed that the longer the period of storage, the higher the values of stiffness and tensile strength for short periods of curing. This behavior was not verified when longer curing periods were used. In general, the use of cold recycled asphalt mixtures as base course of new pavements proved to be a promising alternative to reuse RAP.

## 1. Introduction

Reclaimed asphalt pavement (RAP) is produced from milled deteriorated asphalt pavement and has been used in new hot or cold asphalt mixtures. The advantages of using RAP include reducing the exploration of virgin material, saving cost and decreasing the use of natural resources, and providing less environmental damage [1].

During the 1990s, the technique of pavement base in-place recycling with RAP became a common solution in Brazil. However, the rate of recycling Brazilian asphalt layers for application in new pavements is still low, and it may be

explained by the belief that conventional hot asphalt mixtures have better performance than the recycled ones.

Recycling techniques may be classified in several manners. For example, the Asphalt Recycling and Reclaiming Association (ARRA) defines five categories: cold planning, hot recycling, hot in-place recycling, cold recycling (in-place or in central plant), and full depth reclamation. The selection of which recycling technique is the most appropriate for each rehabilitation project, balancing advantages and disadvantages of each one, depends on several factors, such as level of pavement degradation and equipment and materials availability.

Cold recycling should be the preferred recycling method due to the economic benefits to be achieved by reducing the consumption of production energy and natural resources [2]. When performed at the right time, that is, prior to full degradation of the pavement structure, maintenance costs can be reduced by 30% to 50% over conventional milling and filling solutions [3]. In addition, it is possible to reuse the full asphalt layer, minimizing virgin materials acquisition, transportation, construction periods, and landfilling.

This research has the objective of evaluating the application of a cold recycled asphalt mix using 100% RAP produced with an emulsified asphalt-recycling agent for a new pavement base course. For assessing the mixture's performance in the field, 2 km of a new pavement lane was built as a trial section of a heavy traffic highway in São Paulo, Brazil. The structural behavior was monitored through FWD in the field for 12 months after construction. Additionally, samples of the cold recycled mixture were collected during the construction of the trial section and were used in a laboratory program to investigate the effects of material storage and curing time. The storage period here refers to the time between mixing and compaction and the curing time refers to the time elapsed after compaction until tests are performed.

## 2. Cold Recycled Asphalt Mixtures with Emulsified Asphalt-Recycling Agents

Cold asphalt recycling can be produced with different additives and materials, mixed in place or in specific recycling plants. Thus, the recycling methodology is usually classified as granulometric stabilization, chemical stabilization (with lime, Portland cement, or fly ash), and asphaltic stabilization (emulsified or foamed).

Emulsified asphalt (or asphalt emulsion) is a suspension of small asphalt binder droplets in water with the help of an emulsifying agent by mechanical action [4]. Emulsified asphalt-recycling agents, as designated by ARRA [5] and FHWA [3], are products specifically developed for cold asphalt recycling and can contain mineral or vegetal additives to partially rejuvenate the RAP residual asphalt. An emulsified asphalt-recycling agent is formulated to enhance some characteristics of the final recycled asphalt mix for both mechanical and workability purposes.

Cold recycled mixtures are usually classified as stabilized or asphalt mixtures, depending on their mechanical properties. For example, the stabilized mixture has low amounts of nonactive asphalt binder residue in the RAP, which may have low influence in the mechanical behavior of the mix. In that case, the stabilized mixtures show a hybrid behavior between a granular material and a cemented material or hot mix asphalt [6].

On the other hand, when the asphalt binder residue in the RAP is active, it is considered as an asphalt recycled mixture, so traditional methodologies may be used for the mixture design. In this case, the emulsified asphalt-recycling agent is specifically selected for RAP with active residual asphalt binder [5].

Another aspect that should be recognized is the manner in which the recycling materials coat the RAP. For example, the foamed asphalt is distributed in small spots of asphalt binder in the RAP surface after the asphalt bubbles explode. This procedure creates many bonding points, generating a mix with a behavior between a granular material and an asphalt mixture. Still, in the case of the emulsified asphalt-recycling agent, after the emulsions rupture, the spots of the asphalt binder flow to the RAP surface. Therefore, a thin and continuous asphalt film, such as an asphalt mixture, covers the RAP surface. However, the bonding is weaker than in the latter because of the thickness of the asphalt film [6].

It is important to consider that cold asphalt mixtures, recycled or not, lose moisture over time, which is usually recognized as the curing period. During this period, the cold asphalt mixtures tend to increase the mechanical resistance regarding tensile strength and stiffness. Also, in this period the interaction between the recycling agent and the RAP residual aged asphalt is developed [5], at least with its most external layer. This mechanism could be explained by the molecular mass exchange between the aromatics molecules and the residual asphalt binder [7].

Studies have investigated the influence of different recycling agents, contents, compaction method and energy, granulometry correction, and curing period [8, 9], such as those by Andrade [10]. However, the storage period has not been studied systematically. The influence of the storage period in the mechanical behavior of the final recycled asphalt mix is very important for the logistics when recycling asphalt plants are far away from the construction site. For an overall view, the mechanical properties of cold recycled asphalt mixtures from different studies are summarized in Table 1. It is noted that the curing time, curing temperature, and compaction do not follow a standardized protocol; thus, it is difficult to perform further comparative analysis. The use of cement in cold recycled asphalt mixtures allows the improvement of the strength by promoting demulsification of emulsified asphalt and producing cement hydrates [12].

Additionally, Meocci et al. [2] noted that the commonly used accelerated curing process (72 h at 40°C) did not allow the definitive mixture strength and stiffness to be reached, obtaining higher values after 10 days, a behavior that should also be evaluated in this research with a variation in the curing time. The same authors also observed an evolution of stiffness in deflection measurements with 29 and 90 days in the field.

Finally, another characteristic that affects the curing of recycled mixtures is the influence of temperature. During curing, higher temperatures resulted in higher modulus increase and maximum values, while at low temperatures the curing process is slower, which does not penalize the potential performance of the mixture [14].

## 3. Materials

*3.1. RAP and Emulsified Asphalt-Recycling Agent Characterization.* Ten thousand tons of RAP from maintenance activities of the highway were available for the current study. Three samples were collected at different

TABLE 1: Mechanical properties of cold recycled asphalt mixtures with emulsified asphalt-recycling agent.

Authors	Indirect tensile strength (ITS) <sup>(1)</sup>	Resilient modulus <sup>(1)</sup>	Curing period	Storage period	Compaction	Portland cement?	Observations
David [8]	—	3,000 MPa to 3,500 MPa	24 h at 60°C	Not specified	Marshall	Yes	Resilient modulus at ITS configuration
Silva [9]	0.35 MPa	1,000 MPa to 1,200 MPa	7 and 28 days	Not specified	Modified Proctor	Yes	Resilient modulus at triaxial configuration, almost not influenced by confining stress
Andrade [10]	-	1,000 MPa to 1,200 MPa	28 days at 60°C +	Not specified	Modified Proctor	Yes	Resilient modulus at triaxial configuration, almost not influenced by confining stress
Mollenhauer et al. [11]	0.4 MPa (7 days) 0.6 MPa (14 days) 0.1 MPa (2 days) 0.2 MPa (3 days)	—	7 and 14 days	Not specified	Marshall and gyratory compactor	Yes	Resilient modulus at ITS configuration
Ma et al. [12]	0.3 MPa (4 days) 0.4 MPa (7 days) 0.4 MPa (3 days)	—	2, 3, 4, and 7 days at room temperature and 48 h at 60°C	Not specified	Marshall	Yes	Average ITS from 3 different recycling agents
Meocci et al. [2]	0.7 MPa (13 days)	4,000 MPa 5,000 MPa	72 h at 40°C and additional 10 days at 20°C, resp.	Immediately	Gyratory compactor	Yes	Use of cement increased the values of ITS and RM
Raschia et al. [13]	0.4 MPa (28 days) <sup>(2)</sup> 0.6 MPa (28 days) <sup>(3)</sup>	3,000 MPa <sup>(3)</sup>	14 days at room temperature and 14 days at 40°C	Not specified	Gyratory compactor	No	Values from samples mixed and compacted at 25°C <sup>(2)</sup> soft asphalt <sup>(3)</sup> Hard asphalt
Raschia et al. [13]	0.4 to 0.5 MPa (28 days) <sup>(3)</sup>	2,000 MPa <sup>(3)</sup>	14 days at room temperature and 14 days at 40°C	Not specified	Gyratory compactor	No	Values from samples mixed and compacted at 5°C <sup>(3)</sup> hard asphalt

<sup>(1)</sup>Resilient modulus and indirect tensile strength were measured after the curing time. <sup>(2)</sup>soft asphalt. <sup>(3)</sup>hard asphalt.

points of the pile, and then the RILEM (*Réunion Internationale des Laboratoires d'Essais et de Recherches sur les Matériaux et les Constructions*) guidelines were followed to analyze gradation, binder content, and binder consistency [15] in laboratory. As shown in Figure 1, the three RAP samples were in accordance with the medium gradation suggested by ARRA [16]. The average grading curve after the asphalt binder extraction (white curve) is also shown.

The Soxhlet extraction method was used to determine the asphalt binder content of the RAP samples. The results showed a slight variability among their contents (5.3%, 4.7%, and 4.9% of residual asphalt binder). Also, the Abson method [17] was used to obtain the residual asphalt binder and its penetration, and softening points were analyzed. The results showed penetration between 10 and 11 ( $\times 10^{-1}$  mm) and a softening point between 92°C and 95°C, showing lower

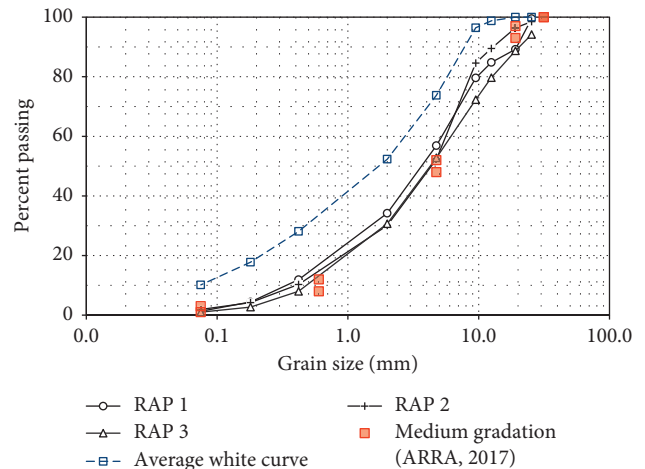


FIGURE 1: Grain-size distribution of the RAP samples.



penetration and a higher softening point than virgin asphalt binder values, even after the Rolling Thin Film Oven Test [18]. The asphalt binder, simulated by the RTFOT test after hot mixing, should have presented a maximum softening point of 60°C and penetration between 15 and 22 ( $\times 10^{-1}$  mm). Therefore, the values obtained demonstrate the aging of the residual asphalt binder.

The emulsified asphalt-recycling agent used in this study contained SBS (Styrene-Butadiene-Styrene), a cationic slow set emulsion with a mineral rejuvenating agent, developed specifically for the RAP under study. It considered the degree of oxidation of the RAP residual binder, the surface energy, and the specific surface area (SSA) characteristics of the RAP [19].

**3.2. Cold Asphalt Recycled Mixture Design.** Marshall Compaction was used to prepare specimens containing 2.0%, 2.5%, and 3.0% of the emulsified asphalt-recycling agent. After compaction with 75 blows per face, specimens were cured for 72 h at 60°C and later maintained at room temperature for 24 h. The results of the Marshall Stability test showed that specimens with 2.5% of the emulsified asphalt-recycling agent had the higher values. This amount was then defined as the design content to be used in the recycling project, following the mix design of ARRA [5].

It is known that the addition of cementitious materials, such as lime or Portland cement, can increase tensile strength and stiffness. However, in this study it was added only the emulsified asphalt-recycling agent.

**3.3. Cold Asphalt Recycled Mixture Production.** The production of the cold asphalt recycled mixtures was performed using a stationary recycling plant, RT-500, shown in Figure 2. This plant has specific parts to crush and sieve the RAP, and a 31 mm sieve was used to limit RAP particles at this maximum size.

During the cold asphalt recycled mixture production, 500 kg of this material was collected for characterization in a laboratory program. This material was stocked loose in the laboratory at room temperature until the respective tests were performed. It is important to mention that the same materials used in the cold recycling plant in this project were provided to the laboratory tests.

As the RAP moisture content was found at 2.5% and the addition of emulsion included 1.0% of water, the final moisture content of the recycled mixture was around 3.5%. In order to prevent the variation of moisture content by either rain or evaporation, the recycled mixture remained covered in the field with plastic, while in laboratory the material remained stored in a closed plastic barrel.

## 4. Laboratory Study

**4.1. Influence of the Method and Energy Compaction.** The first part of this study sought determining which method and energy of compaction would be used in the laboratory program. To evaluate how each compaction method would affect the bulk density of the compacted mix and

consequently the air voids, three methods and six energies were analyzed: (i) modified Proctor (MPT), (ii) Marshall with 50 and 75 blows (M50 and M75) on each side, and (iii) gyratory compactor with 50, 75, and 100 gyrations (G50, G75, and G100). Three specimens were molded per condition. The average results are shown in Figure 3.

As seen in Figure 4, indeed, the specimens molded using a modified Proctor test showed the lowest bulk density and consequently the highest air voids content, while the ones compacted using the gyratory compactor presented higher bulk density and lower air voids. That difference of apparent bulk depending on the type of compaction and the energy applied presents itself as a reasonable explanation of the different results found in this paper when compared to other researches, as shown above.

Although the specimens compacted in the gyratory compactor present higher values of indirect strength and resilient modulus, in Brazil such compaction would hardly be achievable on the field because of the available compaction equipment. For this field research, a tandem roller was first used for the compaction of the cold recycled mix. A 9-wheel roller weighting approximately 25,5t rolled 16 times, and then a tandem roller was again used for finishing. The use of a sheep foot roller was also tested; however, due to the irregularity caused in the layer without a compaction gain, it was decided to use only tandem and tire rollers. Regardless of the number of rollings, it was not possible to achieve a higher compaction density than the one found by the Marshall method with 75 blows per side.

**4.2. Storage and Curing Times Influence.** The storage period and curing time effects on ITS and resilient modulus were evaluated in laboratory. Three storage periods 7, 14, and 28 days were selected in this study to assess the influence of the time between the mixing and the compaction of the cold recycled asphalt mixture with the asphalt emulsified asphalt-recycling agent.

After compaction, the cylindrical specimens were cured for 1, 3, 7, 14, and 28 days, until ITS [20]; and resilient modulus [21] were performed. Three specimens were compacted at each condition of storage periods and curing time using a Marshall compactor with 75 blows per face, as recommended by ARRA [5].

After compaction, each specimen was cured for 72 h at 60°C in a forced air oven to accelerate the initial curing period. Only 1-day specimens were kept at this condition for 24 h. After that, specimens were then cured at room temperature at 25°C. ITS and resilient modulus tests were performed at 25°C. Figures 3 and 5 show the results of both tests, respectively, indirect tensile strength and resilient modulus.

The results show that three days of curing increased significantly the stiffness and strength of the cold recycled mixes. It is observed that storing the loose mixes for 28 days did not spoil their mechanical behavior; on the contrary, the resilient modulus and the tensile strength were increased, proving that these types of mixtures can be stored. After 1-day curing, specimens that were compacted after the storage periods of 7 and 14 days did not have enough cohesion to be



FIGURE 2: Cold in-place recycling train set up as a stationary cold central plant recycling.

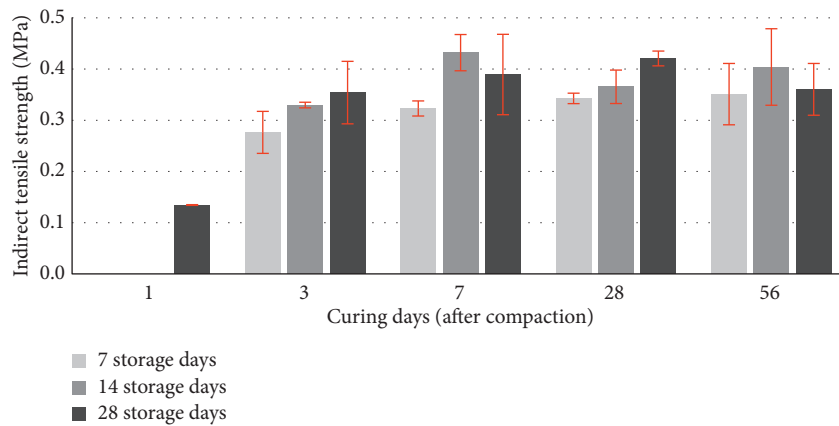


FIGURE 3: Tensile strength after a storage period of loose mix during 7, 14, and 28 days and curing time and compaction of 1, 3, 7, 28, and 56 days.

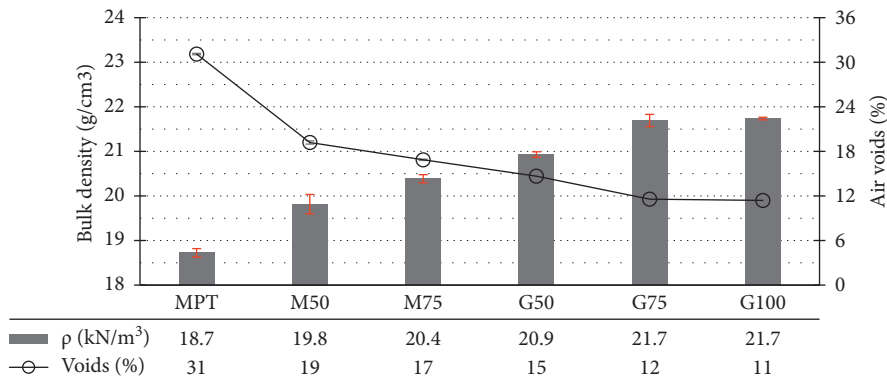


FIGURE 4: Bulk density and air voids depending on the type of compaction and compaction energy.

tested at the tensile strength. This behavior may denote that the moisture reduction is not the only reason for the stiffness and strength increases, but also the time of interaction between the aged asphalt and the emulsified asphalt-recycling agent influences the mechanical behavior of these recycled mixtures.

The mixtures stored for 7 days produced specimens that, after 7 days of curing, had average tensile strength below 0.3 MPa, that is, the minimum recommended value by

ARRA [16]. However, when the same mixtures were stored for 14 and 28 days, the values attended this recommendation, showing again that there was an interaction between the aged asphalt and the emulsified asphalt-recycling agent during the storing period.

The ITS results found in this research were similar to some previously presented studies, with a particularity, with the exception of the mixture evaluated in the study of Raschia et al. [12]; the others had some cement Portland

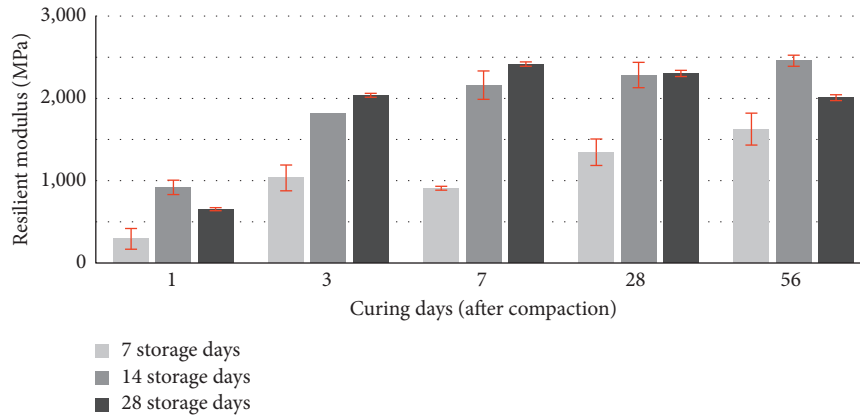


FIGURE 5: Resilient modulus after a storage period of loose mix during 7, 14, and 28 days and curing time and compaction of 1, 3, 7, 28, and 56 days.

content, which may explain similar tensile strength values even for specimens compacted in smaller energies, such as the modified Proctor [9].

When compared to results obtained by Mollenhauer et al. [11] and Raschia et al. [12], ITS values of the current research were lower. In this case, besides the Portland cement content in the study of Mollenhauer et al. [11], the compaction method used by them was the gyratory compaction, which may have provided a better compaction and, consequently, lower air voids. However, when compared to the research of Ma et al. [10], which used the Marshall compactor, the ITS values of the current research were similar, although the curing time was shorter. It is important to point out that Ma et al. [10] used cement Portland in the mixture, which not only enhances the strength, but also quickens the curing process because the cement consumes the water from the mix due to its hydration. Regarding the resilient modulus, results obtained in this study are quite similar to those of other researches previously shown in Table 1, ranging from 1,500 to 2,000 MPa.

When compared, for example, to the values obtained by Silva [9] and Andrade [13], the results of resilient modulus obtained were higher. However, the test configuration and compaction methods were different. Those authors molded the specimens with modified Proctor (resulting in lower specimen compaction) and tested them using a triaxial configuration. In comparison with the research by Raschia et al. [12], when analyzing mixing and compaction at 25°C, lower stiffness values were found. That difference can be correlated with compaction, but in this case the gyratory compactor resulted in better compaction, yielding higher stiffness values.

## 5. Test Section Construction and Monitoring

The designed pavement structure for the trial section was constructed in a heavy traffic highway in Brazil, and it is presented in Figure 6. As seen, 150 mm of the cold recycled mixture was designed as a base course. In addition, keeping the sustainability view of this research, the subgrade

Micro surfacing	12 mm
Hot mix asphalt	50 mm
Base: RAP cold recycled mix	150 mm
Subbase: Well-graded crushed stone	200 mm
Subgrade reinforcement: Recycled construction and demolition	400 mm
Subgrade	-

FIGURE 6: Designed pavement structure for the trial section.

reinforcement was also designed with recycled aggregates from construction and demolition waste.

The average daily number of commercial vehicles in one year is around 9,000. Similar to the trial section in the fast lane (leftmost lane), the heavy traffic vehicles in the project lane correspond to 3% of the total (270 heavy vehicles) and AASHTO Equivalent Single Axle Load (ESAL), in this lane, is  $1.7 \text{ E} + 06$  for a 10-year project, which is 3% of the total in the runway of  $5.7 \text{ E} + 07$  ESALs. As the test section has lighter traffic than the other lanes, it is expected to perform better in the long term regarding permanent deformation and fatigue life.

In terms of the construction process, the cold recycled mixture was produced in the stationary recycling plant and stored for 30 days. The construction of the cold recycled mixture layer was done in two layers, aiming at 150 mm of thickness after compaction. The second layer execution only began when the bottom layer achieved a moisture content under 3%. The tack coat between both cold recycled mix layers was made using the Rapid Set Emulsion at the rate of  $0.4 \text{ l/m}^2$ . Figure 7 shows the cold recycled mixture after the first use of the steel wheel roller.

The compaction control indicated at least  $21.03 \text{ kN/m}^3$ , aiming at achieving a degree of compaction of 95% or higher. After finishing the recycled layers, 50 mm of hot mix asphalt was used as a wearing course. The time between the execution of the second layer of cold asphalt recycled mix and the hot asphalt mix asphalt was between 5 and 15 days, depending on the construction progress and the cold asphalt recycled mix moisture content (3%).





FIGURE 7: Construction of the first layer of the cold recycled mixture.

Subsequently, in an effort to redress the horizontal signing of the road, a 12 mm layer of micro surfacing was placed. The completed additional lane is presented in Figure 8.

Construction activities at the trial section proved that the cold recycled mixtures have good workability and the equipment needed is the same used regularly in the construction of new asphalt pavements.

After the construction of the trial section, the structural monitoring activities began. As a result, the deflection basins were measured using a FWD, with a standard load of 20.1 kN. The analysis of the deflection condition aimed to assess the recycled mixture stiffness increase of regular traffic along the curing process in the field over time. As shown in laboratory evaluation, stiffness of the recycled mixture should increase after the curing process.

The FWD deflection measurements were made after 7, 90, 180, and 360 days of the trial section construction. “ $D_x$ ” corresponds to the deflection value measured at “ $x$ ” mm of the load application point. Thus, the  $D_0$  values (vertical displacement under the point of the load) obtained were corrected to a reference temperature of 25°C and can be seen in Figure 9.

It was noted that the deflection values were reduced during the curing period of the pavement structure. Also, field results show an improvement of the structural behavior in terms of pavement stiffness, probably due to the curing process. As the other pavement layers do not have characteristics that could justify this deflection reduction, curing of the recycled mix may provide a significant stiffness increase over time. However, it is important to point out that the first FWD measurement survey was made right after construction in March, which is the end of the rainy season in the state of São Paulo. In contrast, other measurement surveys occurred in August, October, and again March, 360 days later. Climatic conditions of a city nearby the area of the trial section are presented in Figure 10.

In order to mitigate this doubt, the  $D_{1200}$  (vertical displacement measured at 1200 mm from the load) points from

the deflection basins were also analyzed, aiming at identifying if the moisture content of the subgrade could have influenced the  $D_0$  values. Results showed that the  $D_{1200}$  values have remained in the same baseline as seen in Figure 11. This analysis confirmed that the moisture content of the subgrade might not have influenced the results of  $D_0$  from the first to later field surveys.

Another parameter that can be used to evaluate the base stiffness is the Base Damage Index (BDI). The BDI is the difference between the displacements measured at 300 mm ( $D_{300}$ ) and at 600 mm ( $D_{600}$ ) in the FWD loading plate. It is considered as the best indicator of the pavement base layer condition, being inversely proportional to its stiffness [22]. BDI values greater than 400  $\mu\text{m}$  result in a deficient pavement [23]. The results obtained in this analysis are presented in Figure 12. For the BDI trial section analysis, 100  $\mu\text{m}$  was adopted as a limit for a “great base condition.” It is important to highlight that as this parameter is determined using  $D_{30}$  and  $D_{60}$ , any data distortion due to temperature correction on  $D_0$  would not affect the BDI value.

The BDI assessment showed an expressive stiffness increase of the cold recycled mixture along the curing time. From Figure 12, it is noted that the higher values were about 90  $\mu\text{m}$ , while the lower BDI values are 40  $\mu\text{m}$ . This behavior agrees to the tendency observed previously in this paper regarding the laboratory tests results.

In addition to stiffness, the resistance to permanent deformation was also measured by measuring rutting. A possible deformation could have occurred by any of the granular layers, by deformation of the hot mix asphalt or cold recycled mixture, or by an integration of all deformations. To measure the rutting, a Dynatest pavement scanner equipped with two high-performance 3D lasers was used, which is capable of generating a sectional road surface with a resolution of one millimeter. The measurement was performed one and a half years after the test section construction.

The local transport agency (*Agência de Transporte do Estado de São Paulo* (ARTESP)) requires a maximum



FIGURE 8: Additional lane to the left opened to traffic.

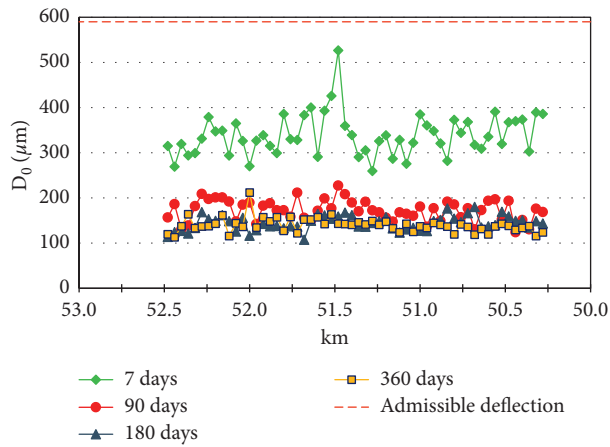


FIGURE 9: Maximum deflection  $D_0$  measured with FWD after 7, 90, 180, and 360 days of the trial section construction.

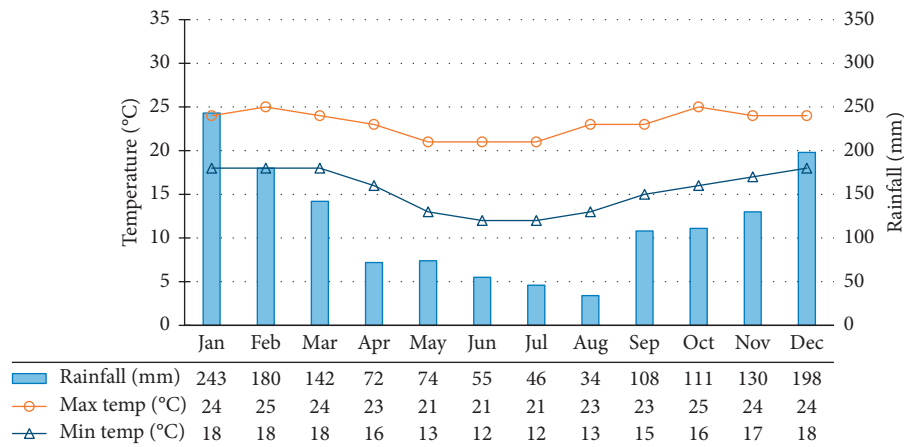


FIGURE 10: Annual temperature and precipitation in the trial section area: Araçariçuama (source: <https://www.climatempo.com.br/climatologia/2206/aracariguama-sp>).

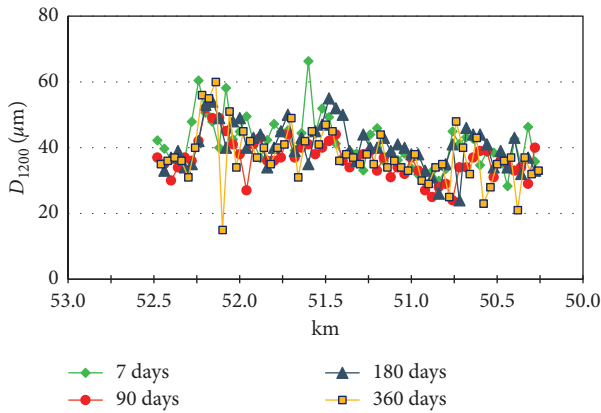


FIGURE 11: Deflections  $D_{1200}$  measured with FWD after 7, 90, 180, and 360 days of the construction.

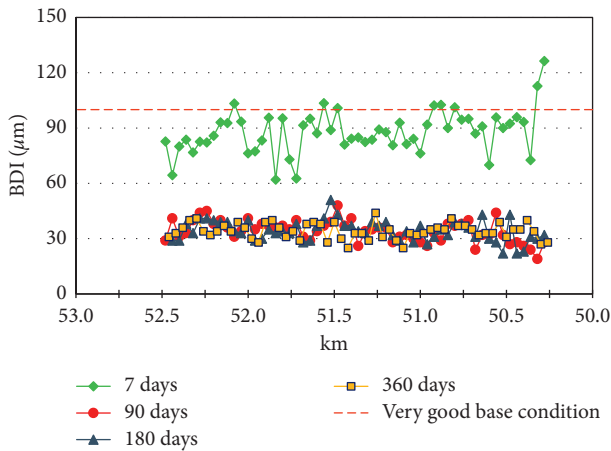


FIGURE 12: Base Damage Index (BDI).

average rutting of 7 mm per kilometer. The rutting was calculated every 40 m, and the average between the left rutting and right rutting was obtained. Figure 13 shows the average rutting values at every 40 m, as well as the average per kilometer.

Although it was not possible to measure the evolution of rutting from construction to the current measurement (545 days), it is possible to verify that one year and six months after construction the average rutting is low, at about 4 mm in the most critical segment, with isolated points measuring a maximum of 6 mm. In addition, as mentioned earlier, the 4 mm corresponds to the sum of the permanent deformations in each of the layers; that is, the deformation of the recycled cold asphalt layer was even less, indicating that it can have a good resistance to permanent deformation.

Another parameter measured was an evolution of longitudinal road profile, by measuring of the International Roughness Index (IRI). Measurements were performed with a laser profilometer 180 and 545 days after the construction of the test section. For a better understanding of the results, the IRI values were integrated every 200 m and are shown in Figure 14.

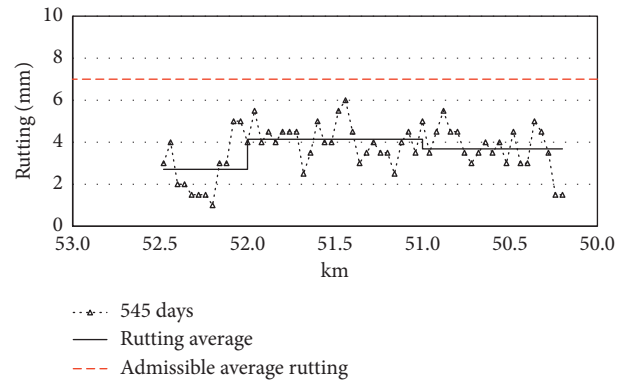


FIGURE 13: Rutting measured with a 3D laser pavement scanner after 545 days of the construction.

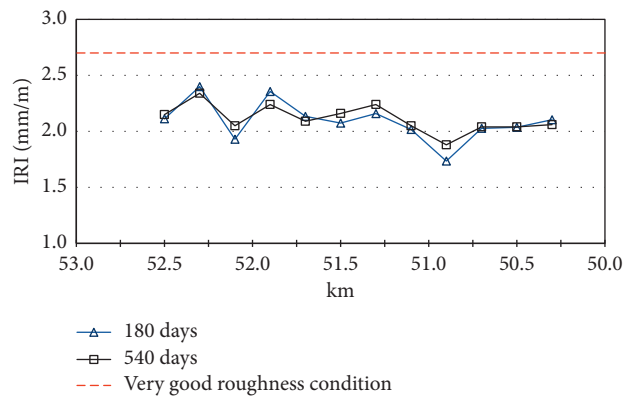


FIGURE 14: International Roughness Index (IRI) after 180 and 545 days of the construction.

The IRI variation was negligible over 1 year. The average IRI in the test section remained at 2.1 mm/m, with small variations in size. Thus, it is possible to affirm that the longitudinal irregularity did not evolve in that first year of evaluation. The evolution of the irregularity may be indicative of the evolution of pavement defects, which was not shown in the analyzed period.

**5.1. Backcalculation.** The last analysis regarding the evolution of the cold recycled mixtures stiffness was the backcalculation in terms of elastic moduli. The software EVERCALC was used, resulting in several simulations of multiple linear elastic layers. Each basin was backcalculated individually, obtaining an elastic modulus for each tested layer.

The first measurement, 7 days after the construction was finished, indicated that the cold recycled mixture layer had an average elastic modulus of 358 MPa and a coefficient of variation (CV) of 43%. When performing the second measurement, despite the wide range of values, the average modulus increased to 1,725 MPa, and CV was 37%. By the third measurement, 180 days later, the elastic modulus remained the same as the previous one, at an average value of

TABLE 2: Main environmental gains with the recycled pavement in section test.

Material	Amount
RAP	2,800 t
Construction and demolition waste	7,900 t
Hot mix asphalt	-610 t
Crushed stone	-14,800 t
Soil excavation and disposal	-4,000 t
Fuel consumption in hot mixing asphalt plants	-45 t

1,840 MPa and a 36% CV. By the last measurement, 360 days later, the average modulus was 1,835 MPa with a CV of 27%.

The values obtained in the trial section were quite similar to those performed using laboratory tests (around 1,800 MPa). This behavior may demonstrate that the evaluation of stiffness in laboratory could properly estimate the stiffness of the cold recycled mixture from the field.

**5.2. Environmental Aspects and Costs.** The execution of the test segment provided several environmental and financial gains when compared to a conventional solution. The traditional pavement had been designed with 80 mm hot mix asphalt, 150 mm well-graded crushed stone, 400 mm dry macadam, and 400 mm ungraded crushed stone. Table 2 shows the main environmental gains with the recycled pavement.

In addition, it is possible to mention the reduction of energy for mixing the hot mix asphalt and reduction of smoke emissions from the hot mix asphalt in the environment.

At this point, a more complete financial analysis seems hasty, as a correct analysis should be made throughout the entire life cycle of the pavement. However, when comparing the structure adopted with the conventional one previously dimensioned for the same 10-year project period, it was possible to obtain a cost reduction of the pavement of about 14% and 8% of the total cost of construction.

## 6. Conclusions

The objective of this study was to evaluate the application of a cold recycled asphalt mix using 100% RAP produced with an emulsified asphalt-recycling agent, without cement, as a new pavement base course.

- (1) Laboratory analyses first assessed the influence of the storage period and the curing time of the cold recycled mixture. It was observed that the storing time enhanced, at first, the mechanical properties of the cold recycled mixtures, probably because of the interaction between the aged asphalt and the emulsified asphalt-recycling agent in the loose condition of the mixtures. Over the curing time, this initial increase became indifferent, with all samples reaching the same levels.
- (2) A minimum 7-day curing time was required to achieve the minimum ITS recommended by ARRA. The final value of the MR after 56 days of curing was

between 1,500 and 2,500 MPa, which was consistent with other researches and the arbitrated values for the design.

- (3) The final deflection and the final BDI indicated a good structural capacity of the base in terms of stiffness. During the trial section monitoring, after one year and half, there was no sign of distress in the surface, and the pavement stiffness increased during the curing time, reproducing the behavior observed in the laboratory. The rutting and the IRI remained within the maximum values established by the road authority, showing no early increase.
- (4) The variation in rainfall and temperature did not affect the deflection measures. The values in opposite climatic conditions 180 and 360 days after construction were similar.
- (5) Also, it is important to mention that this technique can reuse 100% of the RAP, reducing the cost and the environmental impact of this material. In addition, when the RAP cannot be reused locally in the pavement, it is possible to utilize it for different purposes. The testing results showed that cold recycled asphalt mixtures using an emulsified asphalt-recycling agent prompted improved mechanical characteristics that can be used as an alternative to new asphalt pavement courses.

## Data Availability

The data used to support the findings of this study are included within the article.

## Conflicts of Interest

The authors declare that they have no conflicts of interest.

## Acknowledgments

The authors acknowledge the *Grupo CCR*, CCR Highways Research Center, CCR *ViaOeste* Highway Concessionary, and the Polytechnic School of the University of São Paulo for all their support in this research. This research, the trial section construction, the laboratory program, and the field monitoring were funded by Grupo CCR, and its publication was funded by Grupo CCR.

## References

- [1] J. Zhu, T. Ma, and Z. Dong, "Evaluation of optimum mixing conditions for rubberized asphalt mixture containing reclaimed asphalt pavement," *Construction and Building Materials*, vol. 234, 2020.
- [2] M. Meocci, A. Grilli, F. La Torre, and M. Bocci, "Evaluation of mechanical performance of cement-bitumen-treated materials through laboratory and in-situ testing," *Road Materials and Pavement Design*, vol. 18, no. 2, pp. 376–389, 2017.
- [3] FHWA, *Overview of Project Selection Guidelines for Cold In-Place and Cold Central Plant Pavement Recycling*, Federal Highway Administration, Washington, DC, USA, 2018.



- [4] F. Tang, S. Zhu, G. Xu, T. Ma, and L. Kong, "Influence by chemical constitution of aggregates on demulsification speed of emulsified asphalt based on UV-spectral analysis," *Construction and Building Materials*, vol. 212, 2019.
- [5] ARRA, *Basic Asphalt Recycling Manual*, Asphalt Recycling & Reclaiming Association, Annapolis, MD, USA, 2nd edition, 2015.
- [6] G. Tebaldi, *Cold Recycling*, Arizona Pavements and Material Conference, Tempe, AZ, USA, 2013.
- [7] M. Tia and L. E. Wood, "Use of asphalt emulsion and foamed asphalt in cold-recycled asphalt paving mixtures," *Transportation Research Record: Journal of the Transportation Research Board*, vol. 898, 1983.
- [8] D. David, "Misturas asfálticas recicladas a frio: estudo em laboratório utilizando emulsão e agente de reciclagem emulsionado," Master's degree dissertation, UFRGS, Porto Alegre, Brazil, 2006.
- [9] A. H. M. Silva, "Avaliação do comportamento de pavimentos com camada reciclada de revestimentos asfálticos a frio com emulsão modificada por polímero," Master's degree dissertation, University of São Paulo, São Paulo, Brazil, 2011.
- [10] L. R. Andrade, "Comparação do comportamento de pavimentos asfálticos com camadas de base granular, tratada com cimento e com estabilizantes asfálticos para tráfego muito pesado," Master's degree dissertation, University of São Paulo, São Paulo, Brazil, 2016.
- [11] K. Mollenhauer, D. Simnofske, J. Valentin et al., *Mix Designs for Cold Recycled Pavement Materials Considering Local Weather and Traffic Conditions*, 6th Eurasphalt & Eurobitume Congress, Prague, Czech Republic, 2016.
- [12] T. Ma, H. Wang, Y. Zhao, X. Huang, and Y. Pi, "Strength mechanism and influence factors for cold recycled asphalt mixture," *Advances in Materials Science and Engineering*, vol. 2015, Article ID 181853, 10 pages, 2015.
- [13] S. Raschia, D. Perraton, A. Graziani, and A. Carter, "Influence of low production temperatures on compactability and mechanical properties of cold recycled mixtures," *Construction and Building Materials*, vol. 232, 2020.
- [14] M. Bocci, A. Grilli, F. Cardone, and A. Graziani, "A study on the mechanical behaviour of cement-bitumen treated materials," *Construction and Building Materials*, vol. 25, no. 2, pp. 773–778, 2011.
- [15] D. Perraton, G. Tebaldi, E. Dave et al., "Tests campaign analysis to evaluate the capability of fragmentation test to characterize recycled asphalt pavement (RAP)," *Material Work from RILEM TC 237-SIB "Testing and Characterization for Sustainable Innovative Bituminous Materials and Systems"*, 2015.
- [16] ARRA CR102, *Recommended Mix Design Guidelines for Cold Recycling Using Emulsified Asphalt Recycling Agent*, Asphalt Recycling & Reclaiming Association, Glen Ellyn, IL, USA, 2017.
- [17] ASTM D1856, *Standard Test Method for Recovery of Asphalt from Solution by Absorption Method*, American Society for Testing Materials, West Conshohocken, PA, USA, 2009.
- [18] ASTM D2872, *Standard Test Method For Effect Of Heat And Air On a Moving Film Of Asphalt (Rolling Thin-Film Oven Test)*, American Society for Testing Materials, West Conshohocken, PA, USA, 2019.
- [19] F. Tang, G. Xu, T. Ma, and L. Kong, "Study on the effect of demulsification speed of emulsified asphalt based on surface characteristics of aggregates," *Materials*, vol. 11, no. 9, p. 1488, 2018.
- [20] ASTM D6931, *Standard Test Method For Indirect Tensile (IDT) Strength Of Asphalt Mixtures*, American Society for Testing Materials, West Conshohocken, PA, USA, 2017.
- [21] ASTM D7369, *Standard Test Method For Determining The Resilient Modulus Of Bituminous Mixtures By Indirect Tension Test*, American Society for Testing Materials, West Conshohocken, PA, USA, 2011.
- [22] South African Pavement Engineering Manual, 2014.
- [23] Y. R. Kim and H. Park, "Use of falling Weight deflectometer multi-load data for pavement strength estimation," *Final Report FHWA/NC-2002-006*, Department of Civil Engineering, North Carolina State University, Raleigh, North Carolina, 2002.

## Research Article

# Laboratory Evaluation and Construction of Fully Recycled Low-Temperature Asphalt for Low-Volume Roads

Christiane Raab  and Manfred N. Partl

*Empa, Swiss Federal Laboratories for Material Science and Technology, Duebendorf 8600, Switzerland*

Correspondence should be addressed to Christiane Raab; [christiane.raab@empa.ch](mailto:christiane.raab@empa.ch)

Received 18 December 2019; Accepted 28 February 2020; Published 25 March 2020

Guest Editor: Andrea Grilli

Copyright © 2020 Christiane Raab and Manfred N. Partl. This is an open access article distributed under the Creative Commons Attribution License, which permits unrestricted use, distribution, and reproduction in any medium, provided the original work is properly cited.

Growing economy and increasing pollution evoke the need for more environmentally friendly road construction techniques and the saving of natural resources. In this context, cold recycling plays an important role since, on the one hand, it allows to reduce CO<sub>2</sub> emissions drastically and, on the other hand, it offers a variety of opportunities for high percentages of recycling. Inspired by experience in Sweden, the international project “Optimal Recycling of Reclaimed Asphalts for low-traffic Pavement” (ORRAP) for low-volume roads in the Upper Rhine region aims to develop and establish a new strategy for 100% reclaimed asphalt pavement (RAP) at ambient temperature (20°C) without adding virgin bituminous binders or rejuvenators. The still ongoing research project involves laboratory experiments as well as in situ test sections. The link between small-scale laboratory experiments and in situ testing is provided by medium-scale traffic simulation in the laboratory. This paper describes results from medium-scale compaction in the laboratory using different methods as well as traffic simulation with a medium-scale mobile traffic load simulator. The results show that compaction in the laboratory at ambient temperature (20°) is very difficult to achieve. Nevertheless, it was found that compaction at a temperature of 60°C appears possible and provides promising results regarding stability and rutting enabling the in situ construction. The in situ pavement construction at ambient temperature on a low-volume road in Switzerland resulted in a visibly well-compacted and stable base course which was covered by a hot mix asphalt surface course the day after. The test section will be monitored closely over the next 12 months.

## 1. Introduction

For environmental reasons, recycling of reclaimed asphalt pavement (RAP) has become mandatory in many countries and regions worldwide. As a consequence, the accumulation of RAP may lead to enormous piles of RAP which create a problem for local authorities in terms of limited stockyards. This is particularly true, in regions with high-standard infrastructures, dense population, and busy regional road networks, where rehabilitation by far dominates new construction. One of these regions is the Upper Rhine area, combining parts of Germany, France, and Switzerland between the cities of Karlsruhe, Strasbourg, and Basel.

Nowadays, RAP is reused for both hot- and low-temperature asphalt mixtures by adding new material, either as single material components or as certain percentages of new

asphalt mixture [1, 2]. In case of hot recycling, bituminous binders and/or rejuvenators are added whereas, for low-temperature recycling emulsions, foam bitumen and other components are used [3, 4]. However, adding new material means that one can only get close to 100% recycling of RAP.

By applying 100% recycling technology for low-volume roads using RAP at ambient temperature without adding new bituminous binder or other components, the current RAP recycling rate could be further increased, reducing road rehabilitation costs and minimizing environmental impacts, such as CO<sub>2</sub> emissions, energy consumption, and consumption of natural material resources. Thus, significant ecological and economic gains could be realized for the management bodies of low-traffic communal roads, which account for about 50% of the road network in the Upper Rhine region.

The application of such a method using cold recycling of reclaimed asphalt aggregates without binder addition is the aim of the ORRAP “Optimal Recycling of Reclaimed Asphalts for low-traffic Pavements” [5] project funded by ERDF-INTERREG V (3.1 ORRAP) [6], the Canton Aargau, and the Swiss confederation.

The ongoing project ORRAP is based on successful experiences in Sweden where the method was carried out in field trials on municipal roads and on low-traffic highways several years ago [7, 8]. Here, 100% RAP aggregates were used at ambient temperature for base courses, which were later covered with hot asphalt surface layers. According to the Swedish experience, the base courses constructed at ambient temperature require postcompaction by traffic as well as curing to settle and gain their ultimate strength. Therefore, they were left uncovered for at least 6 months. However, during this time, serious restrictions on the traffic regime, such as speed limits, had to be imposed. Since this long maturing process was not considered a feasible strategy for the 3 countries involved in ORRAP, the Swedish recycling technique was re-evaluated proposing an improved recycling and construction technique. In addition, for more homogeneous load distribution and avoiding early restrictions on traffic regimes, the 100% RAP base course of the realized in situ test section was covered with a hot mix surface course.

The ORRAP project includes a comprehensive study of the proposed recycling technique and its application. It consists of 6 work packages as shown in Figure 1.

Since the research is a collaboration between 3 different country regions, all work packages were distributed among the partners and RAP from the 3 different locations in Switzerland, France, and Germany was chosen and tested.

## 2. Objective

The objective of this paper is to present the results and conclusions of the medium-scale compaction evaluation in the laboratory with different compaction methods using different RAP materials provided by Switzerland, France, and Germany. Further, results from the traffic simulation with the medium-scale traffic load simulator and the large wheel rutting tester including all RAP materials from the different countries are shown and discussed. The last part of the paper describes the construction of the Swiss in situ test section, a road connecting the villages of Wahlen and Büsserach in the Canton Basel Landschaft.

## 3. Materials and Methods

The ORRAP project is composed of different work packages and tasks as shown earlier. Work package WP 2 “recipe design” includes material characterization, laboratory testing, and construction of a test section construction. Laboratory testing can be divided into two phases. In the first phase, small-scale laboratory testing was done [9, 10]. In a second phase, a medium-scale traffic simulation in the laboratory was carried out providing the connection to the next phase which aims at constructing an in situ low-traffic

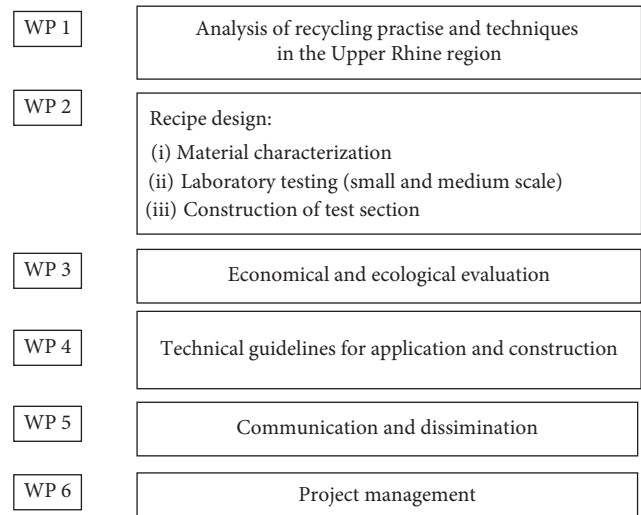


FIGURE 1: ORRAP work packages.

test section in Switzerland with 100% RAP. This test section will be closely inspected and assessed for at least one year, providing practical construction and performance information for producing a technical guideline for application and construction. In this context, the Swiss Federal Laboratories for Material Science and Technology (Empa) was given the task of the medium-scale traffic simulation in the laboratory.

A detailed flowchart of the experimental program of WP2 is depicted in Figure 2. The tasks shadowed in grey colour are those that will be discussed in the following. Hence, this paper mainly concentrates on the medium-scale laboratory compaction and testing as well as the first findings from the construction of the Swiss in situ test section.

**3.1. Material.** The material for laboratory testing was provided by the associate partners of the different countries, coming from 3 different RAP sources. It was taken from existing unprotected open-air piles of stored RAP as shown in Figure 3. The material was processed to the size of 0/16 mm and 0/22 mm (Swiss test section) and transported to the different laboratories in big bags.

Prior to the laboratory investigation and testing, the RAP aggregate material 0/16mm was homogenized and portioned by pouring it through a riffle box as described in the European standard [11]. For the in situ test section between Wahlen and Büsserach, the Swiss RAP 0/22 aggregate material was taken as such.

Figure 4 and Table 1 present the material characteristics of RAP from different countries. All values including the presented grading curve in Figure 4 are mean values of two material characterizations. The results from the recovered bitumen are depicted in Table 2.

**3.2. Methods.** Testing was conducted in two steps. In the first step, the compatibility of small laboratory specimens was investigated. Then, based on these results, in the second step,



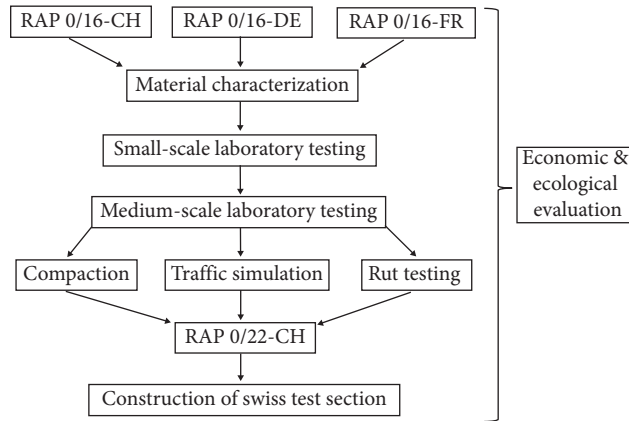


FIGURE 2: Flowchart of the experimental program of WP 2.



FIGURE 3: Pile of asphalt aggregates RAP-CH.

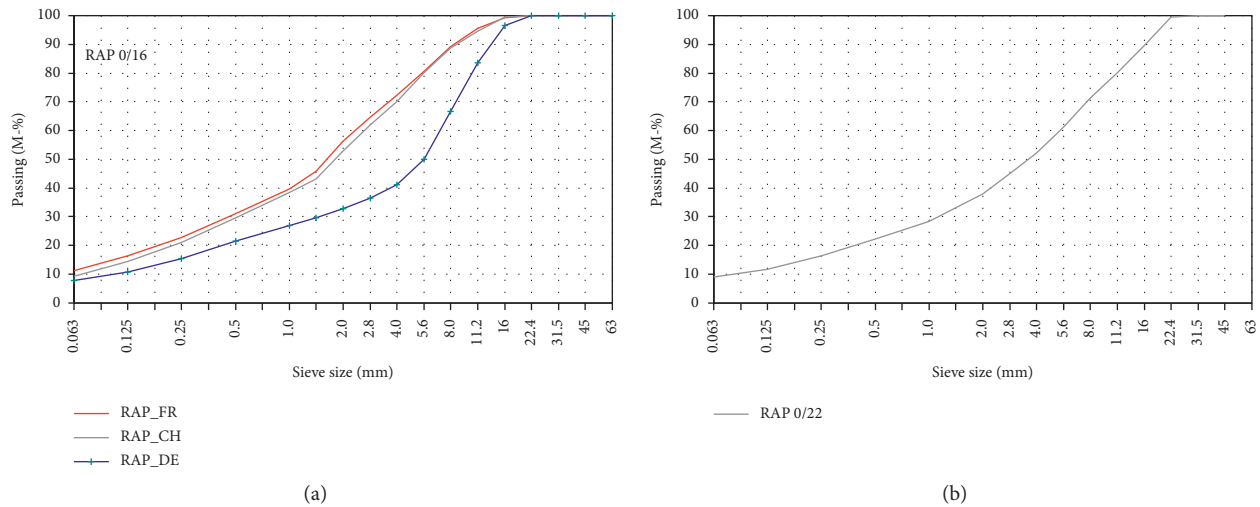


FIGURE 4: Gradation of asphalt aggregates. (a) 0/16 mm RAP. (b) Swiss RAP 0/22.

TABLE 1: RAP Material characteristics (mean values).

RAP source	Binder content (mass-%)	Density (kg/m <sup>3</sup> )	Water content (mass-%)
<i>RAP 0/16</i>			
CH (Switzerland)	6.2	2.371	1.6
DE (Germany)	4.3	2.347	3.5
FR (France)	6.3	2.408	5.0
<i>RAP 0/22 mm</i>			
CH (Switzerland, test section)	4.0	2.387	4.4

the compaction of medium-size specimens was performed. These medium-size specimens were used for an investigation with the standardized, large wheel rutting tester as well as a medium-scale laboratory traffic simulator, the so-called model mobile load simulator MMLS3, for determining their stability and rutting performance.

Small-scale laboratory specimens were compacted using Marshall and gyratory compaction. From this, it became clear that producing stable specimens required increasing either the compaction effort (number of blows or gyrations) or the temperature. In fact, it was found that slightly

TABLE 2: RAP material characteristics (mean values).

RAP source	Penetration (0.1 mm)	Ring & Ball (°C)
CH (Switzerland)	17	69.0
DE (Germany)	17	68.4
FR (France)	16	69.4
CH (Switzerland, test section)	21	68.6

increasing the temperature (60°C instead of room temperature) changed compaction behaviour drastically [10].

For compacting medium-scale laboratory specimens, the following two methods were applied heating up the RAP material to 60°C [10, 12]:

- (i) Medium-size specimens (500 mm × 180 mm, height 100 mm) for the large wheel rutting tester were produced with the compaction as required for the large wheel rutting tests modified with a modified steel roller instead of a pneumatic wheel [13].
- (ii) Medium-size specimens (1300 mm × 430 mm × 65 mm) for the MMLS3 traffic simulator were produced using a special compactor consisting of a steel roller with a width of 90 mm and a diameter of 35 mm. The steel roller is mounted on a metal frame with rails for displacing the roller horizontally as depicted in [10]. A winder enables the steel roller to be moved in the vertical direction. During compaction, the steel roller is sprayed with water. The compaction was done manually by pushing the steel roller back and forth longitudinally in static compaction mode without vibration. A piece of concrete within the metal frame builds the base for compaction. Specimens were compacted using a wooden frame as lateral confinement. This method produced well-compacted specimens with a total aggregate loss of only about 0.1 mass-% and without in-plane inhomogeneities on the specimen surface [10].

Rutting tests were performed with the large wheel rutting tester at 60°C up to 30,000 cycles as required for heavy traffic roads.

For traffic simulation, the MMLS3 was used [14] applying a scaled tire load of 2.1 kN in one trafficking direction with four 1.05 m distant pneumatic 300 mm wheels that were inflated to 600 kPa (see Figure 5). The machine (length × width × height = 2.4 × 0.6 × 1.2 m<sup>3</sup>) enables about 7200 load applications per hour at a speed of 2.6 m/s. This corresponds to a loading frequency of about 4 Hz for a measured tire-pavement contact length of 0.11 m. The first testing for the RAP 0/16 mm from Switzerland was performed during hot summer months at ambient temperature (25°C) up to 80,000 load passings without lateral wandering of the loading tires [10]. Later, another testing campaign for RAP from Switzerland, France, and Germany was conducted at a temperature of 20°C and up to 50,000 load passings. Rutting was measured with an automatic profilometer at 3 different points within the wheel path of the MMLS3, one in



FIGURE 5: Traffic load simulator MMLS3 situated on top of a specimen.

the middle and two others in 300 mm distance both ways from the middle.

## 4. Laboratory Test Results

*4.1. Rutting Test with Large Wheel Rutting Tester.* The rutting test results of all specimens under laterally confined conditions are shown in Figures 6(a)–6(c). Generally, it appears appropriate to approximate the development of the rut depth  $d$  by a power law (equation (1)).

$$d = aN^q, \quad (1)$$

where  $N$  is the number of load cycles and  $a$  and  $q$  are constants.

This is confirmed by  $R^2$  in the order of around 0.95 for the two replicas of RAP specimens from Switzerland (CH1 and CH2) and France (FR1 and FR2). In fact, as shown in Figure 6, the scatter between the replica of CH and FR is comparatively small. However, it is quite high for the DE mixture.

The reason for this is the different behaviour of the two DE specimens. As shown in the five longitudinal rutting profiles Prof. 1 until Prof. 5 in Figure 7(b), DE2 produced already after 30 load cycles on one side a comparatively high rut depth which migrated towards the middle after 100 load cycles. The reason for this sudden local structural collapse and loss of stability is not clear. However, it could be due to sudden reorientation and local breakage of RAP chunks that were unexpectedly large and concentrated on one side of the specimens. This would mean that these chunks did withstand the compaction process with the steel roller but not the repeated kneading loads of the pneumatic rutting wheel at 60°C. For DE1 in Figure 7(a), the rutting in Prof. 1 is generally a little bit lower than that in Prof. 5. Hence, rutting was not created totally symmetrical even in this case. This would mean that preparation and sieving are extremely crucial for this type of low-temperature RAP material.

Ignoring DE2 by assuming that these values were not representative due to this sudden rutting collapse on one side of the specimen, the comparison of the rutting behaviour of the RAP from different countries is shown in Figure 8.

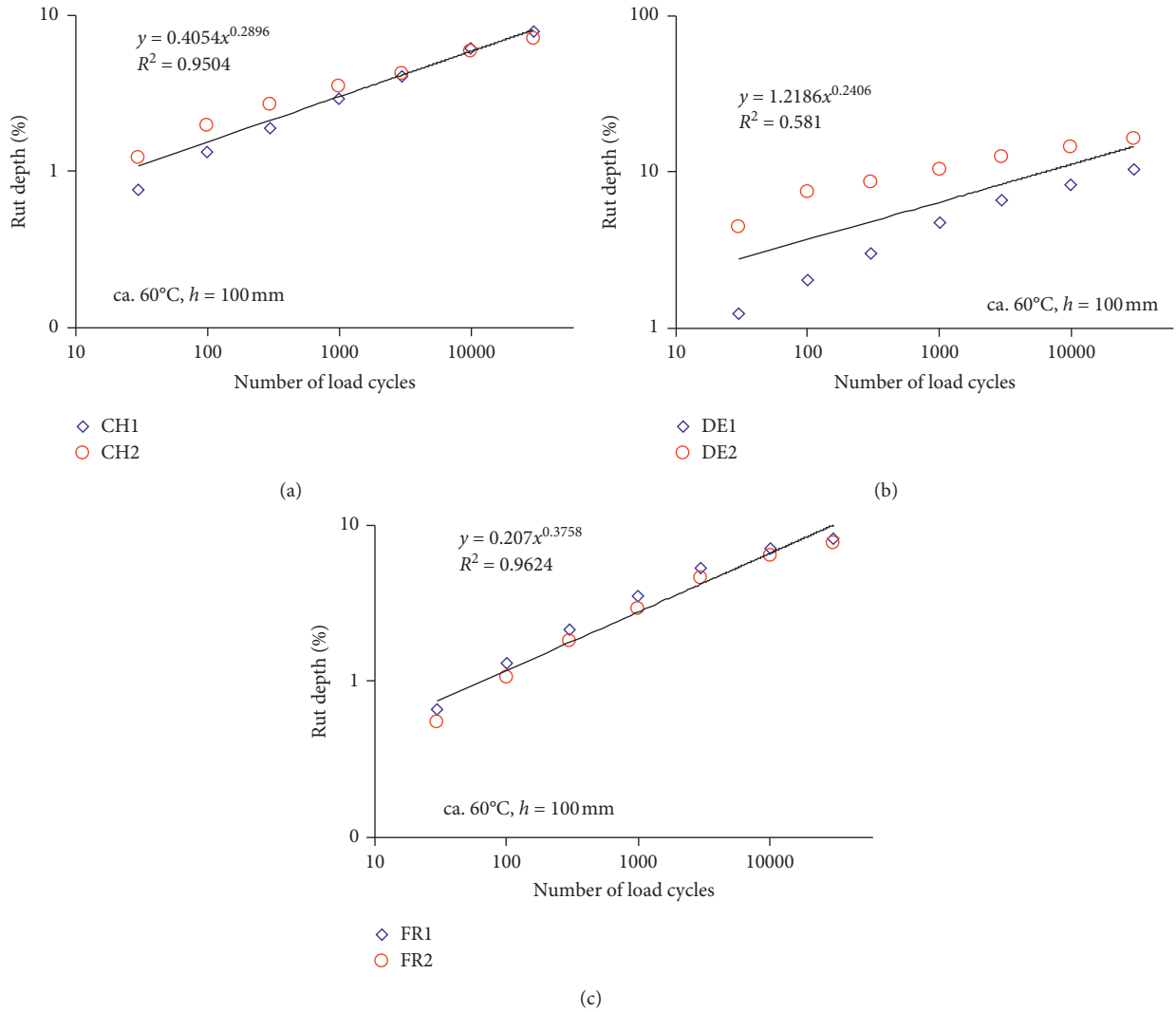


FIGURE 6: Rutting test results: single values and regression calculated from all individual data for each mixture. (a) CH. (b) DE. (c) FR.

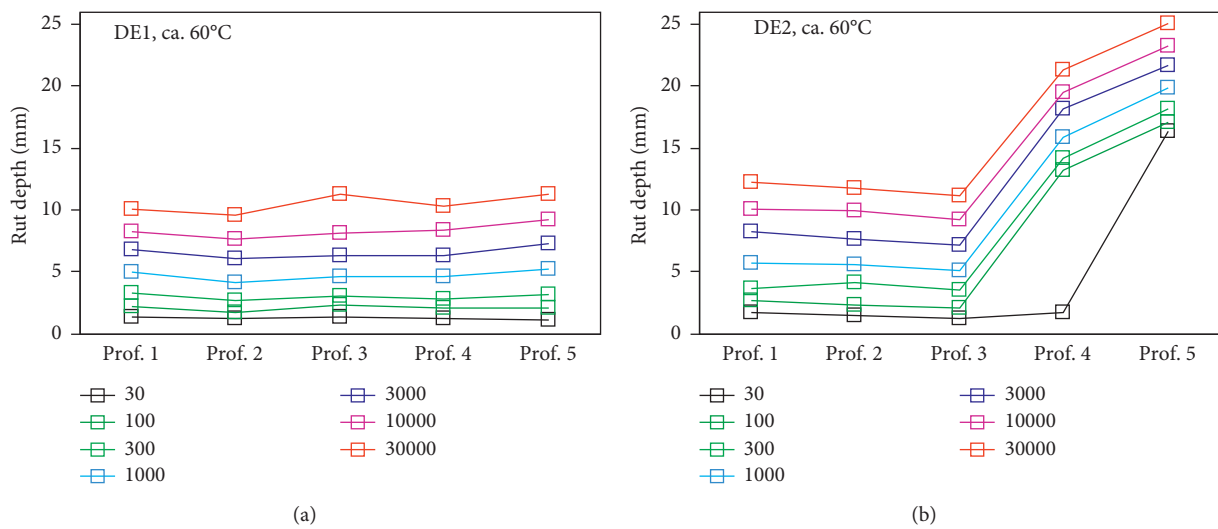


FIGURE 7: Development of length profiles of rutting test for both DE mixtures showing that DE2 behaved unexpectedly in Prof. 4 and Prof. 5 (a) DE1. (b) DE2.

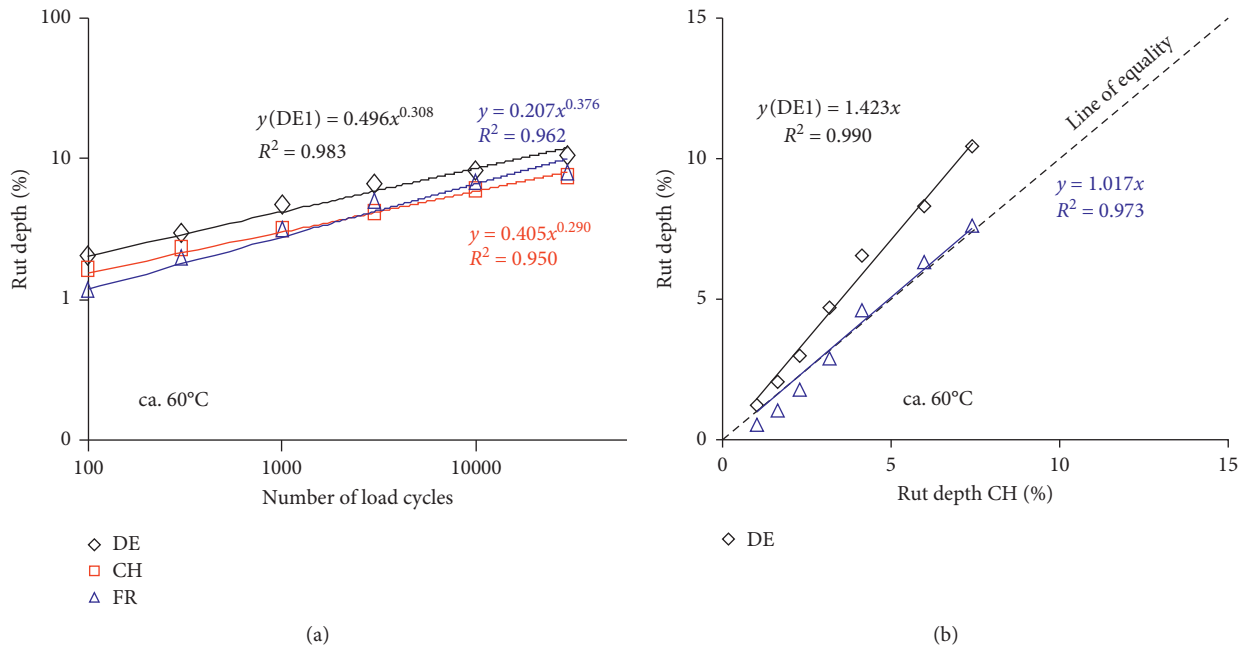


FIGURE 8: Comparison of rutting test results. (a) Rut depth versus load cycles. (b) Rut depth with respect to CH mixture behaviour, ignoring DE2 results.

In this case, the difference is less significant for all the mixtures. However, the slope of the overall power function for the FR mixtures is clearly higher than that for the CH and DE1 mixtures. FR has a higher rutting speed in particular at the beginning. The slope of the DE1 mixture is comparable with CH, but DE1 has a clearly low rutting resistance at the beginning. Overall, the DE1 mixture is still less rutting resistant but produces a reasonable rutting speed.

As compared to the requirements for AC of Swiss standard [15], one can observe that only the CH mixture fulfils the requirements for mixture type S for heavy traffic ( $\leq 10\%$  after 10,000 load cycles) and very heavy traffic H ( $\leq 7.5\%$  after 30,000 load cycles), whereas the FR mixture fulfils only the requirement for type S. When comparing the rut depth of the DE1 and FR mixtures in relation to the CH mixture (Figure 8(b)), one can see that the FR mixture is roughly 1.7% higher than the CH mixture. The comparison with the CH mixture shows a reasonable linear behaviour of DE1. However, the DE1 mixture shows about 42% higher rutting and would still not meet the requirements according to the Swiss standard.

4.2. Rutting Test with Laboratory-Scaled Mobile Traffic Simulator. Figure 9 summarizes the MMLS3 results of all individual mixtures. Table 3 shows the functions of the power law regression curves and the  $R^2$  values. The power law regression curves are calculated in each case considering all single values of the three profiles measured. This is the reason why the  $R^2$  values are so low. The points show the mean values of the three profiles for each mixture.

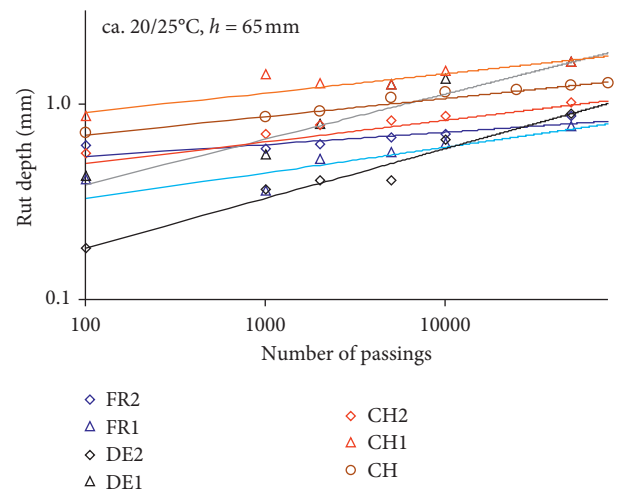


FIGURE 9: Individual MMLS3 rutting curves at ca 20/25°C. Points are mean values of 3 profiles; regressions are calculated from all individual profile points.

TABLE 3: Function of power law regression curves and  $R^2$  values.

RAP source	Function of power law regression curve	$R^2$
CH	$y = 0.453x^{0.093}$	0.467
CH1	$y = 0.571x^{0.099}$	0.464
CH2	$y = 0.297x^{0.111}$	0.227
FR1	$y = 0.179x^{0.131}$	0.048
FR2	$y = 0.401x^{0.063}$	0.235
DE1	$y = 0.133x^{0.232}$	0.557
DE2	$y = 0.057x^{0.054}$	0.557

One can clearly see that all RAP mixtures CH, DE, and FE show considerable scatter. For CH, not only are CH1 and CH2 plotted (which have been tested at ca 20°C), but also the data of an earlier test at ca 25° up to 80,000 passings is shown. It is interesting to see that these results blend nicely with CH1 and CH2 in spite of the fact that the temperature was about 5°C higher. This means that the material scatter was overshadowing the influence of temperature in case of this RAP mixture. Therefore, in principle, these early test results can be blended with the CH1 and CH2 data for calculating the mean value of the rutting behaviour of the CH mixtures.

One can also see that the CH mixtures showed larger rutting at 60°C with MMLS3 than the FE mixtures but similar rutting speed. Rutting of the DE mixtures was clearly lower at the beginning but, due to clearly higher rutting speed, they produced ruts in the same order of magnitude than the other two mixtures at the end of testing.

The remarks made above are confirmed and shown more clearly when comparing the overall mean values for each mixture (see Figure 10). The CH and FR mixtures have similar rutting speeds, but CH shows higher initial rut depth. The DE mixture produces clearly higher rutting speed starting from the lowest initial rutting as mentioned before. The influence of including the earlier CH mixture at 25°C is marginal (Figure 10(b)).  $R^2$  values are extremely low due to the large scatter when calculating the power law regression from all individual profile points. As visible from Figure 10(c),  $R^2$  reduces significantly, when the power law regression is calculated only from the overall mean values.

When comparing the MMLS3 rut depth of the DE and FR mixtures at 20°C in relation to the CH mixture at 20/25°C (Figure 11(a)), one can see that the FR mixture is generally about 40% lower. The DE mixture for low rut depths is clearly different but gets much closer to the CH mixtures for high rut depths. This tendency of high rut resistance at the beginning and equally high rutting with an increasing number of passings leads to a nonlinear relationship. As compared to the large wheel rutting results at 60°C Figure 11(b), the ranking is different. Both the DE and FR mixtures display higher rutting resistance in the MMLS3 test at 20°C but lower and almost equal rutting resistance in the large wheel rutting test at 60°C. Here, the DE rut depths from the large wheel rutting test are calculated as mean from both DE1 and DE2 specimens. It appears that the DE mixture is much more temperature-dependent than the CH mixture. One would also conclude that from the three mixtures the FR mixture was the least rutting susceptible mixture of all mixtures.

This temperature dependency may be due to the RAP binder properties but also due to the type of RAP grading curve and the size of RAP clusters. It may well be that large RAP clusters may be stable in the form of aggregate chunks during MMLS3 testing at 20°C but fall apart easily at higher temperatures such as 60°C during the large wheel rutting test. DE2 could be one example of that. In practice, this would mean that the thermal stability of the RAP clusters is crucial for this type of mixture, in terms of compaction and workability during construction as well as after-compaction from traffic. Very large chunks of RAP are certainly negative

in that respect and careful mechanical pretreatment of the RAP in the plant appears crucial for this 100% RAP approach. Further investigations in that direction may help to understand these mechanisms.

In that context, it may make sense to consider also investigations with the Compaction Flow Test (CFT), as recently developed at the Royal Institute of Technology (KTH) [16]. This test was found to provide an indication about the workability and flow of aggregates during static loading of loose mixtures in a compaction-like laboratory situation based on material lift-up as shown in the X-ray CT images in Figure 12. A combination of CFT with X-ray CT may help to understand the mechanism of decay of RAP chunks under loading. However, such an investigation was out of the scope of this study but may be kept in mind for future studies.

In order to visualize differences in the deformation behaviour, the mean values of the transversal rutting profiles of the different mixtures in the MMLS3 tests at 20°C after 1000 and 50,000 channelized wheel passings are plotted in Figure 13. Obviously, these deformations are quite low, demonstrating that the mixtures were generally of high rutting resistance. However, it is very clear that the CH mixtures suffered most of the rutting already during the first loading cycles with a practically negligible increase during the rest of trafficking (as already mentioned above), whereas rutting of the DE and FR mixtures showed a remarkable increase. The lateral bulging of CH after 1000 passings suggests that a local material flow took place as simulated in the CFT (see Figure 12). For DE and FR, no bulging was observed.

In Figure 14, a comparison of the MMLS3 results with two asphalt concrete (AC) pavements with hot mix asphalt surface layers HMA1 and HMA2 for low-traffic AC 8 L recently compacted and tested with MMLS3 in the field in another context at ca. 32°C and ca. 27°C, shows that the rutting deformations of the cold mixtures CH, DE, and FR with 100% RAP can be considered as small. HMA1 was 28 cm thick containing no RAP and HMA2 was 40 mm thick and contained 80% RAP. The temperatures of the field pavements in 6 cm depth, in particular, of HMA1 were higher than those of the CH, DE, and FR pavements in the lab and had not a homogeneous temperature distribution over the whole cross section (gradient). The different temperature gradients between the field and lab tests as well as the different compaction methods and types of mixtures have certainly influenced the rutting rate of the field tests as compared to the CH, DE, and FR mixtures. One should also not forget that both HMA1 and 2 had a smaller maximum aggregate size of 8 mm as compared to 16 mm of the CH, DE, and FR mixtures. The higher temperature of HMA1 as compared to HMA2 may have created a higher rut depth in that case.

## 5. Construction of In Situ Test Section

The in situ test section constructed between the Swiss villages of Wahlen and Büsserach is a low-traffic volume road with an average daily traffic ADT of 200 vpd. The length of the

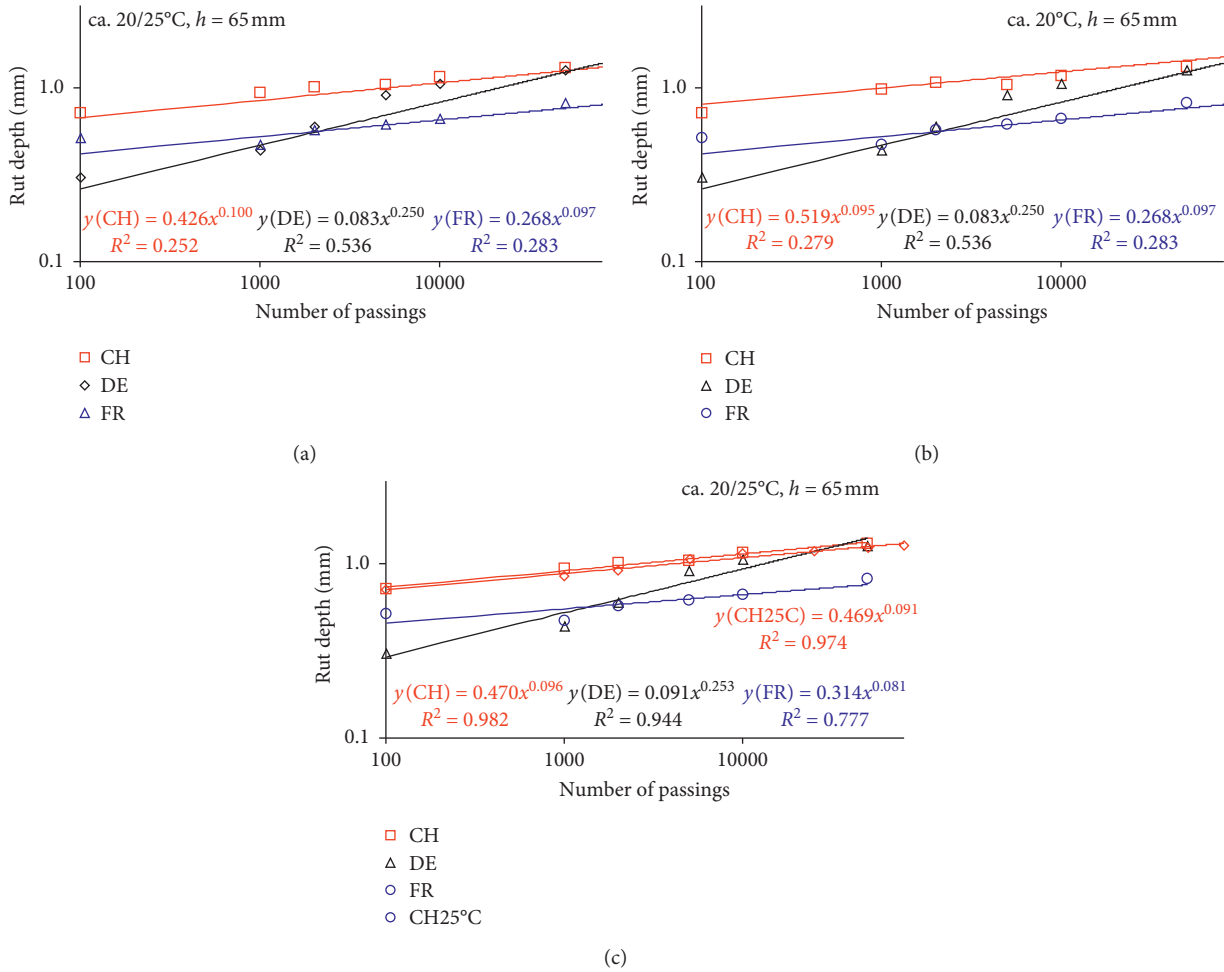


FIGURE 10: Mean values of MMLS3 rutting curves at ca 20/25°C. Points are mean values of all profiles for each mixture. (a) Including and (b) excluding the earlier mixture CH at 25°C, calculating regressions from all individual profile points, and (c) regression only from mean values. CH at 25°C is shown separately.

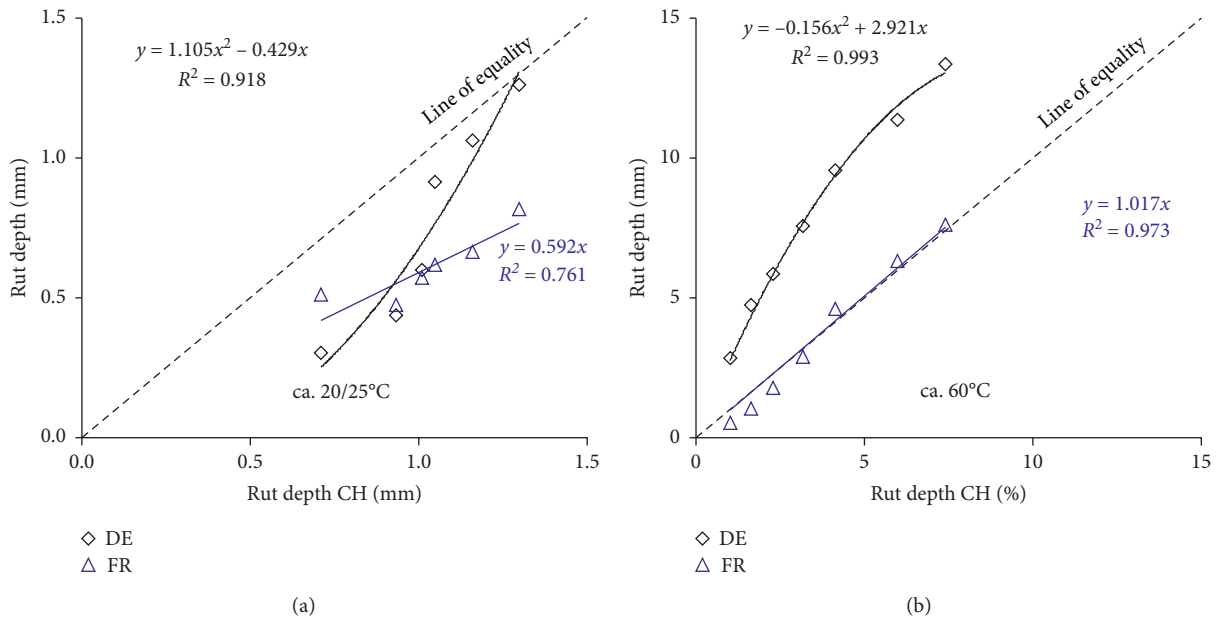


FIGURE 11: Rut depth with respect to CH mixture behaviour, demonstrating clearly the abnormal results of DE in both cases. (a) MMLS3 at 20/25°C. (b) Large wheel rutting test at 20°C.



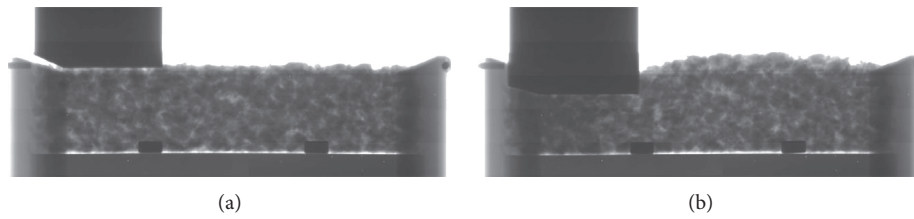


FIGURE 12: Example of X-ray CT images from flow measurements on coarse (0–16 mm) cold mixture specimens. (a) Before and (b) after the CFT [16].

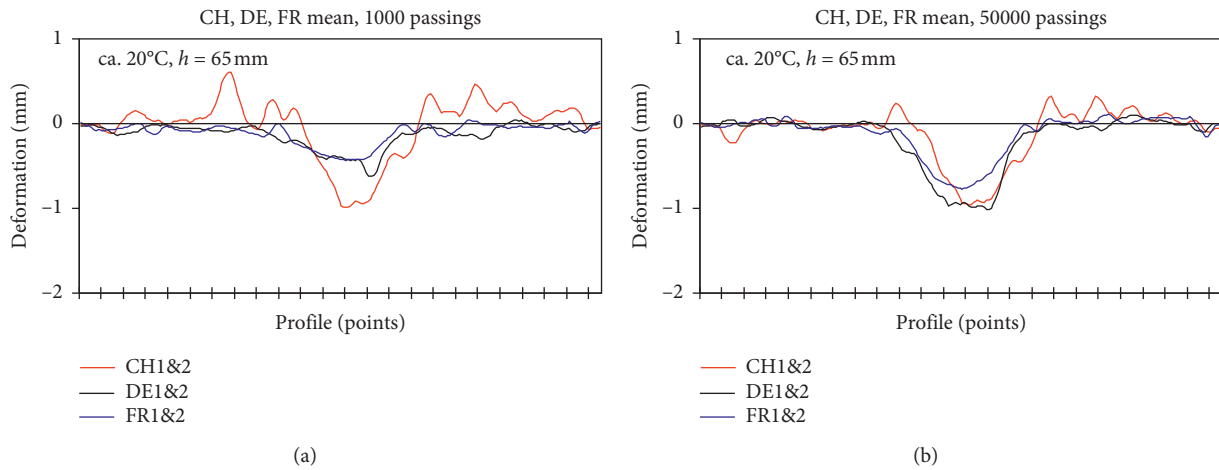


FIGURE 13: Comparison of MMLS3 profiles at 20°C. (a) After 1000 passings. (b) After 50000 passings.

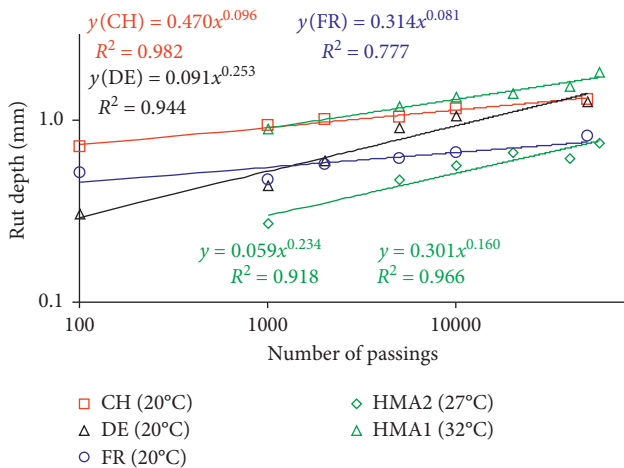


FIGURE 14: Comparison of MMLS3 rutting curves at 20°C for CH, DE, and FE in the lab with the MMLS3 test in the field on two AC asphalt pavements HMA1 and HMA2.

ORRAP test section was 380m. The average width of the road is 5.5 m, with a shoulder width of 1.5 m. For the construction, the existing asphalt layer with a thickness of 10 cm was milled between 3 and 5 cm and the ORRAP material RAP 0/22 with a thickness of 10 cm was placed on top of a tack coat (cationic bitumen emulsion). The day after, the 4 cm thick surface course was constructed consisting of a hot mix asphalt concrete AC 11 N for normal traffic with 11 mm maximum aggregate size and a conventional penetration

grade binder 70/100 according to the Swiss standard (Swiss Standard Annex SN 640431). Since the paved RAP material had no side support, the shoulders were considered as weak points and were therefore constructed 20 cm wider than the surface layer at each side. After the construction of the surface course, the 20 cm was backfilled with soil.

Figure 15 shows the profile of the test section.

The construction took place on a very hot dry summer day with a maximum temperature of 36°C in the afternoon and the sun radiation on the construction was very high.

The material was transported by trucks from the storage place which was about 35 km away from the construction side.

The water content of the RAP 0/22 mm had been determined between 4.2 and 4.6%. However, for better workability and compaction under this hot climate and in order to avoid fast surface drying, water was sprayed onto the material in the paver augers as well as after the paver screed.

Compaction was done using 3 different compactors:

- (i) Steel roller with a weight of 2.5 t for precompaction and levelling partly in vibration mode
- (ii) Pneumatic tire roller with a weight of 4.5 t and
- (iii) Pneumatic tire roller with a weight of 24 t

Compaction with a heavy steel roller compactor (12.5 t) in vibration mode led to transversal cracking as visible in Figure 16(a) and was therefore stopped. Transversal cracking was partly attributed to the fact that the 100% RAP material was paved on the comparatively stiff rest old asphalt pavement after milling.



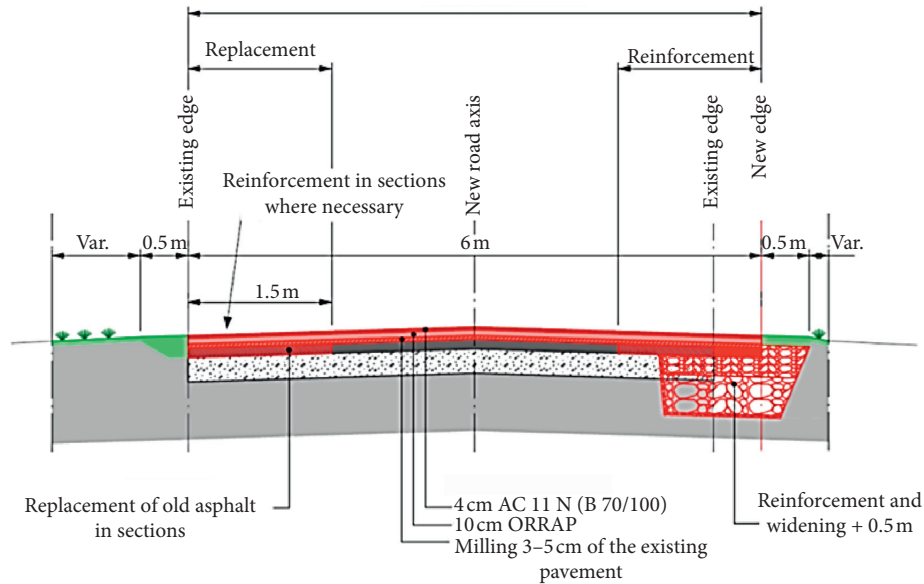
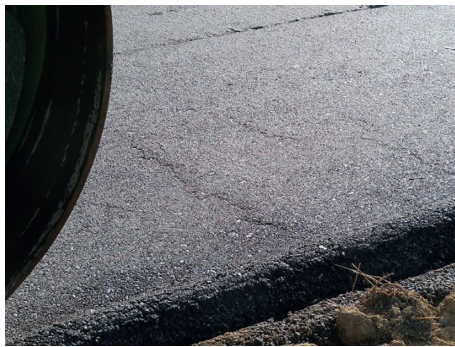


FIGURE 15: Profile of the in situ test section in Switzerland.



(a)



(b)

FIGURE 16: Cracking during compaction. (a) Transversal cracks caused by heavy steel roller compactor in vibration mode. (b) Shoulder instability.

Regarding the anticipated shoulder instability, it was found that this was a real problem with the breaking of edges as shown in Figure 16(b).

Apart from the abovementioned, further problems and noteworthy observations became obvious during construction, especially considering the RAP material in comparison to hot mix asphalt:

- (i) The number of rounded aggregates was found to be considerably high whereas the bitumen coating was considerably low
- (ii) The compaction effort was considerably high, about twice compared to HMA constructions
- (iii) Large aggregates (up to 12 cm) and chunks of material were found in the RAP and had to be taken out of the compacted surface by workers with shovels and the cavities had to be refilled in quite a cumbersome process
- (iv) Besides, of causing cumbersome work, large chunks of RAP material were sometimes blocking the paver



FIGURE 17: Test section with RAP material at the end of compaction.

screed and the construction had to be stopped for more than half an hour

- (v) In addition to these interruptions in construction, further delays occurred when hauling trucks were delayed by traffic jams and the water supply had to be refilled

Despite all difficulties, at the end of the day, the RAP material was well compacted, stable, and even, as depicted in Figure 17, providing a good base course for the hot mix surface course. The pavement will be observed during at least one year, and different material and pavement characteristics such as rutting and evenness will be determined at different time intervals.

## 6. Conclusions

In the present study, a laboratory compaction evaluation and performance characterization of 100% recycled reclaimed asphalt pavement (RAP) were carried out, using different methods and specimen sizes. Particular focus was laid on the rutting behaviour and performance under accelerated traffic loading with a model laboratory traffic simulator. The laboratory study clearly showed the potential of using a high percentage of RAP at low compaction temperatures and was, therefore, very promising for a successful in situ installation of these materials on a test section in Switzerland. From the study which was part of an international project ORRAP, the following conclusions can be drawn:

- (i) Although laboratory compaction at an ambient temperature of 20°C turned out to be insufficient, it was found that increasing the temperature only a little (60°C) changed compaction behaviour drastically allowing the construction of stable and rutting resistant asphalt specimens.
- (ii) Investigation of rutting resistance with the large wheel rutting tester at 60°C as well as the laboratory scaled mobile traffic simulator MMLS3 at ambient temperature, both under laterally confinement of the specimens, generally produced low rut depths with all three RAP materials from the different sources in Switzerland, Germany, and France. However, significant differences were found, revealing different temperature dependencies and rutting susceptibilities. Although only planned for low-traffic volume applications, some specimens investigated with the large wheel rutting device even fulfilled the requirements for heavily trafficked roads according to Swiss standards.
- (iii) Material scatter was comparatively high and overshadowing the influence of temperature during rutting tests. In some cases, it was assumed that RAP clusters may have formed aggregate chunks that remained stable at 20°C but were destroyed due to kneading during rutting tests at 60°C.
- (iv) RAP chunks were also found during field construction blocking the paver screed causing working interruptions. This means that for this RAP application careful mechanical pretreatment of the material in the plant and before compaction is necessary in order to avoid those RAP chunks.
- (v) From the investigation and findings, it seems feasible to construct low-traffic volume roads with

100% of RAP at low compaction temperature as it was the goal of the ORRAP project. Compared to the construction of hot mix asphalt pavements, the compaction effort has to be increased.

Further studies on the test section will show if enough information is available as a basis for producing a technical guideline for application and construction. In any case, selected additional studies, such as studying the effect of oversized RAP clusters on compaction and mechanical behaviour, must be undertaken in order to develop this promising technology into an environmentally friendly affordable standard application for low-traffic volume roads.

## Data Availability

The data used to support the findings of this study have not been made available because the ORRAP “Optimal Recycling of Reclaimed Asphalts for low-traffic Pavements” project is still ongoing and ends on June 30, 2020.

## Conflicts of Interest

The authors declare that there are no conflicts of interest regarding the publication of this paper.

## Acknowledgments

The authors of this article would like to thank Cédric Bensa, a master student from Clermont-Ferrand, France, for his work during the starting phase of the project. ORRAP “Optimal Recycling of Reclaimed Asphalts for low-traffic Pavements” project was funded by ERDF-INTERREG V (3.1 ORRAP), the Canton Aargau, and the Swiss confederation.

## References

- [1] M. Hugener and M. Seeberger, “Optimum RAP content in hot mix asphalt recycling,” in *Proceedings of the 4th ISAP APE Symposium*, p. 11, Tokyo, Japan, November 2015.
- [2] Q. Aurangzeb, I. L. Al-Qadi, I. M. Abuawad, W. J. Pine, and J. S. Trepanier, “Achieving desired volumetrics and performance for mixtures with high percentage of reclaimed asphalt pavement,” *Transportation Research Record: Journal of the Transportation Research Board*, vol. 2294, no. 1, pp. 34–42, Washington, USA, 2012.
- [3] M. Zaumanis, R. Mallick, and R. Frank, “Evaluation of rejuvenator’s effectiveness with conventional mix testing for 100% reclaimed asphalt pavement mixtures,” *Transportation Research Record: Journal of the Transportation Research Board*, vol. 2370, no. 1, pp. 14–25, 2013.
- [4] A. Cannone Falchetto, L. Porot, C. Riccardi, M. Hugener, G. Tebaldi, and E. Dave, “Effects of rejuvenator on reclaimed asphalt binder: an exploratory study of the RILEM TC 264-RAP Task Group 3,” in *Rilem Bookseries: Vol. 20, RILEM 252-CMB Symposium, Chemo-Mechanical Characterization of Bituminous Materials*, L. D. Poulidakos, A. Cannone Falchetto, M. P. Wistuba, B. Hofko, L. Porot, and H. Di Benedetto, Eds., Springer, Berlin, Germany, pp. 195–200, 2019.
- [5] ORRAP (2016–2020), <http://www.interreg-oberrhein.eu/projet/orrapp-optimaales-recycling-von-ausbauasphalt-auf-verkehrsschwachen-strasen>.

- [6] ORRAP (2016–2020), <https://www.orrapp.org/>.
- [7] T. Jacobson, “Reclaimed crushed asphalt—experiences from field studies examples from Jönköping, Västerås, Göteborg municipal roads (asfaltgranulat som obundet bär- och förstärkningslager. Återvinning av krossad asfalt som bäroch förstärkningslager. del 2—erfarenheter från fältstudier) VTI notat 32,” 2002.
- [8] European Union, *European Project: FP 7th Project DIRECT-MAT Dismantling and RECYcling Techniques for Road Materials (2007–2011)*, European Union, Brussels, Belgium, 2012.
- [9] L. Gaillard, C. Chazallon, P. Hornych, J. C. Quezada, and C. Raab, “Thermo-hydro-mechanical behaviour of cold reclaimed asphalt aggregates without binder addition,” *Road Materials and Pavement Design*, vol. 20, no. 1, pp. S49–S63, 2019.
- [10] C. Raab, N. M. Partl, and C. Bensa, “100% recycling of low-temp asphalt for minor roads—lab compaction and traffic simulation,” in *Proceedings of the 5th International Symposium on Asphalt Pavements & Environment (APE) in Padova*, pp. 235–245, Springer Book Series, Padua, Italy, September 2020.
- [11] European Standard EN 932-1, *Tests for General Properties of Aggregates—Part 1: Methods for Sampling*, CEN, Brussels, Belgium, 1996.
- [12] C. Raab, M. Arraigada, M. N. Partl, and F. Schiffmann, “Cracking and interlayer bonding performance of reinforced asphalt pavements,” *European Journal of Environmental and Civil Engineering*, vol. 21, no. 1, pp. 14–26, 2017.
- [13] European Standard EN 12697-22, *Bituminous Mixtures—Test Methods for Hot Mix Asphalt—Part 22: Wheel Tracking*, CEN, Brussels, Belgium, 2003.
- [14] F. Hugo and A. Epps, *Significant Findings from Accelerated Pavement Testing*, NCHRP Synthesis 325, TRB 2004, Washington, DC, USA, 2004.
- [15] Swiss Standard Annex SN 640431 to European Standard EN 13108-1, *Mischgutanforderungen—Teil 1: Asphaltbeton*, Swiss Standard SN 640431-1b-NA, Switzerland, 2014.
- [16] E. Ghafoori Roozbahany, M. N. Partl, and A. Guarin, “Introducing a new method for studying the field compaction,” *Road Materials and Pavement Design*, vol. 18, no. 2, pp. 26–38, 2017.

## Research Article

# Investigation of the Effects of Evaporation Methods on the High-Temperature Rheological and Fatigue Performances of Emulsified Asphalt Residues

Yang Sun,<sup>1</sup> Jin-Chao Yue ,<sup>1</sup> Ri-Ran Wang,<sup>1</sup> Rui-Xia Li,<sup>1</sup> and De-Cai Wang <sup>1,2</sup>

<sup>1</sup>School of Water Conservancy Engineering, Zhengzhou University, Zhengzhou 450001, China

<sup>2</sup>School of Civil Engineering and Communication, North China University of Water Resources and Electric Power, Zhengzhou 450045, China

Correspondence should be addressed to De-Cai Wang; [decaiww@sina.com](mailto:decaiww@sina.com)

Received 8 November 2019; Revised 26 January 2020; Accepted 15 February 2020; Published 16 March 2020

Guest Editor: Andrea Graziani

Copyright © 2020 Yang Sun et al. This is an open access article distributed under the Creative Commons Attribution License, which permits unrestricted use, distribution, and reproduction in any medium, provided the original work is properly cited.

Cold recycling technology is a widely applied asphalt pavement rehabilitation technology. The properties of emulsified asphalt residues after water evaporates play an important role in the performance of the asphalt pavement. This paper investigates the rheological and fatigue properties of emulsified asphalt residues under different evaporation methods. Two different matrix asphalt binders and emulsifiers were selected to prepare the emulsified asphalt. Moreover, the direct heating method (DHM) and the EN13074 and ASTM D7497-09 evaporation methods were used to obtain emulsified asphalt residues. Furthermore, the linear viscoelasticity, the permanent deformation resistance, and the fatigue resistance were evaluated by the temperature sweep and frequency sweep tests, the multiple stress creep recovery (MSCR) test, and the linear amplitude sweep (LAS) test, respectively. The test results show that under the three evaporation conditions, the growth amplitude order of the rutting factor, recovery percent, complex modulus, and fatigue life of emulsified asphalt residues is ASTM D7497-09 > EN13074 > DHM, and as is the attenuation amplitude order of the nonrecoverable creep compliance and phase angle. The results reveal that the evaporation process leads to oxidation and hardening of the residues. The hardening degree of the ASTM D7497-09 evaporation method is higher than that of the EN13074 evaporation method, and the hardening degree of the EN13074 evaporation method is higher than that of the direct heating method. The rheological and fatigue performances of the emulsified asphalt residues depend on the matrix asphalt. Moreover, the residue that was prepared from 70# asphalt has good high-temperature and fatigue properties, but it has higher temperature sensitivity and stress sensitivity.

## 1. Introduction

Cold recycled mixture of emulsified asphalt has become one of the most popular approaches for asphalt pavement maintenance, rehabilitation, and reinforcement, with the advantage of excellent pavement performance, resource conservation, and environmental friendliness [1–4]. Studies have found that the asphalt emulsion has a substantial influence on the rheological characteristics and the mechanical properties of the cold recycled mixture [5, 6]. Moreover, the performance of emulsified asphalt mainly depends on the technical properties of residues after the moisture is evaporated. The emulsified asphalt residue is used as a key

specification and quality control parameter for the emulsified asphalt [7], and also its performance is related to the characteristics during the service period. Therefore, it is necessary to recover residues and investigate their properties.

Similar to asphalt binders, emulsified asphalt residue is a viscoelastic plastic material. Rheological measurement has been proven to be a favorable approach for optimizing the recovery methods of emulsified asphalt residue [8–10]. Common residue recovery methods include distillation, evaporation, moisture analyzer balance (MAB) [11], and the SAFT (stirred air flow test with nitrogen) method [12]. Distillation methods, such as ASTM D6997 and ASTM D7403, are more scientific methods of residue collection and



are more widely used to recover emulsion residue [13, 14]. However, the distillation method easily causes aging and even damage to the microscopic structure of emulsified asphalt residue due to its high-temperature [15]. Thus, the residue obtained by distillation method will not have the same properties as that obtained in the field [5, 16–18]. Evaporation methods mainly include the vacuum drying method, the air blowing evaporation method, the low-temperature evaporation drying method, and other methods. Islam et al. [19] prepared emulsified asphalt residue by the vacuum drying method and studied the effects of variables including the curing time, temperatures, and vacuum pressure on the rheological properties of the recovered asphalt emulsion residue. The direct heating method is mainly used in China and Japan, and the proficiency levels of operators substantially impact the experimental results [20, 21]. Gao and Pang [22] obtained emulsified asphalt residue by the direct heating method and established the relationships between rheological parameters and road performance indexes by interfacial rheology and dynamic shear rheology. The low-temperature evaporation method is favored by researchers because the evaporation temperature is closer to the application temperature of emulsified asphalt. Hanz et al. [17] used the ASTM D7497-09 evaporation method to obtain emulsified asphalt residue and carried out rheological tests on the residues with different curing times. Xu et al. [9] used the recovery method that was proposed by the EN13074 method (including both the recovery and stabilization processes at moderate temperatures) to obtain the residue, and the corresponding matrix asphalt binders were treated via the same method for comparison.

However, the properties of the residues obtained by different evaporation methods are different. Some researchers compared and analyzed the influence of different evaporation methods on the performance of emulsified asphalt residues. Malladi et al. [23] compared the vacuum drying procedure with the AASHTO PP72 procedure and found that the vacuum-dried residues were softer and more viscous than the residues recovered by the AASHTO PP72 procedure. Marasteanu and Clyne [5] used air-curing and RTFOT-curing to recover the residue and evaluated the low- and high-temperature performances of the residues. The results indicated that the residues cured by RTFOT were stiffer, especially the polymer modified residues.

In summary, the research on emulsified asphalt residues mainly focuses on the residue acquisition method and rheological performance and rarely involves the influence of the evaporation method on the residue performance. Although the evaporation temperature of the low-temperature evaporation method is lower, the evaporation time is longer. Compared with other methods to obtain emulsified asphalt residue, whether it will affect the performance of emulsified asphalt residue needs further research. Moreover, there are few studies on the fatigue properties of emulsified asphalt residues, and the fatigue resistance of the asphalt binder significantly affects the overall fatigue performances of asphalt mixtures [24]. Therefore, based on laboratory experiments, the effect of evaporation method on the high-temperature performance and fatigue performance of

emulsified asphalt residues is systematically studied, and the characteristics of cold recycled emulsified asphalt material properties are accurately characterized, thus guiding engineering practice.

## 2. Materials and Testing Methods

*2.1. Materials.* 70# asphalt was supplied by Guangrao Kelida Petrochemical Technology Co., Ltd., Shandong, China, and 90# asphalt was supplied by SK Co., Ltd., Korea. Emulsifiers KZW-803L and Redicote E-4875 were produced by Kangzewe Technology Co., Ltd., Tianjin, China, and Akzo Nobel Co., Ltd., Shanghai, China, respectively. Two emulsifiers are brown liquid and easily soluble in water. The solid content of KZW-803L emulsifier is more than 50%, and the solid content of Redicote E-4875 emulsifier is 48–53%. Technical information about the asphalt binders and emulsifiers is presented in Tables 1 and 2, respectively. A colloidal mill of the model RINKMD-1, which was fabricated in Germany, was used to prepare the emulsified asphalt. The preparation process of the emulsified asphalt is presented in Figure 1 [25]. The prepared emulsified asphalt was referred to as K and E emulsified asphalt.

### 2.2. Testing Methods

*2.2.1. Recovery of the Emulsified Asphalt Residue.* Direct heating method [20] and EN13074 and ASTM D7497-09 (Method A) evaporation methods [16] were selected to prepare emulsified asphalt residues. Figure 2 shows the process of obtaining the emulsified asphalt residues by the evaporation method of EN13074 and ASTM D7497-09 (Method A).

The weights of the recovered residues and the original emulsified asphalt were recorded and used to calculate the water loss percentage of emulsified asphalt. The water loss rate result is presented in Figure 3. More than 86% of the water was evaporated in the first stage. After 42 hours, the water loss rate minimally increased, and the emulsified asphalt residues still contained small amounts of water after 48 hours. Mitchell et al. [26] used size exclusion chromatography (SEC) to assess the presence of residual water and determined that the residue that was obtained by the low-temperature evaporation method contained water. However, the presence of residual water in the residues that were obtained by the ASTM D7497-09 and EN13074 evaporation methods does not affect the rheological properties of the residues [19, 23]. Under the same evaporation conditions, the water loss rate of emulsified asphalt is related to the type of emulsifier. Moreover, the water loss rate of emulsified asphalt under the EN13074 evaporation method is less than that under the ASTM D7497-09 evaporation method. The same change trend is observed for the 90# emulsified asphalt.

*2.2.2. Physical Performance Tests.* Physical tests of the penetration, softening point, and ductility were conducted in accordance with ASTM D5, ASTM D36, and ASTM D113 [27–29], respectively. The penetration test temperature was

TABLE 1: Properties of the 70# and 90# matrix asphalt binders.

Technical parameters	Values	
	70#	SK 90#
Penetration at 25°C, (0.1 mm)	72.0	91.2
Softening point (°C)	48.8	46
Ductility at 15°C (cm)	>150	>150
Viscosity at 135°C (Pa.s)	0.65	0.51

TABLE 2: Technical information on the emulsifiers.

Emulsifier type	Ion type	Demulsification speed	Emulsifier content (%)	Optimum bitumen content (%)	pH requirement
KZW-803L	Cationic	Slow-breaking	3	62	2.0–2.5
Redicote E-4875	Cationic	Slow-breaking	2	63	2.0–3.0

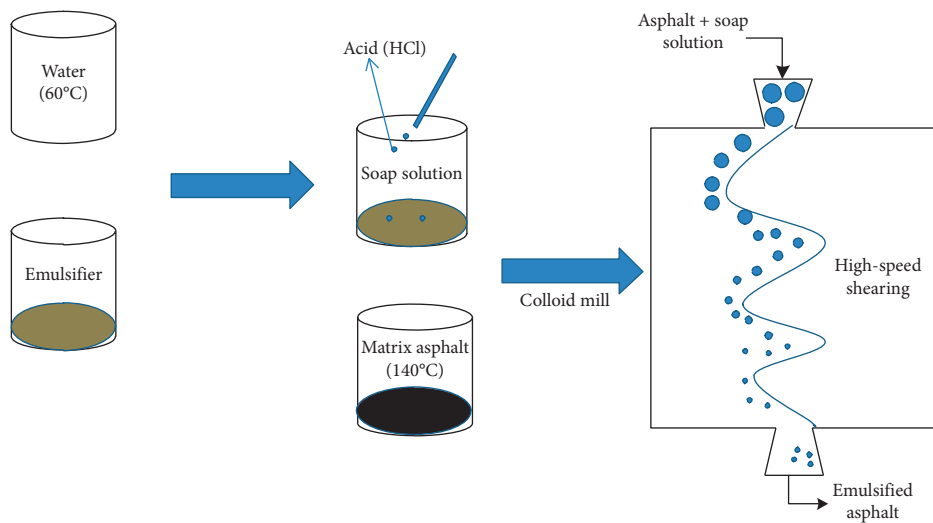


FIGURE 1: Preparation of the emulsified asphalt.

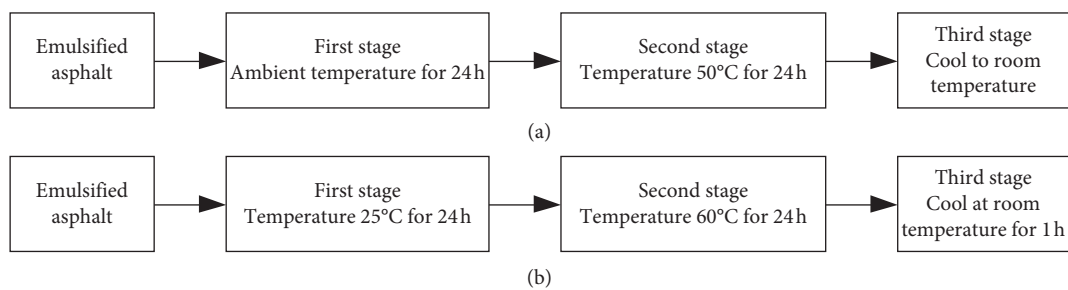


FIGURE 2: Recovery procedure of emulsified asphalt residues, (a) recovery procedure of emulsified asphalt residues according to EN13074, (b) recovery procedure of emulsified asphalt residues according to ASTM D7497-09.

25°C, and the temperature for the ductility test was 15°C. Three samples were prepared to ensure the repeatability of the tests, and the average of three results was finally obtained.

**2.2.3. Temperature Sweep Test.** A DHR-1 hybrid rheometer (TA Instrument, New Castle, Delaware) was utilized to test the rheological and fatigue properties of the emulsified

asphalt residues. The test temperature started at 58°C and increased to 82°C in 6°C intervals. The strain level was 12%, and the testing frequency was 10 rad/s [30]. The parallel plate geometry of 25 mm diameter and 1 mm gap was applied.

**2.2.4. Frequency Sweep Test.** The controlled strain of the frequency sweep test was maintained at 0.1% to ensure that the rheological behaviors of residues were in the linear



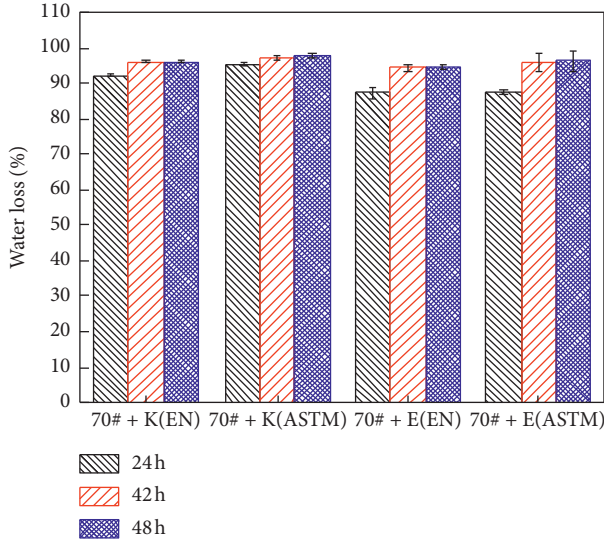


FIGURE 3: Loss percentage of the water content of the emulsified asphalt.

viscoelastic range. The test angular frequencies ranged from 0.1 rad/s to 10 rad/s, and test temperatures were 20°C, 30°C, 40°C, 50°C, and 60°C. A parallel plate of 25 mm in diameter with a 1 mm gap was used when the testing temperature exceeded 30°C, whereas the parallel plate of 8 mm in diameter with a 2 mm gap was used when the testing temperature below 30°C.

The Christensen–Anderson–Marasteanu (CAM) model was used to fit the complex modulus and the phase angle master curves to provide the undamaged material responses [31]. The time-temperature shift factor was fitted with the Williams–Landel–Ferry (WLF) nonlinear function as expressed in equation (1) [32]. The reference temperature of the complex modulus and phase angle main curve was 40°C:

$$\lg \alpha_t = \frac{-C_1(T - T_0)}{C_2 + (T - T_0)}, \quad (1)$$

where  $T_0$  and  $T$  represent the reference temperature and the actual temperature, respectively, and  $C_1$  and  $C_2$  are the fitting parameters.

**2.2.5. Multiple Stress Creep Recovery (MSCR) Test.** The MSCR test can more accurately evaluate the high-temperature performance of the asphalt binder [33, 34]. The MSCR test adopted the parallel plate geometry of 25 mm diameter and 1 mm gap, and the test temperatures were 64°C and 70°C. The emulsified asphalt residue was subjected to 10 cycles of 1 second creep and 9 seconds recovery at a stress level of 0.1 kPa, followed by another 10 cycles of creep and recovery at 3.2 kPa. The performance indicators consist of the nonrecoverable compliance ( $J_{nr}$ ) and the recovery percent ( $R$ ), which can be calculated using equations (2) and (3), respectively. The stress sensitivity  $J_{nr, diff}$  is the difference between the  $J_{nr}$  values at the stress levels of 3.2 kPa and 0.1 kPa, as expressed in equation (4).

$$J_{nr} = \frac{\gamma_u}{\tau}. \quad (2)$$

$$R = \frac{\gamma_p - \gamma_u}{\gamma_p - \gamma_0} \times 100\%. \quad (3)$$

$$J_{nr, diff} = \left[ \frac{J_{nr3.2} - J_{nr0.1}}{J_{nr0.1}} \right] \times 100\%, \quad (4)$$

where  $\gamma_p$  is the peak strain after a one-second creep duration;  $\gamma_0$  is the shear strain at the beginning of the cycle;  $\gamma_u$  is the nonrecoverable strain after a nine-second recovery; and  $\tau$  is the creep stress.

**2.2.6. Linear Amplitude Sweep (LAS) Test.** The LAS test was developed as an accelerated fatigue procedure for evaluating the damage resistance of asphalt binders [35, 36]. The LAS procedure consisted of two steps [37]. First, the frequency sweep was performed from 0.2 to 30 Hz at a strain level of 0.1%, which was in the linear viscoelastic behavior range. This step was used to obtain the undamaged material property ( $\alpha$ ). Then, the emulsified asphalt residues were conducted under an oscillatory strain sweep at a constant frequency of 10 Hz with amplitudes that ranged linearly from 0.1% to 30%. The data of this step were used to calculate the damage property via viscoelastic continuum damage (VECD) mechanics analysis. The LAS testing temperature was 25°C. The damage accumulation in the emulsified asphalt residue is calculated using equation (5):

$$D(t) \cong \sum_{i=1}^N \left[ \pi I_D \gamma_0^2 (|G^*| \sin \delta_{i-1} - |G^*| \sin \delta_i) \right]^{(\alpha/1+\alpha)} \cdot (t_i - t_{i-1})^{(1/1+\alpha)}, \quad (5)$$

where  $I_D$  = the initial value of  $|G^*|$  from the 1.0 percent applied strain interval, MPa;  $|G^*|$  = the complex shear modulus, MPa;  $\gamma_0$  = the applied strain, %;  $\alpha = 1/m$ , where  $m$  = the slope of the logarithmic plot of the storage modulus versus the applied frequency;  $t$  = the testing time, s;

The relationship between  $|G^*| \sin \delta$  and  $D(t)$  can be fitted using the equation (6):

$$|G^*| \sin \delta = C_0 - C_1 (D)^{C_2}, \quad (6)$$

where  $C_0$  = the average value of  $|G^*| \sin \delta$  from the 0.1 percent strain interval;  $C_1$  and  $C_2$  = the coefficients of the curve fitting equations.

The damage failure  $D_f$  is defined as the value of  $D(t)$  that corresponds to a 35 percent reduction in undamaged  $|G^*| \sin \delta(C_0)$ .

$$D_f = 0.35 \left( \frac{C_0}{C_1} \right)^{(1/C_2)}, \quad (7)$$

$$A_{35} = \frac{f(D_f)^k}{k(\pi I_D C_1 C_2)^\alpha},$$

where  $f = 10$  Hz;  $k = 1 + (1 - C_2)$ ;  $\alpha; B = -2\alpha$ .

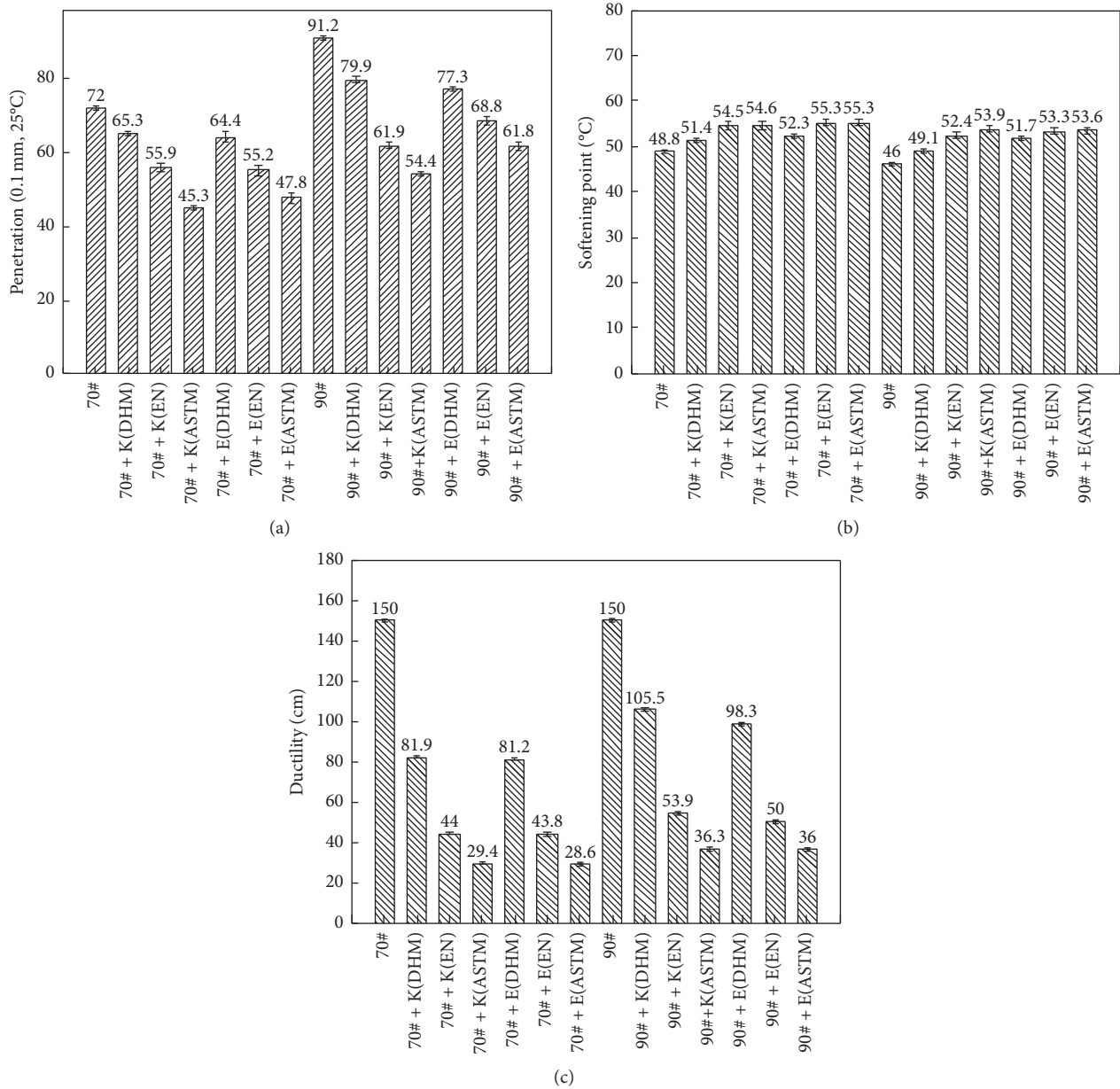


FIGURE 4: Performances of the emulsified asphalt residues.

$$N_f = A_{35} (\gamma_{max})^B, \tag{8}$$

where  $\gamma_{max}$  = the maximum expected binder strain.

### 3. Results and Discussion

3.1. *Physical Performance.* The physical performance test results of the emulsified asphalt residues are shown in Figure 4. The ductility test values for the 70# and 90# matrix asphalt binders were greater than 150 cm and were recorded as 150 cm. As can be seen from Figure 4, the evaporation method has significant effects on the penetration and the ductility of the residue but has little effect on the softening point. The penetration and ductility of the residues that were

obtained by the direct heating method are the largest, followed by those obtained by the EN13074 evaporation method, and those obtained by the ASTM D7497-09 evaporation method are the smallest. The softening point of the residues that were obtained by the ASTM D7497-09 evaporation method is slightly higher than that obtained by the EN13074 evaporation method, and the values for the residues that were obtained by both evaporation methods are higher than that by the direct heating method. In addition, compared with the matrix asphalt, the softening point of emulsified asphalt residues increases and the ductility substantially decreases. The main reason is that the hydrophilic group of the emulsifier is mainly an amine group, and the amine group has a strong affinity with

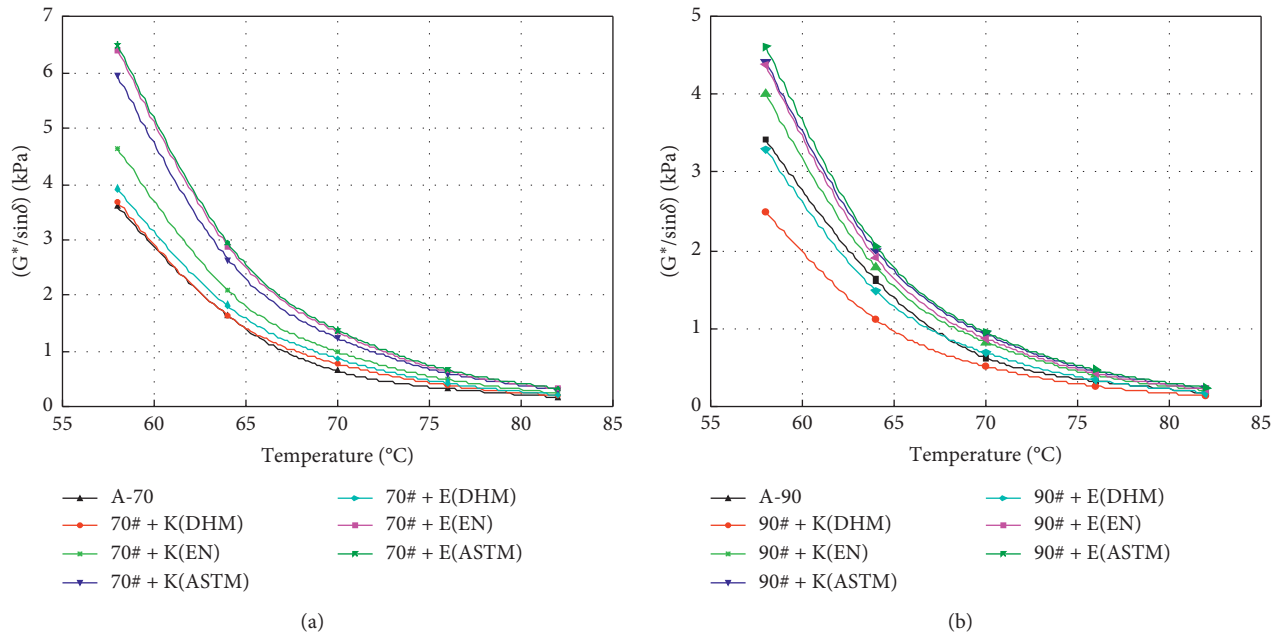


FIGURE 5: Variation of the rutting factor of the emulsified asphalt residue with temperature.

asphalt. When the content of the amine group reaches a certain amount, it will agglomerate the fusion between asphalt molecules and improve the performance of asphalt.

### 3.2. Linear Viscoelasticity of the Emulsified Asphalt Residue

**3.2.1. Temperature Sweep Test Results.** The rutting factor ( $G^*/\sin\delta$ ) was used as an index to characterize the high performance of asphalt in AASHTO M320-05 [38]. The values of  $G^*/\sin\delta$  of the emulsified asphalt residues that were obtained via the different evaporation methods were used to analyze the high-temperature performance, as shown in Figure 5. The rutting factors of the residues decrease gradually with the increase in temperature. Hence, the rutting resistance decreases with the increase in the temperature. According to Figure 5(a), under the same temperature, the rutting factors of the 70#+K emulsified asphalt residues that were prepared by the ASTM D7497-09 evaporation method are the largest, followed by that prepared by the EN13074 evaporation method, and the rutting factors of the residues that were obtained by the direct heating method are the smallest. The 70#+E emulsified asphalt residues that were prepared by the ASTM D7497-09 and EN13074 evaporation methods have approximately the same rutting factors, which are significantly higher than those obtained by the direct heating method. According to Figure 5(b), the evaporation methods are ordered according the rutting factor of each residue as ASTM D7497-09>EN13074>DHM. The test results indicate that the oxidation of the binder during the residue recovery procedure could lead to a stiffer and more elastic response, and the results of Hanz et al. [39] and Islam et al. [19] confirmed this conclusion. Comparing Figures 5(a) and 5(b), the rutting factor of the 90# asphalt binder is less than that of the 70#

asphalt binder, and the rutting factor of the emulsified asphalt residue that was prepared from the 90# asphalt is less than that of the residue that was prepared from the 70# asphalt. The results show that the matrix asphalt significantly affects the properties of the emulsified asphalt residue.

**3.2.2. Complex Modulus and Phase Angle Master Curves.** The complex modulus and the phase angle master curves that correspond to the residues that were recovered using the three methods are plotted in Figure 6. At lower frequencies, these curves show that the complex modulus values of the residues that were prepared by both the ASTM D7497-09 and EN13074 evaporation methods are larger than those that were prepared by the direct heating method. The results show that the ASTM D7497-09 and EN13074-cured residues were stiffer than the direct-heating-method-cured residues for all emulsified asphalt binders. However, at high frequencies, the emulsified asphalt residues under different evaporation conditions have similar complex modulus values. Meanwhile, these curves also show that both the ASTM D7497-09 and EN13074-cured residues have smaller phase angles than the direct-heating-method-cured residues for all emulsified asphalt binders. Specifically, the ASTM D7497-09 and EN13074-cured residues have similar phase angle values for the 70#+E, 90#+K, and 90#+E emulsified asphalt binders, while the 70#+K emulsified asphalt shows significantly smaller phase angle values of the ASTM D7497-09-cured residues. The influences of the evaporation method on the complex modulus and the phase angle of residues differ, which has a strong relationship with the emulsifier type. Comparing Figure 6(a) with Figure 6(c), the slope for the emulsified asphalt residues prepared from 70# asphalt is greater than that for the residues prepared from 90# asphalt. Therefore, the emulsified asphalt residues that were prepared

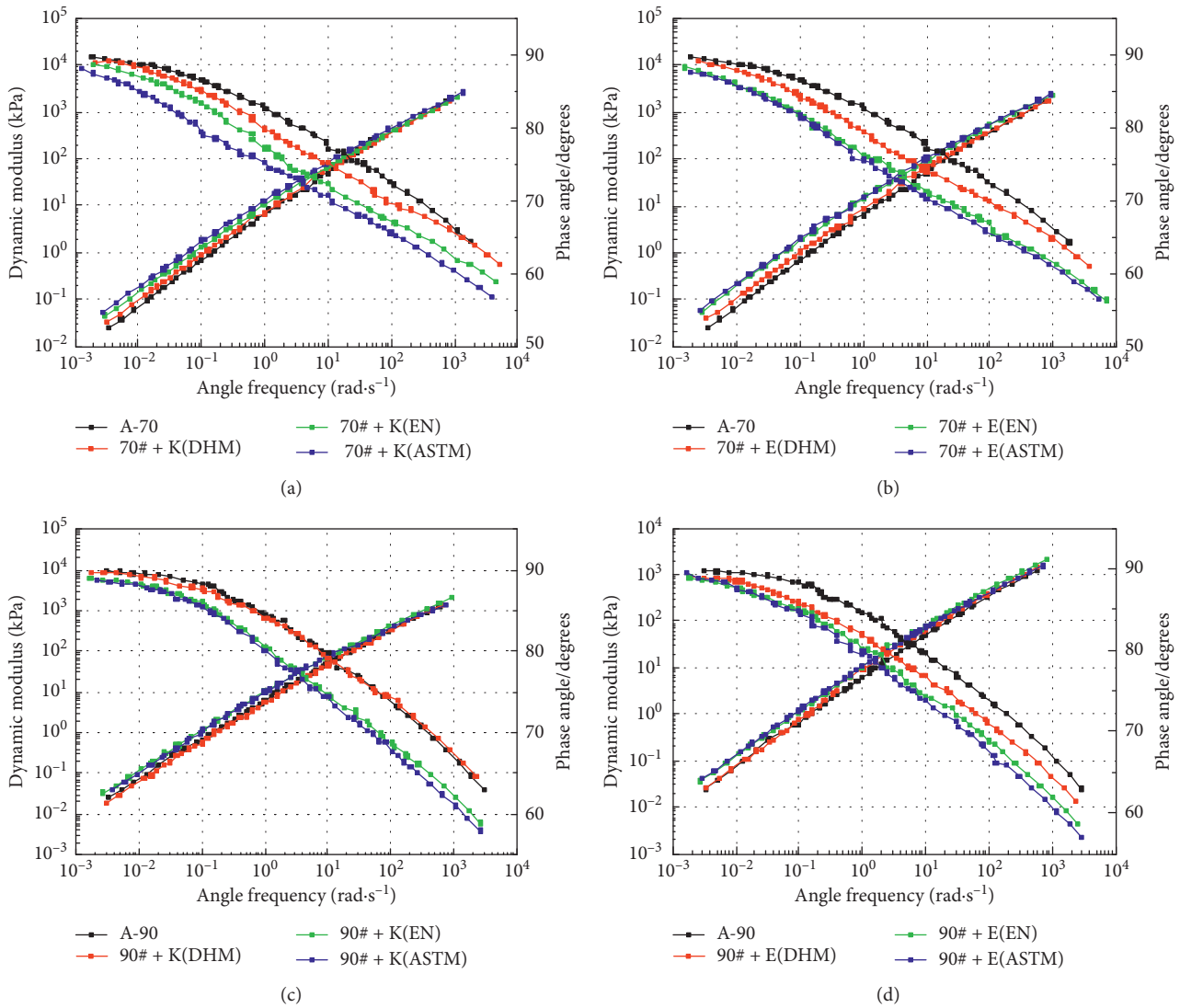


FIGURE 6: Master curves of emulsified asphalt residues at a reference temperature of 40°C.

from 70# asphalt are more susceptible to temperature changes than the emulsified asphalt residues that were prepared from 90# asphalt.

### 3.3. Permanent Deformation Resistance

**3.3.1. Analysis of the Nonrecoverable Compliance and the Percent Recovery.** The calculated performance indicators, namely, the nonrecoverable creep compliance ( $J_{nr}$ ) and the recovery percent ( $R$ ) are summarized in Figures 7 and 8. For all emulsified asphalt binders, the  $J_{nr}$  values of the emulsified asphalt residues that were prepared by the direct heating method are significantly higher than those of the residues that were prepared by the EN13074 and ASTM D7497-09 evaporation methods. Moreover, the  $J_{nr}$  values of the emulsified asphalt residues that were prepared by the ASTM D7497-09 evaporation method are the smallest. At 64°C and 70°C, except for 90#+K (DHM), the  $J_{nr}$  values of the emulsified asphalt residues were found to be smaller than

those of the matrix binders. Hence, the addition of emulsifiers can improve the permanent deformation resistance of the emulsified asphalt. As shown in Figure 7, the  $J_{nr}$  values of the emulsified asphalt residues that were prepared from 90# asphalt are greater than those of the emulsified asphalt residues that were prepared from 70# asphalt, and the higher the temperature is, the larger the  $J_{nr}$  values of the emulsified asphalt residues are.

Figure 8 shows the values of the percent recovery of emulsified asphalt residues under different stresses and temperatures. The evaporation method significantly influenced the percent recovery of the emulsified asphalt residues, especially at the low stress level. Under three different evaporation conditions, all the emulsified asphalt residues show the same trend:  $R$  (ASTM D7497-09) >  $R$  (EN13074) >  $R$  (DHM). This is mainly because the emulsified asphalt residues were aged during the evaporation process, and the light components in the residues were converted into heavy components, which caused the emulsified asphalt residues to

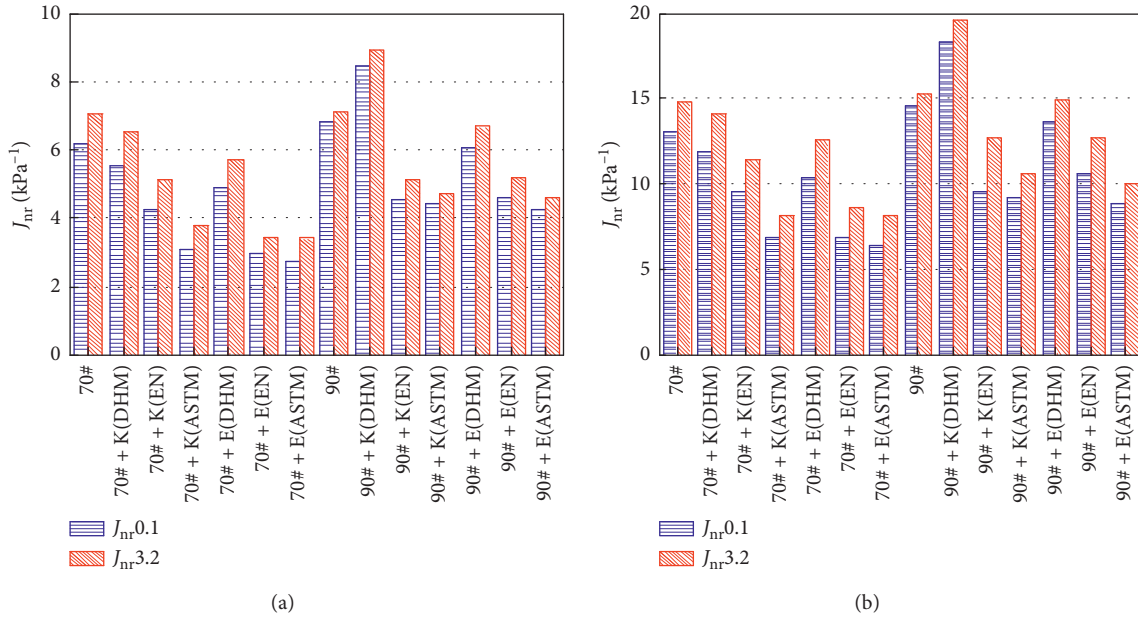


FIGURE 7:  $J_{nr}$  values for emulsified asphalt residues at (a) 64°C and (b) 70°C.

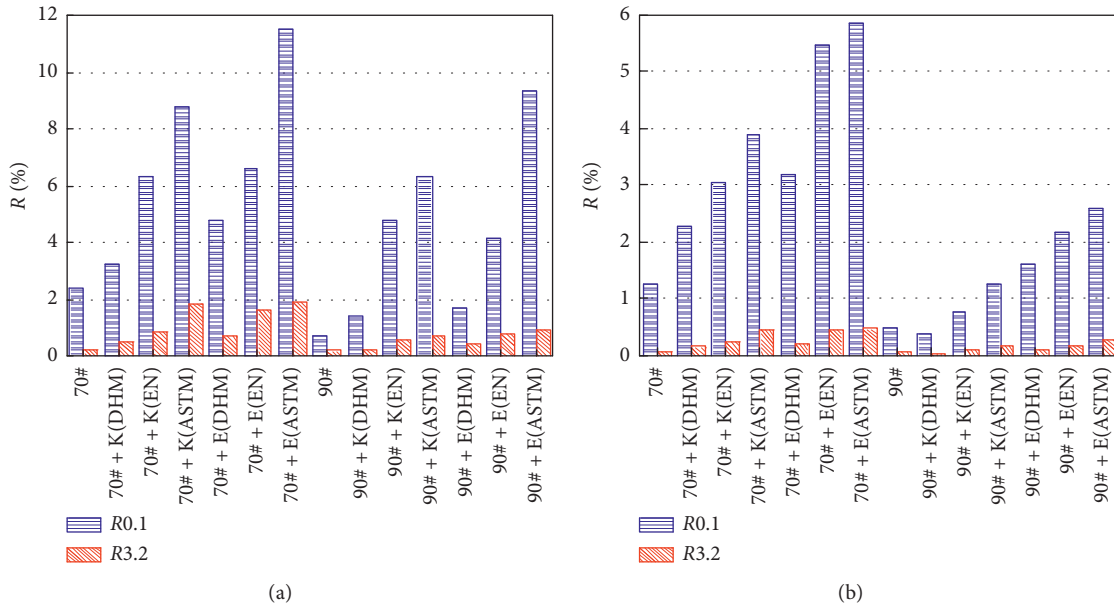


FIGURE 8: Percent recovery results for emulsion asphalt residues at (a) 64°C and (b) 70°C.

harden and the deformation recovery ability to be enhanced. The matrix asphalt has a percent recovery of almost 0% at high stress, compared to approximately 1% at low stress. The addition of emulsifier improves the percent recovery of the matrix binder at both levels of stress, namely, 0.1 kPa and 3.2 kPa. In addition, the recovery percentage values of the residues that were prepared from the 70# asphalt binder are greater than those of the emulsified asphalt residues that were prepared from the 90# asphalt. From the overall MSCR results, together with the rutting factors from temperature sweep test, it is concluded that the presence of an emulsifier increases the rutting resistance and the high-temperature

deformation resistance of the asphalt binder. Furthermore, the residues that were prepared from 70# asphalt have better high-temperature performance than the residues that were obtained from 90# asphalt.

3.3.2. *Analysis of the Stress Sensitivity.* Figure 9 presents the  $J_{nr, diff}$  value results for emulsified asphalt residues at different testing temperatures. At 64°C and 70°C, the  $J_{nr, diff}$  values of all binders were below 75%. Except for 90#+K(EN), the emulsified asphalt residues that were prepared from the 90# asphalt have lower  $J_{nr, diff}$  values than the



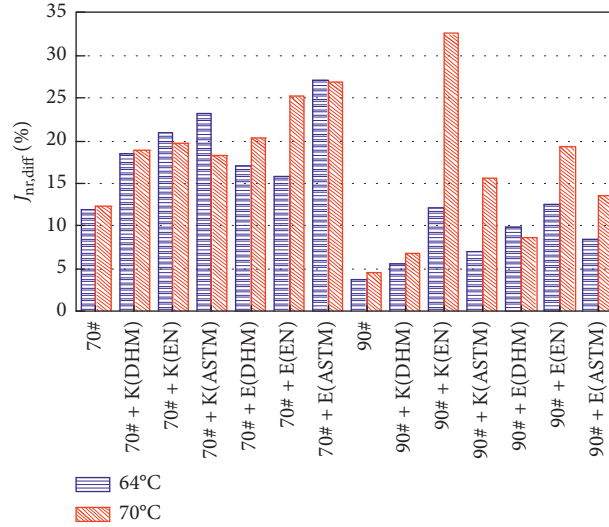
FIGURE 9:  $J_{nr,diff}$  value results for the emulsified asphalt residues.

TABLE 3: VECD analysis parameter results of the LAS test for the emulsified asphalt residues.

Binder type	$C_0$	$C_1$	$C_2$	$A$	$B$	$\alpha$	$\tau_{max}$ (kPa)	$R^2$
70#	1.757	0.048	0.559	213069	-2.325	1.163	127	0.986
70#+K(DHM)	1.246	0.026	0.633	302052	-2.425	1.213	105	0.987
70#+K(EN)	1.508	0.152	0.370	419745	-2.665	1.332	66	0.910
70#+K(ASTM)	1.958	0.314	0.285	565058	-2.826	1.413	70	0.967
70#+E(DHM)	0.448	0.041	0.520	481109	-2.987	1.493	33	0.994
70#+E(EN)	1.664	0.042	0.569	349896	-2.505	1.253	132	0.992
70#+E(ASTM)	0.679	0.041	0.534	494815	-2.805	1.402	43	0.984
90#	1.556	0.045	0.570	145737	-2.229	1.114	118	0.986
90#+K(DHM)	1.304	0.022	0.670	175995	-2.244	1.122	118	0.983
90#+K(EN)	1.505	0.045	0.554	300217	-2.427	1.214	119	0.992
90#+K(ASTM)	1.598	0.044	0.557	457384	-2.606	1.303	126	0.992
90#+E(DHM)	2.217	0.057	0.563	198238	-2.515	1.257	150	0.982
90#+E(EN)	2.059	0.219	0.348	237099	-2.510	1.255	78	0.961
90#+E(ASTM)	1.674	0.031	0.620	228496	-2.335	1.168	132	0.984

emulsified asphalt residues that were prepared from 70# asphalt. When the emulsifier was added to the matrix asphalt binders, the  $J_{nr,diff}$  values increased, namely, the inclusion of the emulsifier caused the emulsified asphalt to be more sensitive to stress. The evaporation method influenced the  $J_{nr,diff}$  values of the emulsified asphalt residues, but the change trend is different. Specifically, for 70#+K and 70#+E emulsified asphalt, the residues obtained by the ASTM D7497-09 evaporation method have the largest  $J_{nr,diff}$  values. For 90#+K and 90#+E emulsified asphalt, the residues obtained by the EN13074 evaporation method have the largest  $J_{nr,diff}$  values.

### 3.4. Fatigue Resistance

**3.4.1. Analysis of the Damage Intensity and Integrity Parameters.** The LAS test fatigue damage values for different emulsified asphalt residues are provided in Table 3. Lower values of  $C_1$  and  $C_2$  correspond to higher binder fatigue performance [35, 40, 41]. According to Table 3, under the

different evaporation methods, the values of parameters  $C_1$  and  $C_2$  have different trends, increasing or decreasing. It is difficult to judge the fatigue performance of the emulsified asphalt residues.

To clearly see the overall impact of the decrease in the integrity parameter, the fatigue damage should be evaluated in combination with the relationship between the damage intensity ( $D$ ) and the integrity parameter ( $C$ ), as presented in Figure 10. The value of  $C$  is 1, which means that the asphalt binder is not damaged, and the value of  $C$  is 0, which means that the asphalt binder is completely damaged. The test results demonstrate that the evaporation method influences the fatigue damage tolerance of the emulsified asphalt residue. According to Figure 10(a), at the specified damage level ( $D$ ), the residues prepared by the evaporation method of ASTM D7497-09 have the lowest integrity, followed by EN13074 evaporation, and the residues prepared by the direct heating method have the highest integrity. However, the emulsified asphalt residues that were prepared from 90# asphalt show more complicated change trends under

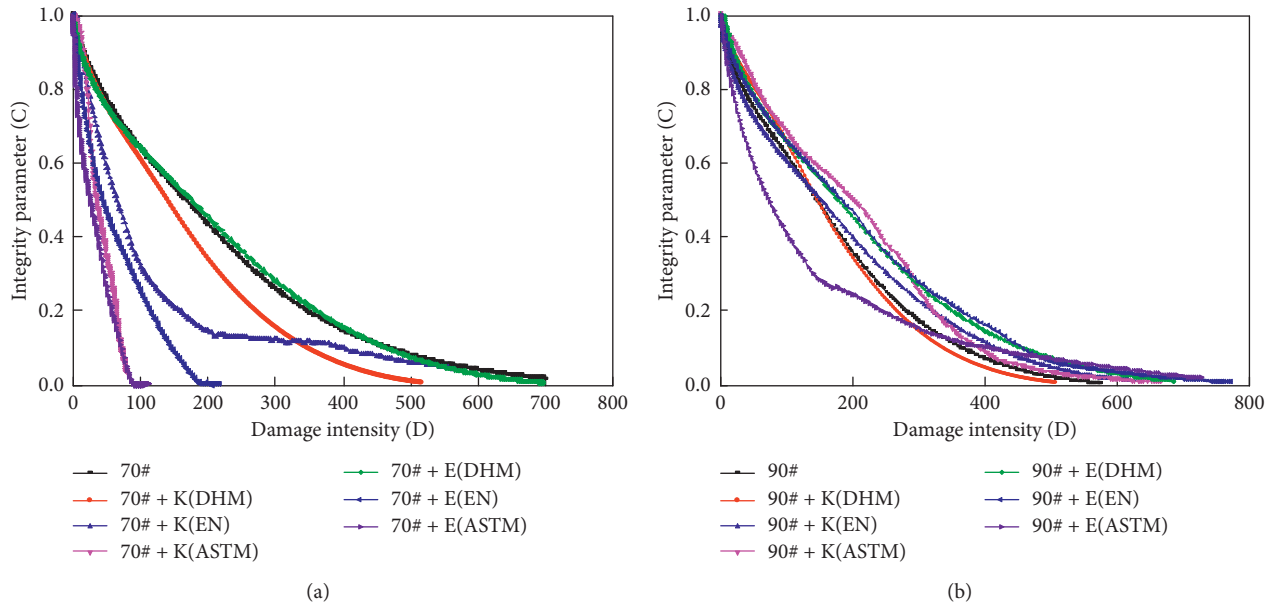


FIGURE 10: Integrity parameter versus damage intensity for the emulsified asphalt residues.

different evaporation methods. According to Figure 10(b), the evaporation methods are ordered in terms of the integrity of the 90#+K emulsified asphalt residues as follows: C (ASTM D7497-09)>C (EN13074)>C (DHM). While the 90#+E emulsified asphalt residues that were prepared by EN13074 and the direct heating method have similar integrities, their integrities are significantly greater than those prepared by the ASTM D7497-09 evaporation method.

3.4.2. Analysis of the Number of Cycles to Fatigue Failure ( $N_f$ ). Figure 11 shows the number of cycles to fatigue failure in the LAS test for the emulsified asphalt residue at the 2.5% strain level. The significant influences of the evaporation method and the emulsifier type on the fatigue performance are demonstrated via an analysis of variance that was conducted at a confidence level of 95%, which identified the evaporation method and the emulsifier type as significant factors, and the average  $p$  values are 0.000 and 0.009, respectively. According to these data, although there are differences among the emulsions, the evaporation method had the most significant impact on the fatigue life. As shown in Figure 11, the three evaporation methods are ordered in terms of the fatigue life of the four emulsified asphalts as follows:  $N_f$  (ASTM D7497-09) >  $N_f$  (EN13074) >  $N_f$  (DHM). In addition, the fatigue life of the K emulsified asphalt residues is greatly affected by the evaporation method. Under the different evaporation methods, the fatigue life change rate of the K emulsified asphalt is greater than that of the E emulsified asphalt residue. The change in the fatigue life is consistent with Hintz et al. [42], who reported that aging was beneficial to the fatigue performance at small strain amplitudes and detrimental at high strain amplitudes. Furthermore, the rate at which the material ages depend on the chemical properties of the emulsifier, and the variation in

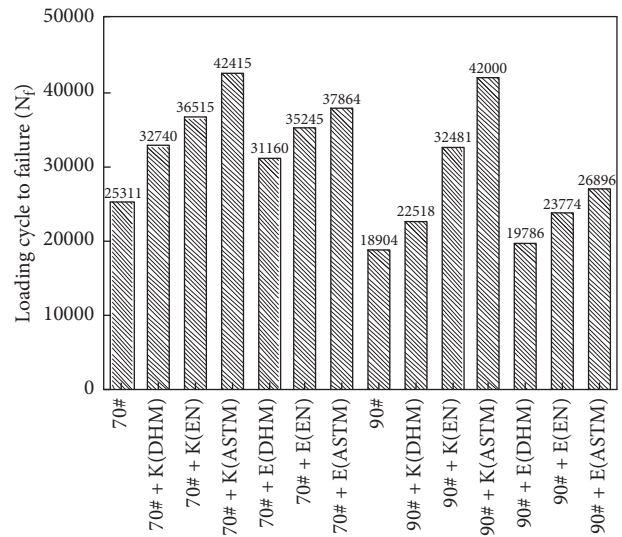


FIGURE 11: LAS test fatigue life of emulsified asphalt residues at the 2.5% strain level.

aging susceptibility is more prevalent in cationic emulsions [42].

To explain the oxidation phenomenon in terms of the binder chemistry, Ge et al. [14] and Malladi et al. [23] conducted a Fourier transform infrared spectroscopy (FTIR) test. Test results showed that compared with S=O and C=O of the emulsified asphalt residue can better characterize the aging of the emulsified asphalt. However, no clear trend was observed in the relative oxidation levels of the emulsion residues that were recovered using various evaporation methods. This problem remains unsolved, and many studies are being conducted to understand the curing procedure of emulsified asphalt residues.

#### 4. Conclusions and Recommendations

This study investigated the effects of evaporation methods on the rheological and fatigue performances of emulsified asphalt residues using physical tests, linear viscoelastic property tests, permanent deformation resistance tests, and fatigue resistance tests. The following conclusions are obtained:

- (1) Under the three evaporation conditions, the penetration and ductility of residues obtained by the direct heating method are the largest, followed by those obtained by EN13074 evaporation method, and the penetration and ductility of residues obtained by the ASTM D7497-09 evaporation method are the smallest. However, the evaporation method has little effect on the softening point of emulsified asphalt residues.
- (2) The growth amplitude order of the rutting factor and the recovery percent values of emulsified asphalt residues is ASTM D7497-09 > EN13074 > DHM, and as is the attenuation amplitude order by the non-recoverable creep compliance. The overall results indicate that the residues obtained by ASTM D7497-09 suffered more serious aging than EN13074 and direct heating methods.
- (3) Compared with the residues obtained by the direct heating method, the emulsified asphalt residues obtained by the EN13074 and ASTM D7497-09 evaporation method have higher complex modulus and exhibit lower phase angle values in terms of various frequencies.
- (4) The results of the variance analysis prove that the evaporation method has more significant influence on the fatigue life of the residues. The three different evaporation methods are ordered according to the fatigue life as  $N_f$  (ASTM D7497-09) >  $N_f$  (EN 13074) >  $N_f$  (DHM).
- (5) The rheological and fatigue performances of the residues depend on the matrix asphalt. Compared with the emulsified asphalt residue that was prepared from 90# asphalt, the residue that was prepared from 70# asphalt has good high-temperature and fatigue properties, but it has higher temperature sensitivity and stress sensitivity.

This research provides an effective strategy for finding a method that most accurately reflects the residual binders that are applied in the field and promotes the application of emulsified asphalt. It is recommended that an investigation of the chemical and rheological properties of the residual binders that are recovered from the field should be conducted to identify the residue recovery procedure that best reflects the residual binder that is placed in the field.

#### Data Availability

The data used to support the findings of this study are included within the article.

#### Conflicts of Interest

The authors declare that there are no conflicts of interest regarding the publication of this paper.

#### Acknowledgments

This work was financially supported by the National Natural Science Foundation of China, China (grant no. 51708513), and the research project of Henan Provincial Department of Transportation, China (grant no. 2019 (J) 1). The authors are sincerely grateful for their support.

#### References

- [1] J. Zhang, Z. Fan, D. Hu, Z. Hu, J. Pei, and W. Kong, "Evaluation of asphalt-aggregate interaction based on the rheological properties," *International Journal of Pavement Engineering*, vol. 19, no. 7, pp. 586–592, 2018.
- [2] X. Sheng, M. Wang, T. Xu, and J. Chen, "Preparation, properties and modification mechanism of polyurethane modified emulsified asphalt," *Construction and Building Materials*, vol. 189, pp. 375–383, 2018.
- [3] H. Taherkhani, F. Firoozei, and J. Bolouri Bazaz, "Evaluation of the mechanical properties of the cement treated cold-in-place recycled asphalt mixtures," *International Journal of Transportation Engineering*, vol. 3, no. 4, pp. 301–312, 2016.
- [4] J. Xiao, W. Jiang, W. Ye, J. Shan, and Z. Wang, "Effect of cement and emulsified asphalt contents on the performance of cement-emulsified asphalt mixture," *Construction and Building Materials*, vol. 220, pp. 577–586, 2019.
- [5] M. O. Marasteanu and T. R. Clyne, "Rheological characterization of asphalt emulsions residues," *Journal of Materials in Civil Engineering*, vol. 18, no. 3, pp. 398–407, 2006.
- [6] S. Sanjeevan, M. Piratheepan, E. Y. Hajj, and A. K. Bush, "Cold in-place recycling in Nevada," *Transportation Research Record: Journal of the Transportation Research Board*, vol. 2456, no. 1, pp. 146–160, 2014.
- [7] D. Salomon, M. Thompson, G. Durand et al., "Comparison of rheological properties for recovered residue from emulsified asphalt obtained by three recovery procedures," in *Proceedings of the International Symposium of Asphalt Emulsion Technology (ISAET)*, Washington, DC, USA, September 2008.
- [8] J. Y. Pang, S. J. Du, and R. T. Chang, "Effect of emulsifier content on the rheological properties of asphalt emulsion residues," *Journal of Applied Polymer Science*, vol. 132, no. 15, 2015.
- [9] G. J. Xu, M. Z. Chen, S. P. Wu, M. Van De Ven, and S. Mookhoek, "Rheological characteristics of residue binder from low penetration grade bitumen emulsion," *Key Engineering Materials*, vol. 509, pp. 328–332, 2012.
- [10] G. N. King, H. King, and L. Galehouse, "Field validation of performance-based polymer-modified emulsion residue tests: the FLH study," in *Proceedings of the First International Conference on Pavement Preservation California Department of Transportation Federal Highway Administration Foundation for Pavement Preservation*, pp. 247–267, Newport Beach, CA, USA, June 2010.
- [11] A. Motamed, D. Salomon, N. Sakib, and A. Bhasin, "Emulsified asphalt residue recovery and characterization," *Transportation Research Record: Journal of the Transportation Research Board*, vol. 2444, no. 1, pp. 88–96, 2014.

- [12] D. G. Hazlett, "Emulsion residue recovery techniques: how do we get emulsion residue representative of in-service binder?" *Journal of the Transportation Research Board*, no. E-C122, 2007.
- [13] J. C. Waters, G. M. Bosma, and P. R. Herrington, *Residual Binder Extraction from Emulsions for Quality Assurance Testing*, Vol. 360, New Zealand Transport Agency, Wellington, New Zealand, 2008.
- [14] D. D. Ge, Z. P. You, and S. Y. Chen, "Residue performance evaluation of emulsified asphalt," in *Proceedings of the 12th International Conference on Low-Volume Roads*, pp. 2–7, Kalispell, MT, USA, September 2019.
- [15] K. Takamura and C. Lubbers, "Comparison of emulsion residues recovered by forced airflow and RTFO drying," in *Proceedings of the ISSA/AEMA Proceedings*, pp. 1–17, Amelia Island, FL, USA, March 2000.
- [16] M. J. Farrar, S. L. Salmans, and J.-P. Planche, "Recovery and laboratory testing of asphalt emulsion residue," *Transportation Research Record: Journal of the Transportation Research Board*, vol. 2370, no. 1, pp. 69–75, 2013.
- [17] A. J. Hanz, P. Johannes, and H. U. Bahia, "Development of emulsion residue testing framework for improved chip seal performance," *Transportation Research Record: Journal of the Transportation Research Board: Transportation Research Record*, vol. 2293, no. 1, pp. 106–113, 2012.
- [18] M. Hospodka, B. Hofko, and R. Blab, "Impact of distillation temperature on the solvent residue and viscoelastic properties of asphalt binders," *Road Materials and Pavement Design*, vol. 19, no. 6, pp. 1275–1287, 2018.
- [19] R. M. Islam, S. S. Ashani, N. M. Wasiuddin, and W. B. King, "Effects of curing time, temperature, and vacuum pressure on asphalt emulsion residue recovered by vacuum drying method," *Journal of Testing and Evaluation*, vol. 43, no. 5, pp. 1134–1145, 2014.
- [20] JTG E20-2011, *Standard Test Methods of Bitumen and Bituminous Mixtures for Highway Engineering*, China communications Press, Beijing, China, 2011.
- [21] Q. Zhang, P. W. Hao, and Z. Y. Bai, "Research on effect of waterborne epoxy resin on modified asphalt emulsion and its mechanism," *Highway Engineering*, vol. 41, no. 2, pp. 109–112, 2016.
- [22] X. W. Gao and J. Y. Pang, "Emulsified asphalt cold recycled mixture based on rheological properties," *Journal of Chang'an University (Natural Science Edition)*, vol. 38, no. 4, pp. 21–28, 2018.
- [23] H. Malladi, M. Asnake, A. LaCroix, and C. Castorena, "Low-temperature vacuum drying procedure for rapid asphalt emulsion residue recovery," *Transportation Research Record: Journal of the Transportation Research Board*, vol. 2672, no. 28, pp. 256–265, 2018.
- [24] C. Wang, W. Xie, Y. Chen, A. Diab, and Z. You, "Refining the calculation method for fatigue failure criterion of asphalt binder from linear amplitude sweep test," *Journal of Materials in Civil Engineering*, vol. 30, no. 2, Article ID 04017286, 2018.
- [25] X. Hou, F. Xiao, R. Guo, Q. Xiang, T. Wang, and J. Wang, "Application of spectrophotometry on detecting asphalt content of emulsified asphalt," *Journal of Cleaner Production*, vol. 215, pp. 626–633, 2019.
- [26] M. R. Mitchell, R. E. Link, and N. Prapaitrakul, "Comparative study on recovered binder properties using three asphalt emulsion recovery methods," *Journal of Testing and Evaluation*, vol. 38, no. 6, pp. 653–659, 2010.
- [27] ASTM D, *Standard Test Method for Penetration of Bituminous Materials*, American Society for Testing and Materials, West Conshohocken, PA, USA, 2013.
- [28] ASTM D, *Standard Test Method for Softening Point of Bitumen (Ring-and-ball Apparatus)*, American Society for Testing and Materials, West Conshohocken, PA, USA, 2014.
- [29] ASTM D, *Standard Test Method for Ductility of Asphalt Materials*, American Society for Testing and Materials, West Conshohocken, PA, USA, 2017.
- [30] AASHTO Designation: T 315-06, *Standard Test Method for Determining the Rheological Properties of Asphalt Binder Using a Dynamic Shear Rheometer (DSR)*, American Society for Testing and Materials, West Conshohocken, PA, USA, 2006.
- [31] M. Marateanu and D. Anderson, "Time-temperature dependency of asphalt binders-an improved model (with discussion)," *Journal of the Association of Asphalt Paving Technologists*, vol. 65, 1996.
- [32] M. L. Williams, R. F. Landel, and J. D. Ferry, "The temperature dependence of relaxation mechanisms in amorphous polymers and other glass-forming liquids," *Journal of the American Chemical Society*, vol. 77, no. 14, pp. 3701–3707, 1955.
- [33] AASHTO Designation: TP 70-10, *Standard Method of Test for Multiple Stress Creep Recovery (MSCR) Test of Asphalt Binder Using a Dynamic Shear Rheometer (DSR)*, American Society for Testing and Materials, West Conshohocken, PA, USA, 2010.
- [34] X. Yang and Z. You, "High temperature performance evaluation of bio-oil modified asphalt binders using the DSR and MSCR tests," *Construction and Building Materials*, vol. 76, pp. 380–387, 2015.
- [35] C. Hintz and H. Bahia, "Simplification of linear amplitude sweep test and specification parameter," *Transportation Research Record: Journal of the Transportation Research Board*, vol. 2370, no. 1, pp. 10–16, 2013.
- [36] G. Xu, H. Wang, and H. Zhu, "Rheological properties and anti-aging performance of asphalt binder modified with wood lignin," *Construction and Building Materials*, vol. 151, pp. 801–808, 2017.
- [37] AASHTO TP 101, *Estimating Damage Tolerance of Asphalt Binders Using the Linear Amplitude Sweep*, American Association of State Highway and Transportation Officials, Washington, DC, USA, 2014.
- [38] AASHTO M. 320-05, *Standard Specification for Performance-Graded Asphalt Binder*, American Society for Testing and Materials, West Conshohocken, PA, USA, 2005.
- [39] A. J. Hanz, Z. A. Arega, and H. U. Bahia, "Rheological behavior of emulsion residues produced by evaporative recovery method," *Transportation Research Record: Journal of the Transportation Research Board*, vol. 2179, no. 1, pp. 102–108, 2010.
- [40] R. Micaelo, A. Pereira, L. Quaresma, and M. T. Cidade, "Fatigue resistance of asphalt binders: assessment of the analysis methods in strain-controlled tests," *Construction and Building Materials*, vol. 98, pp. 703–712, 2015.
- [41] C. Hintz, R. Velasquez, C. Johnson, and H. Bahia, "Modification and validation of linear amplitude sweep test for binder fatigue specification," *Transportation Research Record: Journal of the Transportation Research Board*, vol. 2207, no. 1, pp. 99–106, 2011.
- [42] C. Hintz, R. Velasquez, and Z. Li, "Effect of oxidative aging on binder fatigue performance," *Journal of the Association of Asphalt Paving Technologists*, vol. 80, pp. 527–548, 2011.



## Research Article

# Delivering Sustainable Solutions through Improved Mix and Structural Design Functions for Bitumen Stabilised Materials

**K. J. Jenkins** , **C. E. Rudman**, and **C. R. Bierman**

*Stellenbosch University, Stellenbosch, South Africa*

Correspondence should be addressed to K. J. Jenkins; [kjenkins@sun.ac.za](mailto:kjenkins@sun.ac.za)

Received 5 November 2019; Accepted 24 December 2019; Published 12 March 2020

Guest Editor: Alan Carter

Copyright © 2020 K. J. Jenkins et al. This is an open access article distributed under the Creative Commons Attribution License, which permits unrestricted use, distribution, and reproduction in any medium, provided the original work is properly cited.

The evolution of cold recycling using bitumen stabilisation technology has been supported by progressive research initiatives and best practice guidelines. The first generic guidelines for bitumen stabilised materials (BSMs) were published only in 2002. These guidelines provided a generic approach for the analysis of foamed bitumen and bitumen emulsion technologies. From that point, bitumen stabilisation became the common term for the inclusion of either of the two bituminous binders. The TG2 2<sup>nd</sup> edition guideline of 2009 took a bold step recognising the shear properties of the bitumen stabilised material (BSM) as the key performance indicators. In addition, advancements in structural design and application of BSMs provided practitioners with robust guidelines. The subsequent decade has provided an opportunity to interrogate data from more than 300 BSM mix designs and 69 LTPP sections. The data have led to research developments including significant new performance properties of BSMs, refined mix design methods, and updated new pavement design methods. This includes an entire design process that has been updated with a streamlined mix design procedure and a new frontier curve for the pavement number design method, as well as a new mechanistic design function. It is anticipated that the research findings and implementation of the newly developed technology will lead to improved application in BSM technology.

## 1. Introduction

Since the 1950's, there has been a strong emphasis on finding efficient, cost-effective pavement rehabilitation technologies. Part of this history included Prof. Csanyi [1] experimenting with hot bitumen and water in order to expand its volume and thus improve dispersion in marginal materials at ambient temperatures. Csanyi's development of foamed bitumen using steam was taken further by Acott and Myburgh [2] and Ackeroyd and Hicks [3, 4]. At that time, the impact that foamed bitumen technology was about to have on pavement rehabilitation and sustainable practice was not yet apparent.

In the 1990's, the patent rights that Mobil bought from Csanyi lapsed. In the interim, Mobil developed the foaming technology further by applying accurate dosages of water rather than steam. Applications of foamed bitumen to stabilise crushed aggregates, gravels, sands, and recycled asphalt provided good performance. At the same time,

bitumen emulsion provided an alternate way to stabilise base layers. Both foam and emulsion technologies were providing flexible and durable bases for a range of rehabilitated pavement structures using cold recycling. The need for rigorous mix design methods and structural design procedures led South Africa to develop guidelines and manuals for granular emulsion mixes (GEMS) [5], emulsion-treated bases (ETBs) [6], and foamed bitumen-treated materials [7]. A generic term for the two bitumen binders was created under the title of bitumen stabilised materials (BSMs). The structural design of BSM began with the Sabita GEMS and ETB Manuals, which incorporated mechanistic-empirical (ME) design functions.

In 2002, the first Technical Guideline TG2 was published, for foamed bitumen materials. In TG2, a mechanistic-empirical (ME) structural design function was provided for pavements including cold recycling. However, this function was based on only one data set and was found to be conservative. In 2009, the second edition of TG2 was



released and included a new design method, the pavement number, and the associated design equivalent material classification System. There was no inclusion of ME function.

Ever increasing economic and environmental pressures drive the development of more effective technologies for road construction and rehabilitation. By 2009, overwhelming evidence of the primary distress mechanism for BSMs being permanent deformation and not fatigue cracking was identified. Although the principle of BSM being a noncontinuously bound material is well understood, the prediction of long-term stiffness behaviour and permanent strain development has not been developed to the same degree [8].

Long-term pavement performance (LTPP) sections, i.e., 20 field sites and 7 accelerated pavement testing (APT) sites with 22 sections tested by the Heavy Vehicle Simulator (HVS) tester formed the basis of the data for the 2009 guidelines.

Following this trend, the additional performance data related to pavements with both BSM-foam and BSM-emulsion were expanded in the 10 years following 2009. This paper addresses the developments in mix design and pavement design of BSM based on updated performance data from the LTPP and APT sections. In addition, a new mechanistic-empirical design function has been developed in this period.

The noncontinuous binding behaviour of BSMs is explained in the Asphalt Academy's Technical Guideline (TG2) [9]. The failure mechanism of BSMs, permanent deformation, is also thoroughly explained in the TG2. The design of BSMs should focus on permanent deformation in the layer. The current design methods, specifically the pavement number (PN) method, are based on experience and tend to be very conservative. This paper aims to present a design function for BSMs which relates mechanical material properties and stress conditions to pavement life based on field observations.

## 2. Background

*2.1. Defining a BSM.* Firstly, it is important to provide a brief description of BSM technology and what sets it apart from *grave emulsion* and cold patching mixes. Bitumen stabilisation is typically used in the rehabilitation of existing pavement base layers (granular, cemented, or asphalt) using either foamed bitumen or bitumen emulsion. The granular material is treated with small amounts of bitumen, i.e., less than 3%. A small amount of active filler, typically 1%, is used in the mix to improve the bitumen adhesion to the aggregate. The resulting material is a noncontinuously bound material that differs from hot mix asphalt (HMA) and cement-stabilised material. Stabilisation with bitumen significantly increases the cohesion of the aggregate particles with little or no change in the angle of friction.

The role of the BSM base in a pavement structure is to protect the underlying layers and subgrade from excessive stresses imposed by traffic. BSMs, with resilient modulus values of typically 600 to 1400 MPa, effectively achieve distribution the imposed loads. In this way, the BSM layer provides intermediate stiffness values between the high

modulus of the asphalt layers above and granular support below, thus creating a balanced system to achieve the desired design structural capacity.

*2.2. Factors Influencing Permanent Deformation of BSMs.* Permanent deformation is the accumulation of shear deformation caused by repeated traffic loading. As BSMs fail in permanent deformation, a design function for this material should take the factors influencing permanent deformation into account. The factors influencing permanent deformation of BSMs include

- (1) Grading of the parent material
- (2) Physical properties of the aggregate particles
- (3) Density achieved during compaction
- (4) Moisture content (including equilibrium) and moisture susceptibility
- (5) Number of load repetitions applied to the material
- (6) Magnitude of the applied loads
- (7) Stress history of the material
- (8) Lateral or confining pressure
- (9) The amount of active filler added to the mix

Of these variables, four significant factors were identified for incorporation into a mechanistic design function. The four selected factors are: retained cohesion, percentage of maximum dry density, deviator stress ratio, and permanent strain limit. This was reduced to three factors when the permanent strain limit was included in a reliability function. These factors incorporate an influence of the minor factors to some degree, for example, the grading of the parent material influences the achievable dry density, and the deviator stress ratio includes the effect of moisture in the BSM.

## 3. Mix Design of BSM

*3.1. Review of Mix Design.* The revision of the BSM mix design was encouraged by the evolution of key performance parameters and appurtenant test methods. Key considerations in this review included

- Material variability: selection of appropriate conditioning methods and reliable test methods
- Specifications: appropriate guideline limits to provide reliable performance
- Duration: streamlining of procedures to minimise the mix design time period
- Resource economy: minimisation of new testing equipment and procedures to the essentials
- Performance related: evaluate material properties with a reliable link to performance

To achieve the objective of meeting the road industry's needs, each set of issues needed to be considered and addressed. Fortunately, a database with an excess of 300 mix designs using the latest evaluation approach provided the necessary platform for optimising the mix design procedure.

**3.2. Optimisation of Mix Design.** A two-part process is required to optimise a BSM mix. Each step requires testing of numerous specimens to take account of the mix composition variables and moisture conditioning of the specimens. To keep the sample size of the aggregate within manageable proportions, ITS tests are selected. Each specimen is 152 mm diameter and 95 mm high. The increase from the 100 mm diameter specimens in the previous decade is to reduce the coefficient of variation of the tests, dictated by the ratio of aggregate size to specimen diameter.

Firstly, the selection of active filler must be undertaken. This is achieved by using three variables of active filler: 1% lime, 1% cement or no active filler, and two variables for moisture conditioning: dry or wet. A standard bitumen content is added to each specimen. Three repeat tests are conducted for each set of variables.

Secondly, the selection of optimum bitumen content is undertaken. This includes the selected active filler, four variables of bitumen content, and two variables for moisture conditioning. The trend in ITS results, including the three repeat tests, is plotted as an example in Figure 1.

Taking account of material variability of the repeat tests, the ITS limits from Table 1 can be used to select the design binder content on Figure 2.

The flowchart for BSM mix design is captured in a sequence provided in Figure 2. After ITS testing, there is one final step, i.e., triaxial testing. The challenge was to develop reliable but relatively simple and cost-effective equipment for triaxial testing. This included

Vibratory hammer compaction method: simulates field compaction in producing BSM specimens in the laboratory. Both ITS and triaxial specimens are produced this way.

Triaxial cell: comprises an inflatable tube in a confining cylinder for testing 150 mm diameter × 300 mm high specimens. It enables a standardised testing procedure. The shear parameters that are determined serve as a BSM classification tool in accordance with Table 2, as well as input into performance models for structural design.

For the first time, the shear strength properties of BSM take cognisance of the RA content for the classification. Research shows that the addition of high RA content generally results in an increase in the cohesion and a slight reduction in the friction angle. At the same time, a higher RA content invariably leads to improved moisture resistance for the BSM. This is captured in an increased retained cohesion value measure for triaxial specimens that have been conditioned under water before testing.

The new compaction methods and test protocols are currently being tailored into SANS norms, although in the interim, they will be included in the revised TG2.

### 4. Development of a BSM Transfer Function

**4.1. Architecture of Transfer Function.** The failure mechanism for BSMs, permanent deformation (or rutting), is similar to that of granular materials. Therefore, the transfer function for BSMs is based on the design function for

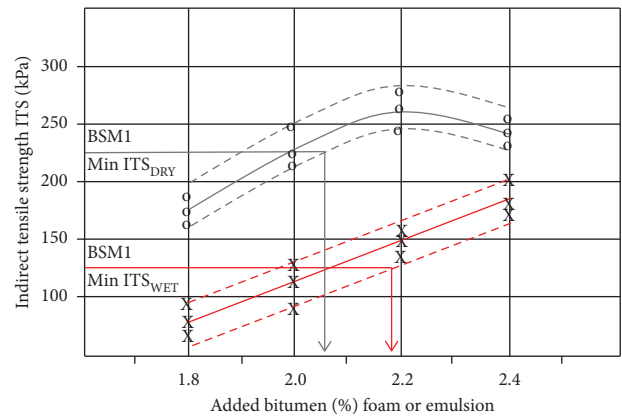


FIGURE 1: Selection of bitumen content from ITS<sub>DRY</sub> and ITS<sub>WET</sub>.

TABLE 1: Indirect tensile strength limits for classification.

Class	ITS limits	
	ITS <sub>DRY</sub> (kPa)	ITS <sub>WET</sub> (kPa)
BSM1	>225	>125
BSM2	>175	>100

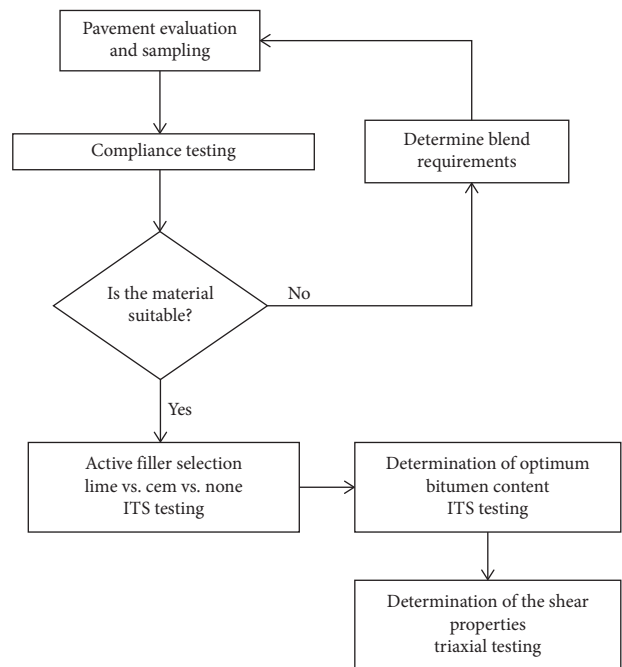


FIGURE 2: Flowchart for BSM mix design steps.

waterbound macadam shown in equation (1) [10]. The waterbound macadam transfer function calculates the bearing capacity in terms of the number of standard axle load repetitions ( $N$ ) that can be sustained before a certain level of plastic strain is induced in the layer:

$$\log N = 1.891 + 0.075(RD) - 0.009(S) + 0.028(PS) - 1.643(SR), \quad (1)$$

where  $N$  = number of standard axles the layer can sustain before reaching the deformation limit,  $RD$  = relative density

TABLE 2: Shear parameter limits for triaxial tests.

Class	RA (%)	Cohesion (kPa)	Triaxial	
			Friction angle (°)	Retained cohesion (%)
BSM 1	<50	250	40	75
	50–100	265	38	75
BSM 2	<50	200	38	65
	50–100	225	35	75

(%),  $S$  = saturation (%),  $PS$  = plastic strain limit as a percentage of the layer thickness (%), and  $SR$  = stress ratio (—)

The resistance to permanent deformation of unbound granular materials under repeated loading can be improved by increasing the density of the material [11]. The durability and performance of a BSM mix depends on its level of compaction [12]. Moisture damage contributes significantly to the deterioration of pavement materials, including BSMs. A reduction in shear strength through moisture ingress, i.e., a higher degree of saturation ( $S$ ), results in an accelerated rate of permanent deformation [13].

Finally, the rate of permanent deformation accelerates with an increase in deviator stress and decreasing confining pressure [14]. The stress ratio ( $SR$ ) used in this equation is a function of the load intensity, the shear properties of the materials, as well as the overall pavement structure.

**4.2. Stellenbosch BSM Transfer Function.** Using the architecture of design function for granular type behaviour, a BSM function can be developed. The new transfer function is based on 14 different roads and 22 different analysis sections as follows:

$$\log N = A - B(DSR)^3 + C(P_{\text{mod}} \cdot \text{RetC}) + D, \quad (2)$$

where  $DSR$  = deviator stress ratio as a fraction (—),  $P_{\text{mod}}$  = maximum dry density as a percentage of modified AASHTO density (%),  $\text{RetC}$  = retained cohesion (%),  $A$  = constant based on design reliability, and  $B$ ,  $C$ , and  $D$  = constants from data correlation (Table 3).

The  $DSR$  term describing the effect of deviator stress on pavement performance yielded a power three function, underlining the importance and sensitivity of this term. The  $DSR$  is evaluated at a depth of 25% of the BSM layer thickness:

$$DSR = \frac{\sigma_1 - \sigma_3}{\sigma_{1,f} - \sigma_3} = \frac{\sigma_1 - \sigma_3}{\sigma_{1,f} - \sigma_3}, \quad (3a)$$

$$\sigma_{1,f} = \frac{(1 + \sin \phi) \cdot \sigma_3 + 2 \cdot C \cdot \cos \phi}{(1 - \sin \phi)}, \quad (3b)$$

where  $DSR$  = deviator stress ratio as a fraction,  $\sigma_1$  = major principal stress (kPa),  $\sigma_3$  = minor principal stress, i.e., confining pressure (kPa),  $\sigma_{1,f}$  = major principal stress at failure (kPa),  $C$  = cohesion of the BSM default value (kPa),  $F$  = friction angle of the BSM default value (°), and  $F$  = friction angle of the BSM default value (°).

**4.3. Calibration of BSM Design Function.** The purpose of this calibration is to determine values for the constants in

TABLE 3: Reliability coefficient and limits.

Reliability (%)	$A$	Rut limit (mm)
95	0.8436	10
90	0.9312	15
80	1.0198	20
50	1.1369	25

equation (2) and to best describe the relative influence of each of the input variables on BSMs. The transfer function relates the number of standard axles the pavement can accommodate with the remaining amount of permanent strain in the BSM layer, i.e., a limiting value set in by design criteria. This enables the designer to specify the amount of permanent deformation that may occur before the BSM is deemed to have failed, linked to the design reliability.

Figure 3 shows the comparison of the accumulation of plastic strain due to repeated loading ( $N_{\text{actual}}$ ) compared to the prediction of remaining life, using the new transfer function ( $N_{\text{TF}}$ ). The calibration process aims to reduce the difference between the estimated life and the actual life of BSMs.

**4.4. Long-Term Pavement Performance Data.** The transfer function can be calibrated to perfectly describe a specific case if the information is sufficient. However, this will not be useful as it will only describe the life of a specific BSM on a local scale, limiting the relevance for design. By investigating a number of pavement structures, with data available at multiple points in time, the transfer function can be calibrated to describe the life of BSMs on a more extensive scale.

Data such as the material properties and subsequent long-term performance of pavement structures were gathered and analysed in the permanent deformation model. For an overall representation of the properties and performance of BSMs, results of fourteen long-term pavement performance (LTPP) studies were interrogated. This was part of a long-term pavement performance study, by SANRAL. Each of these pavements either had a BSM 1 or BSM 2 base layer with a minimum thickness of 100 mm. In total, 69 LTPP sections have played a role in data provisions and shaping the design functions.

The data available for these pavements included densities, moisture contents, layer thicknesses, material types, and classes as well as traffic data. The data also included FWD and rut depth measurements at different stages in their field life. The information used during the analysis of these pavements is discussed in detail by Long and Jooste [15]. A summary of the information available for these pavements is presented in Table 4.

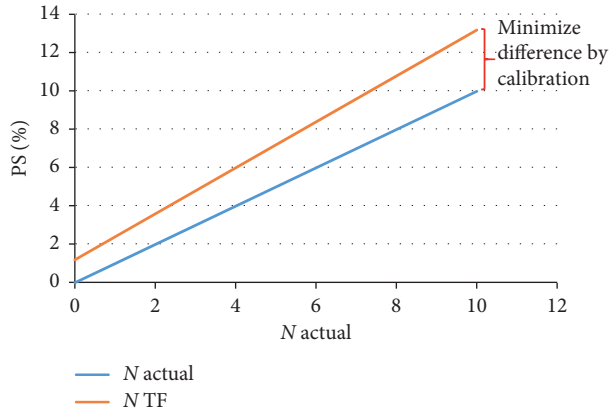


FIGURE 3: Transfer function prediction compared to actual load repetitions [10].

TABLE 4: LTPP pavement information [10].

Road	BSM construction year	BSM thickness (mm)	Standard axles accommodated to date (MESA)
MR27	1988	100	5
MR504 (A)	1995	175	1.6
MR504 (B)	1995	175	1.6
N1-1	1984	100	17
N1-13	1980	150	14
N1-14	1980	150	14
N2-16	1980	140	3.4
N2-20	2000	180	2.4
N4-1	1997	170	5.6
N4-5X	1996	150	6.7
N11-8	2004	280	1.1
N12-19(3)	1974	100	18
N12-19(4)	1974	135	18
P243-1	2000	250	0.48

Areas of insufficient data required assumptions to be made based on the performance and conditions of these pavements. Where cohesion ( $C$ ), friction angle ( $\phi$ ), and retained cohesion values were not available, realistic and representative default values were used. Reasonable and conservative values were applied for each pavement, based on the minimum design values specified in the TG2 [9].

The data obtained from these pavements were used for the calibration of the transfer function. The structures of each of these pavements was modelled in Rubicon Toolbox to determine the critical (highest) DSR value when subjected to an 80 kN standard axle load (E80). The software required the layer thicknesses and material properties for each of the LTPP pavements to calculate the DSR.

**4.5. Permanent Strain Development with Repeated Loading.** The new BSM transfer function uses permanent strain as the limiting factor when determining the life of a BSM. During

the analysis of the pavements used to calibrate the transfer function, rutting measurements were taken at different points in time. The rutting measurements reflect the permanent deformation of the pavement structure as a whole. A percentage of the total permanent deformation was used to obtain the permanent deformation within the BSM base layers.

The accumulated permanent strain in the BSM layers of the LTPP pavements varies for each pavement. This poses a challenge for the calibration of the transfer function. Pavements that showed little deformation would reflect early life permanent deformation behaviour, while pavements that showed more significant deformation would reflect the long-term permanent deformation behaviour. This only allows the rate of permanent deformation accumulation for different pavements to be compared and not the absolute values.

In order to obtain values for the actual traffic at higher strain levels, the Huurman model for permanent strain development was implemented for each pavement. The Huurman model for PS development was used to determine the number of load repetitions at each of these PS levels up to the final level of 10%. The Huurman model for PS prediction is as follows [16]:

$$\varepsilon_p = A \cdot \left( \frac{N}{1000} \right)^B, \quad (4)$$

where  $N$  = number of load repetitions,  $\varepsilon_p$  = plastic strain accumulation (%), and  $A$  and  $B$  = regression constants.

**4.6. Calibration of the New BSM Transfer Function.** The data obtained from the fourteen LTPP pavements were used for the calibration of the transfer function. The transfer function's prediction of the number of load repetitions ( $N_{TF}$ ) to reach a specific level of permanent strain was compared to the estimated traffic ( $N_{estimate}$ ) that the various pavements accommodated to reach that strain level.

Figure 4 illustrates a comparison of the transfer function's predictions compared to the estimated traffic over a range of permanent strain values. An estimation was considered good if it predicted a value close to the estimated value. By using a large number of data points, the slope of linear trendline through the data was used to determine the function's accuracy. A slope greater than one indicates that the function overestimates the life of the layer, whereas a slope smaller than one would indicate underestimation.

The transfer function was calibrated using linear regression to determine the values of  $A$ ,  $B$ ,  $C$ , and  $D$  that yielded a slope of one, while minimizing the dispersion of data points. The comparison between the calibrated transfer function and the estimated traffic is shown in Figure 5. The calibrated transfer function is shown in equation (5). In this figure, the slope of the trendline (the dotted line) correlates very well with the one-to-one relationship.

The trendline for the calibrated transfer function was  $y = 1.0006x + 1.0572$ . The slope of the trendline was deemed to be a good representation of the estimated life. However, the intersect point (1.0572) indicates that the transfer

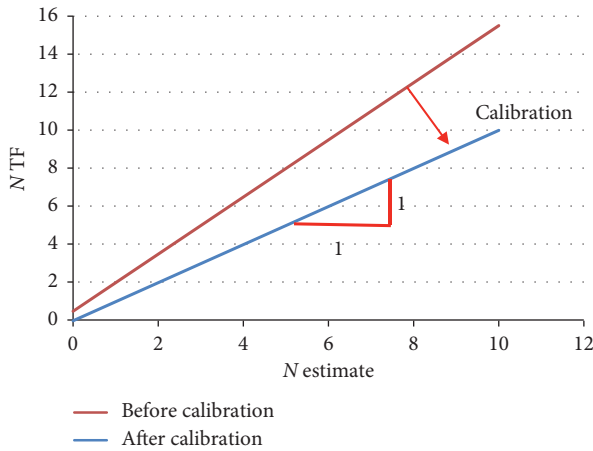


FIGURE 4: Measure of transfer function's accuracy [10].

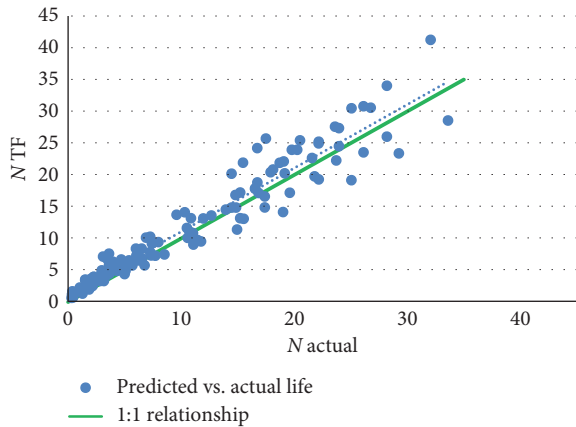


FIGURE 5: Predictions of the calibrated transfer function compared to actual traffic [10].

function may overestimate the life of the material at low remaining strain values. This is due to the logarithmic nature of the function, which produces positive results even when the remaining strain is very small (or zero). Therefore, it is recommended that a limit to the minimum remaining strain is set in place for design purposes.

Permanent strain development obtained from traffic estimation was compared to that of the transfer function for each of the LTPP pavement structures. Figure 6 shows this relationship between predicted and actual life for a section of the MR502. It highlights significant differences in correlation at low strain levels. The slope of transfer function's predicted vs. actual life at higher strain levels is close to parity. This indicates that the transfer function accurately predicts the long-term permanent strain development of the BSM.

**4.7. Safety Adjustments for Design.** The new transfer function for BSMs is calibrated to best describe the observations made from the LTPP data. This function only aimed to describe the observed trends. A design function, however, requires different levels of reliability to be explicitly built into the

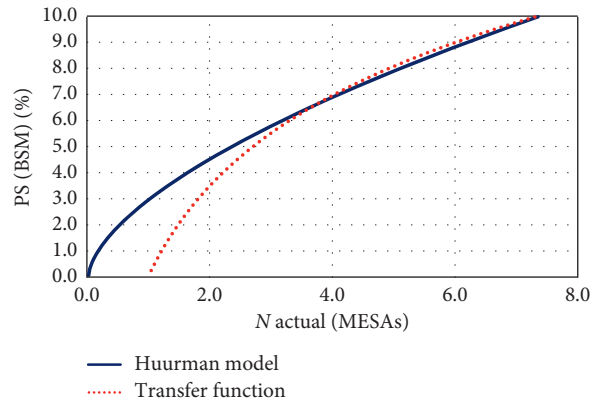


FIGURE 6: Transfer function's permanent strain prediction for MR504 (A) [10].

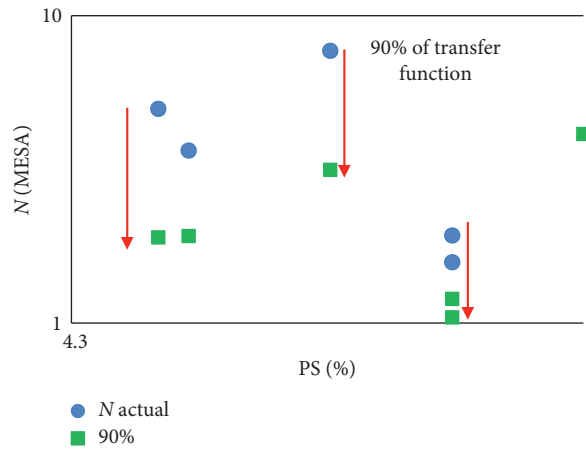


FIGURE 7: Reducing the transfer function's predictions to increase reliability [10].

function. Based on South African pavement design, four categories and appurtenant reliability have been incorporated into the transfer function, i.e., category A (95% reliability), category B (90% reliability), category C (80% reliability), and category D (50%).

The calibration process was repeated by only adjusting the value of constant A, which adjusts the prediction of functions without altering the relationship between the function's variables. Reliability in the transfer function was measured as the percentage of data predicted by the transfer function that had a smaller value than the observed data. Figure 7 illustrates the principles used to calibrate the transfer function to different levels of reliability. It is shown that the transfer function produced lower life predictions than was estimated for 90% of the data points.

The new design function's prediction of the LTPP life compared to the estimated life is shown in Figure 8. The slope of the transfer functions predictions compared to the estimated life reduces with the increase in reliability. The reduction in slope indicates that the transfer function underestimates the life of the material by higher margins. This underestimation increases the probability of a designed material to achieve the calculated design life.



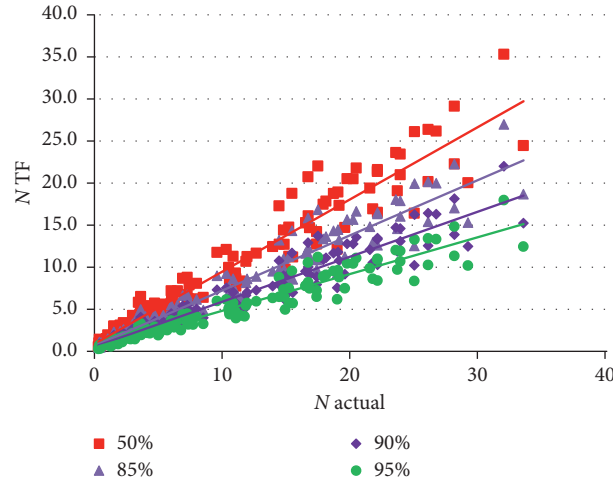


FIGURE 8: Underestimation of life at different levels of reliability [10].

TABLE 5: Pavement structures for design comparison [10].

Pavement	Pavement layer	Material class	Thickness (mm)	Stiffness (MPa)	BSM properties	
1	Surfacing	HMA	35	3500	C (kPa)	250
	Base	BSM 1	250	720	$\varphi$ (°)	40
	Sub-base	G5	250	240	RetC (%)	75
	Selected subgrade	G8	180	120	$P_{mod}$ (%)	100
	Subgrade	G8	N/A	90		
2	Surfacing	HMA	20	2500	C (kPa)	225
	Base	BSM 2	280	500	$\varphi$ (°)	39
	Sub-base	G6	250	200	RetC (%)	70
	Selected subgrade	G8	150	100	$P_{mod}$ (%)	98
	Subgrade	G8	N/A	90		

The new calibrated BSM design function is shown in equation (5). The design function can be used to estimate the life of BSMs for design purposes. However, this function's use should be compliant with rules outlined in TG2 [17] where allocated materials stiffness and analysis positions in the BSM layer are outlined.

$$\log N = A - 57.286(\text{DSR})^3 + 0.0009159(P_{\text{mod}} \cdot \text{RetC}) + 0.86753. \quad (5)$$

## 5. Design Method Comparison

As part of the validation process, the new function was compared to the older design methods for BSMs. In Bierman's research [10], five different pavement structures were initially investigated, and the results were compared. These analyses were carried out before a structural pavement design procedure was developed. The methods included a heuristic design pavement number (PN) method and the mechanistic-empirical (ME) method. Unfortunately, the analysis was carried out before the PN method, which required updating with new data and recalibration. Nevertheless, reasonable pavement life comparisons were developed.

The Stellenbosch BSM design function, however, could be applied using the updated TG2 [17], thus providing more realistic insights. These results are presented in this paper. Focus was placed on a comparison with the old and new PN design methods [7, 18], and the lives of ten different pavement structures were compared. Only two of these structures are highlighted in this paper (see Table 5).

There are fundamental differences between the heuristic PN design method and the ME method. The PN provides an estimate of pavement life of the entire pavement structure based on performance of the LTPP pavements with BSM layers. The architects of the PN methods used ME analysis to develop the design model, so a design only needs to input the pavement materials' classifications and structure. The Stellenbosch BSM design function interrogates the structural mechanics of each layer to determine the "weakest link" and thus determine the design life.

The comparison between the design life of the selected pavements using the different design models is provided in Figures 9(a) and 9(b). The variables included in the life calculation include

Design models: PN method old-2009 and new-2019 as well as Stellenbosch BSM ME Design function

Reliability levels: 95% (category A) and 90% (category B).

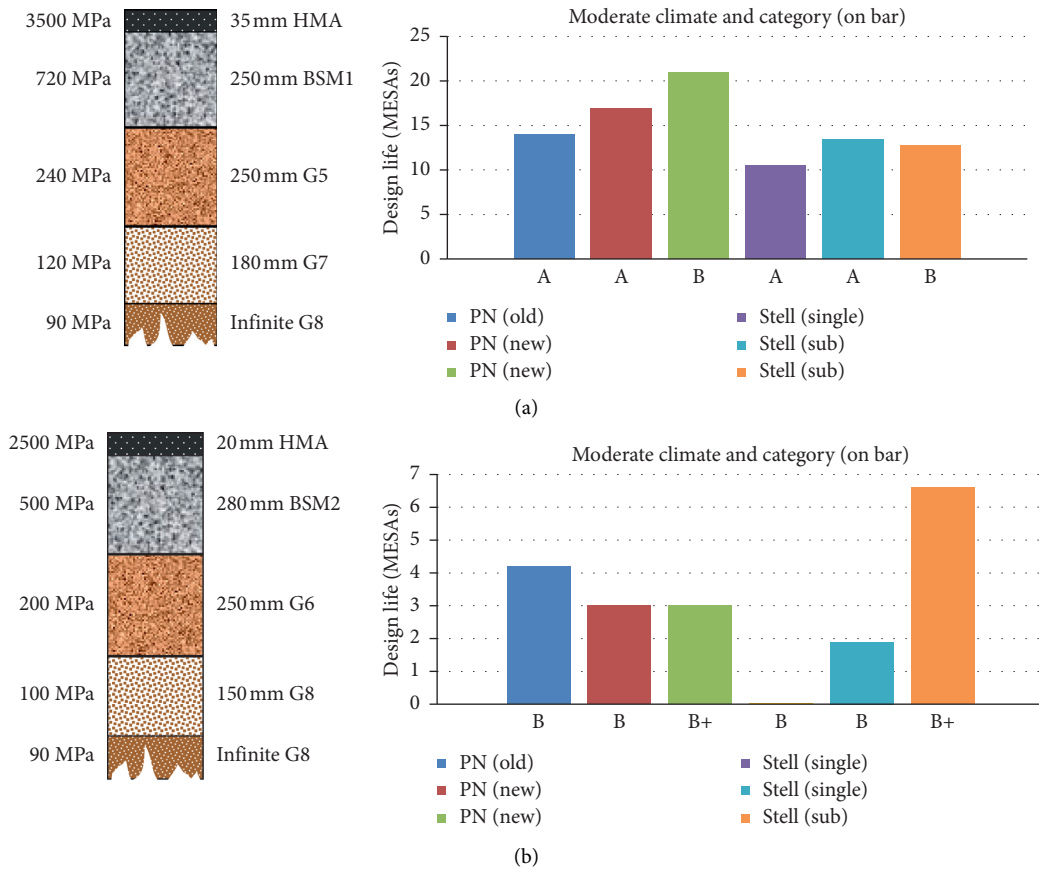


FIGURE 9: (a) Design life of pavement 1 with BSM1 base vs. design method. (b) Design life of pavement 2 with BSM2 base vs. design method.

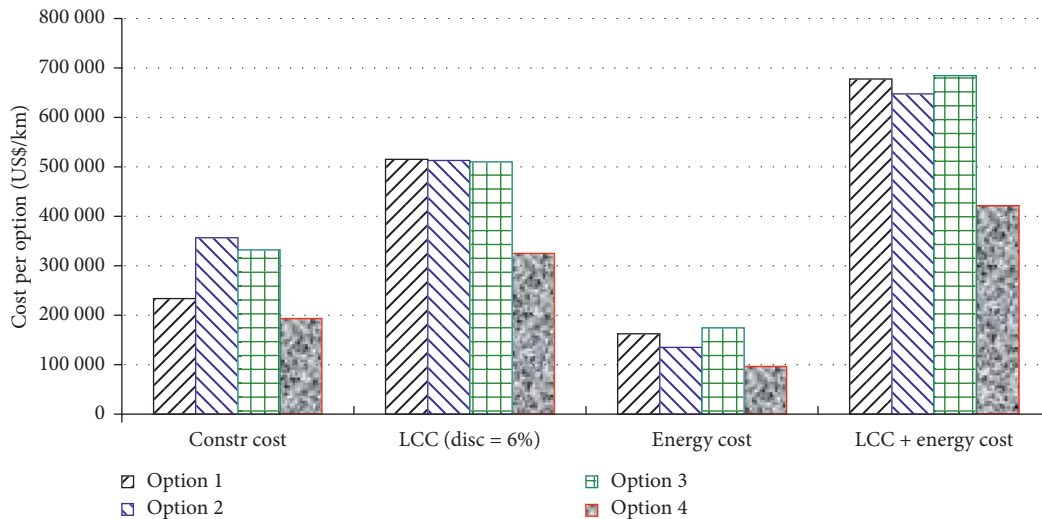


FIGURE 10: Combined life cycle cost and energy consumption [19].

Layer ME analysis of BSM: single layer vs. sublayer (at least 100 mm)

BSM Classification: BSM1 vs. BSM2

Default values for BSM properties based on the TG2 [17] guidelines

The pavement life determined using the PN method compares well with the new Stellenbosch ME BSM design function. Sensitivity to design reliability is evident. Sub-layering of the BSM layer and using an analysis position at 1/4 depth of the layer provide a more realistic design life. It should be noted that sublayering provides a more

representative density profile and resilient modulus profile for a thick layer of material that is stress-dependent.

## 6. Economics

Jenkins and Collings [19] compared four different rehabilitation strategies in terms of life-cycle costing and energy consumption, based on actual projects. The four interventions were

- (1) Patch and overlay
- (2) Mill and replace
- (3) Cement stabilise the existing base + surfacing and overlay
- (4) Recycle using bitumen stabilisation technology.

It is obvious in Figure 10 that initial construction costs alone are inadequate for selection of rehabilitation alternatives. They can provide skewed and unrealistic rehabilitation selection, which will lead to unnecessary wastage of resources. Cheapest is the dearest.

The whole-of-life analysis using PWOC (present worth of costs) provides more realistic financing requirements for pavement upkeep over the entire analysis period. The combined energy and life cycle costs provide the most informative insight into sustainable solutions. For this particular project, bitumen stabilisation technology scores as the most cost-effective and sustainable solution for rehabilitation.

In this case, energy is used as a surrogate for emissions too; however, life cycle analysis (LCA) approach would be the ultimate way to analyse different rehabilitation interventions.

## 7. Conclusions

The past decade has provided the opportunity to gather invaluable performance data of BSMs from several hundred mix designs and 69 LTPP sections. In turn, these data have provided the opportunity to upgrade the design and application and bitumen stabilised materials (BSMs). Some of the highlights of areas where BSMs are being taken forward by many strategic developments include

Guidelines for a refined mix design method for BSMs including:

- Vibratory hammer compaction of ITS and triaxial specimens
- Phased analysis to determine active filler (type and content) and binder content for optimal performance
- Triaxial testing of the proposed mix to evaluate shear properties at equilibrium and wet conditioning to be used in material classification and provide inputs into structural design
- Certification of all test procedures using SANS standards

An updated material classification system that uses significantly more materials data to provide a more robust method for evaluation and design

An upgrade pavement number design system that removed biases and provides for a greater range of types of pavement structures and more accurate design outcomes based on extended data

A new mechanistic-empirical design system for BSMs based on extensive analysis of LTPP sections and performance parameters of the BSM

Economic and environmental (energy consumption) analyses provide important insight into the sustainability of rehabilitation options and highlights the advantages of cold recycling technology

The improved understanding of key performance parameters of BSMs and implementation of these findings in the application of the technology will offer more effective and reliable solutions in pavement rehabilitation.

## Data Availability

The research data that have been used in this publication emanates from research at Stellenbosch University and is clearly referenced. Additional data can be obtained from the accredited publications in the reference list.

## Conflicts of Interest

The authors declare that they have no conflicts of interest.

## Acknowledgments

The authors acknowledge the financial support provided by Roadmac Surfacing Cape to Mr Carl Bierman in carrying out this research project.

## References

- [1] L. H. Csanyi, *Foamed Asphalt in Bituminous Paving Mixes*, Highway Research Board Bulletin, Washington, DC, USA, 1957.
- [2] S. M. Acott and P. A. Myburgh, "Design and performance study of sand bases treated with foamed asphalt," *Transportation Research Record*, vol. 898, pp. 290–296, 1982.
- [3] F. M. L. Akeroyd and B. J. Hicks, *Foamed Bitumen Road Recycling*, Alad Limited, London, UK, 1988.
- [4] F. M. L. Akeroyd, "Advances in foamed bitumen technology," in *Proceedings of the 5th Conference on Asphalt Pavements for Southern Africa*, Mbabane, Swaziland, June 1989.
- [5] SABITA, *GEMS—The Design and Use of Granular Emulsion Mixes*, Southern African Bitumen Association, Cape Town, South Africa, 1993.
- [6] SABITA, *ETB—The Design and Use of Emulsion Treated Bases*, Southern African Bitumen Association, Cape Town, South Africa, 1999.
- [7] SABITA, *The Design and Use of Foamed Bitumen Treated Materials*, Southern African Bitumen Association, Cape Town, South Africa, 2002.
- [8] D. Collings and K. Jenkins, "The long-term behaviour of bitumen stabilised materials," in *Proceedings of the 10th Conference on Asphalt Pavements for Southern Africa*, Drakensberg, South Africa, 2011.
- [9] Asphalt Academy, *Technical Guideline TG2: Bitumen Stabilised Materials: A Guideline for the Design and Use of Bitumen*

- Emulsion and Foamed Bitumen Stabilised Materials*, Asphalt Academy, Cape Town, South Africa, 2009.
- [10] C. R. Bierman, *A Design Function for Bitumen Stabilised Material Performance Based on Laboratory and Field Evaluation: MEng (Research)*, Stellenbosch University, Stellenbosch, South Africa, 2017.
- [11] A. A. Van Niekerk, "Mechanical behavior and performance of granular bases and sub-bases in pavements," Doctoral degree, Technical University Delft, Delft, Netherlands, 2002.
- [12] K. J. Jenkins, "Mix design considerations for cold and half-warm bituminous mixes with emphasis on foamed bitumen," Doctoral degree, University of Stellenbosch, Stellenbosch, South Africa, 2000.
- [13] F. Lekarp, U. Isacsson, and A. Dawson, "State of the art II: permanent strain response of unbound aggregates," *Journal of Transportation Engineering*, vol. 126, no. 1, 2000.
- [14] S. Werkmeister, *Permanent Deformation Behaviour of Unbound Granular Materials in Pavement Constructions*, Technischen Universität Dresden, Dresden, Germany, 2003.
- [15] F. Long and F. Jooste, *Summary of LTTP Emulsion and Foamed Bitumen Treated Sections*, Technical Memorandum, Sabita, Cape Town, South Africa, 2007.
- [16] M. Huurman, "Permanent deformation in concrete block pavements," Doctoral degree, Technical University Delft, Delft, Netherlands, 1997.
- [17] Asphalt Academy, *Technical Guideline TG2: Bitumen Stabilised Materials: A Guideline for the Design and Construction of Bitumen Emulsion and Foamed Bitumen Stabilised Materials*, Asphalt Academy, Pretoria, South Africa, 3rd edition, 2020.
- [18] Asphalt Academy, *Technical Guideline TG2: Bitumen Stabilised Materials: A Guideline for the Design and Construction of Bitumen Emulsion and Foamed Bitumen Stabilised Materials*, Asphalt Academy, Pretoria, South Africa, 2nd edition, 2009.
- [19] K. J. Jenkins and D. C. Collings, "Combining LCC and energy consumption for enhancing decision making regarding rehabilitation options," in *Proceedings of the 10th Conference on Asphalt Pavements for Southern Africa*, Drakensberg, South Africa, 2011.

## Review Article

# On the Recent Trends in Expansive Soil Stabilization Using Calcium-Based Stabilizer Materials (CSMs): A Comprehensive Review

Fazal E. Jalal <sup>1,2</sup>, Yongfu Xu <sup>1,2,3</sup>, Babak Jamhiri <sup>1</sup> and Shazim Ali Memon <sup>4</sup>

<sup>1</sup>State Key Laboratory of Ocean Engineering, Shanghai Jiao Tong University, Shanghai 200240, China

<sup>2</sup>Department of Civil Engineering, Shanghai Jiao Tong University, Shanghai 200240, China

<sup>3</sup>Wentian College of Hohai University, Ma'anshan 243000, China

<sup>4</sup>Department of Civil and Environmental Engineering, Nazarbayev University, Nur-Sultan 010000, Kazakhstan

Correspondence should be addressed to Yongfu Xu; [yongfuxu@sjtu.edu.cn](mailto:yongfuxu@sjtu.edu.cn) and Shazim Ali Memon; [shazim.memon@nu.edu.kz](mailto:shazim.memon@nu.edu.kz)

Received 15 October 2019; Revised 12 December 2019; Accepted 27 January 2020; Published 10 March 2020

Guest Editor: Andrea Graziani

Copyright © 2020 Fazal E. Jalal et al. This is an open access article distributed under the Creative Commons Attribution License, which permits unrestricted use, distribution, and reproduction in any medium, provided the original work is properly cited.

Calcium-based stabilizer materials (CSMs) exhibit pozzolanic properties which improve the properties of clayey soils by hydration, cation exchange, flocculation, pozzolanic reaction, and carbonation. In this comprehensive review, comprising over past three decades from 1990 to 2019, a mechanistic literature of expansive soil stabilization by incorporating CSMs is presented by reviewing 183 published research articles. The advantages and disadvantages of CSMs as the ground stabilizing agent are succinctly presented, and the major outcomes of physicochemical effects on soil properties are discussed in detail. After blending with CSM, the main and interaction effects on soil properties with focus on chemical processes such as X-ray fluorescence, X-ray diffraction analyses, and microstructure interaction by using scanning electron microscopy and thermogravimetric analysis have been reviewed in light of findings of past researchers. This work will help geotechnical engineers to opt for suitable CSM in the field of geoenvironmental engineering in committing to sustainable construction of civil engineering structures over expansive soils.

## 1. Introduction

The behavior of fine-grained soils is largely governed by moisture content variations. Upon interaction with water, the clay particles in such soils are primarily responsible for the expansive nature and hence called “expansive” or “swelling” soils [1]. Among others, the main clay minerals in expansive soils include illite, kaolinite, and montmorillonite (further on referred to as Mt). Owing to the hydrophilic nature and high dispersivity of the clay minerals, they cause high risk to the civil engineering foundations, to landslides triggering [2], and to the road subgrades [3] especially before bituminous coating as soil improvement additives or cold mixtures [4–7]. For practical implications in engineering, the treatment of expansive soils is imperative. The mechanical and chemical soil stabilization improves the engineering characteristics of the problematic soils [8].

Stabilization of soil may be expensive, but it decreases the overall construction cost of buildings and road subgrades [9]. In order to improve the behavior of expansive soils, geotechnical engineers seek help from soil science and geology. The first modern use of soil stabilization was introduced in 1904 in the USA [10]. Brashad [10] explained the phenomenon of clay expansion due to water considering the various interlayer cations in 1950. Petry and Little [10] investigated the stabilization of expansive soils by evaluating the effectiveness of traditional calcium-based stabilizer materials (CSMs) in their state-of-the-practice stabilization during 1940 and 2001. Simons [11] discussed the microstructural processes, chemical interactions, and the waste reuse and sustainability in an attempt to modify expansive soil properties. In yet another study, Behnood [12] reviewed the comparison of calcium (Ca) based and non-Ca-based stabilizers with detailed



discussions on techniques and challenges in soil modification. According to Godenzoni [13], the cementing materials (CMs) are produced by the most conventional stabilizing materials, that is, lime, cement, and their mixes along with other pozzolanic materials. Today, a detailed literature is available, and a worldwide research on expansive soil stabilization using a wide array of classical and emergent materials is still in progress [14–22]. Although well-documented studies on the use of numerous stabilizers are available, to these authors' knowledge, no study made between 1990 and 2019 that explains the main and interaction effects of CSMs on the expansive soils, has been found. Also, the standardization for various additives is unavailable in the field of geotechnical engineering which leads to geoenvironmental issues and affects the environment. This comprehensive review serves three main objectives on the following subjects: (1) gain insights about the history, mechanism, damages associated, and prevalence of expansive soils over last 30 years, (2) review the practice of efficacious stabilization using Ca-based stabilizer materials for civil engineering structures and road pavements, and (3) serve a guideline for researchers and practitioners to select materials under the domain of this study.

## 2. Fundamental Knowledge about Stabilization of Expansive Soils

**2.1. Mechanism.** Improvement in properties of an expansive or problematic soil means increase in the compressive strength and permeability, reduction in plasticity and compressibility, and improvement in durability of these soils. More concisely, "soil stabilization" is mainly the addition of chemical admixtures to soil which results in chemical improvement [23]. Swelling in expansive soils deals mainly with prevalence of type and amount of pore spaces and their interaction with water. The phenomenon of swelling may comprise over a relatively long time ranging between 5 to 8 years during early service life of foundations and pavements [24]. Figure 1 illustrates the pore spaces between the unit layers of clays, also known as interlayer space, which represent the "microporosity," whereas pore spaces between adjacent particles or aggregates, called the interparticle pores or interaggregate pore spaces, respectively, represent the "macroporosity" in the compacted smectite particles. The water present in both these regions differ in terms of their physical states. Swelling takes place when the water enters into the interlayers. Petry and Little [10] outlined the empirical methods to determine the volume change resulted from swelling in expansive soils.

Figure 2 depicts the process of water entry inside clay plates at extended microlevel. The "clay particle" represents an interconnected stack of clay layers with a maximum four layers of crystalline water. The "clay aggregates" are the assembly of "clay particles" forming unit of a compacted clay double structure. The portion of the clay particle surface parallel to that of "clay layers" is called the "particle face." However, the part of the clay particle surface normal to

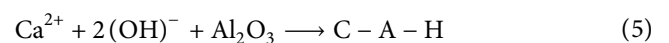
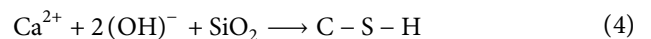
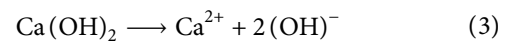
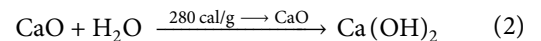
the particle face is known as "particle edge." Diffuse double layers are produced around particle faces with the attached water called "double-layer water." The water other than the diffuse double layers is shown by the "equilibrium solution."

The role of diffused double layer theory comes into play while evaluating the expansivity of clay minerals. Accordingly, the repulsive and attractive forces generated by physicochemical effects are quantified on the particle scale level [26]. This theory is applicable to smectite particles present in monovalent electrolytes with lesser concentration. The thickness of the double layer is shown in the following "Poisson–Boltzmann equation":

$$\frac{1}{K} = \sqrt{\frac{DkT}{8\pi\eta_0\varepsilon^2V^2}} \quad (1)$$

where  $1/K = D_L$ , i.e., thickness of double layer (cm),  $D$  = dielectric constant,  $k$  = Boltzmann constant =  $1.38 \times 10^{-23}$  J/K,  $\eta_0$  = bulk solution of the electrolyte concentration (ions/cm<sup>3</sup>),  $\varepsilon$  = unit electronic charge (esu),  $T$  = absolute temperature (K), and  $\nu$  = cation valence. Note that  $D_L$  is directly proportional to the cation exchange capacity (CEC) and specific surface area (SSA) of clay minerals and has pronounced effect on these entities [27–29].

The clay minerals belong to "phyllosilicates" family and carry a net residual negative charge. The mechanism of clay modification by calcium-rich stabilizers involves dissociation of higher calcium content into calcium ions that react with both silica and alumina leading to the ion exchange, flocculation, and pozzolanic reactions. This process is expressed in equations (2)–(5). Also, the California bearing ratio (CBR) is increased, and the formation of two main components takes place, calcium silicate hydrates (C-S-H) gel, represented by chemical formula  $[5Ca_2SiO_4 \cdot 6H_2O]$ , and calcium aluminate hydrate (C-A-H) gel, with chemical formula  $[Ca_5Si_5Al(OH)O_{17} \cdot 5H_2O]$ . As shown in equations (4) and (5), it is due to this pozzolanic reaction that soil durability is largely improved [30]. It is also notable that, in some cases, calcium aluminate silicate hydrate (C-A-S-H) may form which also adds to the soil strength. The pozzolanic reactions occur in a highly alkaline environment gradually dissolving the aluminosilicates which also contributes to the long-term strength gain [31]. The presence of clay mineral type and calcium ( $Ca^{2+}$ ) ions governs the effectiveness of these reactions. The volumetric stability of the soil matrix is enhanced as  $Ca^{2+}$  tends to replace monovalent  $Na^+$  or  $H^+$  ions. Production of C-S-H and C-A-H gels in this way is called "polymerization process" [32, 33]:



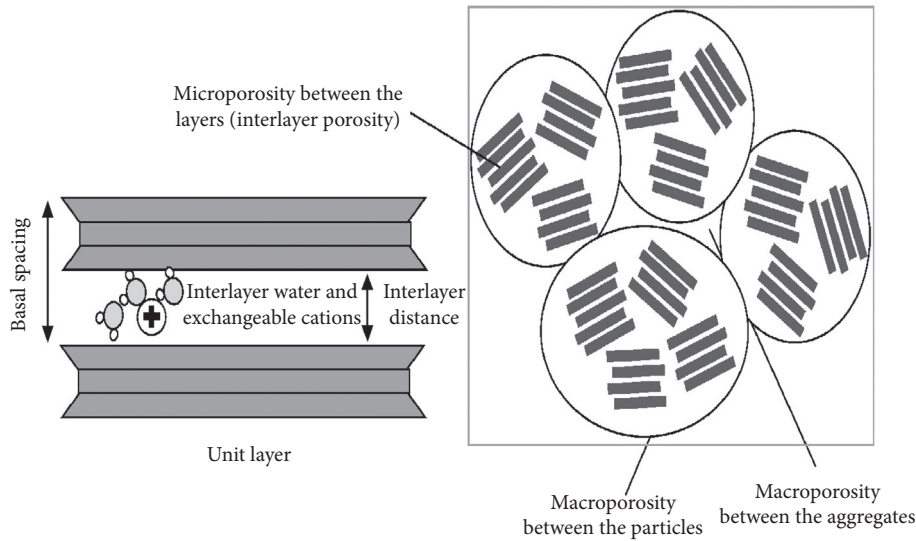


FIGURE 1: Effect of water entry on micro- and macropores of compacted smectite with classification of “microporosity” and “macroporosity,” reproduced with permission from [12].

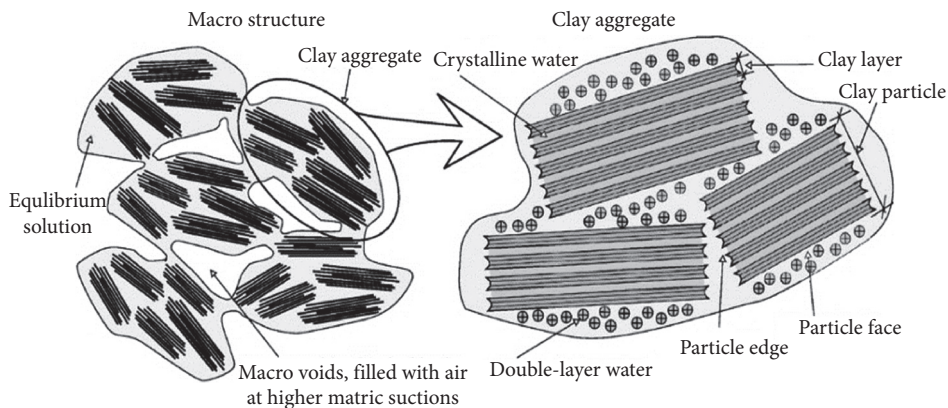


FIGURE 2: Compacted clay structure depicting the process of water entry inside clay plates at the extended microlevel, adapted from [25].

2.2. *Identification and Characterization.* It is essential to quantify the amount of swell pressure ( $P_s$ ) exerted by expansive soil upon water uptake. Expansive soils below the ground surface level extending to a depth of approximately 1.5 meters are more susceptible to swelling pressure in the particular zone called “active zone depth.” However, the region beyond the active zone depth is termed as “zone of constant volume” experiencing lesser volume change with moisture entry [28]. The susceptibility of such soils to volumetric swelling makes them highly unsuitable for use in supporting foundations. Shi et al. [29] presented the common methods to evaluate the swell intensity, i.e., free swell (FS) [34] and  $P_s$ , which were determined using simple tests such as Atterberg limits (liquid limit (LL), plastic limit (PL), and shrinkage limit (SL)), contents of colloids, and activity (A) value of clay. The LL, PL, and SL are index properties used for classification of fine-grained soils and determine the mechanical behavior, i.e., shear strength, compressibility, and swell potential [27]. According to the experimental study by Cantillo et al. [35], the Atterberg

limits contribute very least statistical significance to estimation of  $P_s$  as evidenced by conducting tests on 38 samples obtained from database of material parameters. “Free Swell Index” (FSI), a measure of FS, is the increase in soil volume without any external constraints when submerged in water. “ $P_s$ ” is defined as the pressure exerted by clay when it absorbs water in a confined space. “Activity” (A), the ratio of plasticity index (PI) to the percent of clay fraction, represents the water holding capacity of clay soil and is function of type and amount of clay mineral. Activity of Mt (commonly greater than 4) is highest than for kaolinite and illite. The FS and  $P_s$  [28, 36] are calculated using oedometer in accordance with ASTM standards [37]. Moreover, to determine the  $P_s$ , the zero swell test and oedometer test methods are preferable because of their ease and simple procedure [38, 39]. For a variety of expansive soils in Egypt, it was revealed by Mehmood et al. [40] that, for highly plastic clays with activity between 0.8 and 1.5, the swell potential parameters were calculated using the following equations:

$$P_s = 0.1266 (3.6 \times \text{activity})^{3.47}, \quad (6)$$

$$\text{activity} = 0.2783 (\text{FS})^{0.288}. \quad (7)$$

The identification and characterization of expansive soils are presented in numerous studies during the annals of history. In Table 1, the expansive soils have been classified based on swell tests, Atterberg limits, free swell ratio, dominant clay type, suction, and absorption capability. Unlike the studies in the 70's and 80's, the classifications suggested in 2000 and onwards witnessed a marked difference. For instance, according to the *China Ministry of Construction* (CMC 2004) classification, the expansive soils having a PI less than 15% are low expansive, whereas those exceeding 40% are high expansive soils. The latest classification methods take into account the important soil suction parameter, dominance of clay mineral, and absorption ability of the clay-rich soils in order to improve categorizing the expansive soils to a higher degree of accuracy [45, 46]. According to latest classification based on index properties, it is alluded that clay soils with LL greater than 40%, lying above the A-line on Casagrande's plasticity chart and containing more than 5% Mt content, are known as swelling soils [38, 44, 47].

**2.3. Basic Clay Minerals.** The swelling of expansive soils is mainly attributed with the presence of clay minerals such as illite, kaolinite, and Mt [48, 49] whose mineralogical properties are listed in Table 2. The order of their expansivity is Mt > kaolinite > illite. Mt is combination of silica tetrahedrons and alumina octahedral linked via weak Van der Waal's forces. It has high liquid limit (up to 900%) and SSA (850 g/cm<sup>2</sup>) values [15]. The Mt carries (1) permanent negative charge over the surface, which is function of isomorphous substitution of magnesium and iron ions [50], and (2) positive charge distributed on the edges, which is function of pH of the soil [36]. Kaolinite is the least expansive among the three clay minerals due to presence of fixed K<sup>+</sup> ions. Illite has an expansion index ranging between Mt and kaolinite, while its structure resembles with that of Mt. Illite has also fixed potassium ions between the interlayer spaces which decrease its expansiveness.

When water interacts with the clay minerals, Nelson et al. [47] argues that an intermolecular bonding develops due to the dipolar nature of water which causes ion hydration and adsorption of water on surfaces of clay particles by virtue of four simultaneous mechanisms including hydrogen bonding, cation hydration, osmosis, and dipole attraction. However, according to Labib and Nashed [51] and Akgün et al. [39], the stress equilibrium inside the clay-water mix is disturbed due to presence of H<sup>+</sup> and OH<sup>-</sup> in water because the clay particles carry negative edge charge and positive surface charge, which is responsible for the "expansive" movement. The magnitude of this movement is sometimes several degrees higher, and the theory of consolidation, moisture content, and suction-based techniques are used to predict the resulting movement [23].

### 3. Damages Caused by Expansive Soils in Superstructures and Infrastructures

The damage of expansive soils to lightly loaded civil engineering structures (pathways, highways, boundary walls, one to three storied buildings, water, and sanitation pipelines below the ground surface) is more significant due to large swelling pressure. The swelling phenomenon is complex and hazardous in nature, with  $P_s$  sometimes approaching to lifting up the foundation of structures and pavements, causing partial damage or entire destruction and monetary losses [52–54]. It has been established that almost 33% of total land in Sudan, 20% land area each in Indonesia and India, more than 12% of the Syrian land, and 6% land of China comprise arid regions with presence of expansive soils and/or black cotton soils [23, 41, 55–58]. The annual economic loss due to construction on expansive soils exceeds approximately nine billion US \$ in USA [59], one billion USA \$ in China [60], and USA \$ 0.5 billion in the UK [36]. In another study by Simons [11] and Zhao et al. [61], in USA, between 1970 and 2000, the total annual building loss due to expansive soil damages increased by 140% with cost of damages reaching USA \$4.7 billion. Also, 25% of all homes in the USA were affected by the expansive soil damages [41].

In many cases, for example, in parts of USA and Australia, the maintenance cost of roads built on expansive soils exceeds the cost of construction [1, 2, 11]. Dafalla and Shamrani [62] noted that if preliminary geotechnical investigation of expansive soils in subgrades of pavements is not carried out prior to construction, it may lead to improper drainage and premature structural failures. Puppala and Pedarla [63] stressed the need of utilizing ecofriendly and economical waste materials such as bagasse ash, which offers high strength and more durability, to build subgrades over expansive soils [64–67]. These swelling soils are also present in the Middle East and Gulf countries including Pakistan, Iran, India, Oman, and Saudi Arabia that largely affects the lightly loaded civil engineering structures [40, 68]. Figure 3 shows an overview of the damage to buildings, roads, and embankments across different countries.

If the expansive soils are not dealt properly, the cracks may propagate wider and deeper due to rapid moisture exit, as shown in Figure 4. The cracks are minimized and localized when blending with CSM (calcium carbide residue, in this case) is done. The integrity of sample is also significantly increased by using a higher dose of prescribed stabilizer mix. However, the damage associated with the expansive soils is countless, widespread, and inevitable. Therefore, more studies are required to further explore the complex cracking mechanism in order to gain a real insight about their unknown hazardous behavior.

### 4. Ca-Based Stabilizers in Limelight

**4.1. Stabilization of Expansive Soils Using CSM.** The search for state-of-the-art potential stabilizing materials to deal with the problematic soils is always in progress. The reasons which draw the attention of geotechnical engineers to

TABLE 1: Various classification and characterization criteria available in the literature for expansive soils using basic geotechnical tests.

#1 on the basis of swelling [41]					
Swell potential	Total expansion	US customary (tsf)	Swell pressure SI units (kPa)	Metric units (kg/cm <sup>2</sup> )	Degree of expansion
0–1.5	0–10	<2.05	<196	<2	Low
1.5–5	10–20	2.05–4.1	196–392	2–4	Medium
5–25	20–35	4.1–7.2	392–687	4–7	High
>25	>35	>7.2	>687	>7	Very high
#2 on the basis of Atterberg limits [42]					
Linear shrinkage	Shrinkage index	PI	LL	SL	Expansivity index
0–8%	<25%	<18%	<35%	<14%	Low
8–13%	25–35%	18–25%	35–45%	12–14%	Medium
13–18%	35–50%	25–35%	45–60%	10–12%	High
>18%	>50%	>35%	>60%	<10%	Very high
#3 on basis of free swell ratio (FSR) [43]					
FSR	Soil expansivity	Clay type		Dominant clay mineral	
<1	Negligible	Nonswelling		Kaolinite	
1–5	Low	Swelling and nonswelling		Kaolinite and montmorillonite	
1.5–2	Moderate	Swelling		Montmorillonite	
2–4	High	Swelling		Montmorillonite	
>4	Very high	Swelling		Montmorillonite	
#4 on the basis of liquid limit (LL)					
LL	Classification				
0–20%	No swell				
20–35%	Low swell				
35–50%	Medium swell				
50–70%	High swell				
70–90%	Very high swell				
#5 U.S. Army Waterways Experiment Station (WES 1983)					
Classification of potential swell	Swell potential (%)	LL (%)	PI (%)	Soil suction (kPa)	
Low	<0.5	<50	<25	<160	
Marginal	0.5–1.5	50–60	25–35	160–430	
High	>1.5	>60	>35	>430	
#6 China Ministry of Construction (CMC 2004) [44]					
Standard absorption M.C (%)	PI (%)	Free swell value (%)		Swell potential class	
<2.5	<15	<40		Nonexpansive	
2.5–4.8	15–28	40–60		Low	
4.8–6.8	28–40	60–90		Medium	
>6.8	>40	>90		High	

TABLE 2: Mineralogical properties of basic clay minerals (kaolinite, illite, and montmorillonite).

Clay mineral	Structure	Interlayer bond/ intensity	Isomorphous substitution	Shrink- swell	CEC (meq/100 g)	LL (%)	K (m/s)
Kaolinite (1 : 1 clay mineral)	<p>Alternating sheets of silica tetrahedron and alumina octahedral sheets</p>	Hydrogen, <i>strong</i>	Low	Very low	3–15	30–75	10 <sup>-5</sup> –10 <sup>-7</sup>
Illite (2 : 1 clay mineral)	<p>Alternating sheets of alumina octahedral sheets and silica tetrahedron sheets</p>	K-ion, <i>moderate</i>	Moderate	Low	10–40	60–120	10 <sup>-6</sup> –10 <sup>-8</sup>
Montmorillonite (2 : 1 clay mineral)	<p>Silica tetrahedron sheets sandwiching alumina octahedral sheets between two silica tetrahedrons</p>	Van der Waal, <i>very weak</i>	High	Very high	29–150	Up to 900	10 <sup>-7</sup> –10 <sup>-9</sup>

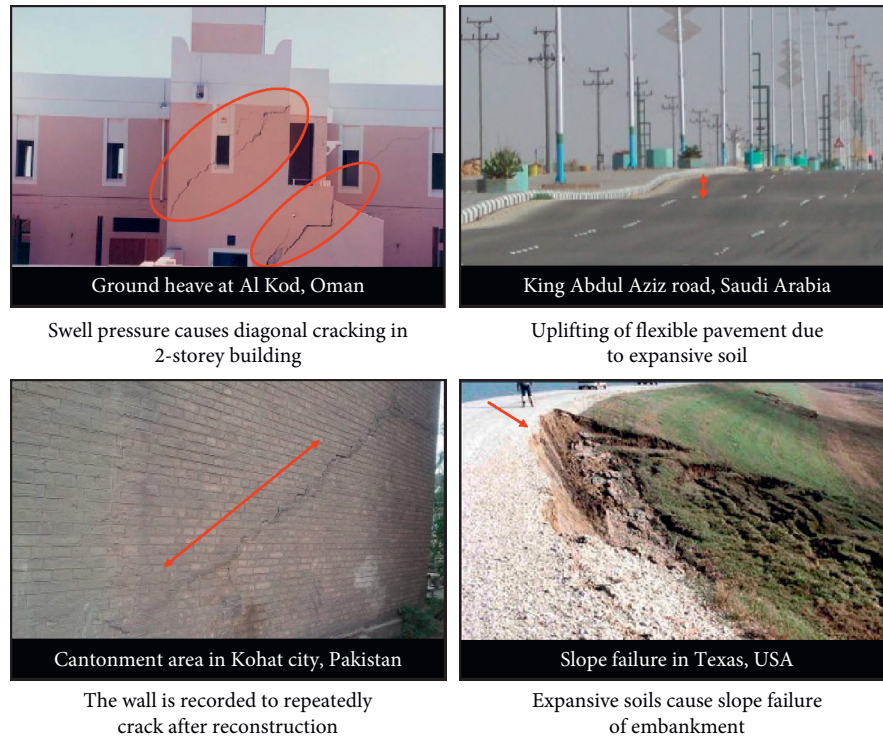


FIGURE 3: Expansive soil damage to civil engineering infrastructure across Oman, KSA, Pakistan, and USA (with some changes for comparison purpose) [62, 69–71].

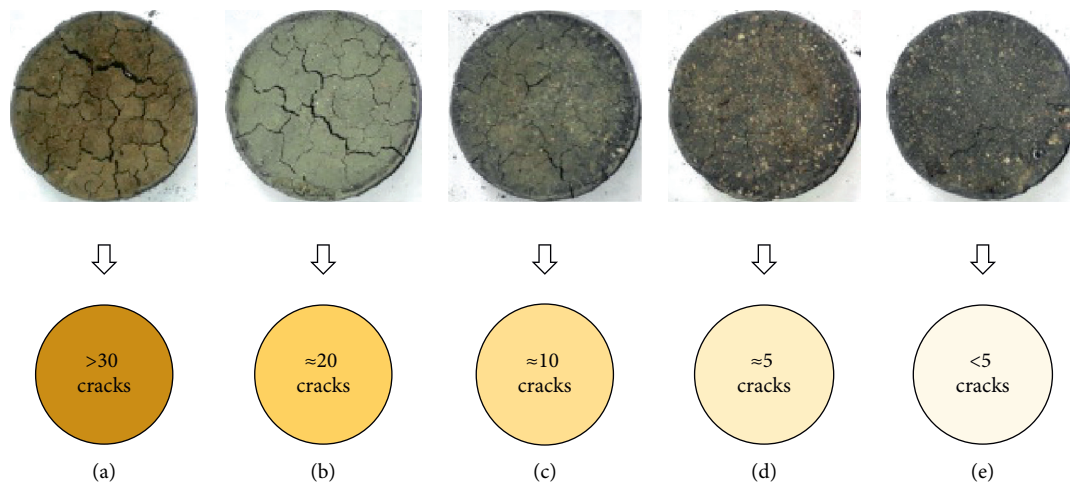


FIGURE 4: Morphology of cracks in expansive soil ( $LL = 77.6\%$ ,  $PI = 40.7\%$ ,  $MDD = 1.47 \text{ g/cm}^3$ , and  $OMC = 28\%$ ) after blending with several mixtures of calcium carbide residue (CCR) and rice husk (RHA) and cured for 28 days [72].

employ CSM are as follows: (1) the replacement with coarse grained materials may be uneconomical because the expansive soil layers are extended deep and in irregular pattern, (2) the presence of  $\text{Ca}^{2+}$  ions speeds up the pozzolanic reactions [63] and tends to decrease the  $P_s$ , (3) it is a hot topic and is widely practiced in field nowadays, (4) the prewetting technique among other takes higher time (several years) for soils with low hydraulic conductivity [73], and (5) recycling gains environmental and economic benefits by reducing the usage of natural resources which leads to development of low-emission and low-energy technologies

[74]. The stabilizing materials with  $\text{Ca}^{2+}$  lower down the  $P_s$  by two mechanisms: (1) by stabilizing the structure of clay particles using cation exchange and (2) by increasing the concentration of cations held between soil within water and thus depleting the double layer thickness [72].

4.2. *Characteristics of CSM.* A large number of CSMs, for instance, lime, cement, fly ash (FA), ground-granulated blast furnace slag (GGBS), bagasse ash (BA), cement kiln dust (CKD), rice husk ash (RHA), silica fume [64], steel slag (SS),



TABLE 3: Summary of oxide composition of traditional Ca-based stabilizer materials (CSMs) from previous studies.

Popular Ca-based stabilizers	CaO (C)	SiO <sub>2</sub> (S)	Al <sub>2</sub> O <sub>3</sub> (A)	SO <sub>3</sub>	Fe <sub>2</sub> O <sub>3</sub>	MgO	K <sub>2</sub> O	TiO <sub>2</sub>	LOI	G <sub>s</sub>	LL (%)
Hydrated lime [84]	70.9	1.20	0.70	—	0.10	0.50	0.10	0.10	26.1	2.32	—
Extinct lime [85]	83.3	2.50	1.50	2.50	2.00	0.50	—	—	—	—	—
Lime [86]	45.0	12.0	1.20	0.00	0.50	0.70	0.80	—	40.0	—	—
Lime sludge [87]	48.0	6.50	1.15	—	1.20	—	—	—	—	—	—
Cement [88]	44.7	27.4	13.1	3.96	3.30	1.19	1.14	—	4.01	—	—
Cement [89]	65.2	20.4	4.10	—	3.20	4.50	0.59	—	—	—	—
Cement [90]	63.0	20.0	6.00	2.00	3.00	—	1.00	—	—	—	—
CKD [91]	63.9	11.9	9.90	0.00	3.40	1.70	0.10	—	4.70	2.80	—
FA [92]	1.60	54.4	28.6	—	3.20	1.40	1.70	1.80	5.00	2.15	32
FA [93]	2.40	58.5	27.8	0.03	8.10	0.70	0.01	—	2.10	—	—
FA [94]	6.70	55.6	26.4	—	3.90	0.60	2.10	1.00	3.68	2.13	46
FA [95]	1.60	54.4	28.6	—	3.20	1.40	1.70	1.80	5.00	2.15	32
FA [96]	48.9	19.9	9.30	7.30	5.70	3.70	0.50	—	3.01	—	—
Class C FA [97]	29.1	31.9	17.5	2.0	5.10	—	—	—	1.00	2.6	NP
Class F FA [98]	14.3	41.3	16.3	0.70	6.30	4.70	2.60	—	0.10	2.53	NP
GGBS [99]	34.0	34.3	17.9	1.64	1.00	6.02	0.64	—	2.66	—	—
GGBS [100]	44.9	29.2	13.8	—	5.50	6.20	1.00	2.10	—	2.84	40
Steel slag [100]	25.8	16.4	2.40	—	26.0	10.0	—	0.80	—	—	—
BA [91]	11.7	47.8	10.2	—	5.70	2.80	2.60	0.80	16.1	—	—
BA [95]	3.20	57.1	29.7	0.02	2.75	—	—	1.13	—	—	—
BA [101]	4.30	67.8	6.90	—	3.84	—	—	—	—	—	—
Coal waste ash (CWA) [102]	2.30	55.7	23.3	—	3.40	0.90	3.50	1.20	38.7	1.94	—
GSA [93]	10.9	33.4	6.8	6.40	2.16	4.72	25.4	—	—	—	—
GSA [103]	15.5	23.9	8.9	5.7	5.2	6.9	22.9	1.02	—	—	—

LOI: loss on ignition; G<sub>s</sub>: specific gravity; NP: nonplastic; —, “no available data.”

sewage sludge ash (SSA), palm oil fuel ash (POFA), fuel oil fly ash (FOFA), groundnut shell ash (GSA) [12, 34, 75–78], are employed in geotechnical engineering. Some “nanomaterials” rich in Ca content [79] also act as CSM, and Sabat [80] suggested these could be used for strength enhancement, plasticity reduction, and limiting swell and shrinkage strains. Also, the mixture of cement, emulsion, and water forms evolutive materials such as cold recycled mixtures (CRMs), which are responsible for the long-term properties in the pavement construction [81–83].

The different CSMs with chemical compositions determined using X-ray fluorescence (XRF) are listed in Table 3. The widely used CSMs are lime (CaO≈40–50% and 70–80%), cement (≈40–50% and 60–70%), FA (<10% and 30%–50%), GGBS (≈30–50%), and BA (<5% and 10–20%). The availability of surplus Ca<sup>2+</sup> tends to replace the monovalent sodium or hydrogen ions rapidly especially in a high pH environment, which gives a higher volumetric stability to expansive soils through ion exchange. This leads to the flocculation reaction, which in turn improves the physical and mechanical behavior of the soil and increases the soil strength.

However, calcium carbonate (CaCO<sub>3</sub>) is produced due to carbonation of lime which is a source of weakness due to its plastic nature which increases the plasticity of expansive soils [23]. Modarres and Nosoudy [87] stated that CaCO<sub>3</sub> formation is related to presence of excess lime and the unavailability of the reactive SiO<sub>2</sub> and Al<sub>2</sub>O<sub>3</sub>.

The advantages and disadvantages of CSMs are briefly summarized in Table 4, which serves as a guide to deal with CSM stabilization of expansive clays, on-site commercially and in the laboratory for research.

## 5. Effect on Geotechnical Properties with Emphasis on Chemical Processes and Microstructure Interaction

*5.1. Main Effect of Lime Stabilization.* Lime stabilization improves the geotechnical properties by changing the microstructure and fabric of expansive clays [112] through four important reactions [113], i.e., (1) cation exchange, (2) flocculation-agglomeration, (3) carbonation, and (4) pozzolanic reaction. It is mainly due to the flocculation-agglomeration reaction that the geotechnical properties of high plasticity clay soils are improved. Because of flocculation, the PI and FSI lower down, whereas compression strength and permeability go up [23, 114–116]. Figure 5 shows that, with lime treatment, the PI reduces by six times the original and transforms from CH to ML showing the efficacy of lime stabilization. The presence of kaolinite, illite, and Mt affects the final stabilization and highly governs the stabilizer characteristics, such as dosage methodology, strength gain, engineering conditions, and curing condition effect [23].

The period of curing is an important parameter in achieving long-term compressive ( $q_u$ ) and split tensile strength ( $q_t$ ), as the pozzolanic reaction progresses towards completion [54, 63, 117]. The strength gain with 4% lime and curing at 28 days for quartz, kaolinite, and Mt were recorded as 330%, 230%, and 130%, respectively, in contrast to samples with 4% lime and tested after one day curing [118]. Increased curing duration is an effective approach in reducing the swell potential of expansive soils treated with lime. At same water content in the modified compaction test, an increase of 133% in UCS is observed

TABLE 4: Summary of advantages and disadvantages of calcium-based stabilizer materials (CSMs).

Stabilizer	Advantages	Disadvantages
Ca based materials (CSMs): lime [12, 104–106], cement [107], FA [12, 24], SF [108], GGBS [109], BA [76, 110], CCR [72], POFA [111], GSA [93]	(i) Long-term strength is achieved as a result of pozzolanic reaction which is time-dependent and lasts for longer duration.	(i) The release of deleterious substances contaminate the underground water. The “ultimate” strength gain reaches several years.
	(ii) Lime-treated soils undergo immediate modification resulting in a relatively denser microstructure and higher strength.	(ii) These cause adverse environmental and economic concerns by vast CO <sub>2</sub> emissions. At early modification stages, lime makes the soil less dense.
	(iii) In viewpoint of economy, usually small amount of material is required as compared with non-CSMs.	(iii) The variation in site conditions with those simulated in a laboratory often leads to marginal errors.
	(iv) The rate of strength gain is much higher and faster in soil stabilized using cement.	(iv) The brittle failure is undesirable with respect to structural stability.
	(v) The PI reduction by lime is the highest for problematic Mt. Alternatively, using quicklime due to its elevated reaction temperature enables stabilization in cold regions.	(v) The effect of lime modification in clays containing quartz is almost negligible due to the increased period of curing is essential.
	(vi) The most commonly used materials comprising aluminosilicates include GGBS and fly ash.	(vi) Class F fly ash contains low calcium and thus requires an activator in order to be used as the stabilizer material.

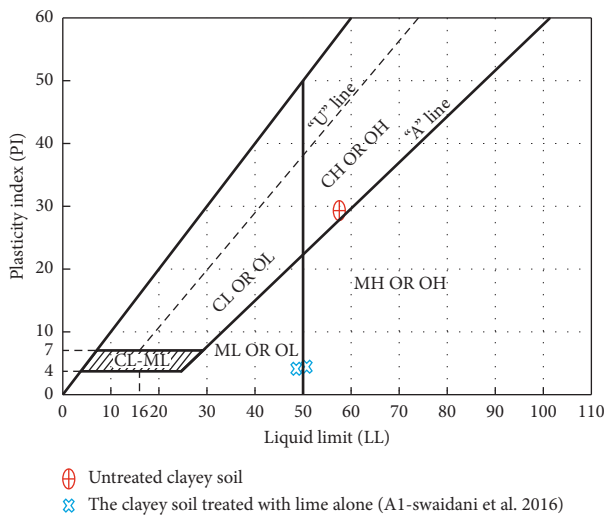


FIGURE 5: The main and interaction effects of lime in comparison with untreated soil, on Casagrande's plasticity chart (with some modifications in the original figure) [112].

for cement-treated samples cured from 7 days to 28 days [119]. Ali and Zulfqar [114] remarked that this behavior is due to the replacement of hydrated lime  $\text{Ca}(\text{OH})_2$  with quicklime  $\text{CaO}$  at earlier days, which in turn intensifies the pozzolanic reaction. This observation was also depicted from their test results.

According to Idris and El-Zahhar [120], the microstructural properties (surface features, size, and shape) of the sampled particles of lime stabilized soil are highly dependent on the curing period. Scanning electron microscopy (SEM) determines the effect of stabilizer treatment on morphological structure with magnifications at micrometer scale. Also, by the virtue of chemical analysis, SEM assists in evaluating the calcium localization on clay particles [118].

The SEM micrographs in Figure 6 show a variety of samples were stabilized with 8% lime and (20% pozzolan + 8% lime) blend, respectively, and upon 7 days curing, the particles of clay soils become coarser at microlevel. The 8% lime treatment contains coarse soil matrix, illustrated in Area 3, and is attributed to plasticity reduction.

It is important to determine how efficient lime acts when it is used as a potential CSM. The suitability of lime in silica-rich soils, soil containing gypsum, sulfate-rich soils, and  $\text{Fe}_2\text{O}_3$ -rich soils is briefly discussed. In order to analyze the efficacy of lime as the stabilizer material, the ratio between lime: silica, lime: alumina, and lime: (silica + alumina), for the poststabilization samples, must be greater. The over dosage of lime is more indicative in  $\text{SiO}_2$ -rich soils, where the formation of highly porous silica gel takes place. So, the strength is substantially undermined due to cementation as the excess gel is porous and has a high water holding capacity. Therefore, it contributes to an overall strength loss and results in higher plasticity and swell potential. In their study on soils containing gypsum, lime treatment of 3% was found as optimum for strength requirement, and thereafter, the effect reversed [121]. In addition, Shi [122] stated that, for  $\text{SO}_4$ -rich soils, the unavailability of hydrated  $\text{CaO}$  makes lime a weaker choice too. A variety of soils with large contents of  $\text{Fe}_2\text{O}_3$  and lime exhibits poor dispersibility, and the particle-to-particle bonding is improved, which aids in restraining both the FS and  $P_s$  [115]. Thus, it can be inferred that lime stabilization of expansive soils ranging from low to high characterization mainly depends on type of clay minerals and environment of lime-soil reactions.

**5.2. Main Effect of Cement and Interaction Effect with Lime.** The ordinary Portland cement (OPC) is the “key material” to housing and infrastructure worldwide which is also employed in soft ground stabilization. But its use is

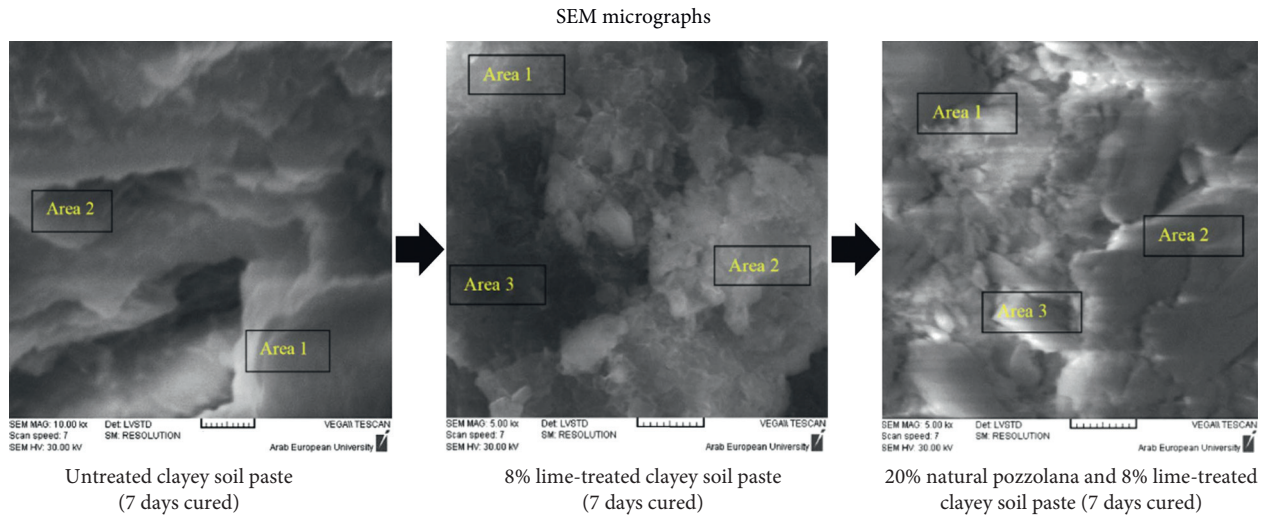


FIGURE 6: Microstructural comparison of clay soil paste cured at 7 days (untreated sample, treated with 8% lime, treated with 20% pozzolan + 8% lime) (modified after [54]).

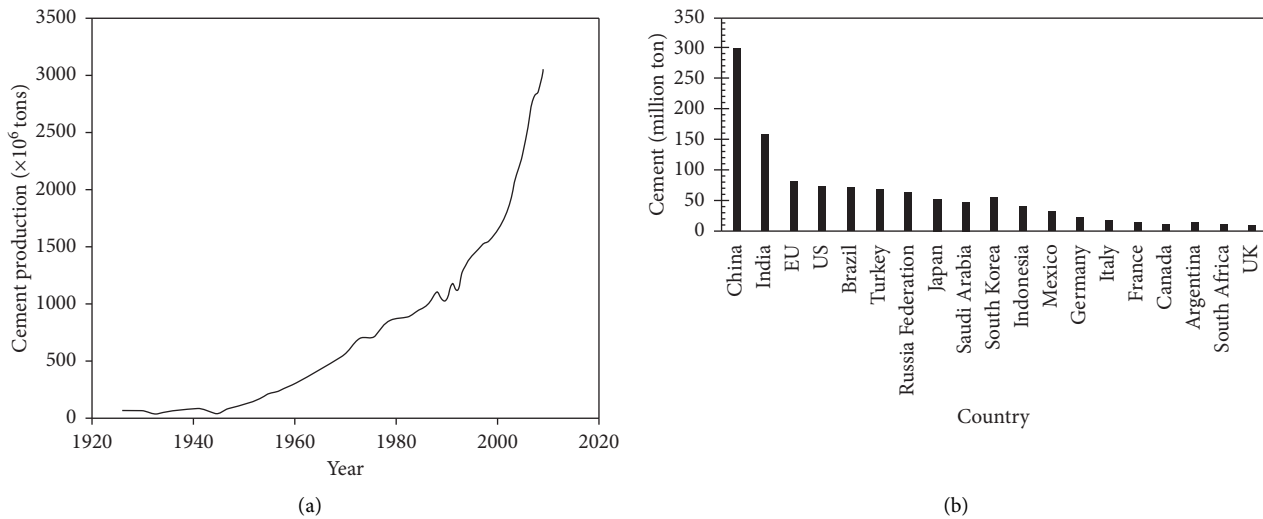


FIGURE 7: Global annual cement production: (a) between 1925–2009 [124]; (b) in different countries [125].

somehow restrained since global warming and rapidly changing climate are challenging global issues of today’s world [22, 123]. Figure 7 indicates the global annual cement production between 1925 and 2009 and the cement production in various countries with China taking the lead as it plans to construct 40 billion square meters of floor space until 2036.

Cement stabilization is specifically recommended and significantly increases the cohesion, strength, and durability of coarse-graded mixtures having a low PI [126]. Zaimoglu [127] refrained the use of cement owing to its high cost and hazardous nature. Cement and lime stabilization are more or less identical in yielding results with respect to mechanism of modification since the formation of C-S-H and C-A-H takes place in both cases which form cementitious links with the untreated clay particles. Lime and cement have their own benefits and ill effects regarding the viewpoint of stabilizing materials.

The effect of cement alone on the geotechnical properties and engineering characteristics is reviewed first. Cement modifies the physical properties of certain waste materials (e.g., marble industrial waste and bottom ash) and decreases their toxicity level [128–130]. The plasticity and swell indices lower down, thereby increasing the shear strength parameters and permeability characteristics. Based on results from past literature, it is illustrated from Figure 8 that, up to 10% addition of cement and lime each, both  $P_s$  and FS values are reduced considerably. The  $P_s$  is necessary to evaluate the nature of problem associated with expansive problems. So, in order to study the effect of stabilizers on  $P_s$ , almost all curves record to follow similar declining trend, from 500 to 700 kPa, for untreated soil to 170 to 300 kPa, for both lime and cement (10% dosage each), with the least amount of variance between lime and cement [71]. The significant reduction in maximum  $P_s$  is observed in the data of Vijayvergiya and Ghazzallay in contrast to almost identical

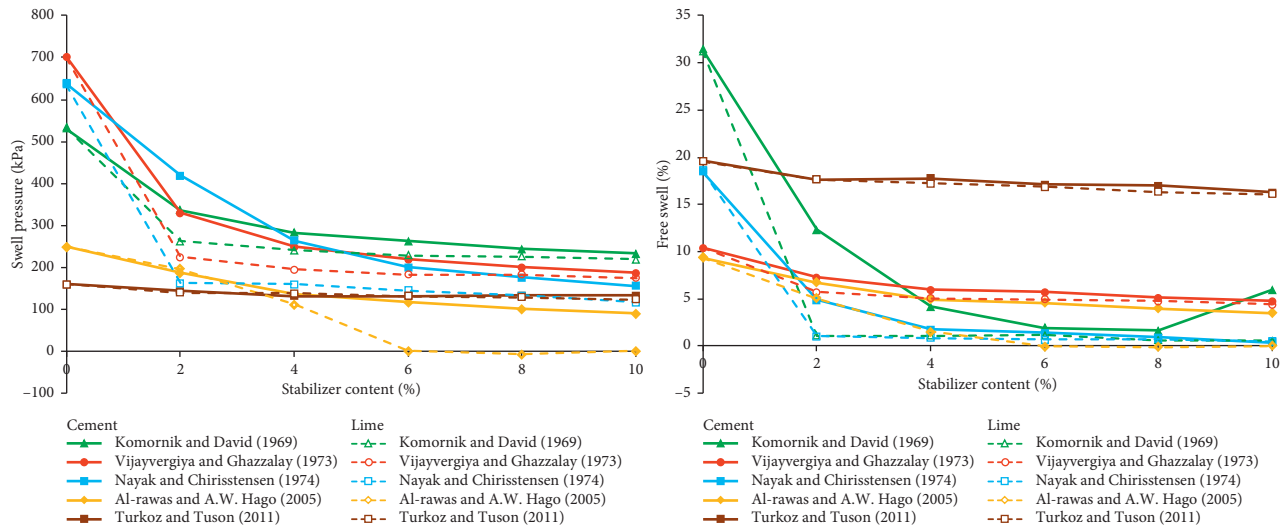


FIGURE 8: Main effect of both cement and lime on the plot of swelling pressure and free swell, from past literature.

values reported by Turkoz and Tuson [131], when considering the initial and final  $P_s$  values on each curve. On the contrary, the treatment of lime and cement within range of 2 to 10% dosage level indicates that FS curves experience wide variance. The trend shown by Komornik and David is most significant, witnessing almost 6 times reduction among untreated and highest dosage values, in contrast to results obtained by Turkoz and Tuson which changes from 20% to merely 15%. Moreover, the remaining three curves for lime and cement are seen to follow a similar trend which illustrates an intermediate effect on the reduction of FS values. Lastly, it can be seen in Figure 8 that the stabilization mechanism of lime and cement for each specified treatment resembles each other, with cement proving to be more effective in terms of minimizing the swell. Note that, by using 9% lime alone, the  $P_s$  becomes zero and the effect on plasticity value is almost the same as recorded for the case of lime-cement mix [132].

The CKD is fine-grained powder-like dust material obtained as a by-product from the manufacturing of cement [133]. It contains traces of reactive CaO and alkaline compounds and is therefore highly fine to be used as the effective soil stabilizing agent. However, the properties of CKD largely differ depending upon the manufacturing plant, cement kiln type, and the characteristics of raw materials employed in cement production [12, 134, 135]. Its production is estimated to be approximately 30 million tons per year, across the globe, of which 80% causes an environmental threat and is not safely disposed [97]. Many researchers have suggested its use as potential stabilizer for clayey soils. The (volcanic ash + 20% CKD) stabilizer mix will yield a significant improvement in mechanical properties [136] and pronounced increase in CBR values (above 80%); therefore, Yu et al. [91] found it suitable for the construction of economical building units and small-scale roadways.

In terms of the final stabilization effects, the interaction effect of cement with lime is more efficacious than lime or

cement alone treatment [116]. The PI decreases by 60%, and the  $P_s$  drops by 82% when (5% lime + 3% cement) blend is used to modify medium expansive soil extracted from depth [71]. The  $P_s$  value is recorded to decrease from 249 kPa for untreated soil to 45 kPa for (5% lime + 3% cement) blend. Their combined effect on geotechnical properties is also summarized succinctly in Table 5.

Recently, it is found that recycled cement can be yielded by burning old OPC pastes at elevated temperatures of 450°C (RC-450), which will lower down the CO<sub>2</sub> emission by 94%, attaining an equivalent strength of OPC. It is obvious from surface morphology studies by SEM that CO<sub>2</sub> is reduced by (1) formation of calcium carboaluminate and (2) C-S-H gels containing calcite, as both are evidenced in the SEM micrographs in Figures 9(a) and 9(b), and in the EDX analyses in Figures 9(c) and 9(d), respectively. In the plots between energy on abscissa and counts on ordinate, the peaks for only calcite, silica, and alumina are shown with almost no traces of other problematic clay minerals [94, 144]. Figures 9(a) and 9(b) also reveal the formation of portlandite and ettringite with a honey-combed structure in the micrograph of OPC being transformed into a denser structure with newly formed carboaluminate at 4 μm magnification level. It is therefore to say that RC-450 (1) is richer in calcium carbonate amount, (2) has densely arranged nanoparticles, and (3) has no portlandite content. Koliass et al. [99] delineated that tobermorite formation leads to a denser and stable soil structure.

The thermogravimetric analysis (TGA) measures change in mass of a material as a function of either temperature or time and is capable to quantify phase compositions in ettringite, portlandite, gehlenite, and calcite [145]. The results of TGA in Figure 9(e) show that CO<sub>2</sub> fixation (that is to combat the challenge of global warming [146]) in case of RC-450 is low (75%) in contrast with that of a higher value for OPC (87%) at same temperature. The trend of reducing weight loss with temperature thus signals a low CO<sub>2</sub> fixation value for RC-450. This shows the significant effect of recycled

TABLE 5: A succinct list of research conducted on Ca-based stabilizer materials for different expansive soils across the world.

Location of expansive soil	Expansive soil properties							Stabilizer		Properties improved	
	$G_s$	LL (%)	PL (%)	PI (%)	Activity	USCS	MDD ( $\text{kN/m}^3$ )	OMC (%)	Type		Optimum amount
Oman, Al-Khoud [71]	2.80	50	29.5	20.5	1.03	MH	17.5	21	Lime (L), cement (C), pozzolan (P)	5% L + 3% C. Other studies: 2% L + 1% C [94] 4% L + 30% red mud [137] 8% L + 4% C [71] 8% L + 20% P [84]	$P_s \downarrow = 249$ to 45 kPa $PI \downarrow = 20$ to 8% $P_s \downarrow =$ by 840%
China, Hefei, Anhui [138]	2.71	42.8	22	20.8	—	MH	17.3	18.9	Fly ash (F), sand (S), basalt fiber (B)	10% F + 8% S + 0.4% B	LL $\downarrow$ , PI $\downarrow$ , PL $\uparrow$ UCS $\uparrow = 345$ to 900 kPa (with 0.4% Ba fibers)
USA, Idabel, Oklahoma [121]	—	79	25	54	1.30	CH	—	—	Lime (L) and Class C fly ash (CFA)	5, 10, 15, and 20% [54] L and CFA each	Shrinkage $\downarrow =$ maximum at 20% lime
India, Calcutta (80% BC + 20% Na-bentonite) [95]	2.66	78	45	33	3	CH	—	—	Fly ash (F) and GGBS (G)	20% mixture of F and G [121] (F:G 70:30) + 1% L 25% B (modest effect on strength)	UCS $\uparrow = 270$ to 450 kPa (28 days curing) Addition of 1% Lime: 270 to 875 kPa
Australia, Queensland [68]	2.65	86	37	49	1.66	CH	12.65	36.5	Bagasse ash (B) and lime (L)	10%B + 10% L [95]	MDD $\downarrow$ , swelling $\downarrow$ UCS $\uparrow$ (0–25% BA + lime mix)
Pakistan, Kohat city, KPK [139]	2.71	43	41	22	0.6	CL	18.1	14.9	Bagasse ash (B) and marble dust (M) [68]	4–6 % B 8–10% M [140] Combined effect: 8% B + 16% lime sludge [139]	B: swelling $\downarrow$ , UCS $\uparrow$ till 5% B, MDD $_{5\%} \uparrow$ M: swelling $\downarrow$ , UCS $\uparrow$ At 10% M, MDD $_{4\%} \uparrow$
India, Dadri (100% bentonite) Dadri [96]	2.71	412	60	352	3.5	CH	12.6	41.0	Dadri fly ash and lime (L)	10–15% [141] (with 3% L)	UCS $\uparrow$ (strength of cured sample > uncured samples) $P_s = \downarrow$ (as F and L content increases)
China, Guangxi province [14]	2.73	77	34	43	—	CH	17.2	—	$P_s$ versus $\omega$ , MDD relation	—	Models developed which needs to be validated due to lack of experimental results
Algeria, S-H clay, M'sila [142]	—	84	33	51	1.98	CH	19.7	19.43	Portland cement (P) and lime (L)	12% P and L each. (lime is a much better option)	PI: $\downarrow$ , methylene blue values $\uparrow$ , CBR $\downarrow$ , shear strength $\uparrow$
Iran, taleghan city [87]	—	47	21	26	<1	CL	16.4	18.0	Coal ash (C) and hydrated lime (HL)	9% C + 6% HL	With coal: less effect on properties coal + h. lime, UCS $\uparrow$ PI $\downarrow$ , CBR $\uparrow$
Taiwan, taipei [137]	—	30	20	10	>1	CL	16.6	16.8	Sewage sludge ash (S) and lime (L)	8% admixture (S:L 4:1)	CBR $\uparrow$ , UCS $\uparrow$ , PI $\downarrow$
Sudan, Khartoum [123]	2.64	76	24	52	1.3	CH	1.49	26.0	Fly ash (F)	10% F (F: SiO $_2$ is 54%, alumina 34%, CaO is 3.6%)	$P_s \downarrow$ (50% to 70%), at 25% F, $P_s \downarrow$ (90%), UCS $\uparrow$ (almost 100%)
Brazil, curitiba city [143]	2.71	53	32	21	<1	MH	13.8	28.5	Lime (L)	9% L	UCS (by 75%) Porosity $\downarrow$ , MDD $\uparrow$
Spain, Granada [21]		69	48	21	1.4	CH	15.7	40	Lime (L), steel slag (S)	Dolomite L (effective as commercial L) S: also good	Increase in pH $\uparrow$ Increase in CO $_3 \uparrow$ UCS $\uparrow$ , plasticity $\downarrow$

$\uparrow$  represents an increase;  $\downarrow$  represents a decrease, in the corresponding property.



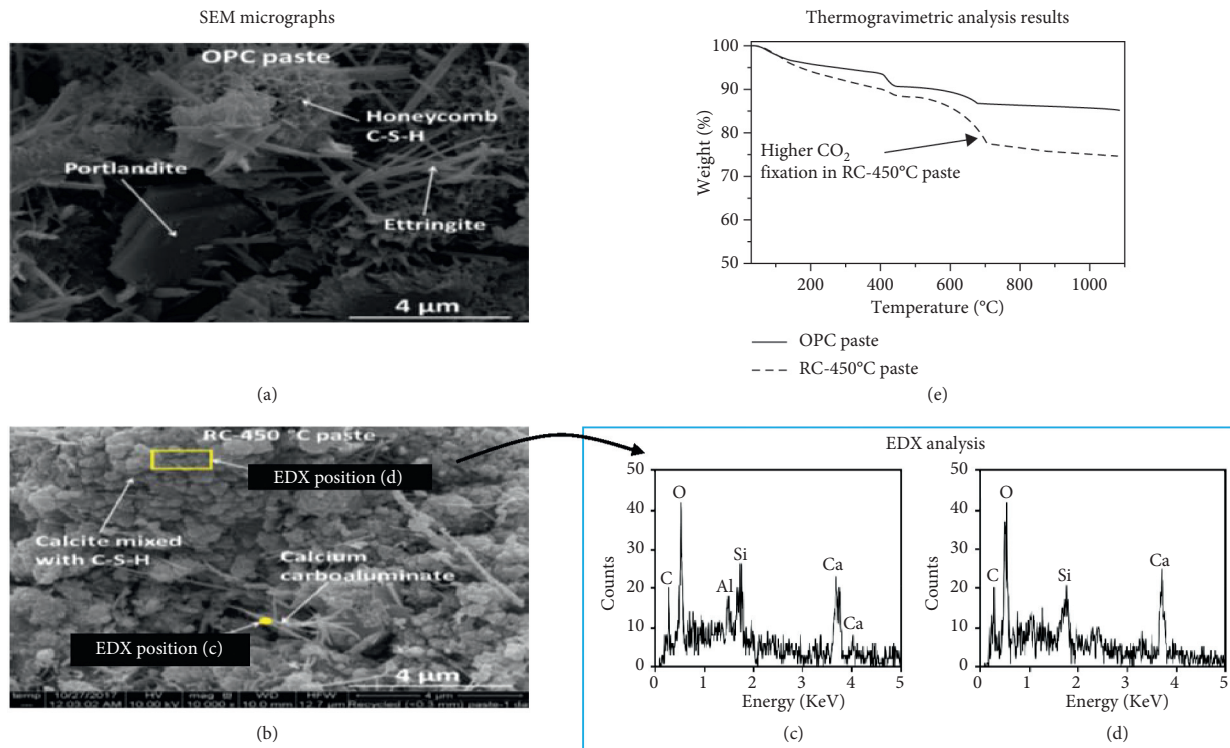


FIGURE 9: Comparison of SEM micrographs and TGA along with EDX analysis on specified locations for OPC and recycled cement (RC) 450°C (modified after [129]).

cement at an elevated temperature on the microstructure of expansive clay soil. So, cement proves to be more efficacious in controlling swell potential, and it is obvious that the mechanism of cement and lime stabilization of soils follows a similar pattern and yields identical results.

**5.3. Main Effect of Fly Ash and Interaction with Lime and Cement.** Fly ash (FA) controls the swell potential in expansive soils [24, 137] and is classified into several types based on the source of extraction and nature of pozzolanic behavior. The ASTM categorizes the noncrystalline FA into Class N, Class F, and Class C [71], represented here as NFA, FFA, and CFA, respectively. One advantage inherent to FA is its pozzolanic nature. CFA is obtained when subbituminous coal is burnt in plants, while generating electricity [129]. This form of CFA is being considered as an additive with high-calcium fly ash (HCFA) in conjunction with other catalytic binders and a waste material rich in silica-alumina to develop a new cold mixture for asphalt binders and emulsion mixtures in pavement design and practice [147]. In India alone, as of 2005, according to Dahale [97] the total production of FA reached 75M tons/year, 92% of which would go useless in contrast with findings of He et al. [129] for the western countries, stating the effective utilization of 70% of total FA produced. In the Table 3, Kate reported the FA with CaO approximately equals to 49% [96]. It can be observed from the table that all FA types have silica + alumina + iron oxide content exceeding 80% and is therefore defined as “pozzolan”, according to ASTM [148].

Fly ash is a geopolymer, i.e., a cementitious additive capable of reacting with H<sub>2</sub>O in the presence of alkaline activators [96]. Activation of FA prior to stabilization using different activators (such as NaOH, Na<sub>2</sub>SO<sub>4</sub>, and K<sub>2</sub>SO<sub>4</sub>) is necessary for their performance. In order to elevate the pH environment, generally 1% CaO is incorporated in the industrial wastes for initiating the chemical reaction. The cementitious nature lacks because the CaO content in FA is less than 10% although the Al<sub>2</sub>O<sub>3</sub> and SiO<sub>2</sub> contents are generally high. Therefore, lime, cement, or GGBS are incorporated to enhance the pozzolanic behavior of FA [149].

Of all ASTM types of FA, the CFA proves to significantly improve the expansivity. This results in decreasing permeability, PI, FS, and  $P_s$  of soft clays [12, 95, 150]. The cementation in expansive clays stabilized with lime, lime-FA, and OPC is associated with formation, setting, and intergrowth of gelatinous reaction products (such as crystalline, hydrous calcium silicates, and aluminates). Figure 10 highlights the particulate characteristics of four types of pozzolan. The environmental scanning electron microscopy (ESEM) is an advanced form of SEM [151]. It is shown in Figure 10 that trass pozzolan (T) has the capability to absorb large amount of water in contrast to tuff pozzolan (A) exhibiting roundish and rough surface which witnesses a lower water uptake, owing to their mineral shape, size, and orientation. The subsequent increase in angularities of pozzolan K (sharp edged, split-like grains, more even, and dense structural surface) and P (sharp-edged, split-like grains, glassy-like, and even more even and dense surface)

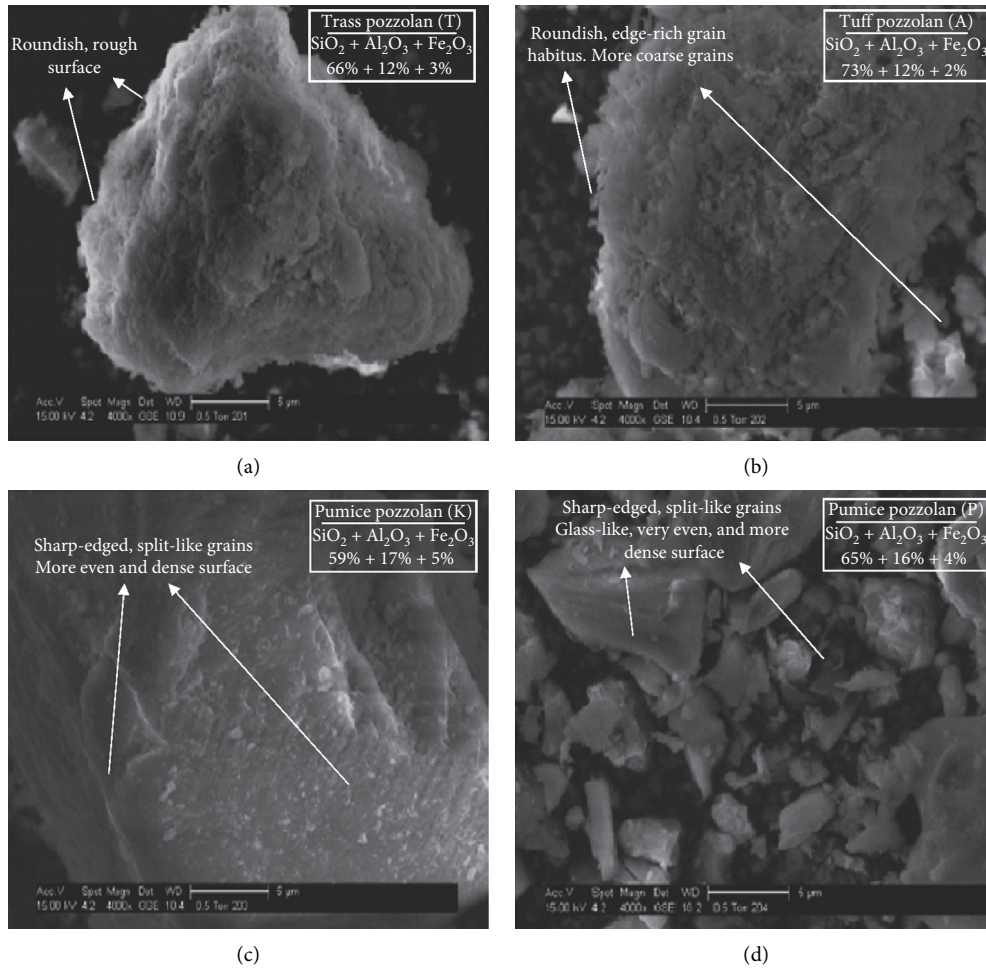


FIGURE 10: Environmental scanning electron microscope (ESEM) images of various types of pozzolans providing an insight to particulate characteristics (reproduced from research study by [121] with some modifications).

(Figures 10(c) and 10(d), respectively) also leads to reduced water penetration [121].

In addition, the indirect tensile strength of specimen stabilized with FA can be calculated, which is helpful for soils subjected to traffic load, differential temperature, and/or nonuniform settlement, and an equation is employed on the basis of which a correlation (25% FA treatment) has been developed to determine the Brazilian tensile strength (BTS), using the unconfined compression strength (UCS) value, in equation (8) [152]. For a given value of LL, the PI can be directly evaluated using correlation suggested in equation (9) and can further be used to determine BTS from the derived equation (10), after original equations by past researchers:

$$\text{BTS} = 0.026 \times \text{UCS}^{1.116}, \quad (8)$$

$$\text{PI} = 0.11 \times \text{LL}^2, \quad (9)$$

$$\text{BTS} = 0.0012 \times \text{PI}^{0.558}. \quad (10)$$

The main and interaction effects of FA are briefly discussed. According to Kommu et al. [153], the FA aids in

increasing OMC whereas accounts for a reduction in MDD in the presence of sand, which acts as the filler material to improve compaction characteristics due to capillary bridge. Also, by keeping FA content constant and increasing the amount of sand, the results were inverted. In terms of strength characteristics evaluation, a highest UCS value is attained with an addition of 10% FA and 8% sand in the expansive soil sample, which is attributed to C-S-H gel and AFt phase formation because of FA hydration and thus significantly improving cohesion between clayey particles.

The CFA has been used in conjunction with cement and waste gypsum [97], and the maximum UCS is achieved at 28 days (0.36 MPa to 3.49 MPa) with strength reporting to be decreased by 36% at 56 days. While dealing with coal ash, the probable chromium (Cr) and lead [97] concentration is to be kept in limits [154]. According to Koliass et al. [99], the FA increases the tobermorite formation which enhances the strength, while further addition of cement provides improved setting and hardening. The mixture of cement-FA yields high early and final strength for treated soils. The FA less than 50% is optimum and achieves the highest UCS and shear strength values. However, the strength drops beyond this threshold.

TABLE 6: Comparison of lime-activated GGBS (LAS) and lime-activated Portland cement (LPC), in perspective of stabilization.

LAS~LPC-treated clay	Soaked in Na <sub>2</sub> SO <sub>4</sub> for 120 days (durability check)	C-S-H formation (before soaking)	C-S-H formation (after soaking)	Compressive strength (start till soaking)
LAS-treated clays	No cracks, more durable	More	Less	Steady drop (775 kPa to 625 kPa)
LPC-treated clays	Extensive cracks, less durable	Less	More	Sharp loss in strength gain (after 28 days)

LAS: lightweight alkali-activated GGBS; LPC: lightweight Portland cement.

**5.4. Main Effect of GGBS and Interaction Effect with Lime and Cement.** The ground granulated blast furnace slag (GGBS) is a prominent industrial waste that helps in giving long-term strength to problematic soils [155, 156], and sometimes, it is also used as a replacement of cement due to its high cementitious nature. Unlike lime, the GGBS is far more efficacious to stabilize the sulfate bearing soils. Much has been learnt about the physical, mechanical, and hydraulic behavior of clayey soils stabilized using GGBS and their activation with lightweight alkalis (lightweight alkali-activated GGBS (LAS)). As shown in Table 6, use of this particular CSM experiences no cracks visible to naked eye when dipped in sodium sulfate solution for four months, thereby yielding a higher compressive strength [157, 158]. It can also be observed that C-S-H formation before soaking in case of LAS-treated clays is in more quantity than that of LPC-treated clays, and after soaking, it is vice versa. The LAS-treated clays are more durable and experience fewer number of cracks when dipped in sodium sulfate solution for 120 days, in contrast with LPC-treated clays which are less durable and witness more cracks.

The role of GGBS, alone and in combination with FA and lime, in affecting the engineering characteristics is of vital importance to soil engineers, practitioners, and scientists. According to Sivapullaiah [159], the slags with a larger amount of Ca<sup>2+</sup> ions (such as in the case of GGBS) than Na<sup>2+</sup> ions, such as Cu slags, tend to minimize swell potential more effectively. It suggests that suitability of stabilizer is highly dependent on its chemical composition. In addition, Sharma and Sivapullaiah [95] and Jiang et al. [160] employed GGBS for investigating effects on expansive soils to control the uncontrollable swelling, mainly occurring in sulfate-rich soils upon CaO or cement addition, concluding that GGBS is a suitable material for pavement stabilization, owing to its high wear resistance. The use of GGBS in combination with lime and RHA (20%, 5%, and 10%, respectively) is effective, as plasticity reduces drastically by 67% and the strength increases by 95% in contrast to that of virgin soil [98]. Moreover, considering the wide variation in properties of GGBS and FA, for instance, the deficiency of CaO in FA and the excess of CaO in GGBS make their “interaction effect” as superadvantageous, in terms of treating expansive soil. With using almost 10% steel slag, the MDD is expected to rise and the UCS also increases by 50%. However, beyond this amount, the strength loss is reported at a much slower rate. Also, the reduction of 70% in PI is recorded at 30% steel slag content. Moreover, by using 20% optimum blend of GGBS and FA for stabilization of high plastic clays along with 1% lime, the test results indicate reduction in LL and PI, whereas shrinkage limit, MDD, UCS, and amount of C-S-H gel produced are significantly increased. Despite high cement

prices and/or unavailability of lime in some places, the GGBS-FA mix binder is cost-effective and significantly reduces the burden on environment [161].

**5.5. Main Effect of Bagasse Ash and Interaction Effect with Lime and Cement.** The bagasse ash is a waste in the form of agricultural byproducts which is obtained from sugarcane industry. The juice extracted from sugarcane forms a mass resembling fiber called “bagasse.” When bagasse is burnt, an ash is produced in the form of fine residue, with coarse-grained structure and lower G<sub>s</sub> value than that of soil, termed as “bagasse ash [95].” The BA is a serious issue and is usually dumped without any economic value. Being rich in SiO<sub>2</sub> content, it is used as a pozzolanic material because the amount of alumina, silica, and calcium oxide exceeds 70%. ASTM defines such materials as Class N or Class F pozzolan, while if the accumulated percentage exceeds 50%, then it is categorized as Class C pozzolan [149]. In addition, it has been confirmed from leaching tests on expansive soil stabilized with bagasse ash that it is suitable for stabilization of road subgrades owing to its nonhazardous nature [162, 163]. The addition of BA reduces the PI, swell, alkalinity of soil matrix, and cation exchange value while increases the CaCO<sub>3</sub> content and the total soluble solids [3].

The improvement mechanism of BA is identical to the chemical reaction involved in cement stabilization. The clay reacts with lime and BA resulting in flocculation and the cation exchange phenomenon that is a “short-term reaction.” Then, the formation of C-S-H and C-A-H gels takes place, due to the pozzolanic reaction, giving “long-term strength” to the soils [164, 165]. However, the strength gain and durability are quite low when BA is used alone for purpose of stabilization. However, it effectively lowers the PI, FS, and P<sub>s</sub> values [68]. The UCS of high expansive soil, when treated with 0.5% BA + 6.25% lime mix and cured for three days, witnessed a dramatic increase of almost 96% as compared to when no lime treatment was done. Similarly, for the same dosage levels of stabilizer contents cured for 28 days, the percentage increase in strength was about 150%, reflecting the effectiveness of curing in the strength gain process [166]. The MDD drops, and the OMC rises when (8% BA + 16% lime sludge) mix is incorporated in expansive soil (LL = 60%, PI = 28%, P<sub>s</sub> = 128 kN/m<sup>2</sup>) [167]. In Figure 11, the increase in RHA from 0 to 7.5% indicates a gradual increase in the UCS and later drops when further increased up to 12.5%. The trend of CDA is almost similar to that of SCBA. In contrast, following the same pattern, RHA experiences a sharp rate of strength gain and strength loss. Therefore, it can be concluded that BA is a less effective stabilizer and its performance is highly improved when lime

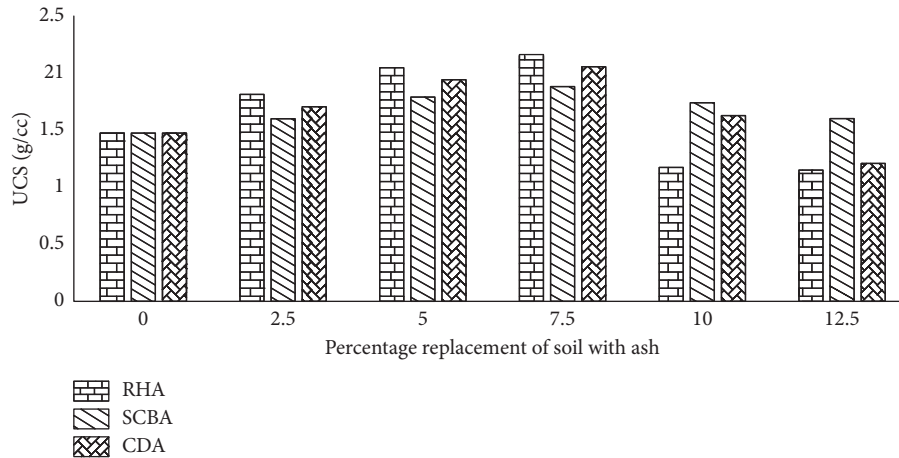


FIGURE 11: Stabilization of subgrade soil in India using indigenous nonplastic materials such as rice husk ash (RHA), sugarcane bagasse ash (SCBA), and cow dung ash (CDA). The in situ soil (depth of 1.5 m–2.5 m) was intermediate plastic clay (figure taken from [168]).

is added to it, and the curing period is increased up to 28 days.

#### 5.6. Efficacy of Other Eco-Friendly Stabilizer Materials.

The extent of other CSMS cannot be comprehensively enclosed in one research paper; however, few eminent materials are presented in this section, for instance, calcium carbon residue (CCR), groundnut shell ash (GSA), and sewage sludge ash (SSA).

When acetylene is burnt, calcium carbon residue (CCR) is produced. It is deleterious in nature but rich in lime [138] content; therefore, it can be used to modify the properties of expansive soils [169]. The stabilization with CCR achieves better results than with lime from the viewpoint of economy and environment [170]. Horpibulsuk categorized the strength development of CCR-stabilized soils into three zones, namely, active, inert, and deterioration zones. Only the first two zones are beneficial with respect to strength improvement. In the first zone (i.e., CCR less than 7%), the natural pozzolanic material is sufficient for the pozzolanic reaction. Hence, the FA is not required to further improve the strength. But, in the inert zone (i.e., CCR between 7% and 11%), the strength gain is achieved by adding FA which helps in densification and speeding up the pozzolanic reaction [78]. Moreover, Somna et al. [171] utilized CCR-RHA mix and recorded 22% increase in the UCS upon curing from 28 days to 180 days. These materials are also employed for yielding high strength concrete in construction. In addition, BA and CCR are mixed in combination for making the stabilized mix more ductile. In the stabilization of soft Bangkok clay, the pozzolanic reaction intensified as the amorphous Si from BA was dissolved in alkaline environment and reacted with the CCR [172]. With 8% CCR treatment, for no BA content and with 9% BA after 36 days curing, the change in UCS was as high as 400% [173].

Ground nuts are grown in abundance in different regions of the world approximately 20,000,000 hectares per annum [174]. The use of GSA, a form of agricultural waste, is useful in waste management. It needs to be safely disposed to

avoid polluting the environment [93]. Addition of GSA to black cotton soil (LL = 83.36% and PI = 89.32%) significantly improved the compaction and strength characteristics. However, it cannot be used as standalone stabilizer for road construction owing to the smaller value of CBR after stabilization [175]. Venkatraman et al. [176] concluded from his study on the settlement behavior of clayey soil using the plate load test that the GSA stabilization enhances the ultimate bearing capacity. GSA and cement increased the optimum moisture content [177] whereas slightly decreased the dry density as well as the modulus of elasticity of soil. The (2% GSA + 0.1% cement) blend may be used as a feasible alternative in pavement construction and for stabilizing soil where load is emplaced [103]. The GSA with dosage levels increased from 4% to 6% was applied to low plasticity clay and a rise of 15% in UCS at 7 days was recorded, which fell short of standard requirement for stabilization of base materials [178]. Behnood [12] enumerated that 8% GSA is helpful in mitigating the swell by effectively lowering down the PI value.

SSA resembles FA in terms of cementitious nature has a higher percentage of  $\text{Ca}^{2+}$  in SSA (8%) than in FA (3 to 5%) [162] and acts as an efficient stabilizer. Sewage sludge blended with coal fly ash (CFA) can lower the availability of heavy metals such as Cu, Zn, and Cd in the sludge [179]. Behnood [12] outlined that SSA effectively modifies the properties of CL soil by increasing their UCS, CBR, cohesion, and shear strength while reducing the swelling and angle of internal friction [180]. The UCS of specimens was improved 3–7 times by using incinerated sewage sludge ash (ISSA) and cement. Also, the swelling behavior was reduced by 10–60%, and the improvement in the CBR values was up to 30 times [181]. 8% SSA + lime can change untreated expansive from weak subgrade soil to better subgrade soil in road construction [137].

## 6. Discussion

It has been evolved to this day that the evaluation of stabilization of expansive soils is well documented in a



series of diverse philosophies laid down, wherein a variety of CSM have been employed for stabilizing low to high range expansive soils. However, one significant shortcoming associated with the use of CSM is the increased brittleness; therefore, several stabilized elements are incorporated to overcome this problem [173]. The two prominent and conventional CSMs, lime and cement, witness brittle failure in the modified soil matrix system. Lime stabilization is commonly and widely used for road pavements. According to findings of Bell [117] and Mukhtar et al. [118], the optimum percentage of lime (for pH = 12.4) ranges between 4% and 8%, depending upon the soil conditions and type of soil. However, if used in excess that is 6% and more, Tran et al. [119] emphasized that lime treatment may undergo significant reduction in compressive and shear strength (of up to 30%, or even more) because of requirement of large amount of water and higher initial porosity. As a result, the unconsumed hydrated lime becomes unreactive in the strength gain process [120]. Cement provides the highest strength among other CSMs, whereas lime containing excess of free lime is suitable for materials with PI > 10% as the free lime reacts with clay particles to reduce the plasticity. Lime cement blends are usually limited to stabilize materials with PI < 10%. The strength achieved depends on amount of stabilizing agent incorporated and the type of material treated. However, excessive cement may be detrimental for the subgrade performance as it could form semibrittle materials [13].

The results of XRD and XRF of lime-treated soils revealed the significant mineralogical changes upon treatment. The long-term strength is improved when curing is done, and the strength increase upon treatment of 4% lime in low swelling clays (i.e., kaolinite) is the highest in comparison to the lowest strength for the case of high swelling clay minerals (e.g., Mt). This is associated with the replacement of calcium hydroxide with calcium oxide at the early stages of lime mixing with the soil. According to Behnood [12], soil stabilization with lime in the regions exposed to severe weathering is less effective (at low lime content) because the beneficial effect of lime stabilization in reducing the swell potential of lime-treated soil is reduced in this condition. However, for many other scenarios, lime stabilization of expansive soils is still regarded as an effective approach to minimize the swelling potential. According to Dafalla et al. [104], when laminated clay is stabilized using lime, the PI value reduces more effectively for soils containing calcic Mt or sodic Mt than clays with kaolinite. However, Al-Rawas [71] argue that lime modification may be unsuitable for soils with content of Mt in excess of 40%, which is having 8% as the optimum lime dosage level. It is explained by the notion that, with increase in Mt percentage in the clay fraction, a simultaneous increase in volumetric strain is also accompanied, depicting the effect of mineralogical properties of expansive clay on long-term characteristics of chemical stabilizer materials. The microstructural characteristics indicate that PI is significantly increased with 8% lime due to [50] formation of C-S-H and C-A-H gels [117], which fill the pores in clays with discontinuous

structure [122] and (2) increase in calcium to silica ratio. According to Dash and Hussain [115], these studies are in good agreement with those observed for microstructural behavior of expansive soils. Thus, lime stabilization is feasible for SiO<sub>2</sub>-rich soils, soils having gypsum, and the soils containing iron with varying optimum percentage of lime for each, depending on presence of respective ingredient. However, in SO<sub>4</sub>-rich soils, the use of lime is not recommended since there is no hydrated calcium oxide available. Because when in absence of sulfates, the CEC of the soil greatly depends on its negatively charged particles [182]. Thus, it can be inferred that lime stabilization of expansive soils is mainly function of environment of lime-soil reactions and type of clay minerals.

For cement versus lime stabilization, it is often misinterpreted that both stabilizers are identical in yielding results in terms of C-S-H and C-A-H formation, but cement proves to be a relatively better choice. Few common characteristics related to the cement stabilization are briefly discussed. Cement assists in minimizing the toxicity level from certain wastes, for instance, agricultural or industrial waste, and causes reduction in PI and swell potential. Generally, 10% cement is considered as optimum for treating medium to high expansive soils, whereas the variation in improvement widely varies when it is used between 2–10% because of varying soil type, weathering effects, and period of curing. Cement is not used for soils with PI higher than 30%. Therefore, lime is usually added to the soil prior to cement mixing for workability. Cement reduces swell more effectively than lime does. It can be inferred that (i) the rate of decrease for both FS and  $P_s$  with the addition of 2% cement is significant. An increase up to 12% cement causes uniform and gradual reduction in  $P_s$  and a relatively non-uniform but a gradual decrease in FS. Also, the modification mechanism of cement and lime is more or less similar because C-S-H and C-A-H gels formation leads to cementitious links with the untreated expansive soil particles particularly containing organic matter. [183] A general increasing trend is observed in UCS values with higher CKD content along with the curing time for problematic soil (with a potential for a time-dependent increase in strength). So, strength increases with more curing. Therefore, further studies on longer curing times and possibly increased CKD contents are required. CKD, volcanic ash, and their mixes are helpful in reducing cost of construction of small-scale houses and pavements, in terms of strength and durability aspects [171]. It is important to mention here that blend of 5% lime and 3% cement will effectively reduce the PI by 60% and  $P_s$  by 82%. Thus, cement is more efficacious in controlling swell potential although the mechanism behind stabilizing soils by cement and lime follows a similar pattern and results in general.

Fly ash less than 50% is suffice for increasing the OMC and reducing the MDD in expansive soils, thereby achieving higher UCS and shear strength values. But a successful treatment requires an alkali activator due to the inherent lack of calcium oxide (less than 10%) in FA. It is said that 1% lime is suited for compensation, but the rate of increase of OMC and MDD is still important. While modifying the



capacity against expansion, FA is also proven to increase the strength of expansive soils, such as adding 10%. But an optimized dosage for a joint application, for example, both increasing UCS while reducing expansion is still open for further investigation leading to introduction of multipurpose FAs. To this end, modified FAs, such as CFA, FA-sand-marble dust, and variety of similar materials are incorporated to reduce the PI, FS, and  $P_s$  of soils as feasible mixtures in practice as, for example, in flexible pavement where both strength and expansion are significant.

The ground-granulated blast furnace slag is another highly cementitious one, and it also needs an activator, generally with lightweight alkali. GGBS lacks binder leading to a more CaO presence compared with lime which due to less cementitious nature has less CaO content. As a result, both GGBS and lime are used in conjunction, and it is established that 20% GGBS and 1% lime will effectively reduce LL and PI and increase the MDD, UCS, and C-S-H formation. The ground basic oxygen furnace slag (GBOFS) performs better than the GGBS. In a study by Goodarzi and Salimi [109], 10% GBOFS is sufficient to eliminate dispersion in soil, whereas a greater percentage of GGBS (i.e., 20–25%) is required for achieving the same impact. It is attributed to the lower activity (crystalline nature) of GGBS in contrast to that of GBOFS. One associated shortcoming is that the ultimate improvement in engineering properties requires still a higher percentage (15–20%) of GBOFS along with increased curing time [12].

Owing to its nonhazardous nature and suitability for road subgrades, bagasse ash alone used for stabilizing soil affects the durability. The improvement mechanism of BA resembles with that of cement stabilization. For better results, lime should be added to the BA. It is observed that 0.6% BA and 6.25% lime will increase the strength by 96% after curing for three days, suggesting that curing plays a major role. Indicating the fact that BA is a less effective stabilizer, its performance is highly improved when lime is added to it with increased curing.

## 7. Conclusions and Recommendations

This study reviews the trends in stabilization of low to high expansive soils with Ca-based materials (CSMs). The influence of the effectively proven CSMs on the engineering, geotechnical, and microstructural properties of expansive soils used in soil stabilization has been evaluated. In addition, the recent studies stressing the use of more environmentally friendly and nonconventional stabilization materials and techniques have also been discussed. In the light of discussions in this study, the main conclusions and findings are stated as follows:

- (1) The microstructure of expansive soil is a key parameter in evaluating the swell-shrink properties, compressive strength behavior, and the environmental potential in various soil stabilization projects. A successful and reliable choice of stabilizers should be on the basis of their subsequent effect on the microstructure.

- (2) Along with the microstructure effects, the rate of hydration and pozzolanic reactions in the polymerization process and cementation play a major role in the required duration and condition of soil curing. Before soil stabilization with the selected CSM, an optimum dosage and methodology of practical application on the host soil should be characterized.
- (3) In accordance with the past literature, Table 5 is created with the knowledge of the variety of expansive soils across the globe using different CSMs in order to quantify the main and interaction effects of the type of stabilizers in terms of the applicable host soil, optimum CSM dosage incorporated, and the associated improved properties.
- (4) Despite cement being the widely used CSM, considering the expenses and challenge of CO<sub>2</sub> emission and associated toxicity levels in treated soils, lime alongside other pozzolans (FA, BA, GGBS, CCR, GSA, and SSA in order of their practical efficiency) is more beneficial option for stabilizing expansive soils.

In addition, this study identifies research needs for future including energy perspectives with respect to sustainable local construction and developing a satisfactory protocol explaining the stabilization mechanisms. The search for choosing environmentally friendly biomaterials and numerous waste materials is still under investigation and is needed to maintain global sustainability standards.

## Conflicts of Interest

The authors declare that they have no conflicts of interest.

## Acknowledgments

The key project of the National Natural Science Foundation of China (Grant no. 41630633) is acknowledged for the financial support. The authors would like thank Professor Shui Long Shen for his motivation in writing this manuscript and Engr. Aminul Haque and Engr. Farjad Iqbal for their valuable comments in finalizing this review article. The authors also wish to thank the esteemed referees for providing insightful suggestions to improve this manuscript.

## References

- [1] L. C. Dang, B. Fatahi, and H. Khabbaz, "Behaviour of expansive soils stabilized with hydrated lime and bagasse fibres," *Procedia Engineering*, vol. 143, pp. 658–665, 2016.
- [2] H. King: *Expansive Soils and Expansive Clay: The Hidden Force behind Basement and Foundation Problems*, 2015, [http://www.coinspection.com/uploads/1/1/2/4/11243167/geology.com\\_articles\\_expansive-soil.pdf](http://www.coinspection.com/uploads/1/1/2/4/11243167/geology.com_articles_expansive-soil.pdf).
- [3] C. Rajakumar and T. Meenambal, "Experimental study of bagasse ash utilisation for road application on expansive soil," *Nature Environment & Pollution Technology*, vol. 14, no. 4, 2015.

- [4] S. A. Aiban, "Compressibility and swelling characteristics of Al-Khobar Palygorskite, eastern Saudi Arabia," *Engineering Geology*, vol. 87, no. 3-4, pp. 205–219, 2006.
- [5] B. Zhang, W. Shen, J. Wang, W. Zhang, W. Zhu, and Y. Liu, "Slight-expansive road base course binder: properties, hydration and performance," *Construction and Building Materials*, vol. 150, pp. 626–633, 2017.
- [6] G. M. S. Abdullah and H. I. Al-Abdul Wahhab, "Evaluation of foamed sulfur asphalt stabilized soils for road applications," *Construction and Building Materials*, vol. 88, pp. 149–158, 2015.
- [7] P. K. Gautam, P. Kalla, A. S. Jethoo, R. Agrawal, and H. Singh, "Sustainable use of waste in flexible pavement: a review," *Construction and Building Materials*, vol. 180, pp. 239–253, 2018.
- [8] H. Jiang, B. Wang, H. I. Inyang, J. Liu, K. Gu, and B. Shi, "Role of expansive soil and topography on slope failure and its countermeasures, Yun County, China," *Engineering Geology*, vol. 152, no. 1, pp. 155–161, 2013.
- [9] M. Gougazeh and A. Al-Shabatat, "Geological and geotechnical properties of soil materials at Tannur dam, Wadi Al Hasa, South Jordan," *Journal of Taibah University for Science*, vol. 7, no. 4, pp. 216–224, 2013.
- [10] T. M. Petry and D. N. Little, "Review of stabilization of clays and expansive soils in pavements and lightly loaded structures—history, practice, and future," *Journal of Materials in Civil Engineering*, vol. 14, no. 6, pp. 447–460, 2002.
- [11] K. B. Simons, "Limitations of residential structures on expansive soils," *Journal of Performance of Constructed Facilities*, vol. 5, no. 4, pp. 258–270, 1991.
- [12] A. Behnood, "Soil and clay stabilization with calcium- and non-calcium-based additives: a state-of-the-art review of challenges, approaches and techniques," *Transportation Geotechnics*, vol. 17, pp. 14–32, 2018.
- [13] C. Godenzoni: *Multiscale Rheological and Mechanical Characterization of Cold Mixtures*, 2017, [https://scholar.google.com/scholar?hl=en&as\\_sdt=0%2C5&q=Multiscale+Rheological+and+Mechanical+Characterization+of+Cold+Mixtures&btnG=](https://scholar.google.com/scholar?hl=en&as_sdt=0%2C5&q=Multiscale+Rheological+and+Mechanical+Characterization+of+Cold+Mixtures&btnG=).
- [14] K. Yan and L. Wu, "Swelling behavior of compacted expansive soils, recent advancement in soil behavior," in *Proceedings of the Situ Test Methods, Pile Foundations, and Tunneling: Selected Papers from the 2009 GeoHunan International Conference*, pp. 1–6, Changsha, China, August 2009.
- [15] C. C. Ikeagwani and D. C. Nwonu, "Emerging trends in expansive soil stabilisation: a review," *Journal of Rock Mechanics and Geotechnical Engineering*, vol. 11, no. 2, pp. 423–440, 2019.
- [16] I. Yilmaz and B. Civelekoglu, "Gypsum: an additive for stabilization of swelling clay soils," *Applied Clay Science*, vol. 44, no. 1-2, pp. 166–172, 2009.
- [17] C. Kurtulus, F. Sertcelik, M. M. Canbay, and İ. Sertcelik, "Estimation of Atterberg limits and bulk mass density of an expansive soil from P-wave velocity measurements," *Bulletin of Engineering Geology and the Environment*, vol. 69, no. 1, pp. 153–154, 2010.
- [18] P. Priyadharshini, K. Ramamurthy, and R. G. Robinson, "Reuse potential of stabilized excavation soil as fine aggregate in cement mortar," *Construction and Building Materials*, vol. 192, pp. 141–152, 2018.
- [19] M. L. Nehdi, "Clay in cement-based materials: critical overview of state-of-the-art," *Construction and Building Materials*, vol. 51, pp. 372–382, 2014.
- [20] E. Celik and Z. Nalbantoglu, "Effects of ground granulated blastfurnace slag (GGBS) on the swelling properties of lime-stabilized sulfate-bearing soils," *Engineering Geology*, vol. 163, pp. 20–25, 2013.
- [21] M. Sol-Sánchez, J. Castro, C. G. Ureña, and J. M. Azañón, "Stabilisation of clayey and marly soils using industrial wastes: pH and laser granulometry indicators," *Engineering Geology*, vol. 200, pp. 10–17, 2016.
- [22] M. F. Iqbal, Q.-F. Liu, I. Azim et al., "Prediction of mechanical properties of green concrete incorporating waste foundry sand based on gene expression programming," *Journal of Hazardous Materials*, vol. 384, p. 121322, 2020.
- [23] J. K. Mitchell and K. Soga, "Fundamentals of soil behavior," *Fundamentals of Soil Behavior*, Vol. 3, John Wiley & Sons, New York, NY, USA, 2005.
- [24] J. Nelson and D. J. Miller, *Expansive Soils: Problems and Practice in Foundation and Pavement Engineering*, John Wiley & Sons, Hoboken, NJ, USA, 1997.
- [25] D. Mašin and N. Khalili, "Swelling phenomena and effective stress in compacted expansive clays," *Canadian Geotechnical Journal*, vol. 53, no. 1, pp. 134–147, 2015.
- [26] Y. Xu, "Fractal model for the correlation relating total suction to water content of bentonites," *Fractals*, vol. 26, no. 3, Article ID 1850028, 2018.
- [27] V. Ouhadi and R. Yong, "The role of clay fractions of marly soils on their post stabilization failure," *Engineering Geology*, vol. 70, no. 3-4, pp. 365–375, 2003.
- [28] R. Katti, U. Kulkarni, A. Katti, and R. Kulkarni, "Stabilization of embankment on expansive soil—a case study," in *Proceedings of the Experimental and Applied Modeling of Unsaturated Soils GeoShanghai International Conference*, pp. 181–189, Shanghai, China, June 2010.
- [29] C. Shi, Y. Wu, C. Riefler, and H. Wang, "Characteristics and pozzolanic reactivity of glass powders," *Cement and Concrete Research*, vol. 35, no. 5, pp. 987–993, 2005.
- [30] L. Liu, "Prediction of swelling pressures of different types of bentonite in dilute solutions," *Colloids and Surfaces A: Physicochemical and Engineering Aspects*, vol. 434, pp. 303–318, 2013.
- [31] A. M. Awad, S. M. Shaikh, R. Jalab et al., "Adsorption of organic pollutants by natural and modified clays: a comprehensive review," *Separation and Purification Technology*, vol. 228, Article ID 115719, 2019.
- [32] Y.-J. Cui, "On the hydro-mechanical behaviour of MX80 bentonite-based materials," *Journal of Rock Mechanics and Geotechnical Engineering*, vol. 9, no. 3, pp. 565–574, 2017.
- [33] A. A. Boateng and D. A. Skeete, "Incineration of rice hull for use as a cementitious material: the Guyana experience," *Cement and Concrete Research*, vol. 20, no. 5, pp. 795–802, 1990.
- [34] S. Pourakbar, A. Asadi, B. B. K. Huat, and M. H. Fasihnikoutalab, "Stabilization of clayey soil using ultrafine palm oil fuel ash (POFA) and cement," *Transportation Geotechnics*, vol. 3, pp. 24–35, 2015.
- [35] V. Cantillo, V. Mercado, and C. Pájaro, "Empirical correlations for the swelling pressure of expansive clays in the city of Barranquilla, Colombia," *Earth Sciences Research Journal*, vol. 21, no. 1, pp. 45–49, 2017.
- [36] H. Elbadry, "Simplified reliable prediction method for determining the volume change of expansive soils based on simply physical tests," *HBRC Journal*, vol. 13, no. 3, pp. 353–360, 2017.

- [37] N. Huvaj and E. Uyeturk, "Effects of drying on atterberg limits of pyroclastic soils of northern Turkey," *Applied Clay Science*, vol. 162, pp. 46–56, 2018.
- [38] A. A. Basma, A. S. Al-Homoud, and A. Husein, "Laboratory assessment of swelling pressure of expansive soils," *Applied Clay Science*, vol. 9, no. 5, pp. 355–368, 1995.
- [39] H. Akgün, A. Günel Türkmenoğlu, A. Arslan Kelam, K. Yousefi-Bavil, G. Öner, and M. K. Koçkar, "Assessment of the effect of mineralogy on the geotechnical parameters of clayey soils: a case study for the Orta County, Çankırı, Turkey," *Applied Clay Science*, vol. 164, pp. 44–53, 2018.
- [40] E. Mehmood, M. Ilyas, and K. Farooq, "Effect of initial placement conditions on swelling characteristics of expansive soils," in *Proceedings of the Geo-Frontiers 2011: Advances in Geotechnical Engineering*, pp. 2397–2403, Dallas, TX, USA, March 2011.
- [41] B. Shi, H. Jiang, Z. Liu, and H. Fang, "Engineering geological characteristics of expansive soils in China," *Engineering Geology*, vol. 67, no. 1-2, pp. 63–71, 2002.
- [42] A. A. Al-Rawas, "The factors controlling the expansive nature of the soils and rocks of northern Oman," *Engineering Geology*, vol. 53, no. 3-4, pp. 327–350, 1999.
- [43] D. R. Katti, M. I. Matar, K. S. Katti, and P. M. Amarasinghe, "Multiscale modeling of swelling clays: a computational and experimental approach," *KSCE Journal of Civil Engineering*, vol. 13, no. 4, pp. 243–255, 2009.
- [44] K. Prakash and A. Sridharan, "Free swell ratio and clay mineralogy of fine-grained soils," *Geotechnical Testing Journal*, vol. 27, no. 2, pp. 220–225, 2004.
- [45] Y. Xu, "Peak shear strength of compacted GMZ bentonites in saline solution," *Engineering Geology*, vol. 251, pp. 93–99, 2019.
- [46] ASTM, *Standard Test Methods for One-Dimensional Swell or Settlement Potential of Cohesive Soils*, ASTM, West Conshohocken, PA, USA, 2003.
- [47] J. D. Nelson, K. C. Chao, D. D. Overton, and E. J. Nelson, *Foundation Engineering for Expansive Soils*, John Wiley & Sons, Hoboken, NJ, USA, 2015.
- [48] A. Aqeel, "Investigation of expansive soils in Obhor Sabkha, Jeddah-Saudi Arabia," *Arabian Journal of Geosciences*, vol. 9, no. 4, p. 314, 2016.
- [49] B. A. Hakami and E.-S. S. A. Seif, "Expansive potentiality of Sabkha soils of Rabigh Lagoon, Saudi Arabia: a case study," *Arabian Journal of Geosciences*, vol. 12, no. 4, p. 107, 2019.
- [50] I. M. Idriss and R. W. Boulanger, "SPT-based liquefaction triggering procedures," *Report UCD/CGM-10/02, Department of Civil and Environmental Engineering*, University of California, Davis, CA, USA, p. 259, 2010.
- [51] M. Labib and A. Nashed, "GIS and geotechnical mapping of expansive soil in Toshka region," *Ain Shams Engineering Journal*, vol. 4, no. 3, pp. 423–433, 2013.
- [52] A. Puppala, L. Hoyos, C. Viyanant, and C. Musenda, "Fiber and fly ash stabilization methods to treat soft expansive soils," in *Proceedings of the Soft Ground Technology*, pp. 136–145, Noordwijkerhout, Netherlands, May 2001.
- [53] M. M. Zumrawi, "Construction problems of light structures founded on expansive soils in Sudan," *International Journal of Science and Research (IJSR)*, vol. 4, no. 8, pp. 896–902, 2015.
- [54] A. Al-Swaidani, I. Hammoud, and A. Meziab, "Effect of adding natural pozzolana on geotechnical properties of lime-stabilized clayey soil," *Journal of Rock Mechanics and Geotechnical Engineering*, vol. 8, no. 5, pp. 714–725, 2016.
- [55] S. I. Cetiner, *Stabilization of Expansive Soils by Çayirhan Fly Ash and Desulphogypsum*, Middle East Technical University, Ankara, Turkey, 2004.
- [56] D. W. Smith, G. A. Narsilio, and P. Pivonka, "Numerical particle-scale study of swelling pressure in clays," *KSCE Journal of Civil Engineering*, vol. 13, no. 4, pp. 273–279, 2009.
- [57] Y. S. Wibowo, "Perilaku Sifat Fisik dan Keteknikaan Tanah residual Batuan Vulkanik Kwartier Di Daerah Cikijing, Majalengka, Jawa Barat," *RISSET Geologi Dan Pertambangan*, vol. 21, no. 2, pp. 131–139, 2011.
- [58] P. V. Muthyalu, K. Ramu, and G. P. Raju, "Study on performance of chemically stabilized expansive soil," *International Journal of Advances in Engineering & Technology*, vol. 2, no. 1, p. 139, 2012.
- [59] M. Malekzadeh and H. Bilsel, "Hydro-mechanical behavior of polypropylene fiber reinforced expansive soils," *KSCE Journal of Civil Engineering*, vol. 18, no. 7, pp. 2028–2033, 2014.
- [60] F. Mousavi, E. Abdi, and H. Rahimi, "Effect of polymer stabilizer on swelling potential and CBR of forest road material," *KSCE Journal of Civil Engineering*, vol. 18, no. 7, pp. 2064–2071, 2014.
- [61] H. Zhao, L. Ge, T. M. Petry, and Y.-Z. Sun, "Effects of chemical stabilizers on an expansive clay," *KSCE Journal of Civil Engineering*, vol. 18, no. 4, pp. 1009–1017, 2014.
- [62] M. Dafalla and M. Shamrani, "Road damage due to expansive soils: survey of the phenomenon and measures for improvement," in *Proceedings of the Design, Construction, Rehabilitation, and Maintenance of Bridges*, pp. 73–80, Hunan, China, 2011.
- [63] A. J. Puppala and A. Pedarla, "Innovative ground improvement techniques for expansive soils," *Innovative Infrastructure Solutions*, vol. 2, no. 1, p. 24, 2017.
- [64] A. Al-Taie, M. M. Disfani, R. Evans, A. Arulrajah, and S. Horpibulsuk, "Swell-shrink cycles of lime stabilized expansive subgrade," *Procedia Engineering*, vol. 143, pp. 615–622, 2016.
- [65] W. D. Lawson, *A Survey of Geotechnical Practice for Expansive Soils in Texas, Unsaturated Soils 2006*, American Society of Civil Engineers, Reston, VA, USA, 2006.
- [66] M. Iqbal, Q. Liu, and I. Azim, "Experimental study on the utilization of waste foundry sand as embankment and structural fill," in *Proceedings of the IOP Conference Series: Materials Science and Engineering*, Article ID 012042, Bangkok, Thailand, May 2019.
- [67] M. De Beer, *Aspects of the Design and Behaviour of Road Structures Incorporating Lightly Cementitious Layers*, University of Pretoria, Pretoria, South Africa, 2008.
- [68] H. Hasan, L. Dang, H. Khabbaz, B. Fatahi, and S. Terzaghi, "Remediation of expansive soils using agricultural waste bagasse ash," *Procedia Engineering*, vol. 143, pp. 1368–1375, 2016.
- [69] R. N. Yong and V. R. Ouhadi, "Experimental study on instability of bases on natural and lime/cement-stabilized clayey soils," *Applied Clay Science*, vol. 35, no. 3-4, pp. 238–249, 2007.
- [70] H. H. Adem and S. K. Vanapalli, "Review of methods for predicting in situ volume change movement of expansive soil over time," *Journal of Rock Mechanics and Geotechnical Engineering*, vol. 7, no. 1, pp. 73–86, 2015.
- [71] A. A. Al-Rawas, A. W. Hago, and H. Al-Sarmi, "Effect of lime, cement and Sarooj (artificial pozzolan) on the swelling potential of an expansive soil from Oman," *Building and Environment*, vol. 40, no. 5, pp. 681–687, 2005.

- [72] Y. Liu, Y. Su, A. Namdar et al., "Utilization of cementitious material from residual rice husk ash and lime in stabilization of expansive soil," *Advances in Civil Engineering*, vol. 2019, pp. 1–17, 2019.
- [73] M. M. Zumrawi, "Geotechnical aspects for roads on expansive soils," *International Journal of Scientific Research*, vol. 4, pp. 896–902, 2015.
- [74] C. Godenzoni, A. Graziani, E. Bocci, and M. Bocci, "The evolution of the mechanical behaviour of cold recycled mixtures stabilised with cement and bitumen: field and laboratory study," *Road Materials and Pavement Design*, vol. 19, no. 4, pp. 856–877, 2018.
- [75] M. A. Rahgozar, M. Saberian, and J. Li, "Soil stabilization with non-conventional eco-friendly agricultural waste materials: an experimental study," *Transportation Geotechnics*, vol. 14, pp. 52–60, 2018.
- [76] A. Kumar and D. Gupta, "Behavior of cement-stabilized fiber-reinforced pond ash, rice husk ash-soil mixtures," *Geotextiles and Geomembranes*, vol. 44, no. 3, pp. 466–474, 2016.
- [77] V. Ortega-López, J. M. Manso, I. I. Cuesta, and J. J. González, "The long-term accelerated expansion of various ladle-furnace basic slags and their soil-stabilization applications," *Construction and Building Materials*, vol. 68, pp. 455–464, 2014.
- [78] S. Horpibulsuk, C. Phetchuay, A. Chinkulkijniwat, and A. Cholaphatsorn, "Strength development in silty clay stabilized with calcium carbide residue and fly ash," *Soils and Foundations*, vol. 53, no. 4, pp. 477–486, 2013.
- [79] Y. Shang and Y. Fu, "Experimental study of the mechanical properties of expansive soil with added nanomaterials," *Arabian Journal of Geosciences*, vol. 11, no. 8, p. 180, 2018.
- [80] A. K. Sabat, "Statistical models for prediction of swelling pressure of a stabilized expansive soil," *Electronic Journal of Geotechnical Engineering*, vol. 17, pp. 837–846, 2012.
- [81] A. Graziani, C. Iafelice, S. Raschia, D. Perraton, and A. Carter, "A procedure for characterizing the curing process of cold recycled bitumen emulsion mixtures," *Construction and Building Materials*, vol. 173, pp. 754–762, 2018.
- [82] A. Graziani, C. Iafelice, S. Raschia, A. Carter, and D. Perraton, *A Laboratory Approach for Characterizing the Evolutive Behavior of Cold Recycled Mixtures*, 2018.
- [83] E. Otte, *A Structural Design Procedure for Cement-Treated Layers in Pavements*, University of Pretoria, Pretoria, South Africa, 2013.
- [84] A. Seco, F. Ramírez, L. Miqueleiz, and B. García, "Stabilization of expansive soils for use in construction," *Applied Clay Science*, vol. 51, no. 3, pp. 348–352, 2011.
- [85] M. R. Taha, "Geotechnical properties of soil-ball milled soil mixtures," in *Nanotechnology in Construction 3*, Z. Bittnar, P. J. M. Bartos, J. Němeček et al., Eds., pp. 377–382, Springer, Berlin, Germany, 2009.
- [86] R. P. Freitas, V. S. Felix, M. O. Pereira et al., "Micro-XRF analysis of a Brazilian polychrome sculpture," *Microchemical Journal*, vol. 149, p. 104020, 2019.
- [87] A. Modarres and Y. M. Nosoudy, "Clay stabilization using coal waste and lime—technical and environmental impacts," *Applied Clay Science*, vol. 116–117, pp. 281–288, 2015.
- [88] M. Khemissa and A. Mahamedi, "Cement and lime mixture stabilization of an expansive overconsolidated clay," *Applied Clay Science*, vol. 95, pp. 104–110, 2014.
- [89] K. M. A. Hossain, M. Lachemi, and S. Easa, "Stabilized soils for construction applications incorporating natural resources of Papua New Guinea," *Resources, Conservation and Recycling*, vol. 51, no. 4, pp. 711–731, 2007.
- [90] A. K. Sabat, "Engineering properties of an expansive soil stabilized with rice husk ash and lime sludge," *International Journal of Engineering and Technology*, vol. 5, no. 6, pp. 4826–4833, 2013.
- [91] B.-W. Yu, Y.-J. Du, F. Jin, and C.-Y. Liu, "Multiscale study of sodium sulfate soaking durability of low plastic clay stabilized by reactive magnesia-activated ground granulated blast-furnace slag," *Journal of Materials in Civil Engineering*, vol. 28, no. 6, Article ID 04016016, 2016.
- [92] A. Rana, P. Kalla, and L. J. Csetenyi, "Sustainable use of marble slurry in concrete," *Journal of Cleaner Production*, vol. 94, pp. 304–311, 2015.
- [93] F. Oriola and G. Moses, "Groundnut shell ash stabilization of black cotton soil," *Electronic Journal of Geotechnical Engineering*, vol. 15, no. 1, pp. 415–428, 2010.
- [94] K. M. A. Hossain and L. Mol, "Some engineering properties of stabilized clayey soils incorporating natural pozzolans and industrial wastes," *Construction and Building Materials*, vol. 25, no. 8, pp. 3495–3501, 2011.
- [95] A. K. Sharma and P. V. Sivapullaiah, "Ground granulated blast furnace slag amended fly ash as an expansive soil stabilizer," *Soils and Foundations*, vol. 56, no. 2, pp. 205–212, 2016.
- [96] J. M. Kate, "Strength and Volume Change Behavior of Expansive Soils Treated with Fly Ash," *Innovations in Grouting and Soil Improvement*, American Society of Civil Engineers, Reston, VA, USA, pp. 1–15, 2005.
- [97] P. Dahale, P. Nagarnaik, and A. Gajbhiye, "Effect OF flyash and lime on stabilization of expansive soil," *Journal on Civil Engineering*, vol. 6, no. 2, p. 8, 2016.
- [98] A. A. Al-Rawas, "Microfabric and mineralogical studies on the stabilization of an expansive soil using cement by-pass dust and some types of slags," *Canadian Geotechnical Journal*, vol. 39, no. 5, pp. 1150–1167, 2002.
- [99] S. Koliass, V. Kasselouri-Rigopoulou, and A. Karahalios, "Stabilisation of clayey soils with high calcium fly ash and cement," *Cement and Concrete Composites*, vol. 27, no. 2, pp. 301–313, 2005.
- [100] M. Dayioglu, B. Cetin, and S. Nam, "Stabilization of expansive Belle Fourche shale clay with different chemical additives," *Applied Clay Science*, vol. 146, pp. 56–69, 2017.
- [101] I. Akinwumi, "Soil modification by the application of steel slag," *Periodica Polytechnica Civil Engineering*, vol. 58, no. 4, pp. 371–377, 2014.
- [102] L.-W. Kong and A.-G. Guo, "Bearing strength and swelling behavior of jingmen expansive soil," in *Proceedings of the GeoFlorida 2010: Advances in Analysis, Modeling & Design*, pp. 2571–2580, Palm Beach, FL, USA, February 2010.
- [103] E. R. Sujatha, K. Dharini, and V. Bharathi, "Influence of groundnut shell ash on strength and durability properties of clay," *Geomechanics and Geoengineering*, vol. 11, no. 1, pp. 20–27, 2016.
- [104] M. Dafalla, E. Mutaz, and M. Al-Shamrani, "Compressive strength variations of lime-treated expansive soils," in *Proceedings of the International Foundations Congress and Equipment Expo*, pp. 1402–1409, San Antonio, TX, USA, March 2015.
- [105] T. Y. Elkady, "The effect of curing conditions on the unconfined compression strength of lime-treated expansive soils," *Road Materials and Pavement Design*, vol. 17, no. 1, pp. 52–69, 2016.

- [106] A. A. B. Moghal, B. C. S. Chittoori, and B. M. Basha, "Effect of fibre reinforcement on CBR behaviour of lime-blended expansive soils: reliability approach," *Road Materials and Pavement Design*, vol. 19, no. 3, pp. 690–709, 2018.
- [107] M. R. Hausmann, *Engineering Principles of Ground Modification*, McGraw-Hill, New York, Ny, USA, 1990.
- [108] D. Bergado, L. Anderson, N. Miura, and A. Balasubramaniam, *Soft Ground Improvement in Lowland and Other Environments*, ASCE, Reston, VA, USA, 1996.
- [109] A. R. Goodarzi and M. Salimi, "Stabilization treatment of a dispersive clayey soil using granulated blast furnace slag and basic oxygen furnace slag," *Applied Clay Science*, vol. 108, pp. 61–69, 2015.
- [110] F. G. Bell, *Engineering Treatment of Soils*, CRC Press, Boca Raton, FL, USA, 2014.
- [111] M. F. Javed, N. H. Ramli Sulong, S. A. Memon, S. K.-u. Rehman, and N. B. Khan, "Experimental and numerical study of flexural behavior of novel oil palm concrete filled steel tube exposed to elevated temperature," *Journal of Cleaner Production*, vol. 205, pp. 95–114, 2018.
- [112] T. Thyagaraj, S. M. Rao, P. Sai Suresh, and U. Salini, "Laboratory studies on stabilization of an expansive soil by lime precipitation technique," *Journal of Materials in Civil Engineering*, vol. 24, no. 8, pp. 1067–1075, 2012.
- [113] T. Olinic and E. Olinic, "The effect of quicklime stabilization on soil properties," *Agriculture and Agricultural Science Procedia*, vol. 10, pp. 444–451, 2016.
- [114] L. Ali and Z. Zafar, "Construction on expansive soils in semi arid zone," in *Proceedings of the Instrumentation, Testing, and Modeling of Soil and Rock Behavior*, American Society of Civil Engineers, Hunan, China, June 2011.
- [115] S. K. Dash and M. Hussain, "Lime stabilization of soils: reappraisal," *Journal of Materials in Civil Engineering*, vol. 24, no. 6, pp. 707–714, 2011.
- [116] Y. Cheng, S. Wang, J. Li, X. Huang, C. Li, and J. Wu, "Engineering and mineralogical properties of stabilized expansive soil compositing lime and natural pozzolans," *Construction and Building Materials*, vol. 187, pp. 1031–1038, 2018.
- [117] F. G. Bell, "Lime stabilization of clay minerals and soils," *Engineering Geology*, vol. 42, no. 4, pp. 223–237, 1996.
- [118] M. Al-Mukhtar, S. Khat tab, and J.-F. Alcover, "Micro-structure and geotechnical properties of lime-treated expansive clayey soil," *Engineering Geology*, vol. 139–140, pp. 17–27, 2012.
- [119] S. Horpibulsuk, R. Rachan, A. Chinkulkijniwat, Y. Raksachon, and A. Suddepong, "Analysis of strength development in cement-stabilized silty clay from micro-structural considerations," *Construction and Building Materials*, vol. 24, no. 10, pp. 2011–2021, 2010.
- [120] A. M. Idris and A. A. El-Zahhar, "Indicative properties measurements by SEM, SEM-EDX and XRD for initial homogeneity tests of new certified reference materials," *Microchemical Journal*, vol. 146, pp. 429–433, 2019.
- [121] R. L. Buhler and A. B. Cerato, "Stabilization of Oklahoma expansive soils using lime and class C FLY ash," in *Proceedings of the Problematic Soils and Rocks and in Situ Characterization*, pp. 1–10, Denver, Co, USA, February 2007.
- [122] C. Shi, "Studies on several factors affecting hydration and properties of lime-pozzolan cements," *Journal of Materials in Civil Engineering*, vol. 13, no. 6, pp. 441–445, 2001.
- [123] M. M. Zumrawi and A. A.-A. Babikir, "Laboratory study of steel slag used for stabilizing expansive soil," *University Of Khartoum Engineering Journal*, vol. 6, no. 2, 2017.
- [124] G. Constantinides, "Nanoscience and nanoengineering of cement-based materials," in *Nanotechnology in Eco-Efficient Construction*, Elsevier, Amsterdam, Netherlands, 2013.
- [125] A. Jamshidi, K. Kurumisawa, T. Nawa, and T. Igarashi, "Performance of pavements incorporating waste glass: the current state of the art," *Renewable and Sustainable Energy Reviews*, vol. 64, pp. 211–236, 2016.
- [126] A. Grilli, E. Bocci, and A. Graziani, "Influence of reclaimed asphalt content on the mechanical behaviour of cement-treated mixtures," *Road Materials and Pavement Design*, vol. 14, no. 3, pp. 666–678, 2013.
- [127] A. S. Zaimoglu, "Optimization of unconfined compressive strength of fine-grained soils modified with polypropylene fibers and additive materials," *KSCE Journal of Civil Engineering*, vol. 19, no. 3, pp. 578–582, 2015.
- [128] M. Schneider, M. Romer, M. Tschudin, and H. Bolio, "Sustainable cement production-present and future," *Cement and Concrete Research*, vol. 41, no. 7, pp. 642–650, 2011.
- [129] Z. He, X. Zhu, J. Wang, M. Mu, and Y. Wang, "Comparison of CO<sub>2</sub> emissions from OPC and recycled cement production," *Construction and Building Materials*, vol. 211, pp. 965–973, 2019.
- [130] S. Saride, S. R. Chikyala, A. J. Puppala, and P. J. Harris, "Effects of organics on stabilized expansive subgrade soils," in *Proceedings of the Ground Improvement and Geosynthetics*, pp. 155–164, Conshohocken, PA, USA, 2010.
- [131] M. Turkoz and H. Tosun, "The use of methylene blue test for predicting swell parameters of natural clay soils," *Scientific Research and Essays*, vol. 6, no. 8, pp. 1780–1792, 2011.
- [132] M. Rahman, S. Rehman, and O. Al-Amoudi, "Literature review on cement kiln dust usage in soil and waste stabilization and experimental investigation," *International Journal of Research and Reviews in Applied Sciences*, vol. 7, no. 1, pp. 77–87, 2011.
- [133] R. A. Shawabkeh, "Solidification and stabilization of cadmium ions in sand-cement-clay mixture," *Journal of Hazardous Materials*, vol. 125, no. 1–3, pp. 237–243, 2005.
- [134] S. Peethamparan and J. Olek, "Study of the effectiveness of cement kiln dusts in stabilizing Na-Montmorillonite clay," *Journal of Materials in Civil Engineering*, vol. 20, no. 2, pp. 137–146, 2008.
- [135] S. Peethamparan, J. Olek, and J. Lovell, "Influence of chemical and physical characteristics of cement kiln dusts (CKDs) on their hydration behavior and potential suitability for soil stabilization," *Cement and Concrete Research*, vol. 38, no. 6, pp. 803–815, 2008.
- [136] S. L. Cui, J. D. Wang, X. D. Wang, Y. F. Du, and X. P. Wang, "Mechanical behavior and micro-structure of cement kiln dust-stabilized expansive soil," *Arabian Journal of Geosciences*, vol. 11, no. 17, p. 521, 2018.
- [137] D.-F. Lin, K.-L. Lin, M.-J. Hung, and H.-L. Luo, "Sludge ash/hydrated lime on the geotechnical properties of soft soil," *Journal of Hazardous Materials*, vol. 145, no. 1–2, pp. 58–64, 2007.
- [138] Q.-Y. Ma, Z.-M. Cao, and P. Yuan, "Experimental research on microstructure and physical-mechanical properties of expansive soil stabilized with fly ash, sand, and basalt fiber," *Advances in Materials Science and Engineering*, vol. 2018, Article ID 9125127, 13 pages, 2018.
- [139] F. E. Jalal, K. Shahzada, S. Saeed, I. Ahmad, and K. Khan, "Stabalization of medium expansive soils in Pakistan using marble industrial waste and bagasse ash," *International Journal of Earth Sciences and Engineering*, vol. 10, no. 4, pp. 885–891, 2017.



- [140] R. Alavéz-Ramírez, P. Montes-García, J. Martínez-Reyes, D. C. Altamirano-Juárez, and Y. Gochi-Ponce, "The use of sugarcane bagasse ash and lime to improve the durability and mechanical properties of compacted soil blocks," *Construction and Building Materials*, vol. 34, pp. 296–305, 2012.
- [141] C. Okagbue and T. Onyeobi, "Potential of marble dust to stabilise red tropical soils for road construction," *Engineering Geology*, vol. 53, no. 3-4, pp. 371–380, 1999.
- [142] A. Mahamedi and M. Khemissa, "Stabilization of an expansive overconsolidated clay using hydraulic binders," *HBRC Journal*, vol. 11, no. 1, pp. 82–90, 2015.
- [143] J. D. J. A. Baldovino, R. L. D. S. Izzo, E. B. Moreira, and J. L. Rose, "Optimizing the evolution of strength for lime-stabilized rammed soil," *Journal of Rock Mechanics and Geotechnical Engineering*, vol. 11, no. 4, pp. 882–891, 2019.
- [144] L.-X. Mao, Z. Hu, J. Xia et al., "Multi-phase modelling of electrochemical rehabilitation for ASR and chloride affected concrete composites," *Composite Structures*, vol. 207, pp. 176–189, 2019.
- [145] Q. T. Phung, N. Maes, and S. Seetharam, "Pitfalls in the use and interpretation of TGA and MIP techniques for Ca-leached cementitious materials," *Materials & Design*, vol. 182, p. 108041, 2019.
- [146] F. S. Pereira, E. R. deAzevedo, E. F. da Silva et al., "Study of the carbon dioxide chemical fixation-activation by guanidines," *Tetrahedron*, vol. 64, no. 43, pp. 10097–10106, 2008.
- [147] A. Dulaimi, H. A. Nageim, F. Ruddock, and L. Seton, "Performance analysis of a cold asphalt concrete binder course containing high-calcium fly ash utilizing waste material," *Journal of Materials in Civil Engineering*, vol. 29, no. 7, Article ID 04017048, 2017.
- [148] S.-G. Lu, F.-F. Sun, and Y.-T. Zong, "Effect of rice husk biochar and coal fly ash on some physical properties of expansive clayey soil (Vertisol)," *Catena*, vol. 114, pp. 37–44, 2014.
- [149] ASTM, *Standard Specification for Coal Fly Ash and Raw or Calcined Natural Pozzolan for Use in Concrete*, ASTM, West Conshohocken, PA, USA, 2012.
- [150] Q. Zeng, K. Li, T. Fen-chong, and P. Dangla, "Determination of cement hydration and pozzolanic reaction extents for fly-ash cement pastes," *Construction and Building Materials*, vol. 27, no. 1, pp. 560–569, 2012.
- [151] B. Lin and A. B. Cerato, "Applications of SEM and ESEM in microstructural investigation of shale-weathered expansive soils along swelling-shrinkage cycles," *Engineering Geology*, vol. 177, pp. 66–74, 2014.
- [152] B. R. Phani Kumar and R. S. Sharma, "Effect of fly ash on engineering properties of expansive soils," *Journal of Geotechnical and Geoenvironmental Engineering*, vol. 130, no. 7, pp. 764–767, 2004.
- [153] S. Kommu, S. S. Asadi, and A. V. S. Prasad, "Leaching behavior and strength characteristics of black cotton soil stabilized with fly ash," *Materials Today: Proceedings*, vol. 5, no. 9, pp. 17974–17981, 2018.
- [154] A. R. Pourkhorshidi, M. Najimi, T. Parhizkar, F. Jafarpour, and B. Hillemeier, "Applicability of the standard specifications of ASTM C618 for evaluation of natural pozzolans," *Cement and Concrete Composites*, vol. 32, no. 10, pp. 794–800, 2010.
- [155] C. Gupta and R. K. Sharma, "Influence of marble dust, fly ash and beas sand on sub grade characteristics of expansive soil," *Journal of Mechanical and Civil Engineering*, pp. 13–18, 2014.
- [156] D. C. Sekhar and S. Nayak, "Utilization of granulated blast furnace slag and cement in the manufacture of compressed stabilized earth blocks," *Construction and Building Materials*, vol. 166, pp. 531–536, 2018.
- [157] M. Temimi, M. A. Rahal, M. Yahiaoui, and R. Jauberthie, "Recycling of fly ash in the consolidation of clay soils," *Resources, Conservation and Recycling*, vol. 24, no. 1, pp. 1–6, 1998.
- [158] I. Azim, J. Yang, S. Bhatta, F. Wang, and Q.-f. Liu, "Factors influencing the progressive collapse resistance of RC frame structures," *Journal of Building Engineering*, p. 100986, 2019.
- [159] P. Sivapullaiah, *Use of Solid Waste to Enhance Properties of Problematic Soil of Karnataka*, Indian Institute of Science, Bangalore, India, 2014.
- [160] N.-J. Jiang, Y.-J. Du, and K. Liu, "Durability of lightweight alkali-activated ground granulated blast furnace slag (GGBS) stabilized clayey soils subjected to sulfate attack," *Applied Clay Science*, vol. 161, pp. 70–75, 2018.
- [161] A. A. Ashango and N. R. Patra, "Behavior of expansive soil treated with steel slag, rice husk ash, and lime," *Journal of Materials in Civil Engineering*, vol. 28, no. 7, Article ID 06016008, 2016.
- [162] J. T. Hatmoko and H. Suryadharma, "Shear behavior of calcium carbide residue - bagasse ash stabilized expansive soil," *Procedia Engineering*, vol. 171, pp. 476–483, 2017.
- [163] M. De Beer, *Behaviour of Cementitious Subbase Layers in Bitumen Base Road Structures*, University of Pretoria, Pretoria, South Africa, 2009.
- [164] K. Ganesan, K. Rajagopal, and K. Thangavel, "Evaluation of bagasse ash as supplementary cementitious material," *Cement and Concrete Composites*, vol. 29, no. 6, pp. 515–524, 2007.
- [165] W. Fedrigo, A. T. Visser, W. J. Steyn, and W. P. Núñez, "Flexural behaviour of lightly Cement stabilised materials: South Africa and Brazil," *Road Materials and Pavement Design*, pp. 1–26, 2019.
- [166] K. C. P. Faria, R. F. Gurgel, and J. N. F. Holanda, "Recycling of sugarcane bagasse ash waste in the production of clay bricks," *Journal of Environmental Management*, vol. 101, pp. 7–12, 2012.
- [167] L. D. Nguyen, B. Fatahi, and H. Khabbaz, "A constitutive model for cemented clays capturing cementation degradation," *International Journal of Plasticity*, vol. 56, pp. 1–18, 2014.
- [168] A. K. Yadav, K. Gaurav, R. Kishor, and S. Suman, "Stabilization of alluvial soil for subgrade using rice husk ash, sugarcane bagasse ash and cow dung ash for rural roads," *International Journal of Pavement Research and Technology*, vol. 10, no. 3, pp. 254–261, 2017.
- [169] S. Horpibulsuk, C. Phetchuay, and A. Chinkulkijniwat, "Soil stabilization by calcium carbide residue and fly ash," *Journal of Materials in Civil Engineering*, vol. 24, no. 2, pp. 184–193, 2011.
- [170] C. Subhacini, M. Ranjitha, S. Dhanapal, and K. A. Prakash, "Expansive soil stabilization using waste from sugarcane Industry," *Journal for Studies in Management and Planning*, vol. 1, no. 3, pp. 345–352, 2015.
- [171] K. Somna, C. Jaturapitakkul, and P. Kajitvichyanukul, "Microstructure of calcium carbide residue-ground fly ash paste," *Journal of Materials in Civil Engineering*, vol. 23, no. 3, pp. 298–304, 2010.
- [172] S. Vichan and R. Rachan, "Chemical stabilization of soft Bangkok clay using the blend of calcium carbide residue and biomass ash," *Soils and Foundations*, vol. 53, no. 2, pp. 272–281, 2013.

- [173] A. K. Sabat, "Utilization of bagasse ash and lime sludge for construction of flexible pavements in expansive soil areas," *Electronic Journal of Geotechnical Engineering*, vol. 17, pp. 1037–1046, 2012.
- [174] B. Madhusudhana, "A survey on area, production and productivity of groundnut crop in India," *IOSR Journal of Economics and Finance*, vol. 1, no. 3, pp. 1–7, 2013.
- [175] N. Gajera, K. Thanki, N. Gajera, and K. Thanki, "Stabilization analysis of black cotton soil by using groundnut shell ash," *International Journal for Innovative Research in Science & Technology*, vol. 2, no. 1, pp. 158–162, 2015.
- [176] K. Venkatraman, P. Dayakar, R. Venkatakrishnaiah, and B. BIST, "Study ON effect OF groundnut shell ash IN index properties OF clay soil," *International Journal of Pure and Applied Mathematics*, vol. 119, no. 12, pp. 9265–9277, 2018.
- [177] M. H. Zhang, R. Lastra, and V. M. Malhotra, "Rice-husk ash paste and concrete: some aspects of hydration and the microstructure of the interfacial zone between the aggregate and paste," *Cement and Concrete Research*, vol. 26, no. 6, pp. 963–977, 1996.
- [178] A. Kampala and S. Horpibulsuk, "Engineering properties of silty clay stabilized with calcium carbide residue," *Journal of Materials in Civil Engineering*, vol. 25, no. 5, pp. 632–644, 2012.
- [179] D. C. Su and J. W. C. Wong, "Chemical speciation and phytoavailability of Zn, Cu, Ni and Cd in soil amended with fly ash-stabilized sewage sludge," *Environment International*, vol. 29, no. 7, pp. 895–900, 2004.
- [180] M. M. Ai-sharif and M. F. Attom, "A geoenvironmental application of burned wastewater sludge ash in soil stabilization," *Environmental Earth Sciences*, vol. 71, no. 5, pp. 2453–2463, 2014.
- [181] L. Chen and D.-F. Lin, "Stabilization treatment of soft subgrade soil by sewage sludge ash and cement," *Journal of Hazardous Materials*, vol. 162, no. 1, pp. 321–327, 2009.
- [182] H. Gadouri, K. Harichane, and M. Ghrici, "Effect of sodium sulphate on the shear strength of clayey soils stabilised with additives," *Arabian Journal of Geosciences*, vol. 10, no. 10, p. 218, 2017.
- [183] W. Gong, Y. M. Tien, C. H. Juang, J. R. Martin II, and J. Zhang, "Calibration of empirical models considering model fidelity and model robustness—focusing on predictions of liquefaction-induced settlements," *Engineering Geology*, vol. 203, pp. 168–177, 2016.

## Research Article

# Property Improvement of Cement Emulsified Asphalt Paste Modified by Graphene Oxide

Yu-wei Ma, Hong-yan Zhao, Gang Li , Zhen-jun Wang, Hua Tang, and Ai-qin Wang

*College of Water Conservancy and Architectural Engineering, Shihezi University, Shihezi 832000, China*

Correspondence should be addressed to Gang Li; [gangli@shzu.edu.cn](mailto:gangli@shzu.edu.cn)

Received 9 December 2019; Accepted 20 January 2020; Published 7 March 2020

Guest Editor: Jian Ouyang

Copyright © 2020 Yu-wei Ma et al. This is an open access article distributed under the Creative Commons Attribution License, which permits unrestricted use, distribution, and reproduction in any medium, provided the original work is properly cited.

Cement emulsified asphalt paste (CEAP) is widely used as a construction and building material by combining the advantages of cement rigidity and asphalt flexibility. However, the properties of CEAP can be evidently reduced due to the addition of emulsified asphalt. In this work, graphene oxide (GO) was prepared by the Hummers method and was innovatively used to improve the workability and strength of CEAP. The viscosity of CEAP was tested by Brookfield viscometer. In addition, the effects of GO on the setting time of CEAP were studied. The adsorption between cement and asphalt with GO was tested through an ultraviolet-visible spectrophotometer and the stability of CEAP was tested by zeta potentiometer. The effects of GO on the strength of CEAP were studied. The reinforcement effects of GO on CEAP were analyzed. The results show that the viscosity of CEAP and cement hydration products can increase after adding a reasonable dosage of GO to CEAP. The setting time of CEAP first decreases and then increases with the increase of GO dosage. The adsorption and viscosity of cement and asphalt increase with the increase of GO dosage. GO can reduce CEAP stability and make the paste easier to agglomerate. The flexural strength and the compressive strength of CEAP at 28 curing days first increase and then decrease with the increase of GO dosage, but excessive GO can hinder cement hydration. The reasonable dosage of GO in CEAP can be determined as 0.06% in asphalt weight.

## 1. Introduction

Cement emulsified asphalt paste (CEAP) is widely used as a construction and building material, which has the rigidity of cement-based materials and flexibility of asphalt-based materials [1–3]. The addition of emulsified asphalt into cement can significantly improve many properties of cement material, such as rheological performance and elasticity [4, 5]. However, the addition of emulsified asphalt can affect the cement hydration process and decrease the mechanical strength of mixtures [6–9]. At present, the main improvement technique is to add reinforcing materials, such as rebar, reinforcing fibers and inorganic binders, and slag powder.

Graphene oxide (GO) is an oxide of graphene and it is usually in the form of a solution, powder, or flake [10–12]. Its structure contains a hydroxyl group (-OH), carboxyl group (-COOH), epoxy group (-O-), and other hydrophilic groups [13]. GO can evenly disperse in aqueous solution due to the electrostatic repulsion between functional groups [14, 15].

GO has been applied in wide fields for its properties are more active than graphene. The properties of cement-based composites can be improved by the reaction between active functional groups [16]. Some researchers have found that the fluidity of cement paste was decreased and the compressive strength and flexural strength were improved with the addition of GO [17–20]. The compressive strength and flexural strength of cement-based materials are increased by 38.9% and 60.7%, respectively, when the dosage of GO is 0.03% [21, 22]. GO can influence the microscopic morphology of cement hydrates and make it regularly grow with GO as a template [23]. GO can improve the freeze-thaw cycle resistance of cement-based materials [24]. In addition, the setting time of cement can be shortened by 30 min when the dosage of GO is 0.05% in cement weight [18, 25]. In addition, GO can promote the cement hydration and improve the workability of cement-based composites [26–29]. GO affects not only cement-based materials but also emulsified asphalt. GO can promote the demulsification of oil in the water

system; the demulsification efficiency was as high as 99.94% when the dosage of GO was about 30 mg/L [30, 31]. GO can improve the high and low-temperature properties of asphalt and the aging resistance of asphalt [32, 33]. In addition, GO can enhance the rutting resistance of asphalt [34].

In this work, GO was adopted to solve the problem of strength reduction of CEAP. The improvement effect of GO on CEAP was studied. The microscopic morphology of cement hydrates before and after adding GO was compared. The effect of GO on the viscosity and setting time of CEAP was tested. The influence of GO on adsorption between cement and emulsified asphalt was studied by ultraviolet-visible spectrophotometer. Then, the influence of GO on the stability of CEAP was tested by the zeta potentiometer. Finally, the influence of GO on the mechanical properties of CEAP was studied. The results of this work can effectively solve the problem of low strength of CEAP and provide a theoretical basis for improving the properties of CEAP.

## 2. Raw Materials and Experiments

**2.1. Raw Materials.** Ordinary Portland cement was used in this work and its physical and chemical properties are shown in Table 1. Original asphalt was used to prepare emulsified asphalt and its physical and chemical properties are shown in Table 2. The properties of emulsified asphalt are shown in Table 3, which can meet with *The Technical Specification for Construction of Highway Asphalt Pavements in China (JTG F40-2004)*.

### 2.2. Experiment Methods

**2.2.1. Preparation and Characterization of GO.** In this work, the Hummers method was adopted to prepare GO. The experimental process was divided into three stages by different temperatures: low-temperature stage, medium temperature stage, and high-temperature stage. The GO preparation process was as follows: (a) low-temperature stage: the flake graphene,  $\text{NaNO}_3$ , and  $\text{KMnO}_4$  were added to a beaker with concentrated  $\text{H}_2\text{SO}_4$  under stirring in a preprepared ice-water bath, and the reactive temperature was maintained at about  $4^\circ\text{C}$  for 90 min; (b) medium temperature stage: the reaction temperature was increased to  $37^\circ\text{C}$  and stirring process was continued for 30 min; (c) high-temperature stage: 46 mL water was added to the beaker and the reaction temperature was increased to  $98^\circ\text{C}$ . Then, 10 mL  $\text{H}_2\text{O}_2$  (30% concentration) was slowly added in order to ensure that graphite is fully oxidized and the reaction is sustained for 20 min. Finally, GO specimens were obtained after washing and drying. The preparation schematic diagram of GO prepared by the Hummers method is shown in Figure 1. As can be seen from Figure 2, the prepared GO samples by the Hummers method can show a lamellar structure.

**2.2.2. Preparation of GO-Modified Asphalt Emulsion.** The preparation chart of GO-modified asphalt emulsion is shown in Figure 3. Water ( $60^\circ\text{C}$ ), emulsifier, and  $\text{CaCl}_2$

stabilizer were weighed and mixed, and then the pH of the mixtures was adjusted to 2–3 with hydrochloric acid. Emulsified asphalt can be obtained by pouring the prepared emulsified soap into the colloid mill and then the weighed original asphalt was slowly poured into the colloid mill. The emulsified asphalt was added to the mixer and then GO was added to obtain GO-modified asphalt emulsion. In this work, 0.02%, 0.04%, 0.06%, 0.08%, and 0.10% GO in asphalt weight was used to prepare GO-modified asphalt emulsion, respectively. The mix proportion of GO-modified emulsified asphalt is shown in Table 4.

**2.2.3. Preparation of GO-Modified CEAP.** The dosage of GO-modified asphalt emulsion was 8.0% in cement weight in CEAP [28]. The water-cement ratio in CEAP was 0.38. The water consumption of emulsified asphalt was included in the total water consumption. The specimens were placed at room temperature to cure for 24 h; then the CEAP specimens were cured for 28 days at the temperature of  $20^\circ\text{C}$  and the humidity of 90%. The mix proportion of CEAP is shown in Table 5. The laboratory tests of CEAP conducted in this work are shown in Table 6.

**2.2.4. ESEM Test.** In this work, firstly, a small number of samples were ground into fine powders with a mortar and then pasted on the conductive adhesive. The conductivity of the samples is improved after the gold spraying treatment. Finally, the microscopy morphology of CEAP was studied with the environmental scanning electron microscope (ESEM) with observing the microscopic morphology of paste before and after adding GO with 0.06% in asphalt weight. The ESEM test was carried out at the resolution of 1 nm and the temperature of  $20^\circ\text{C}$ .

**2.2.5. Viscosity Test.** According to *Standard Test Methods of Bitumen and Bituminous Mixtures for Highway Engineering (JTG E20-2011)*, the Brookfield rotational viscometer was used to test the viscosity of CEAP with different dosages of GO at initial, 30 min, and 60 min setting time. The 21# standard rotor was used in the test; the rotator speed was 50r/min and the sample was weighed  $8.5 \pm 0.5$  g for each test. The test temperature was  $20^\circ\text{C}$  and the resolution was 0.01 Pa·s. The average results of three samples from each group were adopted as the testing results.

**2.2.6. Setting Time Tests.** The setting process of CEAP consists of two stages, initial setting and final setting. The influences of GO on the initial and final setting time of CEAP were tested in accordance with *Test Methods for Water Requirement of Normal Consistency, Setting Time and Soundness of the Portland Cement (GB/T 1346-2011)*.

**2.2.7. Adsorption Test.** Adsorption between cement and asphalt emulsion with different asphalt emulsion concentrations was measured by ultraviolet-visible spectrophotometer. The absorbance of emulsified asphalt with different

TABLE 1: Properties of ordinary Portland cement.

Setting time (min)		Flexural strength (MPa)		Compressive strength (MPa)		Main chemical composition (%)	
Initial	Final	3 days	28 days	3 days	28 days	CaO	SiO <sub>2</sub>
140	271	3.8	6.9	18.1	45.2	60.1	20.8

TABLE 2: Properties of original asphalt.

Penetration (25°C, 0.1 mm)	Ductility (15°C, cm)	Softening point (°C)	Solubility (%)	Flash Point (°C)	Density (g/cm <sup>3</sup> )	Wax content (%)
65.0	15.0	45.2	99.6	265.0	1.03	2.37

TABLE 3: Properties of asphalt emulsion.

Evaporation residue content (%)	Residue on 1.18 mm sieve (%)	Penetration of residue (25°C, 0.1 mm)	Softening point of residue (°C)	Ductility of residue (cm, 15°C)	Storage stability (% at 25°C)	
					1d	5d
60.9	0.04	77.1	45.7	49.8	0.4	2.2

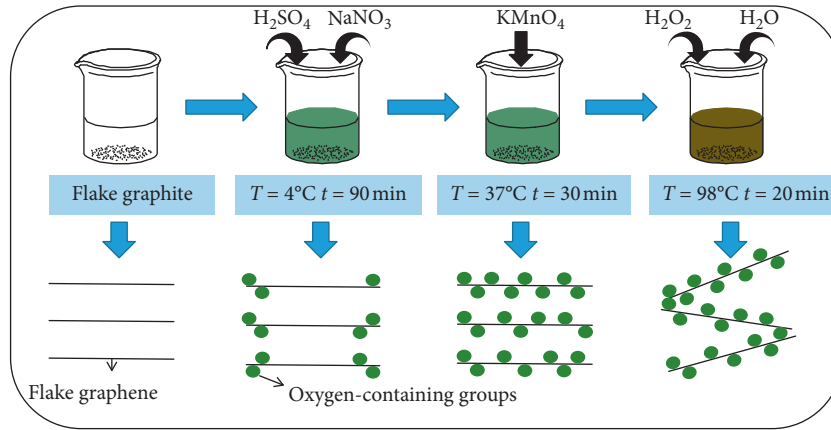


FIGURE 1: Schematic diagram of GO preparation by Hummers method.

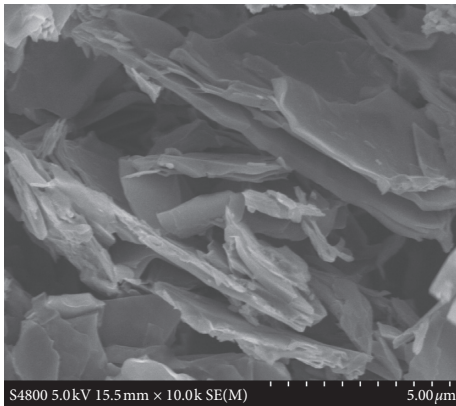


FIGURE 2: ESEM picture of graphene oxide.

concentrations was measured at 750 nm wavelength [35]. When the function had fitted, the emulsified asphalt was firstly prepared and the absorbance was measured to obtain its concentration. Then, cement was added to the emulsion of emulsified asphalt. The supernatant fluid concentration

was tested after the paste was stirred and allowed to stand for 30 minutes. Finally, the adsorption rate between cement and emulsified asphalt can be calculated by

$$D = \frac{10m_1}{m_2} \times (c_1 - c_2), \quad (1)$$

where  $D$  is the adsorption rate between cement and asphalt emulsion (mg/g),  $m_1$  is emulsified asphalt weight (g),  $m_2$  is cement weight (g),  $c_1$  is the initial concentration of emulsified asphalt (%), and  $c_2$  is the concentration of emulsified asphalt at one moment (30 min, in this work) (%). The adsorption test process is shown in Figure 4.

**2.2.8. Zeta Potential Test.** The stability of CEAP suspension was evaluated by measuring the surface charge of particles. CEAP with different GO dosages was used to obtain zeta potential by zeta potential test. The effect of different GO dosages on the stability of CEAP was also analyzed. The potential test was carried out at the temperature of 20°C.



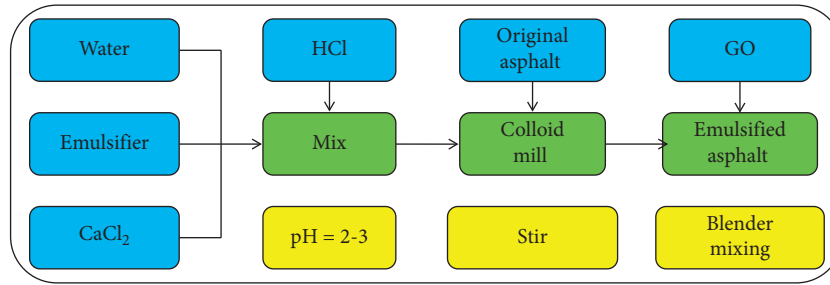


FIGURE 3: Preparation chart of GO-modified asphalt emulsion.

TABLE 4: Mix proportion of GO-modified emulsified asphalt.

GO dosage (%)	Original asphalt (g)	Water (g)	GO dosage (g)
0.02	600	400	0.12
0.04	600	400	0.24
0.06	600	400	0.36
0.08	600	400	0.48
0.10	600	400	0.60

TABLE 5: The mix proportion of CEAP.

GO (%)	Cement (g)	Water (g)	GO-modified emulsified asphalt		
			Asphalt (g)	Water (g)	GO (g)
0.02	1350	469.8	64.8	43.2	0.013
0.04	1350	469.8	64.8	43.2	0.026
0.06	1350	469.8	64.8	43.2	0.039
0.08	1350	469.8	64.8	43.2	0.052
0.10	1350	469.8	64.8	43.2	0.065

TABLE 6: The laboratory tests of CEAP.

Laboratory tests	Properties	Objectives
ESEM test	Micromorphology	Effects of GO on the morphology of the paste
Viscosity test	Viscosity	Effects of GO on the adsorption between cement and asphalt
Setting time test	Setting time	Effects of GO on cement hydration and asphalt demulsification
Adsorption test	Adsorption	Effects of GO on adsorption between cement and asphalt
Zeta potential test	Stability	Effects of GO on the stability of the paste
Mechanical property tests	Mechanical properties	Effects of GO on mechanical properties of the paste

**2.2.9. Mechanical Property Tests.** The specimens with sizes of 40 mm × 40 mm × 160 mm were prepared for strength tests, such as flexural strength and compressive strength. The flexural strength and compressive strength of CEAP were tested according to *Method of Testing Cements-Determination of Strength (GB/T17671-1999)*. The flexural strength and the compressive strength of CEAP were tested three times and six times, respectively, and the average value was adopted as the test result.

### 3. Results and Discussion

**3.1. Viscosity Test Results.** The adsorption between cement and asphalt is closely related to the stability of CEAP. The stronger the adsorption between cement and asphalt, the

faster hydration of cement and the demulsification of emulsified asphalt, and the greater the viscosity of the paste. Therefore, the adsorption between cement and asphalt can be characterized by testing the viscosity of the paste. The adsorptions between cement and asphalt with different GO dosages can be reflected by the viscosity of CEAP.

Figure 5 shows the viscosity of paste increases with the increase of GO dosage at initial, 30 min, and 60 min setting time. The phenomenon can be explained by the following reasons. GO can be evenly dispersed in the paste. GO can result in the aggregation of free water and promote cement hydration. The addition of GO can also absorb the free water, which can result in the difference of the free water concentration in the paste and promote the demulsification of emulsified asphalt. In addition, the asphalt can wrap the

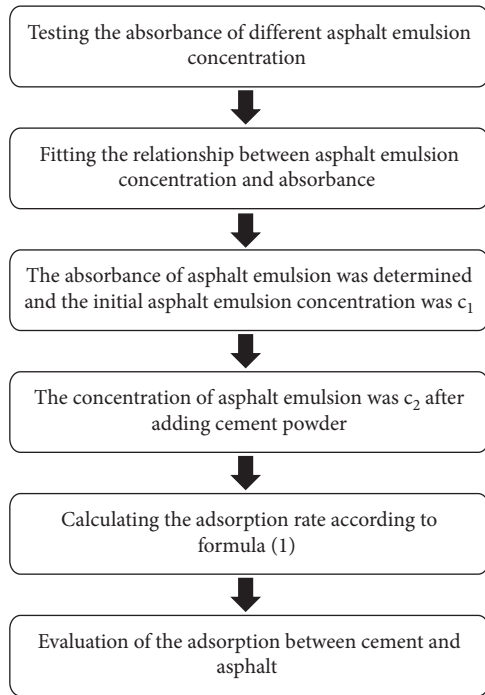


FIGURE 4: The process for the adsorption test.

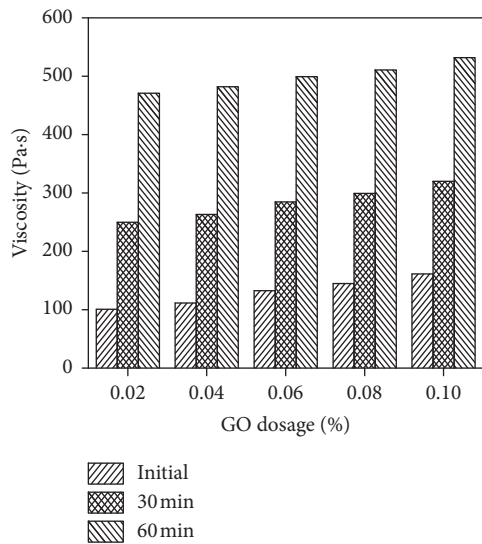


FIGURE 5: Viscosity of CEAP with different GO dosage.

cement hydration products, which can form a complex spatial network structure. Therefore, the viscosity of CEAP is increased.

**3.2. Setting Time Test Results.** The setting time has an important influence on the strength development of CEAP. When the flexible emulsified asphalt is added to the rigid cement paste, the setting time of cement paste can be increased. However, the addition of GO can shorten the setting time of cement-based materials. Therefore, the effect of GO on the setting time of CEAP was studied.

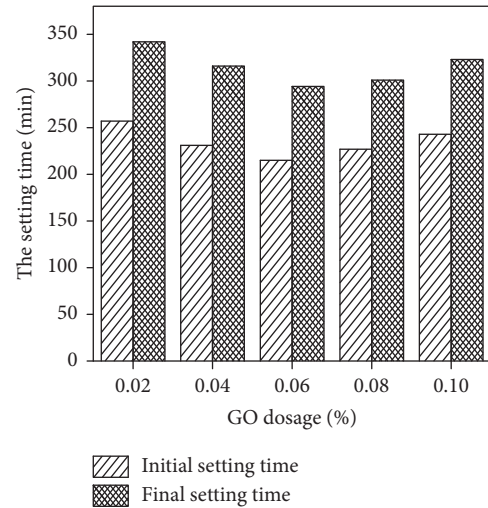


FIGURE 6: Setting time of CEAP with different GO dosages.

The setting time test results of CEAP with different dosages of GO are shown in Figure 6. It shows that the initial and final setting time of CEAP first decreases and then increases with the increase of GO dosage. Some reasons can be used to explain this phenomenon. The effect of GO on cement is higher than that of GO on emulsified asphalt when the dosage of GO is little. The free water in the paste is agglomerated and the cement hydration is promoted due to lots of hydrophilic groups on the surface of GO. Consequently, the setting time of CEAP is decreased. However, the effect of GO on emulsified asphalt is higher than that of GO on cement when the dosage of GO increases (more than 0.06% in asphalt weight). The difference in free water concentration caused by GO can promote emulsified asphalt demulsification, hinder cement hydration, and increase the setting time of CEAP.

**3.3. Absorptions in GO-Modified CEAP.** Figure 7 shows the absorbance results of CEAP at different asphalt emulsion concentrations. The concentration of asphalt emulsion can be obtained from Figure 7 through testing the absorbance of the solution. The absorbance increases gradually with the increase of asphalt emulsion concentration. It is mainly due to the increase of asphalt emulsion concentration, the increase of asphalt concentration, and the thickness of asphalt film in the solution. At the same time, the absorbance increased with the increase of GO dosage. This phenomenon can be explained by these reasons. On the one hand, the increase of GO dosage can result in the increase of solution concentration; on the other hand, GO can promote the demulsification of emulsified asphalt and reduce the intensity of refraction light. As a result, the absorbance between cement and emulsified asphalt increases.

The fitting curve expression of emulsified asphalt with different GO dosages and the corresponding absorbance values are shown in Table 7. It shows that the  $(c_1 - c_2)$  value of CEAP increases with the increase of GO dosage. In other words, the adsorption of cement and asphalt increases with the increase of GO dosage. Therefore, the addition of GO is

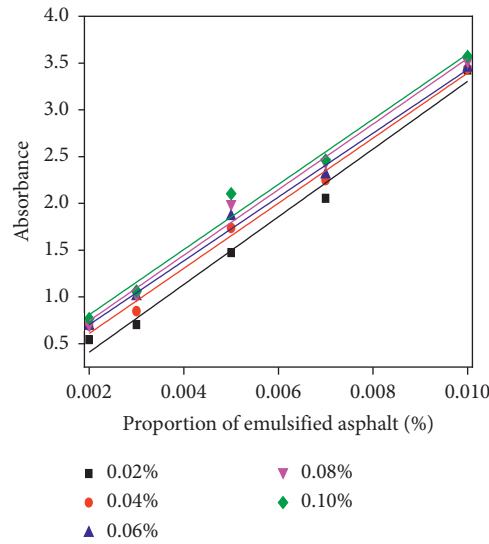


FIGURE 7: Absorbance results of CEAP with different emulsified asphalt concentrations.

TABLE 7: Effects of GO on absorption between cement and emulsified asphalt.

GO dosage (%)	Regression curve	Absorbance		Proportion of emulsified asphalt (%)		$(c_1 - c_2)$ (%)
		Mixed cement	Unmixed cement	Mixed cement	Unmixed cement	
0.02	$y = 362.08x - 0.32$	0.762762	0.735821	0.00299	0.00292	0.00008
0.04	$y = 348.13x - 0.09$	0.859808	0.811187	0.00273	0.00259	0.00014
0.06	$y = 341.08x + 0.02$	0.997323	0.875902	0.00287	0.00251	0.00036
0.08	$y = 350.74x + 0.04$	1.103588	0.902976	0.00303	0.00246	0.00057
0.10	$y = 348.66x + 0.11$	1.342773	1.130586	0.00354	0.00293	0.00062

helpful to the combination of asphalt and cement. The interaction among GO, cement, and emulsified asphalt is shown in Figure 8. GO has numbers of active functional groups on its surface, which can generate physical and chemical reactions between GO and asphalt molecules and increase the combination between GO and asphalt. In addition, cement hydrates can grow around with GO as the template and the combination between GO and cement hydrates can increase [36]. Therefore, GO is equivalent to a bridge connecting cement and emulsified asphalt to strengthen the combination between cement and asphalt. Consequently, GO can increase the adsorption between cement and asphalt.

**3.4. Stability of CEAP.** Workability stability is an important parameter to evaluate the performance of CEAP. The potential of CEAP with different GO dosages was tested by zeta potentiometer and the results are shown in Figure 9. It shows that the zeta potential value decreases with the increase of GO dosage. It indicates that the stability of CEAP is decreased with the increase of GO dosage and the paste is more condensable. Some reasons can explain this phenomenon. Firstly, for the presence of oxygen-containing functional groups on the surface of GO, it is easy to absorb ions or cement particles with opposite charges in CEAP to generate agglomeration and flocculation, which can reduce the stability of the paste. Secondly, GO can adsorb water molecules

and promote the cement hydration process in cement materials.

At the same time, GO also can adsorb ions with opposite charges in cement to cause agglomeration and flocculation of cement particles. When GO adsorbs water molecules, hydration products preferentially form polyhedral structure. Then, the cement hydration products grow around with the polyhedral structure as the template. The grown cement hydration products can shield the attraction of GO to opposite charges and can reduce the agglomeration and flocculation of the paste. Finally, GO can cause agglomeration and flocculation of cement particles and can affect the cement hydration, which can decrease the workability stability of CEAP. In other words, CEAP is easier to agglomerate.

**3.5. Mechanical Properties of CEAP.** Flexural strength and compressive strength test results of CEAP cured at 28 days are shown in Figure 10. It shows that the flexural and compressive strength of CEAP first increases and then decreases with the increase of GO dosage. The addition of GO can improve the flexural and compressive strength of CEAP. The flexural and compressive strength of CEAP can reach the maximum value when the dosage of GO is 0.06% in asphalt weight.

The microstructures of CEAP before and after adding 0.06% GO were observed by ESEM and the results are shown

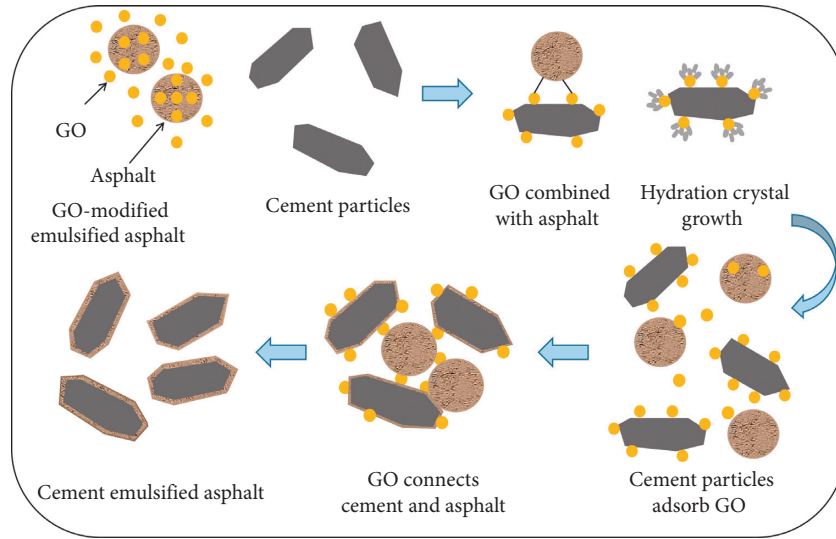


FIGURE 8: Diagrammatic sketch of absorption in CEAP.

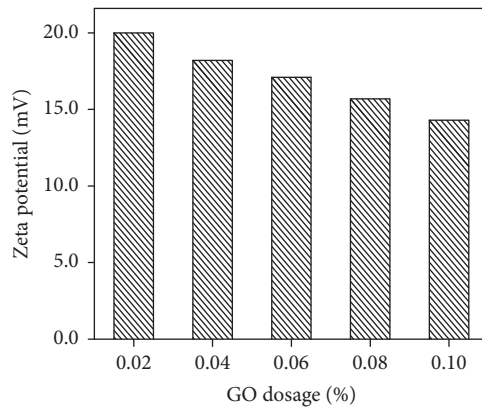


FIGURE 9: Zeta potential of CEAP with different GO dosages.

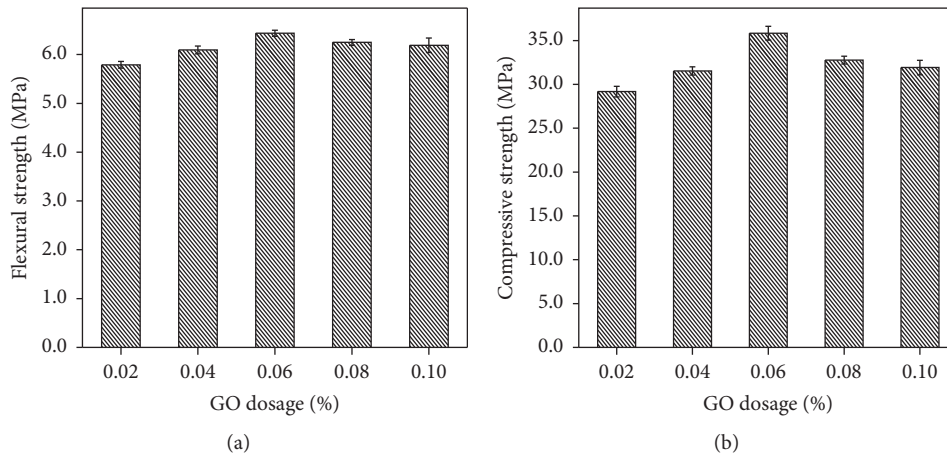


FIGURE 10: Effects of GO on the strength of CEAP. (a) Flexural strength. (b) Compressive strength.

in Figure 11. In contrast to the microscopic morphology of CEAP before and after adding GO, it is found that there are some cracks and fewer hydration products. A part of cement

particles is wrapped with asphalt and there exists loose structure in CEAP without GO. However, the number of cracks decreases, the hydration products increases, and the

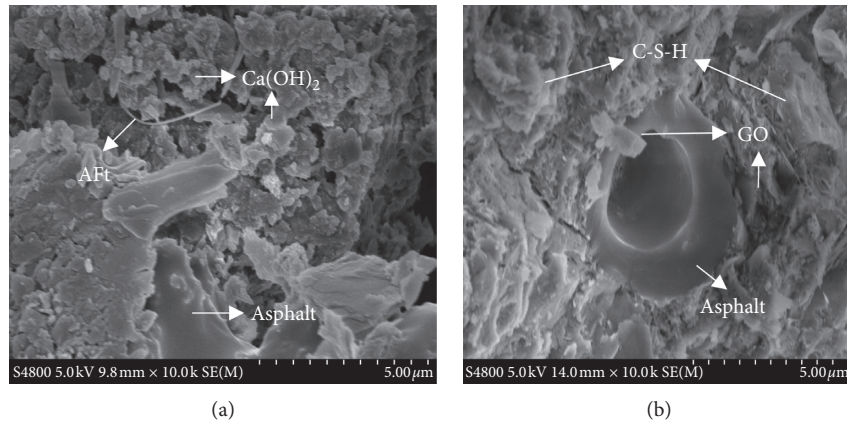


FIGURE 11: ESEM pictures of CEAP: (a) without GO and (b) with GO.

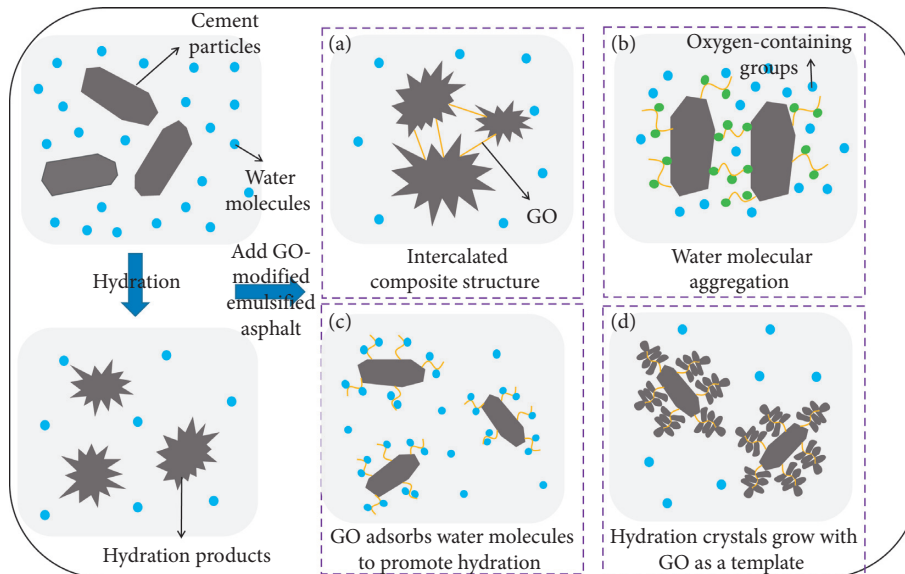


FIGURE 12: Diagrammatic sketch of interaction between GO and cement emulsified asphalt.

structure becomes denser when GO is added in CEAP. The reason is that GO can promote cement hydration and increase the cement hydration products in CEAP. Therefore, GO can improve the flexural and compressive strength of CAEP.

**3.6. Mechanism of GO-Modified CEAP.** GO is easy to form intercalation structure with cement hydration products, which can increase the properties of CEAP. The reasons are that the strong oxidant gradually adsorbs on the edge of graphite, oxidizes, and intercalates the edge part in the low-temperature reaction. A part of intermolecular forces is gradually destroyed and the oxygen-containing functional groups are generated. The reaction temperature is increased after the low-temperature oxidation. The oxidation and intercalation ability of strong oxidant is gradually enhanced with the increase of reaction temperature. More oxygen-containing functional groups are generated between graphite sheets, which put forward the foundation for the

stripping of graphite sheets. The residual intermolecular forces are destroyed after the addition of deionized water and hydrogen peroxide in the high-temperature stage, which can make the graphite sheets strip “to” which will peel off the graphite sheets. The increase of the active sites of GO will increase the reaction with cement paste.

In addition, it is easy to form an intercalated composite structure with hydration products to increase the properties of CEAP, due to the high strength and flexibility of GO. The electrostatic interaction between oxygen-containing groups on the GO surface and cement particles results in agglomeration and flocculation. The free water of the system is lost because this function requires a large amount of free water. Therefore, the friction between the cement particles is increased, the fluidity of CEAP is decreased, the setting time is shortened, and the strength of CEAP is increased. GO adsorbs water molecules in cement paste after adding GO. It leads to aggregation of free water and promotes cement hydration reaction [16]. In addition, the oxygen-containing functional groups of GO can react with the reactive groups



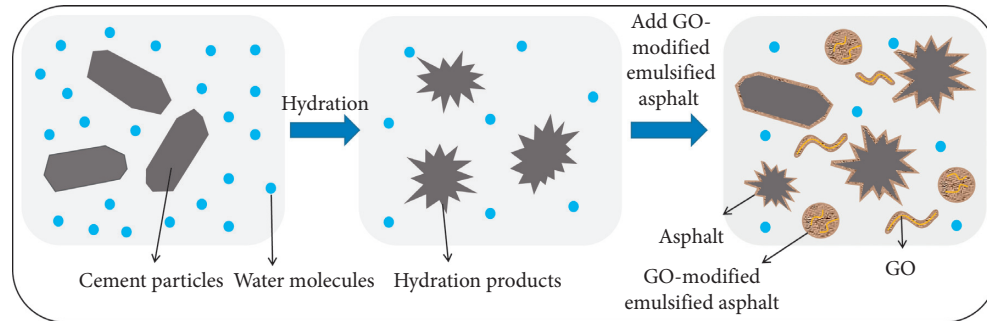


FIGURE 13: Diagrammatic sketch of GO influence on CEAP.

$C_3S$ ,  $C_3A$ ,  $C_2S$ , and  $C_4AF$  in the cement to form hydrated crystals in the process of the hydration process. The hydration products are preferentially fixed on the GO sheet and the cement hydration products grow continuously around GO template. Interwoven, cross-linked, dense, and uniform network structure is formed, which can increase the properties of CEAP [21].

The interaction between GO and cement emulsified asphalt binders in CEAP is shown in Figure 12. Cement hydration can produce amounts of calcium hydroxide, which causes the cement paste to be alkaline. GO is agglomerated due to the difference of pH value in the alkaline paste, which can result in the uneven dispersion of GO in CEAP and can affect the mechanical properties of the paste. However, GO can be evenly dispersed in emulsified asphalt due to the existence of hydrophilic groups on the surface of GO.

However, the properties of CEAP decrease with the increase of GO dosage again. As can be seen from Figure 13, the nonhydrated cement particles and hydration products are covered by GO, which can hinder the cement hydration and reduce the properties of CEAP. In addition, redundant GO is encapsulated in asphalt particles, which cannot make contact with cement and reduce the strengthening effect of GO on CEAP. Therefore, the mechanical properties of CEAP are reduced.

#### 4. Conclusions and Recommendations

In this work, GO was prepared by the Hummers method and it was adopted in emulsified asphalt to prepare GO-modified emulsified asphalt. Then, the GO-modified asphalt emulsion was used to prepare CEAP. The effects of GO on the viscosity and setting time of CEAP were tested and analyzed. The influences of GO on properties of CEAP were analyzed with microcharacterizations, such as an ultraviolet-visible spectrophotometer, zeta potentiometer, and ESEM. In addition, the strengthening effect of GO on CEAP was tested. Finally, the mechanism of GO-modified CEAP was analyzed. The following conclusions are drawn:

- (1) The viscosity and setting time of CEAP with different dosage GO was tested. The results show that the viscosity of CEAP increases with the increase of the GO dosage. The setting time of CEAP first decreases

and then increases with the increase of GO dosage. Therefore, a small amount of GO can promote cement hydration. However, it can also promote the emulsified asphalt demulsification and hinder the cement hydration with the increase of GO dosage.

- (2) The adsorption between cement and emulsified asphalt with GO was tested by an ultraviolet-visible spectrophotometer. The results show that the adsorption between cement and emulsified asphalt increases with the increase of the GO dosage. Therefore, the addition of GO is beneficial to form reinforcing binders by promoting the combination of cement and asphalt.
- (3) The zeta potential decreases with the increase of the GO dosage, which indicates that the stability of CEAP decreases. GO can adsorb the oppositely charged particles in the paste, which can result in agglomeration and flocculation of cement particles. Therefore, GO can reduce the stability of the CEAP and make the paste easier to agglomerate.
- (4) The flexural strength and compressive strength of CEAP first increase and then decrease with the increase of the GO dosage. GO can improve the strength of CEAP through promoting the growth of cement hydration products. However, the flexural strength and compressive strength decrease because excessive GO can result in the emulsified asphalt demulsification and then can hinder the cement hydration.
- (5) GO with suitable dosage can improve the viscosity, setting time, and stability of CEAP and increase the strength of hardened CEAP. According to the test results of the workability and mechanical properties of CEAP, the reasonable dosage of GO in CEAP is determined and recommended as 0.06% in asphalt weight.

#### Data Availability

All data generated or analyzed during this study are included in this article.

#### Conflicts of Interest

There are no conflicts of interest regarding the publication of this paper.

## Acknowledgments

This work was supported by the Science and Technology Development Project of the Xinjiang Production and Construction Corps (no. 2019AB013).

## References

- [1] X.-t. Qin, S.-y. Zhu, S.-f. Chen, X. Li, and H.-b. Dou, "Comparative study on the deformation behaviors of cement emulsified asphalt mortars," *Materials and Structures*, vol. 48, no. 10, pp. 3241–3247, 2015.
- [2] T. Rutherford, Z. Wang, X. Shu, B. Huang, and D. Clarke, "Laboratory investigation into mechanical properties of cement emulsified asphalt mortar," *Construction and Building Materials*, vol. 65, pp. 76–83, 2014.
- [3] Z. Wang, N. Dai, X. Wang, J. Zhang, and H. Guo, "Laboratory investigation on effects of microwave heating on early strength of cement bitumen emulsion mixture," *Construction and Building Materials*, vol. 236, Article ID 117439, 2020.
- [4] Y. Du, L. Kong, and T. Wei, "Laboratory investigation into early-age strength improvement of cold recycled asphalt mixture containing asphalt emulsion and cement," *Advances in Civil Engineering*, vol. 2019, pp. 1–10, 2019.
- [5] S. Al-Merzah, S. Al-Busaltan, and A. N. Hassan, "Characterizing cold bituminous emulsion mixtures comprised of palm leaf ash," *Journal of Materials in Civil Engineering*, vol. 31, no. 6, Article ID 04019069, 2019.
- [6] X. Yan, Z. Wang, M. Rao, and M. Li, "Investigation of cement-emulsified asphalt in plastic concrete," *Advances in Materials Science and Engineering*, vol. 2018, Article ID 3929682, 13 pages, 2018.
- [7] T. Ma, H. Wang, Y. Zhao, X. Huang, and Y. Pi, "Strength mechanism and influence factors for cold recycled asphalt mixture," *Advances in Materials Science and Engineering*, vol. 2015, Article ID 181853, 10 pages, 2015.
- [8] J. Ouyang, W. Yang, J. Chen, B. Han, Y. Meng, and T. Tang, "Effect of superplasticizer and wetting agent on the pavement properties of cold recycled mixture with bitumen emulsion and cement," *Advances in Materials in Civil Engineering*, vol. 2020, Article ID 6251653, 11 pages, 2020.
- [9] J. Ouyang, J. Zhao, and Y. Tan, "Modeling mechanical properties of cement asphalt emulsion mortar with different asphalt to cement ratios and temperatures," *Journal of Materials in Civil Engineering*, vol. 30, no. 10, Article ID 04018263, 2018.
- [10] L. Chen, Y. Li, Q. Du et al., "High performance agar/graphene oxide composite aerogel for methylene blue removal," *Carbohydrate Polymers*, vol. 155, pp. 345–353, 2017.
- [11] M. S. Usman, M. Z. Hussein, S. Fakurazi, and F. F. A. Saad, "Gadolinium-based layered double hydroxide and graphene oxide nano-carriers for magnetic resonance imaging and drug delivery," *Chemistry Central Journal*, vol. 11, no. 1, pp. 275–278, 2017.
- [12] R. Wang, J. Yue, R. Li, and Y. Sun, "Evaluation of aging resistance of asphalt binder modified with graphene oxide and carbon nanotubes," *Journal of Materials in Civil Engineering*, vol. 31, no. 11, Article ID 04019274, 2019.
- [13] V. Kumar Gupta, S. Agarwal, M. Asif, A. Fakhri, and N. Sadeghi, "Application of response surface methodology to optimize the adsorption performance of a magnetic graphene oxide nanocomposite adsorbent for removal of methadone from the environment," *Journal of Colloid and Interface Science*, vol. 497, pp. 193–200, 2017.
- [14] V. Loryuenyong, K. Totepvimarn, P. Eimburanapratvat, W. Boonchompoo, and A. Buasri, "Preparation and characterization of reduced graphene oxide sheets via water-based exfoliation and reduction methods," *Advances in Materials Science and Engineering*, vol. 2013, Article ID 923403, 5 pages, 2013.
- [15] L. Liu, L. Wang, J. Gao, J. Zhao, X. Gao, and Z. Chen, "Amorphous structural models for graphene oxides," *Carbon*, vol. 50, no. 4, pp. 1690–1698, 2012.
- [16] A. Mohammed, J. G. Sanjayan, W. H. Duan, and A. Nazari, "Incorporating graphene oxide in cement composites: a study of transport properties," *Construction and Building Materials*, vol. 84, pp. 341–347, 2015.
- [17] F. Babak, H. Abolfazl, R. Alimorad, and G. Parviz, "Preparation and mechanical properties of graphene oxide: cement nanocomposites," *The Scientific World Journal*, vol. 2014, Article ID 276323, 10 pages, 2014.
- [18] Q. Wang, J. Wang, C.-x. Lu, B.-w. Liu, K. Zhang, and C.-z. Li, "Influence of graphene oxide additions on the microstructure and mechanical strength of cement," *New Carbon Materials*, vol. 30, no. 4, pp. 349–356, 2015.
- [19] Z. Lu, D. Hou, L. Meng, G. Sun, L. Cong, and Z. Li, "Mechanism of cement paste reinforced by graphene oxide/carbon nanotubes composites with enhanced mechanical properties," *RSC Advances*, vol. 5, no. 5, pp. 100598–100605, 2015.
- [20] W. Li, X. Li, S. J. Chen et al., "Effects of graphene oxide on early-age hydration and electrical resistivity of Portland cement paste," *Construction and Building Materials*, vol. 136, pp. 506–514, 2017.
- [21] S. Lv, Y. Ma, C. Qiu, T. Sun, J. Liu, and Q. Zhou, "Effect of graphene oxide nanosheets of microstructure and mechanical properties of cement composites," *Construction and Building Materials*, vol. 49, pp. 121–127, 2013.
- [22] K. Gong, Z. Pan, A. H. Korayem et al., "Reinforcing effects of graphene oxide on portland cement paste," *Journal of Materials in Civil Engineering*, vol. 27, no. 2, Article ID A4014010, 2014.
- [23] L. Lu and D. Ouyang, "Properties of cement mortar and ultra-high strength concrete incorporating graphene oxide nanosheets," *Nanomaterials*, vol. 7, no. 7, p. 187, 2017.
- [24] A. Mohammed, J. G. Sanjayan, W. H. Duan, and A. Nazari, "Graphene oxide impact on hardened cement expressed in enhanced freeze-thaw resistance," *Journal of Materials in Civil Engineering*, vol. 28, no. 9, Article ID 04016072, 2016.
- [25] Z. Lu, D. Hou, H. Ma, T. Fan, and Z. Li, "Effects of graphene oxide on the properties and microstructures of the magnesium potassium phosphate cement paste," *Construction and Building Materials*, vol. 119, pp. 107–112, 2016.
- [26] W.-J. Long, J.-J. Wei, H. Ma, and F. Xing, "Dynamic mechanical properties and microstructure of graphene oxide nanosheets reinforced cement composites," *Nanomaterials*, vol. 7, no. 12, p. 407, 2017.
- [27] X. Li, C. Li, Y. Liu et al., "Improvement of mechanical properties by incorporating graphene oxide into cement mortar," *Mechanics of Advanced Materials and Structures*, vol. 25, no. 15-16, pp. 1313–1322, 2016.
- [28] O. Xu, Z. Wang, and R. Wang, "Effects of aggregate gradations and binder contents on engineering properties of cement emulsified asphalt mixtures," *Construction and Building Materials*, vol. 135, pp. 632–640, 2017.
- [29] W. Li, X. Li, S. J. Chen, G. Long, Y. M. Liu, and H. Wen, "Effects of nanoalumina and graphene oxide on early-age hydration and mechanical properties of cement paste,"

- Journal of Materials in Civil Engineering*, vol. 29, no. 9, Article ID 04017087, 2017.
- [30] J. Liu, X. Li, W. Jia, Z. Li, Y. Zhao, and S. Ren, "Demulsification of crude oil-in-water emulsions driven by graphene oxide nanosheets," *Energy & Fuels*, vol. 29, no. 7, pp. 4644–4653, 2015.
  - [31] J. Liu, H. Wang, X. Li, W. Jia, Y. Zhao, and S. Ren, "Recyclable magnetic graphene oxide for rapid and efficient demulsification of crude oil-in-water emulsion," *Fuel*, vol. 189, pp. 79–87, 2017.
  - [32] W. Zeng, S. Wu, L. Pang, Y. Sun, and Z. Chen, "The utilization of graphene oxide in traditional construction materials: Asphalt," *Materials*, vol. 10, no. 1, p. 48, 2017.
  - [33] S. Wu, Z. Zhao, Y. Li, L. Pang, S. Amirkhanian, and M. Riara, "Evaluation of aging resistance of graphene oxide modified asphalt," *Applied Sciences*, vol. 7, no. 7, p. 702, 2017.
  - [34] K. Liu, K. Zhang, and X. Shi, "Performance evaluation and modification mechanism analysis of asphalt binders modified by graphene oxide," *Construction and Building Materials*, vol. 163, pp. 880–889, 2018.
  - [35] Z. Wang, H. Wang, T. Zhang, and C. Xu, "Investigation on absorption performance between cement and emulsified asphalt with UV-Vis spectrophotometer," *Construction and Building Materials*, vol. 136, pp. 256–264, 2017.
  - [36] M. Wang, R. Wang, H. Yao, Z. Wang, and S. Zheng, "Adsorption characteristics of graphene oxide nanosheets on cement," *RSC Advances*, vol. 6, no. 68, pp. 63365–63372, 2016.

## Research Article

# Rheological Properties Comparing Hot and Cold Bituminous Mastics Containing Jet Grouting Waste

Rosa Veropalumbo <sup>1</sup>, Francesca Russo <sup>1</sup>, Nunzio Viscione<sup>1,2</sup>,  
and Salvatore A. Biancardo <sup>1</sup>

<sup>1</sup>Department of Civil, Architectural and Environmental Engineering, Federico II University of Naples, Via Claudio 21, 80125 Naples, Italy

<sup>2</sup>Iterchimica Srl, Via Guglielmo Marconi, 21, 24040 Suisio, BG, Italy

Correspondence should be addressed to Rosa Veropalumbo; [rosa.veropalumbo@unina.it](mailto:rosa.veropalumbo@unina.it)

Received 6 November 2019; Revised 12 January 2020; Accepted 23 January 2020; Published 22 February 2020

Guest Editor: Andrea Grilli

Copyright © 2020 Rosa Veropalumbo et al. This is an open access article distributed under the Creative Commons Attribution License, which permits unrestricted use, distribution, and reproduction in any medium, provided the original work is properly cited.

The use of reclaimed asphalt pavement is a practice that is adding significant environmental value to road technologies, not only due to the reduction of materials sent to landfill but also because of the mechanical properties of the reclaimed asphalt (RA) that can be reused. This research focuses on the rheological properties of hot and cold bituminous mastics made up as follows: (1) hot mastics mixed with limestone filler (LF) and bitumen, (2) hot mastics, made from bitumen mixed with jet grouting waste (JW), a mixture of water, cement, and soil derived from land consolidation work in underground tunnels, and (3) hot mastics mixed with LF and JW as filler and bitumen. Three different ratios (0.3, 0.4, and 0.5) of filler per unit of neat bitumen (B50/70) were studied. The same number was used for mixing cold mastics, by using an appropriate laboratory protocol designed since the adoption of a cationic bituminous emulsion. A total of 18 mastics were prepared and investigated. The comparison was carried out using the frequency sweep (FS) test, analysing shear modulus  $G^*$ , applying the multistress creep and recovery (MSCR) test (40°C and 60°C) as well as the delta ring and ball ( $\Delta R\&B$ ) test, focusing on two main issues: (1) the stiffening effect caused by the filler type used for mixing each mastic, and (2) a comparison, in terms of stiffening effects and nonrecoverable creep compliance ( $J_{nr}$ ) of hot and cold mastic performance to highlight JW reuse in mastics. The results showed that the best  $G^*$  performance at test temperatures higher than 30°C is given by cold mastic after 28 days of curing time when JW is added to LF and bitumen. The lowest  $J_{nr}$  value was 40°C and 60°C for the same mastic.

## 1. Introduction

Pavement engineering researchers have been developing numerous new technologies to achieve more environment-friendly and energy-efficient pavement maintenance/construction solutions in order to reduce the costs of maintenance operations, enhancing and redeveloping road heritage [1]. Since road maintenance involves milling existing old layers (RA) [2], the cold recycling technique has become an increasingly popular alternative for road pavement construction as it minimizes financial and environmental impact through high performance.

Cold recycling techniques provide considerable advantages, i.e., limited exploitation of environmental resources

due to reduced aggregate extraction, greater productivity throughout the entire process, and, on the same layer, they offer identical levels of durability as layers made from virgin materials, energy savings by reducing the temperatures for heating virgin aggregates and, in the case of on-site recycling, the transportation of materials to and from the work site is eliminated, in addition to reductions in fuel fumes, dust, and gas released into the atmosphere from heating and transportation.

A validated design procedure for cold bituminous mixtures is not yet available, and many researchers are trying to develop a more appropriate procedure [3].

Flores et al. [4], for example, proposed a design methodology for cold recycled emulsion mixtures, evaluating air



void content, indirect tensile stress (ITS), indirect tensile strength ratio (ITSR), rutting resistance, stiffness modulus, and fatigue damage. They studied a series of possible dosages of bituminous emulsion contents of 2, 3, and 4% and cement contents of 0, 1, and 2% over the weight of the aggregates; in light of the results of the laboratory tests, a methodology was proposed and a single value “GPI” (Global Performance Index) has been proposed, taking into account the results obtained from previous laboratory tests. The results showed a strong relationship between GPI with gradation curves, bituminous emulsions, and cement.

Du [5] proposed a mix design procedure based first of all on a preliminary investigation of an optimum water content to add to an optimum bituminous emulsion content to investigate the properties of a cold recycled mixture made up of composite Portland cement (CPC), hydrated lime (HL), and a combination of hydrated lime and ground-granulated blast-furnace slag (GGBF). The CPC helped reach best performance in terms of ITS, moisture, and rutting resistance.

RA gradation does not always meet the requirements of technical specifications, and virgin aggregates and filler powders need to be added. Lyu et al. [6], for example, suggested a potentially effective mix design made up of 3.8% bituminous emulsion, 2% cement, 80% RA, and 20% virgin aggregates.

Kuna and Guttumukkala [7] further investigated the performance of cold reclaimed asphalt pavement using the dynamic modulus. The results showed that cold mixtures have lower entity variation from the highest to lowest temperatures compared with hot mix asphalt (HMA), where higher increments occur.

Filler is added to correct the lower part of a granulometric curve for both cold and hot mixture and to fill the gaps between grains left by larger elements. The filler bonds closely with the binder to form a bituminous mastic, which envelops the stone phase and provides full cohesion through the entire mixture, affecting the final stiffness of the mixture. The stress-strain response of flexible pavements is strictly linked to the rheological behaviour of the binder and its interaction with the lithic skeleton.

Many studies have focused on investigating the properties of the mastics with reference to cold bituminous mixture with RA.

Godenzoni et al. [8] evaluated the effects of different mineral fillers on the linear viscoelastic (LVE) properties of cold bituminous mastics. The shear modulus was measured on bituminous mastics prepared with calcium carbonate and cement as filler at filler-to-bitumen volume ratios of 0.15 and 0.3. It has been shown that  $G^*$  values are higher for mastics containing cement than those containing calcium carbonate as an added mineral; specifically,  $G^*$  increases with a higher cement concentration ratio and LVE behaviour evolves from that of liquid material to that of solid material.

Some studies have shown that the multistress creep and recovery (MSCR) method is the most appropriate for measuring the rutting resistance performance of asphalt binder. Indeed, it is widely accepted that, compared to the existing superpave rutting factor  $G^*/\sin \delta$  ( $\delta$  = phase angle), nonrecoverable creep compliance  $\bar{J}_{nr}$  following the MSCR

test is more closely related to the rutting resistance performance of asphalt mixture [6].

Vignali et al. [9] have measured to what extent cement and limestone filler contents affect the rutting response of two mastics produced using cationic bituminous emulsion: (1) 75% bitumen and 25% cement and (2) 75% bitumen, 12.5% filler, and 12.5% cement per volume. The results have confirmed that the presence of limestone filler improves mastic stiffness at high temperatures with a  $G^*$  higher than mastic with cement; this was confirmed by the MSCR results, where the mastic containing limestone filler accumulated less deformation at both test temperatures (46°C and 58°C) and both stress levels (0.1 kPa and 3.2 kPa).

Garilli et al. [10] focused on asphalt emulsion cement (AEC) mastic mixing to evaluate the behaviour of cold in-place recycling in the phase of coexistence of viscoelastic and brittle materials using a bending beam rheometer (BBR). The authors proposed introducing glass microspheres to act as an “inert solid skeleton” in the production of AEC mastics for BBR prismatic beams, to study the interaction between bituminous emulsion and cement in thin film, and to limit the specimens’ shrinkage and warpage during the curing period.

Following the main results available in scientific literature on cold bituminous mixtures (CBM) and mastics, the research presented here aims to bridge a gap in the laboratory protocol for mixing the cold bituminous mastics and to appreciate the main differences in relation to hot bituminous mastics.

Different mastics were prepared based on a filler-to-bitumen weight ratio of 0.3, 0.4, and 0.5. The fillers adopted were of the limestone (LF) and jet grouting waste (JW) types, while neat bitumen 50/70 (B50/70) was adopted for hot mastics, and bituminous emulsion (BE) made up of 60% neat bitumen and 40% water was used for the cold ones; mixing was carried out without adding cement trying to substitute it with JW in the cold bituminous mixture production since the JW is also a mixture made up of cement.

$G^*$  (at 10, 20, 30, 40, 50, and 60°C, at frequencies from 0.1 Hz to 10 Hz), MSCR (test temperatures 40°C and 60°C at 0.1 kPa and 3.2 kPa), and delta ring and ball ( $\Delta R\&B$ ) tests were performed for all mastics. Figure 1 shows the flowchart for the number of specimens in the series of experiments.

## 2. Materials and Methods

**2.1. Materials.** Different mastics were prepared according to the filler-to-bitumen ratios of 0.3, 0.4, and 0.5. Three types of mastics were prepared for each ratio: (1) LF plus B50/70 (hot) and LF plus BE (cold), (2) JW plus B50/70 (hot) and JTW plus BE (cold), and (3) JW plus LF plus B50/70 (hot) and JW plus LF plus EB (cold).

JW is a mixture of water and cement injected into the soil at high pressure; its element composition is shown in Table 1(a), where the presence of calcium (25.7%), silicon (67.6%), magnesium (1.7%), and other elements (0.006%) can be observed.

Before moving on to mastic preparation, the JW was subjected to a crushing process using a ball mill and curve gradation measurement (Figure 2).



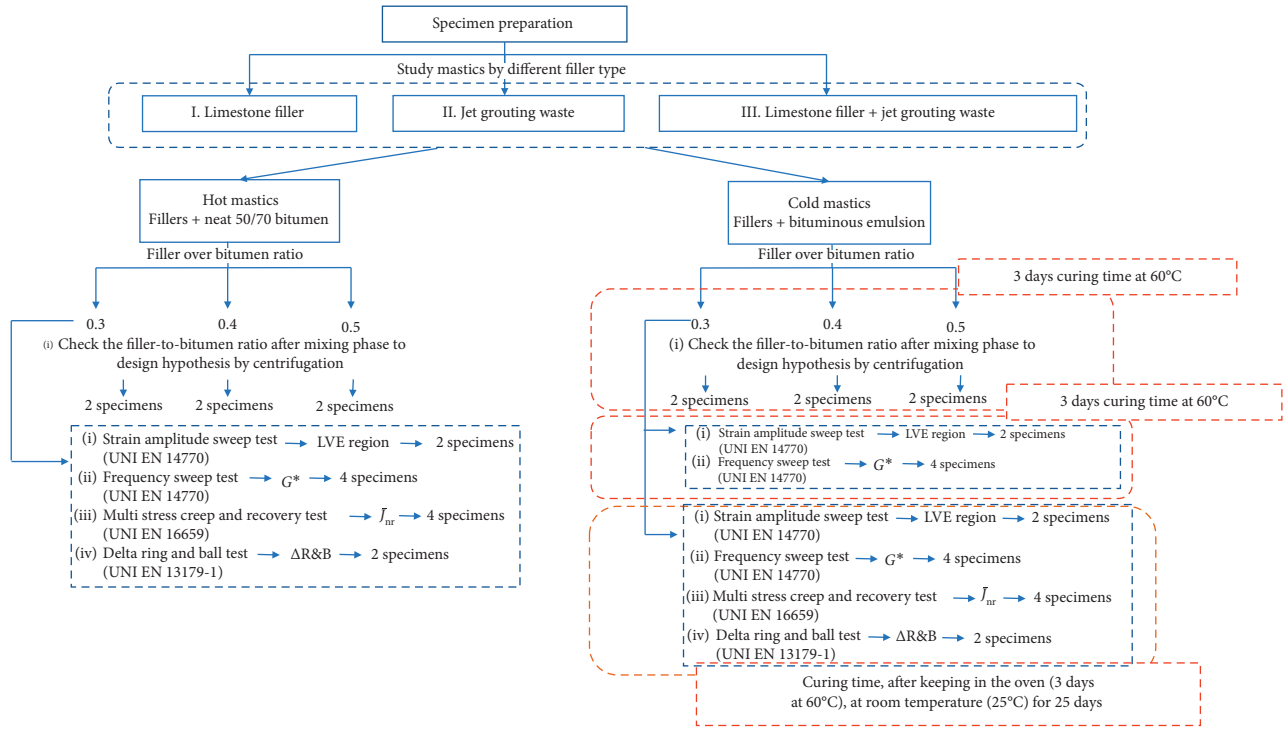


FIGURE 1: Flowchart for the mixed specimens in laboratory investigations.

TABLE 1: Main properties of materials: (a) chemical composition of JW filler, and (b) JW and LF specific gravity and Rigden voids.

(a)		
Elements	Results (%)	
Ca	25.701	
Fe	4.859	
Si	67.642	
Mg	1.735	
As	0.003	
Be	0.003	
Co	0.004	
Cr	0.008	
Ni	0.004	
Cu	0.007	
Zn	0.026	
Others*	0.006	
(b)		
Filler	Specific gravity (g/cm <sup>3</sup> )	Rigden voids (%)
LF	2.737	41.440
JW	2.687	51.360

\*Sn, V, Cd, Ti, and Mn.

LF and JW (see main properties in Table 1(b)) were adopted in bituminous mastics production as a total passing through a 0.063 mm sieve.

Hot and cold mastics were prepared: hot-process neat bitumen 50/70 produced by an oil refinery in southern Italy was used, while a bituminous emulsion mixture of 60% neat bitumen 50/70 and 40% water was used for the cold process.

The main properties of the bitumen and bituminous emulsion are shown in Table 2.

**2.2. Mastic Preparation.** The mastics were prepared adopting two different laboratory protocol procedures for hot and cold mastics.

For the hot mastics, suitable mixing temperatures were chosen according to AASHTO T316 using rotational viscosimetry. An RW 20 DZM N mechanical mixer was used to mix the filler and binder at the traditional temperature of 150°C used for the HMA mixture.

The mixing process was performed carefully to obtain homogenous matrices: a stainless-steel beaker was used, cleaned, and kept in an oven at test temperature with the asphalt binder. The beaker was put on a hot plate to maintain a constant mixing temperature; a mixer running at 500 rpm was then used. An amount of filler preheated to 150°C, in compliance with each of the three mentioned filler-to-bitumen study ratios, was gradually added to the beaker while stirring; the mixing process lasted for at least 30 minutes, until a homogenous binder-filler mastic was obtained (Figure 3).

In the case of cold mastics (Figure 3), the bituminous emulsion and filler were put into two different boxes and heated in an oven to 60°C according to the technical workability specification of the bituminous emulsion, until homogenous conditioning was reached.

The mixing process was different from that adopted for the hot mastics. An initial water content hypothesis was assumed for a suitable mastic workability level in compliance with UNI EN 1744-1; consequently, a filler-to-water content per mass of 0.5 ( $f/W = 0.5$ ) was used for all three study filler-to-extracted bitumen (0.3, 0.4, and 0.5) ratios. Table 3 shows the minimum quantity of water for each mastic, which was guaranteed by varying the



FIGURE 2: Jet grouting waste before and after the grinding process. (a) Before grinding. (b) Grinding device. (c) After grinding.

TABLE 2: Binder properties: (a) neat bitumen 50/70, (b) bituminous emulsion 60/40, and (c) bitumen contained in bituminous emulsion.

Properties	Unit	Standard	Value
(a)			
Penetration at 25°C	dmm	UNI EN 1426	64
Softening point (R&B)	°C	UNI EN 1427	46
Dynamic viscosity at 150°C			0.25
Dynamic viscosity at 135°C	Pa s	UNI EN 13702	0.413
Dynamic viscosity at 60°C			3.220
Fraass	°C	UNI EN 12593	-9
Characteristics	Unit	Value	Standard
(b)			
Water content	%	40	UNI EN 1428
pH value	—	4.2	UNI EN 12850
Settling tendency at 7 days	%	5.8	UNI EN 12847
Properties	Unit	Standard	Value
(c)			
Penetration at 25°C	dmm	UNI EN 1426	62
Softening point (R&B)	°C	UNI EN 1427	47

filler type and according to the three abovementioned ratios.

For only the cold mastics containing LF or JW filler, the bituminous emulsion broke up within 15 minutes after adding filler with water (see amount of mastic mixing per 100 gr of the study sample in Table 3). 15 minutes were long enough to allow the separation of the bituminous emulsion into water and bitumen.

On the contrary, for mastics made from LF plus JW filler added to BE previously mixed with a suitable amount of water to obtain workability, the BE broke up at the close of the 24th hour.

The water remaining from the separation of the water and bitumen was removed, and the cold mastic obtained was subsequently subjected to a 72 h conditioning process in the oven at 60°C until the remaining water was fully expelled.

A comparison of bitumen produced from bituminous emulsion after conditioning in the oven for 72 h at 60°C and aged bitumen made from bituminous emulsion using a rolling thin film oven (RTFO) procedure (Figure 4) has

shown that the values of the latter, in terms of softening point and penetration grade at 25°C, are not comparable to the previous one as they are higher (Table 4); the conditioning process was therefore such that it did not cause aging of the bitumen contained in the cold mastics.

After the conditioning process, the actual filler content for each of the 18 mastics was checked.

Ten grams of mastic were poured into glass test tubes, and a suitable quantity of “perchloroethylene” was added to submerge the mastic; the sample was stirred for ten minutes (Figure 5). Centrifugation was performed on four samples at the same time to verify the repeatability of the results achieved; the four samples (mastic plus perchloroethylene) reached the same weight. In fact, before inserting the four glass test tubes into the centrifuge, the correct balance of sample quantities (mastic plus solvent) was checked to avoid imbalance during centrifugation. Centrifugation lasted 30 minutes at a speed of 6,000 revolutions/minute. At the end of the centrifuge process, the solvent was removed using a filter paper to help retain filler particles. To remove all quantities



FIGURE 3: Mastic preparation using jet grouting waste. (a) Filler preparation: (A) cold mastic and (B) hot mastic. (b) Adding filler to the binder: (A) cold mastic and (B) hot mastic. (c) Final mastic: (A) cold mastic and (B) hot mastic.

TABLE 3: Amount of mastic mixing materials per 100 gr of the study sample.

Type	Filler-to-bitumen ratio (%)	Label	Materials (gr)					
			LF	JW	Water $f/W = 0.5$ (added + contained in BE)	B50/70	BE (60% bitumen + 40% water)	
Hot mastics	0.3	LH <sub>0.3</sub>	30	—	—	—	70	—
		JH <sub>0.3</sub>	—	30	—	—	70	—
		LJH <sub>0.3</sub>	15	15	—	—	70	—
	0.4	LH <sub>0.4</sub>	40	—	—	—	60	—
		JH <sub>0.4</sub>	—	40	—	—	60	—
		LJH <sub>0.4</sub>	20	20	—	—	60	—
	0.5	LH <sub>0.5</sub>	50	—	—	—	50	—
		JH <sub>0.5</sub>	—	50	—	—	50	—
		LJH <sub>0.5</sub>	25	25	—	—	50	—
Cold mastics	0.3	LC <sub>0.3</sub>	30	—	60 (13.2 added + 46.8 contained in BE)	—	117 (70.2 bitumen + 46.8 water)	
		JC <sub>0.3</sub>	—	30	60 (13.2 added + 46.8 contained in BE)	—	117 (70.2 bitumen + 46.8 water)	
		LJC <sub>0.3</sub>	15	15	60 (13.2 added + 46.8 contained in BE)	—	117 (70.2 bitumen + 46.8 water)	
	0.4	LC <sub>0.4</sub>	40	—	80 (40 added + 40 contained in BE)	—	100 (60 bitumen + 40 water)	
		JC <sub>0.4</sub>	—	40	80 (40 added + 40 contained in BE)	—	100 (60 bitumen + 40 water)	
		LJC <sub>0.4</sub>	20	20	80 (40 added + 40 contained in BE)	—	100 (60 bitumen + 40 water)	
	0.5	LC <sub>0.5</sub>	50	—	100 (66.8 added + 33.2 contained in BE)	—	83 (49.8 bitumen + 33.2 water)	
		JC <sub>0.5</sub>	—	50	100 (66.8 added + 33.2 contained in BE)	—	83 (49.8 bitumen + 33.2 water)	
		LJC <sub>0.5</sub>	25	25	100 (66.8 added + 33.2 contained in BE)	—	83 (49.8 bitumen + 33.2 water)	





FIGURE 4: RTFO device.

TABLE 4: Bitumen from EB 60/40 properties after aging and curing.

Properties	Unit	Standard	Aged bitumen from EB60/40	Bitumen from EB60/40 after 72 h at 60°C
Penetration at 25°C	dmm	UNI EN 1426	40	60
Softening point (R&B)	°C	UNI EN 1427	54.5	49

of solvent, the filter papers and each glass test tube were put in an oven heated to above the boiling temperature of the solvent for a maximum of around one hour to reach a constant weight. The amount of residual filler and, therefore, its ratio to bitumen are expressed in the following equation:

$$\frac{f}{b} = \frac{P_2 - P_3}{P_3 - P_1}, \quad (1)$$

where  $f/b$  is the actual ratio of the mastic being tested;  $P_1$  is the weight of the glass test tubes, in grams;  $P_2$  is the weight of the glass test tubes plus the quantity of mastic before centrifuge, in grams; and  $P_3$  is the weight of the glass test tubes with the residual amount of filler after the curing process, in grams.

The results in Table 5 show that, in the case of hot mastics, the amount of filler obtained following the abovementioned procedure is the same as that adopted in the first phase of mastic preparation and no change in the filler-to-bitumen ratio was observed before and after centrifugation.

On the contrary, a loss of filler was observed when cold mastic was prepared with filler-to-bitumen ratios of 0.4 and 0.5 after centrifugation for all the filler types adopted here. Consequently, the ratios of 0.4 and 0.5 were not investigated further as the mixture is chemically unstable and produces insufficient adhesion for the solution proposed here. Consequently, only a filler-to-bitumen ratio of 0.3 was examined further, as it satisfies the test proposed here due to the component materials adopted, and will therefore be simply labelled LC (LF added to EB), JC (JW added to EB), and LJC (LF plus JW added to EB) in the rest of this paper.

**2.3. Methods.** The bituminous binder has extremely varied mechanical behaviour that ranges from a typical elastic solid

at low temperatures to that of a Newtonian-type viscous fluid at high ones. These boundary conditions include intermediate viscoelastic stages, i.e., characterized by the simultaneous presence of elastic and viscous phases. The elastic and viscous responses make the material time dependent. Reactions to traffic and environmental conditions can be observed through its rheological properties, clearly connected to the performance of an asphalt binder such as shear modulus  $G^*$  and nonrecoverable creep compliance  $J_{nr}$ .

**2.3.1. Frequency Sweep Test.** An ‘‘Anton Paar’’ dynamic shear rheometer (DSR) (Figure 6) was used to analyze the dynamic mechanical properties of bitumen and the stiffening effect connected to the addition of two fillers: mineral filler (LF) and alternative filler (JW), which were adopted to mix mastics.

The complex shear modulus  $G^*$  is calculated as follows:

$$G^* = \frac{\tau_{\max}}{\gamma_{\max}}, \quad (2)$$

$$\tau_{\max} = \frac{T \cdot r}{I},$$

where  $\tau_{\max}$  is the maximum value of the shear stress,  $T$  is the maximum torque applied, and  $I = \int_0^r u^2 dA$  = moment of inertia, where  $u$  is the speed of the torque and  $r$  is the radius of the specimen (either 12.5 or 4 mm):

$$\gamma = \frac{u}{h} \theta \longrightarrow \gamma_{\max} = \frac{r}{h} \theta, \quad (3)$$

where  $\gamma$  is the shear strain,  $h$  is the specimen height (either 1 or 2 mm),  $\gamma_{\max}$  is the maximum value of the shear strain, and  $\theta$  is the rotation angle.

The test at the selected temperatures starts at the highest frequency and moves to the lowest falling within the LVE region. In this context, it is important to investigate the LVE properties in order to understand how the proportion of each filler type can affect the entire LVE behaviour of the associated mixture. Different proportions generating various microstructures can produce a wide range of bituminous material behaviours [11].

An FS test was conducted at a range of frequencies between 0.01 and 10 Hz, at temperatures of 10, 20, 30, 40, 50, and 60°C. An 8 mm plate with a 2 mm gap was used below 30°C, and above this temperature, a 25 mm plate and a 1 mm gap were used. In the FS test, the complex shear modulus ( $G^*$ ) was measured and analyzed from the point of view of master curves. [12].

Master curves were then plotted using the time-temperature superposition principle by shifting the modulus data at various temperatures with respect to frequency until the curves merged into a single function of the modulus in relation to the reduced frequency. The shift factor  $a(T)$  is the amount of shift required to form the master curve at each temperature.

The shift factor depends on the nature of the material and should therefore be assessed experimentally. The common equation used take the name of the Williams–Landel–Ferry law is as follows:

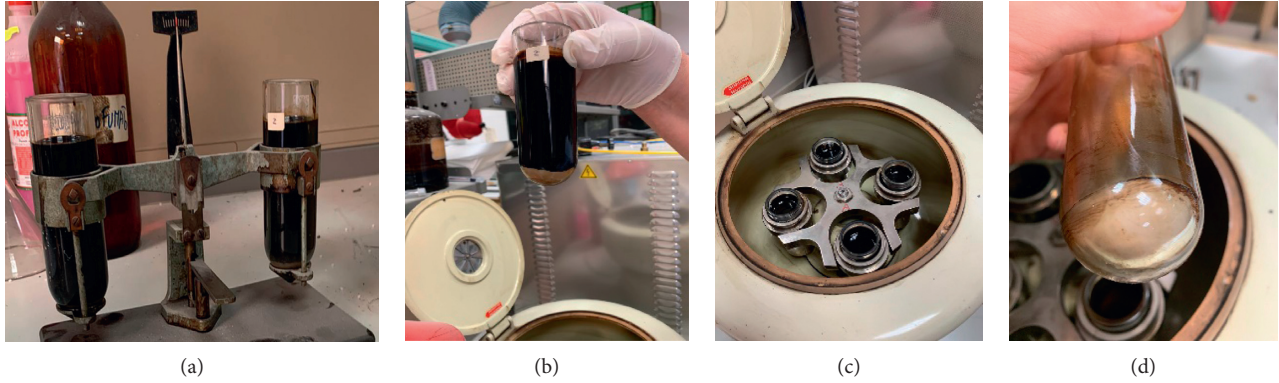


FIGURE 5: Checking filler content: (a) calibration of the glass test tubes, (b) specimen ready for the centrifuge, (c) centrifuge equipment, and (d) residual filler.

TABLE 5: Filler-to-bitumen ratio results.

		Hot mastics					
		LH		JH		LJH	
f/b	Weight	Specimen 1	Specimen 2	Specimen 1	Specimen 2	Specimen 1	Specimen 2
0.3	P1	112.230	115.880	135.970	126.160	112.200	115.830
	P2	122.260	126.000	145.990	136.190	122.200	125.860
	P3	114.480	118.105	138.279	128.469	114.450	118.121
	f/b	<b>0.289</b>	<b>0.282</b>	<b>0.299</b>	<b>0.299</b>	<b>0.290</b>	<b>0.296</b>
0.4	P1	112.210	115.830	135.930	126.120	112.200	115.880
	P2	122.210	226.780	145.930	137.120	122.900	125.880
	P3	115.036	147.530	138.739	129.183	115.259	118.726
	f/b	<b>0.394</b>	<b>0.400</b>	<b>0.391</b>	<b>0.386</b>	<b>0.400</b>	<b>0.398</b>
0.5	P1	112.230	115.860	135.910	126.150	112.180	115.860
	P2	122.430	125.960	145.910	136.350	122.580	125.860
	P3	115.627	119.163	139.243	129.486	115.627	119.153
	f/b	<b>0.499</b>	<b>0.486</b>	<b>0.500</b>	<b>0.486</b>	<b>0.496</b>	<b>0.491</b>
		Cold mastics					
		LC		JC		LJC	
f/b	Weight	Specimen 1	Specimen 2	Specimen 1	Specimen 2	Specimen 1	Specimen 2
0.3	P1	136.000	126.120	112.220	115.880	135.990	126.150
	P2	146.100	136.120	122.230	125.900	146.100	136.140
	P3	138.331	128.412	114.520	118.000	138.302	128.455
	f/b	<b>0.300</b>	<b>0.297</b>	<b>0.298</b>	<b>0.268</b>	<b>0.296</b>	<b>0.300</b>
0.4	P1	135.980	126.160	112.210	115.870	135.960	126.110
	P2	146.680	136.260	122.210	125.990	146.160	136.130
	P3	138.584	128.754	114.719	118.332	138.490	128.497
	f/b	<b>0.322</b>	<b>0.346</b>	<b>0.335</b>	<b>0.322</b>	<b>0.330</b>	<b>0.313</b>
0.5	P1	135.000	126.110	112.230	115.880	135.970	126.130
	P2	145.100	136.110	122.390	126.150	146.330	136.330
	P3	137.613	128.753	114.845	118.371	138.710	128.620
	f/b	<b>0.349</b>	<b>0.359</b>	<b>0.347</b>	<b>0.320</b>	<b>0.360</b>	<b>0.323</b>

$$\log \frac{a(T)}{a(T_0)} = \frac{-C_1 \cdot (T - T_0)}{C_2 + T - T_0}, \quad (4)$$

where  $a(T)$  and  $a(T_0)$  are the shift factors at temperatures  $T$  and  $T_0$ ,  $T$  is the shift temperature,  $T_0$  is the temperature of reference for the shift, and  $C_1$  and  $C_2$  are the constants that depend on the nature of the material.

**2.3.2. Multistress Creep and Recovery Test.** To assess bituminous binders at high service temperatures, and especially

to evaluate stress or loading resistance [13], the MSCR test was performed in accordance with UNI EN 16659.

Nonrecoverable creep compliance  $J_{nr}$  is an indicator of the resistance of bitumen and bituminous mastics to permanent deformation under repeated load.

The test was performed at 40 and 60°C in light of the main results from the FS test where the 25 mm parallel plate geometry was used with a 1 mm gap setting. The test consists of an initial loading phase kept constant for one second, followed by a recovery phase of nine seconds; ten creep and



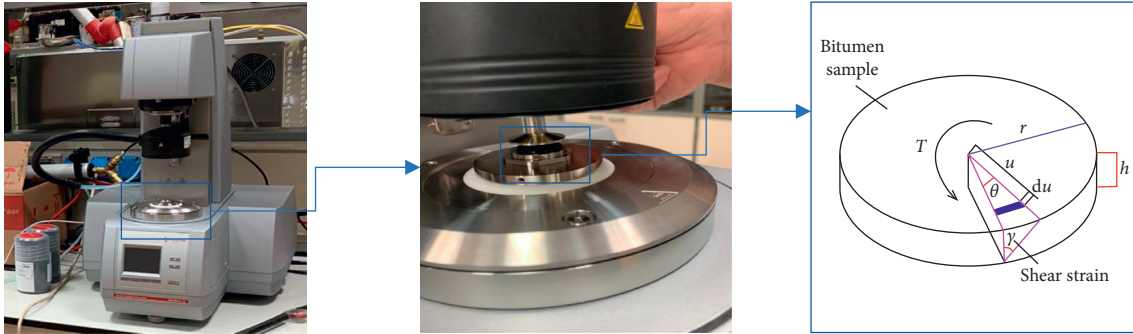


FIGURE 6: The dynamic shear rheometer used for investigating rheological properties.

recovery cycles are run at 0.100 kPa creep stress followed by ten more cycles at 3.200 kPa creep stress.

MSCR results show that adding filler leads to reduced susceptibility, to permanent deformation, and an enhanced elastic response depending on the combination of filler types [14].

The results obtained from the MSCR test are expressed as follows:

- (i)  $J_{nr}$ , nonrecoverable creep compliance, calculated by dividing the residual strain postrecovery phase by the stress applied during creep loading
- (ii)  $\bar{J}_{nr}$ , the average nonrecoverable creep compliance, calculated as the mean of 10  $J_{nr}$  values
- (iii)  $\bar{J}_{nr}$  and  $J_{TOT}$ , the ratio between the residual strain and accumulated strain at the end of the creep phase, where  $J_{TOT}$  is evaluated immediately before load removal
- (iv)  $J_{nr, ratio}$ , the ratio between the average creep compliance ( $\bar{J}_{nr}$ ) of the mastic containing alternative filler (LJH and LJC28d (cold mastic with LF and JW after 28 days curing time)) and the respective mastic containing limestone filler (LH and LC28d (cold mastic with LF after 28 days curing time)) at the same stress level and test temperature

### 3. Results

**3.1. Frequency Sweep Test.**  $G^*$  was taken as the rheological benchmark used to characterize and compare the nine mastics prepared by adopting a filler-to-bitumen ratio of 0.3. Test temperatures were between 10°C and 60°C with an increment of 10°C, and a test frequency ranges from 0.1 to 10 Hz across the 19 obtained measures. Strain amplitude sweep (SAS) tests were performed first with the aim of identifying the LVE limit and defining a suitable range of strain level for hot and cold mastics with all filler types. The SAS tests were performed at 10°C using 8 mm parallel plate geometry and a 2 mm gap, applying a constant frequency of 10 rad/s (1.59 Hz). A unique strain level of 0.05% was adopted as the LVE limit for all mastics in order to simplify the testing procedure. This value was selected on the basis of the LVE limit identified for the LH mastic, although the other mastics had higher LVE limits [8, 15–17].

Figure 7 shows the master curves for the three hot mastics ((1) hot mastics made with LF filler added to B50/70, (2) hot mastics with JW filler added to B50/70, and (3) hot mastics with LF plus JW added to B50/70). It may be noted that adding the filler to the three hot mastics increases stiffness when compared to B50/70. In greater detail, LH returns the lowest  $G^*$  values for all test temperatures and frequencies investigated compared to JH and LJH; on the contrary, at a test temperature of 10°C, JH behaves in a similar way to LH. It should also be noted that the highest  $G^*$  values were observed for LJH; specifically, at a low test temperature, there were no great differences between LH and JH, with behaviour very close to that of B50/70. Otherwise, at high temperatures, LJH gave higher  $G^*$  performance than LH and B50/70, albeit quite close to that of JH. The phase angle behaviour of mastics follows the base bitumen trend; neither filler changes the viscoelastic response of the bitumen, giving a completely viscous response at high temperatures and an elastic approach at low temperatures.

Before moving on to assess the cold mastics from the point of view of  $G^*$  and  $\delta$ , an assessment of the behaviour of B50/70 in terms of  $G^*$  and  $\delta$  and the bitumen extracted (EB60/40) from the bituminous emulsion was carried out. Figure 8 shows the master curve results for the two bitumens, with no variation when moving from high to low test temperatures. Further clarification will be provided by the MSCR test in Section 3.3.

Three cold study mastics (LC, JC, and LJC) were prepared following the procedures shown in Section 2.2 and kept in an oven for 3 days at 60°C until a constant weight was reached. On the third day, no variation in weight had occurred, so after this period, three specimens of the cold mastics were tested for  $G^*$  configuration according to the geometric configuration of the plates and gap shown in Section 2.3.1.

The master curves for the cold mastics are shown in Figure 9. What is immediately evident is the remarkable difference between the cold mastics after 3 days of curing time and the EB60/40 at low temperatures, where the former (LC, JC, and LJC) show lower  $G^*$  values compared to EB60/40; on the contrary, JC reaches performance at temperatures up to 40°C and seems to produce the same behaviour as EB60/40. In comparison with the other two cold mastics at 10°C, the LC shows a dramatic fall in  $G^*$ . In terms of the phase angle, it is possible to observe a lower  $\delta$  value at high temperatures for LC than for EB60/40, with slightly elastic

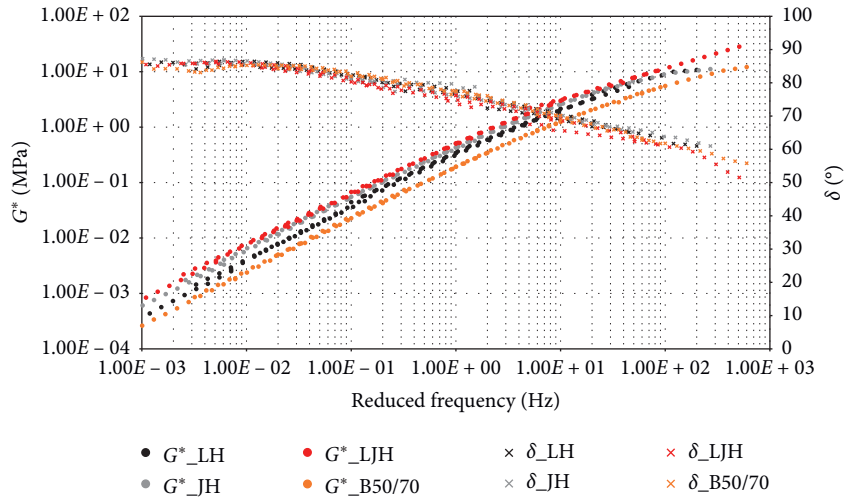


FIGURE 7: Master curve for hot mastics and neat bitumen 50/70.

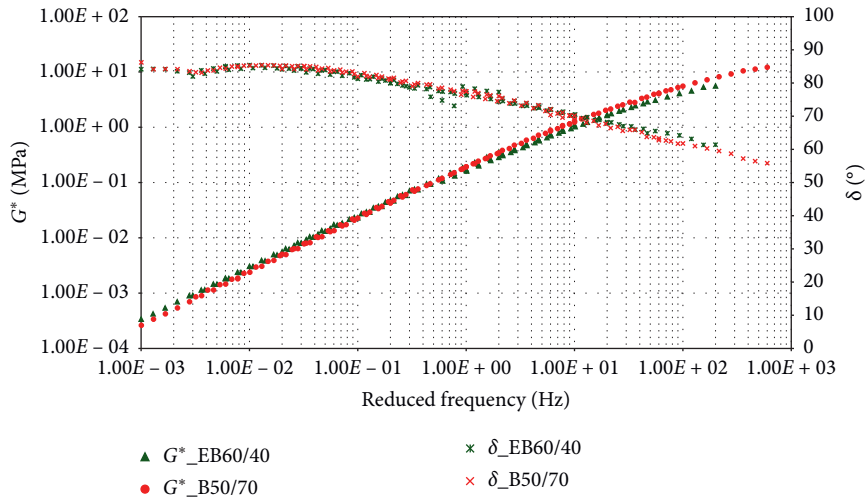


FIGURE 8: Master curve of bitumen and bitumen contained in emulsion.

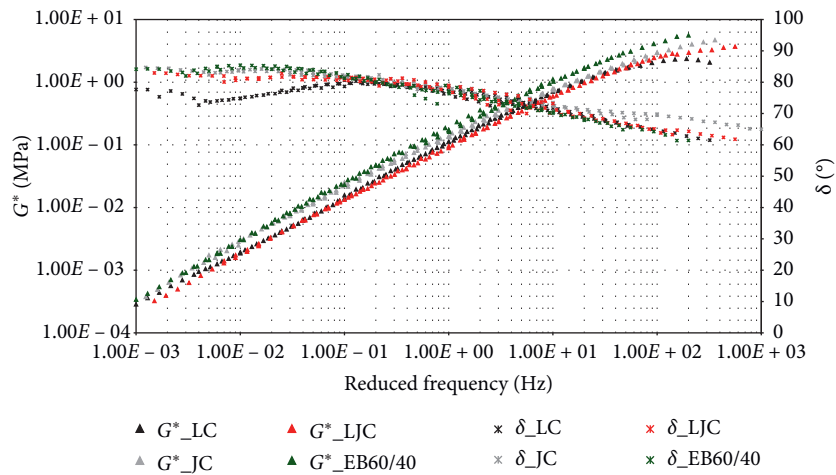


FIGURE 9: The master curves of the cold mastics after 3 days of curing time in an oven heated to 60°C and EB60/40.

behaviour, which is the opposite of what happens at low temperatures, where the  $\delta$  value for JC is higher than for EB60/40.

In particular, it can be observed that the trend of the phase angle at low temperatures for JC is the opposite of the trend for  $G^*$  modulus; in this case, the behaviour of JC, unlike the other mastics, approaches that of a pseudoplastic material, which may mean that a mastic mix using only JW as a filler cannot increase the stiffness of bitumen after 3 days.

Since many studies carried out on CBM have demonstrated that maximum mechanical performance in terms of ITS and/or stiffness can be achieved on the 28th day of curing time [18], cold mastics that had been kept for 3 days at 60°C were subsequently kept at room temperature for 25 days (for a total of 28 days' curing time) and then subjected to  $G^*$  evaluation (labelled LC28d (LF added to EB after 28 days of curing time), JC28d (JW added to EB after 28 days of curing time), and LJC28d (LF plus JW added to EB after 28 days of curing time)).

The results of the FS test in terms of master curves are reported in Figure 10. Unlike the previous results for all cold mastics,  $G^*$  always resulted higher than EB60/40, highlighting the stiffening effects of the fillers in the bitumen. In particular, it can be noted that, although JC28d  $G^*$  is higher than EB60/40 at low temperatures (10–20–30°C), JC28d is comparable to LC28d; on the contrary, at high temperatures (40–50–60°C), it displays worse behaviour with a reduction in  $G^*$ . When JW filler is added to the bitumen without LF, JC28d  $G^*$  is lower than the remaining mastics. On the contrary, when JW is added to bitumen with LF, the  $G^*$  value increases at all temperatures and for all frequency ranges (see LJC28d).

The phase angle behaviour of mastics follows the bituminous emulsion trend; in particular the LC28d  $\delta$  values at higher temperatures resulted lower for all the mastics and the bituminous emulsion, while JC28d shows greater elasticity than the others at low temperatures. Furthermore, greater viscosity was observed when both LF and JW were added to bituminous emulsion.

Therefore, cold interaction between LF filler with bitumen favours the best mechanical performance of all the prepared mastics, including the hot ones (Figure 10).

On the basis of the results achieved so far, focusing only on the mastics that returned better performance during comparison when hot and cold procedures were used, it can be observed in Figure 11 that three main regions can be identified taking into account  $G^*$  values: (1) for region I (test temperatures >30°C), it may be observed that LJC28d shows higher performance in terms of  $G^*$  than LJH; (2) for region II (test temperatures from 20°C to 10°C), LJC28d shows the same performance in relation to  $G^*$  as LJH; and (3) for region III (test temperatures <10°C), LJC28d displays poorer performance than LJH, which, on the contrary, has a higher  $G^*$ .

**3.2. MSCR Test.** The passage of traffic loads generates stress within the pavement causing accumulated strain in the

mixture. The rutting resistance of cold bituminous mixtures, like those of a traditional HMA, is due to (a) the interlocking of the aggregates and their form and (b) the stiffening effect of the mastic [19].

In the research presented here, mastic response to permanent deformation was estimated using the MSCR test. As the results shown in the previous sections demonstrated that best performance of cold mastics can be achieved at the end of the 28th day of curing time, the MSCR test was carried out using the abovementioned mastics and the hot mastics (LH, JH, and LJH) as control systems to measure the performance of the cold ones.

Table 6 shows  $\bar{J}_{nr}$  values for each of the six mastics (LH, JH, LJH, LC28d, JC28d, and LJC28d) at temperature of 40°C and 60°C and 0.1 kPa and 3.2 kPa stress levels.

As expected,  $\bar{J}_{nr}$  increases as the temperature rises both for binders (B50/70 and EB60/40) and mastics. This is due to lower viscosity during the bituminous phase at higher temperatures, which results in higher permanent strain in the material under stress.

First of all, from a comparison between hot and cold mastics at the same test temperatures and load levels, all the cold mastics show a reduction of  $\bar{J}_{nr}$ ; in particular, at 40°C and at 3.2 kPa stress level, a greater reduction was observed, comparing the cold mastics with the corresponding hot mastics, for LJC28d, associated with a 68%  $\bar{J}_{nr}$  reduction compared with LJH; a reduction of 57% was observed moving from LH to LC28d and a 21%  $\bar{J}_{nr}$  reduction when moving from JH to JC28d.

The experimental data highlight the contribution of adding alternative fillers to the bitumen and the bitumen derived from bituminous emulsion. The presence of JW improves the resistance of bitumen to permanent deformations, especially when added together with LF to bituminous binder. In fact, at temperatures of 40°C and 60°C, when JW is added to B50/70 for hot packaging, the  $\bar{J}_{nr}$  values decrease by 38% and 21%, respectively, compared with LH; as for the cold mastics, LJC28d returned the highest reduction compared with the remaining cold mastics. In particular, LJC28d is characterized by a 74%  $\bar{J}_{nr}$  reduction at a 40°C test temperature and 52%  $\bar{J}_{nr}$  at a 60°C test temperature compared to LH.

Figure 12 shows the differences between hot and cold bituminous mastics in terms of accumulated strain during 10 creep and recovery cycles; when adding LF and JW to bitumen contained in bituminous emulsion (LJC28d), the stiffening effect reaches its highest value both at 40°C and 60°C. This confirms the results obtained previously for  $\bar{J}_{nr}$ .

The ability of each mastic to recover from deformation at the end of the creep phase was evaluated in terms of  $J_{nr}/J_{TOT}$ .

If the material is unable to recover from any deformation, and the strain measured at the end of the creep phase remains the same at the end of the recovery phase,  $J_{nr}/J_{TOT}$  will be 1. On the contrary, if the material is totally elastic and able to recover from all the accumulated deformation,  $J_{nr}/J_{TOT}$  will be 0 [14].

The results, in terms of  $J_{nr}/J_{TOT}$  expressed as percentages, are reported in Figure 13 but only at a test temperature of 60°C and 3.2 kPa, as the results shown in Table 6 highlighted the most critical situations under these conditions.

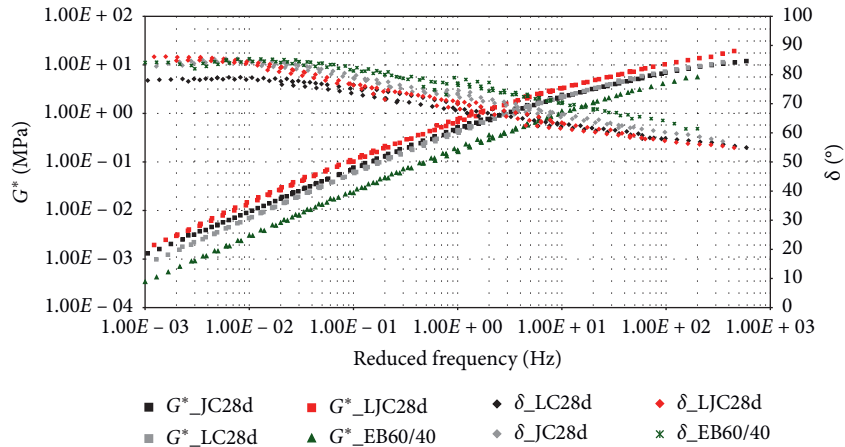


FIGURE 10: Master curves of the cold mastics subsequent to curing time, after being kept in the oven for three days at 60°C and at room temperature (25°C) for 25 days.

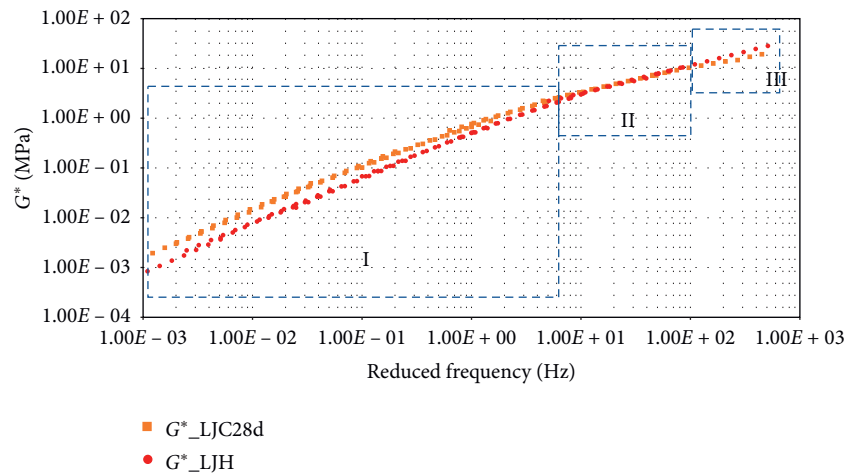


FIGURE 11: Master curves comparison between LJC28d and LJH.

TABLE 6:  $\bar{J}_{nr}$  value of hot and cold mastics.

ID	Specimens	Test temperatures			
		40°C		60°C	
		$J_{nr-0.1 \text{ kPa}}$	$J_{nr-3.2 \text{ kPa}}$	$J_{nr-0.1 \text{ kPa}}$	$J_{nr-3.2 \text{ kPa}}$
1	B50/70	0.128	0.139	4.149	4.321
2	EB60/40	0.112	0.128	3.387	3.829
3	JH	0.083	0.091	2.312	2.503
4	JC28d	0.053	0.062	2.059	2.211
5	LH	0.137	0.143	3.002	3.054
6	LC28d	0.051	0.072	1.767	2.394
7	LJH	0.104	0.108	2.745	2.753
8	LJC28d	0.036	0.052	1.360	1.529

Table 7 shows that more than 30% of elastic deformation is recovered by LJC28d and positive performance was also observed for LC28d, which regains more than 25% of the deformation, while JC28d returns less than 25% of elastic deformation. These results match previously achieved results in terms of  $G^*$ . Hot mastics have poorer performance in terms of recovery from elastic deformation when compared with cold mastics and, in all cases, less than the hot mastics.

JH shows the best performance (recovery of elastic deformation less than 15%). This circumstance also confirms the results previously achieved in terms of  $G^*$  for the cold mastics.

In order to further evaluate the stiffening effect of the JW when added to hot and cold bituminous mastics, a ratio between  $\bar{J}_{nr}$  for mastics containing JW with LF (as results for  $G^*$  and  $J_{nr}/J_{TOT}$  demonstrated how these mastics achieved the best performance) and  $\bar{J}_{nr}$  for mastics containing only LF, defined  $J_{nr, ratio}$ , was calculated from results in Table 6.

The results in Table 7 show that JW filler improves mastic stiffening during both hot and cold mixing. In particular, under hot conditions, the increase in stiffening caused by the addition of JW changes with the temperature but is not affected by stress levels. Under hot conditions, JW filler helps increase stiffening by almost 25% compared with LH mastic at a test temperature of 40°C. In the case of hot mixing, the stiffening effect decreases from 40°C to 60°C, making up only around 10% of a further increase in stiffness due to the presence of JW in the mastic.

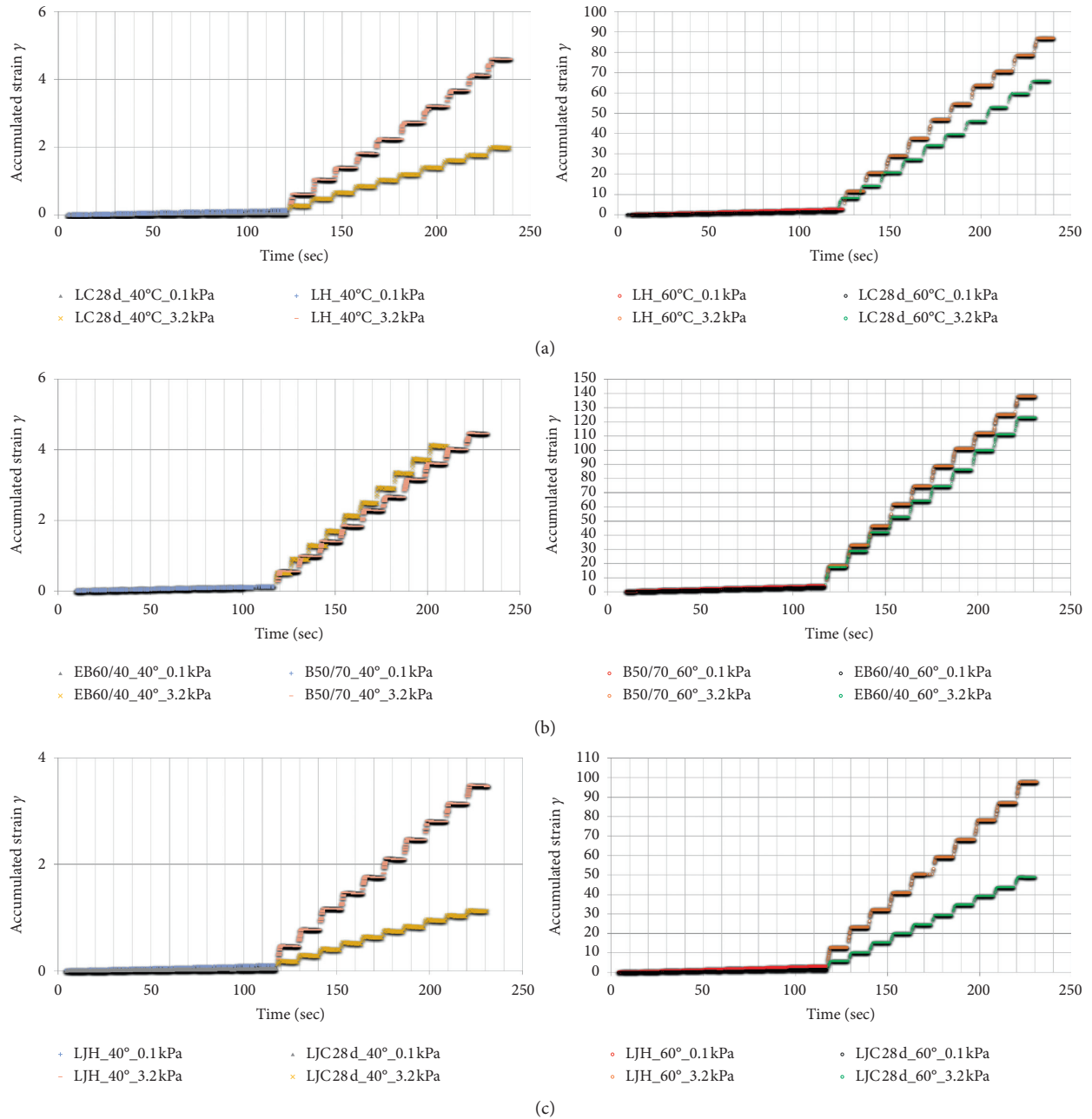


FIGURE 12: Accumulated strain results at the end of every 10 creep-recovery cycles of hot and cold bituminous mastics: (a) LH vs LC28d (I at 40°C and II at 60°C), (b) JH vs JC28d (I at 40°C and II at 60°C), and (c) LJH vs LJC28d (I at 40°C and II at 60°C).

The greatest benefits can be achieved when the mastics are prepared under cold conditions: JW increases stiffness, both at 40°C and 60°C. At 0.1 and 3.2 kPa, the increase is around 30% compared with cold mastic made up of limestone filler and bitumen.

3.3. Mean Correlation Comparing Delta Ring and Ball and  $\bar{J}_{nr}$ . The final test carried out was the most common  $\Delta R\&B$  (UNI EN 13179-1) assessment, measuring the difference between the R&B of each mastic (LH, JH, LJH, LC28d, JC28d, and LJC28d) and the R&B of the binder adopted for

mixing mastics (B50/70 and EB60/40) with a filler-to-bitumen ratio of 0.3 (see Section 2.2 for more details).

Figure 14 shows the  $\Delta R\&B$  value for each mastic plotted as a function of two variables: the x-axis shows the study mastics (a total of six), while the y-axis shows the mean value of the stiffening increase produced by the addition of each filler to a mastic, compared with the binder, taking into account the effects produced at two test temperatures (40°C and 60°C) and two stress levels (0.1 and 3.2 kPa). The last parameter is called  $\bar{J}_{temp, stress}$  and can be calculated for each hot mastic using equation (5) and for each cold mastic using equation (6) as follows:



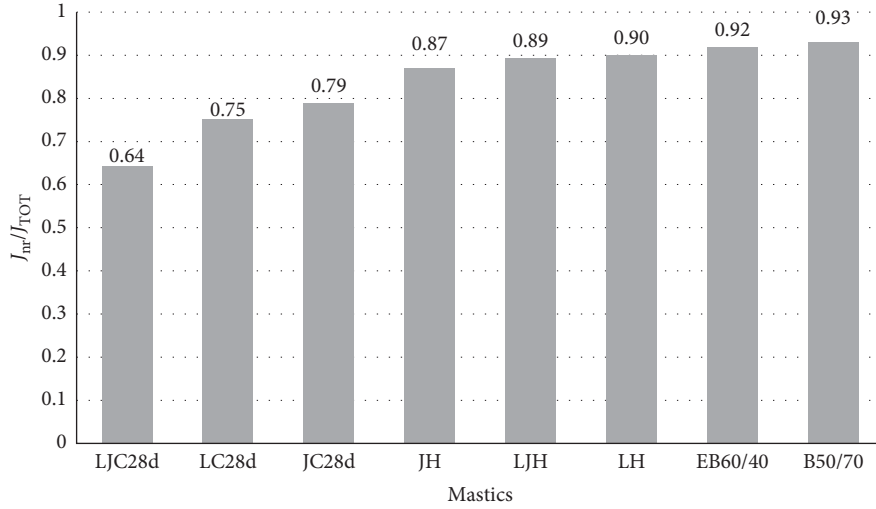
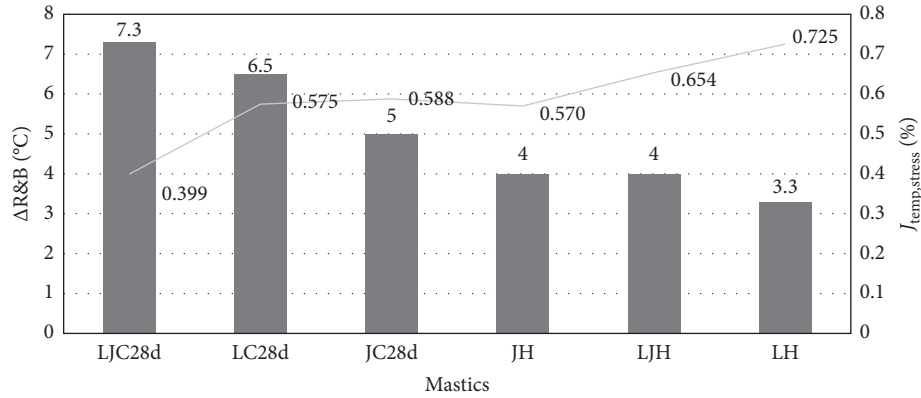

 FIGURE 13:  $J_{nr}/J_{TOT}$  results under 3.2 kPa and 60°C.

 TABLE 7:  $J_{nr,ratio}$  results: (a) LJH/LH and (b) LJC28d/LJ28d.

Mastics	Temperature			
	40°C		60°C	
	$J_{nr,ratio}-0.1 \text{ kPa}$	$J_{nr,ratio}-3.2 \text{ kPa}$	$J_{nr,ratio}-0.1 \text{ kPa}$	$J_{nr,ratio}-3.2 \text{ kPa}$
(a) LJH	0.763	0.755	0.914	0.901
(b) LJC28d	0.706	0.694	0.770	0.639


 FIGURE 14: Delta ring and ball results compared with  $\bar{J}_{temp,stress}$ .

$$\bar{J}_{temp,stress} = \frac{1}{n} \sum_{i,j} \left( \frac{\bar{J}_{nr \text{ hot mastici},j}}{\bar{J}_{nr \text{ B50/70},i,j}} \right), \quad (5)$$

where  $\bar{J}_{nr \text{ hot mastici},j}$  refers to  $J_{nr}$  measured for each hot mastic at  $i$ -th temperature (40° or 60°C) and  $j$ -th stress level (see rows 3 to 5 in Table 6),  $\bar{J}_{nr \text{ B50/70},i,j}$  refers to  $J_{nr}$  measured for B50/70 at  $i$ -th temperature (40° or 60°C) and  $j$ -th stress level (see row 1 in Table 6), and  $n$  is the number of combined conditions at test temperatures and stress levels equal to 4 in the case study (Table 6):

$$\bar{J}_{temp,stress} = \frac{1}{n} \sum_{i,j} \left( \frac{\bar{J}_{nr \text{ cold mastici},j}}{\bar{J}_{nr \text{ EB60/40},i,j}} \right), \quad (6)$$

where  $\bar{J}_{nr \text{ cold mastici},j}$  refers to  $J_{nr}$  measured for each cold mastic at  $i$ -th temperature (40° or 60°C) and the  $j$ -th stress level (see rows 6 to 8 in Table 5),  $\bar{J}_{nr \text{ EB60/40},i,j}$  refers to  $J_{nr}$  measured for EB60/40 at  $i$ -th temperature (40° or 60°C) and the  $j$ -th stress level (see row 2 in Table 5), and  $n$  is the number of combined conditions test temperatures and stress levels equal to 4 in the case study (Table 5).

Firstly, it may be observed that the  $\Delta R\&B$  trend is inversely related to  $\bar{J}_{temp,stress}$ , where an increasing  $\Delta R\&B$  corresponds to a decreasing  $\bar{J}_{temp,stress}$ : based on the results in Figure 14, the more suitable solution among these mastics (highest  $\Delta R\&B$ , lowest  $\bar{J}_{temp,stress}$ ) is LJC28d, while the lower performances are found for LH traditional mastics.

#### 4. Discussion

The study described in this paper focuses first of all on the construction of a laboratory mixing protocol for cold bituminous mastics and on the examination of their rheological performance and main differences in terms of shear modulus  $G^*$  and nonrecoverable creep compliance  $J_{nr}$  when compared to hot mastics. Specifically, the addition of jet grouting waste as a filler for bitumen with and without additional LF led to the best response in cold mastics.

Three filler-to-bitumen ratios (by weight) were investigated, namely, 0.3, 0.4, and 0.5 (Table 3); after submitting the cold and hot mastics to centrifuge, no loss of filler was observed for a filler-to-bitumen ratio 0.3 (Table 5). This made it possible to proceed with the analysis by examining the performance of mastics following the ratio mentioned above.

The FS test showed that hot mastics with JW filler (JH and LJH) have a higher  $G^*$  value than traditional LH (Figure 7), with  $\delta$  values that do not differ from those obtained from the binder used for the mixing phase, and  $G^*$  results for all the cold mastics showed that a curing time period of 3 days at 60°C in the oven, where 60°C is the typical laying temperature for CBM, is not enough to reach a suitable level of mechanical performance in cold mastics (Figure 9). Further curing time at room temperature is needed up to the 28<sup>th</sup> day to obtain adequate rheological performance; in particular, it was observed how cold mastics with only JW as a filler allow good performance at low temperatures (<30°C), while JW and limestone fillers should be added to bituminous emulsion at high temperatures (Figure 10).

Since no differences exist between neat bitumen 50/70 and bitumen contained in bituminous emulsion used for mixing cold mastic (with no variations in terms of master curves  $G^*$  (Figure 8)), a comparison between the hot and cold mastics was carried out where LJC28d returned greater stiffening behaviour than traditional hot LH in terms of  $G^*$ .

The deformation recovery capacity of binders and mastics in both hot and cold specimens was assessed using an MSCR test. The nonrecoverable creep compliance  $J_{nr}$  of all mastics was lower than  $J_{nr}$  of bitumen, which indicates the extent of contribution of fillers to increasing the stiffness of the mastics of which they are a component. Specifically, when JW and LF are used as binder fillers for mixing, it was observed that the cold mastics recovered accumulated deformation after the 28th day of curing time at room temperature (LJC28d), showing a  $J_{nr}$  reduction of 74% at 40°C and 52% at an average temperature of 60°C compared to the traditional LH (Table 6). The effect of the stiffness of each mastic produced by adding alternative filler is further confirmed by calculating the following ratio:  $J_{nr}$  mastic with JW filler to  $J_{nr}$  mastic with LF as a filler.

The results showed that the stiffening effect produced by the presence of JW is not stress dependent for either hot and cold mastics but is temperature dependent when moving from 40°C to 60°C in the case of LJH; LJC28d produced the highest stiffening performance at all test temperatures, and the stress levels allowed a mean reduction of almost 30% of accumulated deformation compared with traditional LH (Table 7).

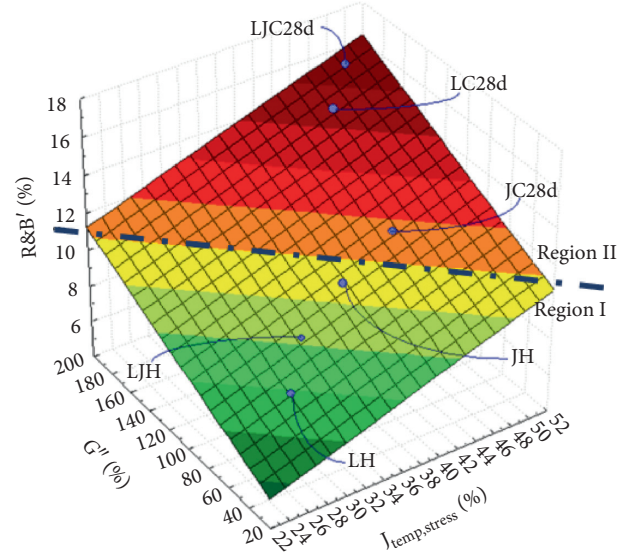


FIGURE 15: R&B' against  $\bar{J}'_{temp, stress}$  and  $G^*$ .

Based on the observation listed above, the stiffening effect of the fillers in bituminous mastics is summarised in Figure 15; specifically, the stiffening effect was estimated by observing many parameters. Figure 15 shows R&B' vs  $\bar{J}'_{temp, stress}$  and  $G^*$  calculated according to equations (7)–(9), respectively, as follows:

$$R\&B' = \left( \frac{R\&B_{mastic}}{R\&B_{binder}} - 1 \right) \cdot 100, \quad (7)$$

where  $R\&B_{mastic}$  is the ring and ball value calculated for each mastic (hot and cold) and  $R\&B_{binder}$  is the ring and ball value of each binder (B50/70 for hot mastics and EB60/40 for cold mastics):

$$J'_{temp, stress} = (\bar{J}_{temp, stress} - 1) \cdot 100, \quad (8)$$

where  $\bar{J}_{temp, stress}$  is calculated according to equation (5) for hot mastics and equation (6) for cold ones:

$$G^* = \left( \frac{\bar{G}_{mastic}^*}{\bar{G}_{binder}^*} - 1 \right) \cdot 100, \quad (9)$$

where  $\bar{G}_{mastic}^*$  is the average of the  $G^*$  values for the test temperatures 40°, 50°, and 60°C of each mastic (hot and cold) and  $\bar{G}_{binder}^*$  is the average of the  $G^*$  values for the test temperatures 40°, 50°, and 60°C of each binder (B50/70 for hot mastics and EB60/40 for cold ones).

Figure 15 shows that the stiffening effect of the fillers is different for hot and cold mastics and two different regions of interest emerge. The highest area of region I identified for hot mastics is occupied by JW when it is added to B50/70, while the highest area of region II identified for cold mastics, which is also the peak of the total region, is identified for JW when it is added together with LF into EB. This different filler behaviour for cold and hot mastics may be due to the very high temperature in the hot mastic mixture, which leads to a reduction in the stiffening effect of the fillers within the mastics.

## 5. Conclusions

On the basis of the results discussed above, the following observations can be made:

- (i) Cold mastics mixing jet grouting waste, limestone filler, and bituminous emulsion were made at 60°C using a filler-to-bitumen weight ratio of 0.3; the separation of bitumen from water into bituminous emulsion took place without the addition of cement as traditionally happens with cold bituminous mixtures; and this is due to the role and contribution of jet grouting waste comprising water, cement, and soil available in site.
- (ii) It was observed that cold mastics after 3 days of curing time at 60°C return a worse  $G^*$  performance than neat bitumen 50/70 contained in bituminous emulsion.
- (iii) The contribution of the jet grouting waste in terms of  $G^*$  is higher when it is adopted for hot mastics than cold mastics; the effects of jet grouting waste seriously affects  $G^*$  when it is added to limestone filler making cold mastics. The last combination allows us to reach a reduction of the phase angle compared to remaining mastics.
- (iv) The combination of jet grouting waste and limestone filler in cold mastics increases the stiffness response, returning a higher  $G^*$  modulus, confirmed also by a reduction of the accumulated deformation obtained from a multistress creep and recovery test.

These conclusions may constitute a starting point for the further study of cold mastics: increasing the filler ratio and changing the type of bituminous emulsion or even adding a rejuvenator; a mastic mixture without using cement could be produced in order to verify the contribution offered by jet grouting waste alone. These will be no more than small-scale analysis results to be transferred full scale in the proportions required to mix cold bituminous mixtures designed without the addition of cement.

## Data Availability

The data used to support the findings of this study are available from the corresponding author upon request.

## Disclosure

The research was carried out within the terms of employment of the authors at Federico II University of Naples.

## Conflicts of Interest

The authors declare that no conflict of interest exists regarding the publication of this paper.

## References

- [1] M. Amouzadeh Omrani and A. Modarres, "Stiffness and fatigue behaviour of emulsified cold recycled mixture containing waste powder additives: mechanical and microstructural analysis," *Journal of Materials in Civil Engineering*, vol. 31, no. 6, Article ID 04019061, 2019.
- [2] V. Antunes, A. C. Freire, and J. Neves, "A review on the effect of RAP recycling on bituminous mixtures properties and the viability of multi-recycling," *Construction and Building Materials*, vol. 211, pp. 453–469, 2019.
- [3] S. Du, "Interaction mechanism of cement and asphalt emulsion in asphalt emulsion mixtures," *Materials and Structures*, vol. 47, no. 7, pp. 1149–1159, 2014.
- [4] G. Flores, J. Gallego, L. Miranda, and J. R. Marcobal, "Design methodology for in situ cold recycled mixtures with emulsion and 100% rap," *Construction and Building Materials*, vol. 216, pp. 496–505, 2019.
- [5] S. Du, "Performance characteristic of cold recycled mixture with asphalt emulsion and chemical additives," *Advances in Materials Science and Engineering*, vol. 2015, Article ID 271596, 2015.
- [6] Z. Lyu, A. Shen, X. Qin, X. Yang, and Y. Li, "Grey target optimization and the mechanism of cold recycled asphalt mixture with comprehensive performance," *Construction and Building Materials*, vol. 198, pp. 269–277, 2019.
- [7] K. Kuna and B. Gottumukkala, "Viscoelastic characterization of cold recycled bituminous mixtures," *Construction and Building Materials*, vol. 199, pp. 298–306, 2019.
- [8] C. Godenzoni, M. Bocci, and A. Graziani, "Rheological characterization of cold bituminous mastics produced with different mineral additions," *Transport Infrastructure and Systems: Proceedings of the AIIT International Congress on Transport Infrastructure and Systems*, p. 185, Rome, Italy, 2017.
- [9] V. Vignali, F. Mazzotta, C. Sangiorgi, A. Simone, C. Lantieri, and G. Dondi, "Rheological and 3D DEM characterization of potential rutting of cold bituminous mastics," *Construction and Building Materials*, vol. 73, pp. 339–349, 2014.
- [10] E. Garilli, F. Autelitano, and F. Giuliani, "Use of bending beam rheometer test for rheological analysis of asphalt emulsion-cement mastics in cold in-place recycling," *Construction and Building Materials*, vol. 222, pp. 484–492, 2019.
- [11] M. Elnasri, G. Airey, and N. Thom, "Experimental investigation of bitumen and mastics under shear creep and creep-recovery testing," in *Airfield and Highway Pavement 2013: Sustainable and Efficient Pavements*, pp. 921–932, American Society of Civil Engineers, Reston, VA, USA, 2013.
- [12] G. Dondi, F. Mazzotta, C. Sangiorgi et al., "Influence of cement and limestone filler on the rheological properties of mastic in cold bituminous recycled mixtures," *Sustainability, Eco-Efficiency, and Conservation in Transportation Infrastructure Asset Management*, vol. 61, 2014.
- [13] H. Soenen, T. Blomberg, T. Pellinen, and O.-V. Laukkanen, "The multiple stress creep-recovery test: a detailed analysis of repeatability and reproducibility," *Road Materials and Pavement Design*, vol. 14, no. sup1, pp. 2–11, 2013.
- [14] F. Cardone, F. Frigio, G. Ferrotti, and F. Canestrari, "Influence of mineral fillers on the rheological response of polymer-modified bitumens and mastics," *Journal of Traffic and Transportation Engineering (English Edition)*, vol. 2, no. 6, pp. 373–381, 2015.
- [15] A. Foroutan Mirhosseini, A. Kavussi, M. H. Jalal Kamali, M. M. Khabiri, and A. Hassani, "Evaluating fatigue behavior

- of asphalt binders and mixes containing date seed ash,” *Journal of Civil Engineering and Management*, vol. 23, no. 8, pp. 1164–1175, 2017.
- [16] C. Hintz and H. Bahia, “Simplification of linear amplitude sweep test and specification parameter,” *Transportation Research Record: Journal of the Transportation Research Board*, vol. 2370, no. 1, pp. 10–16, 2013.
- [17] A. Foroutan Mirhosseini, A. Kavussi, S. A. Tahami, and S. Dessouky, “Characterizing temperature performance of bio-modified binders containing RAP binder,” *Journal of Materials in Civil Engineering*, vol. 30, no. 8, 2018.
- [18] A. Graziani, C. Godenzoni, F. Cardone, and M. Bocci, “Effect of curing on the physical and mechanical properties of cold-recycled bituminous mixtures,” *Materials & Design*, vol. 95, pp. 358–369, 2016.
- [19] S. Ullah and B. F. Tanyu, “Methodology to develop design guidelines to construct unbound base course with reclaimed asphalt pavement (RAP),” *Construction and Building Materials*, vol. 223, pp. 463–476, 2019.

## Research Article

# Macroscopic and Microscopic Characterization of the Effect of “Activation” Process on the Performance of Buton Rock Asphalt-Modified Asphalt

Yafei Li,<sup>1,2</sup> Meng Guo ,<sup>3</sup> and Xu Liu<sup>3</sup>

<sup>1</sup>School of Transportation Science and Engineering, Harbin Institute of Technology, Harbin 150090, Heilongjiang, China

<sup>2</sup>Research & Consulting Department of Road Structure & Materials Research Center, China Academy of Transportation Sciences, Beijing 100029, China

<sup>3</sup>The Key Laboratory of Urban Security and Disaster Engineering of Ministry of Education, Beijing University of Technology, Beijing 100083, China

Correspondence should be addressed to Meng Guo; [mguo@ustb.edu.cn](mailto:mguo@ustb.edu.cn)

Received 23 October 2019; Accepted 6 January 2020; Published 30 January 2020

Guest Editor: Alan Carter

Copyright © 2020 Yafei Li et al. This is an open access article distributed under the Creative Commons Attribution License, which permits unrestricted use, distribution, and reproduction in any medium, provided the original work is properly cited.

In the process of using Buton rock asphalt- (BRA-) modified asphalt, in order to improve the utilization rate of Buton rock asphalt and the performance of the modified asphalt, this paper puts forward the process of “activation” treatment of Buton rock asphalt, that is, grinding and heating of BRA to make natural asphalt precipitate. Laboratory tests show that compared with modified asphalt without activation process, the penetration of the modified asphalt decreases, the softening point rises, the ductility at 5°C and the kinematic viscosity at 135°C all have been increased, and the performance of the modified asphalt increases with the increase of the content of activated BRA. In order to further clarify the effect of “activation” process on the properties of BRA-modified asphalt from microlevel, atomic force microscopy (AFM) was used to test the microproperties of Buton rock asphalt before and after activation. It is found that the Derjaguin–Muller–Toporov (DMT) modulus of the modified asphalt is about 2.5 times that of base asphalt, which indicates that the viscous degree of modified asphalt with activated BRA has been greatly increased and the modification effect is remarkable.

## 1. Introduction

Buton rock asphalt (BRA) is natural rock asphalt produced in the Buton island of Indonesia. It is an asphalt residual substance derived from the combined action of heat energy, pressure, oxidation, and catalyst bacteria after the seepage and overflow of ancient oil after hundreds of thousands of years of deposition and change. Buton rock asphalt is a special asphalt-mineral blend with stable properties and strong peeling resistance, which has developed micropore and strong adsorption capacity for free asphalt. The surface and interior of active minerals with high crystallinity also have strong adsorption capacity for pure asphalt with high viscosity. It usually has high softening point, high viscosity, strong oxidation resistance, and antimicrobial corrosion ability. It contains no wax, has a large molecular weight, is easy to store and process, and has a good water sensitivity

and weather resistance. Similar to the chemical structure of matrix asphalt, it has good compatibility and no segregation. Modified asphalt as a modifier can improve the performance of asphalt pavement, especially high temperature stability, water damage resistance, and durability. Social and economic benefits are very significant [1–4].

Li et al. found the presence of more calcium carbonate in BRA. In the BRA-modified asphalt, asphalt and BRA particles were present infiltrated, forming a two-phase continuous structure with interlacing. The number of aggregates in BRA-modified asphalt decreased, and the temperature stability is improved [5]. Liu et al. revealed that the asphalt in Buton rock can obviously improve the high-temperature performance of base asphalt but, at the same time, reduce its low-temperature performance [6]. Zou et al.’s test results show that, with increasing BRA content, the binder’s penetration decreased, softening point increased, dynamic



viscosity at 60°C increased, and complex modulus increased. The incorporation of BRA in the binder also changed the viscoelastic property of the asphalt binder [7]. Liu et al. used the uniaxial penetration test to study the high-temperature performance of Buton rock asphalt mixture with different mixing process in a mixing plant. The results showed that the high-temperature performance of Buton rock asphalt mixture prepared by BRA postprocessing process was better than that of conventional process [8]. Wu et al. systematically studied the high-temperature performance of Buton rock asphalt-modified asphalt through the conventional high-temperature performance test and dynamic shear rheological test. They found that the high-temperature performance of Buton rock asphalt-modified asphalt was significantly better than that of No. 70 base asphalt [9].

Li et al. studied the effect of BRA on the physical and mechanical properties of asphalt binder and asphalt mixture. They found that the activation treatment can effectively enhance the molecular polarity of Buton rock asphalt but the micromechanism needs to be explained [10]. Tan and Guo studied the cohesion and adhesion of asphalt mastic by using surface free energy method. They found that a good correlation exists between complex modulus  $G^*$  of asphalt mastic and work of adhesion [11]. Furthermore, they investigated the interaction between asphalt and mineral fillers and its correlation to mastics' viscoelasticity in detail and found that the interfacial behavior had a significant effect on the bulk property [12]. These findings imply that BRA could be improved by some interface treatment. The BRA looks like the asphalt mastic, but it has more complicated interfacial structure.

The content of natural asphalt in Buton rock asphalt ranges from 20% to 30%. Most of the natural asphalt is distributed in the cracks of BRA. If it is not treated, it can be modified directly by blending it with base asphalt, which results in the effective asphalt that can play a very few role [10, 13]. Nowadays, China only regards natural asphalt as a special asphalt modifier and has not formed a set of relatively perfect technical performance standard system. Most of the existing related research is limited to the mix design and road performance verification of modified asphalt mixtures, lacking in-depth study on the modification mechanism of natural asphalt [14]. In order to improve the utilization rate of Buton rock asphalt and improve the performance of modified asphalt, this paper puts forward the "activation" treatment of Buton rock asphalt; that is, the natural asphalt in the cracks of Buton rock asphalt can be precipitated after grinding the BRA to a certain size range and heating at 150–180°C. In order to clarify the effect of "activation" process on the performance of BRA-modified asphalt, the following research is carried out in this paper.

## 2. Materials and Methods

**2.1. Raw Materials.** Buton rock asphalt raw material is made of BRA dry powder produced by Hubei ZhengKang Natural Asphalt Technology Co., LTD., and the base asphalt is road asphalt 70. Specific performance indicators are shown in Tables 1 and 2. The technical indicators meet the specifications [15–17].

TABLE 1: Technical index of BRA.

Items	Units	Test results	Technical indices
Colour character	—	Brown powder	Black or brown powder
Ash content	%	73.6	≤80
Moisture content	%	<0.6	<2

TABLE 2: Technical index of #70 road petroleum asphalt.

Items	Unit	Test results	Technical requirements
Penetration at 25°C	0.1 mm	73	60~80
Softening point	°C	47	>46
Ductility at 5°C	cm	100	100
Kinematic viscosity at 135°C	m <sup>2</sup> /s	0.45	<3

**2.2. Activation Technology of Buton Rock Asphalt.** The crushed BRA particles with particle size less than 3 mm were added to the activation equipment, dehydrated, stirred, and maintained for 9 minutes at 150°C–180°C, and the moisture content of dehydrated BRA particles was controlled below 2%. The process activates the resin composition in natural BRA, and the activated oil was coated with sand grains, which can transform the original BRA into colloidal asphalt, which is beneficial to improve the use effect of asphalt. Through microscopic image characterization, we observed the preactivated and activated BRA, in which the activated BRA surface was covered with a large number of natural asphalt, as shown in Figure 1 [18].

## 3. Results and Discussion

**3.1. Effect of "Activation" of Buton Rock Asphalt on the Performance of Modified Asphalt.** Unactivated and activated Buton rock asphalt was added into matrix bitumen according to 10%, 20%, 30%, and 40%, respectively. Modified bitumen with different content of Buton rock asphalt was prepared by an indoor small colloidal mill. The penetration at 25°C, softening point, ductility at 5°C, and kinematic viscosity at 135°C were measured. The specific test results are shown in Figures 2–5.

From Figures 2–5, it can be seen that the penetration and ductility at 5°C of modified asphalt decrease with the increase of BRA content, and the softening point and viscosity increase with the increase of BRA content, regardless of whether the former or the latter, indicating that the viscosity of asphalt increases with the increase of BRA, which is beneficial to the improvement of the high-temperature deformation resistance of modified asphalt.

Compared with BRA-modified asphalt before activation, the penetration of modified asphalt decreased, softening point increased, and ductility at 5°C and kinematic viscosity at 135°C increased after adding activated BRA, and the trend became more and more obvious with the increase of the content of activated BRA, indicating that the activation process further enhanced the viscosity of BRA-modified asphalt. Specifically, when the content of

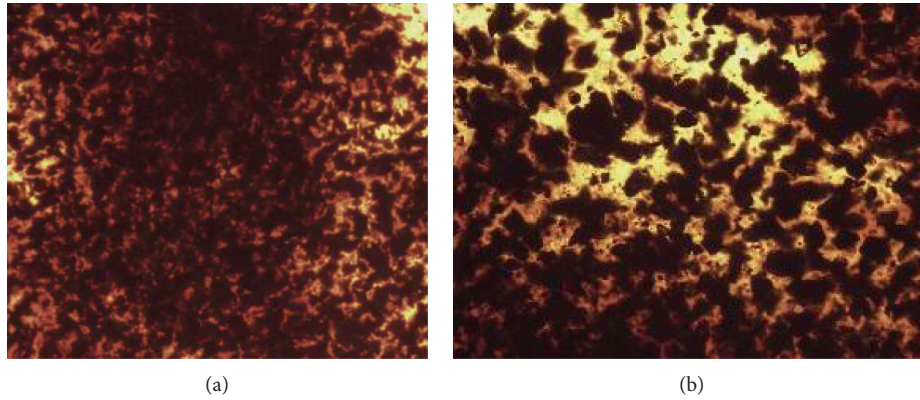


FIGURE 1: Preactivated (a) and activated (b) BRA microscopic images.

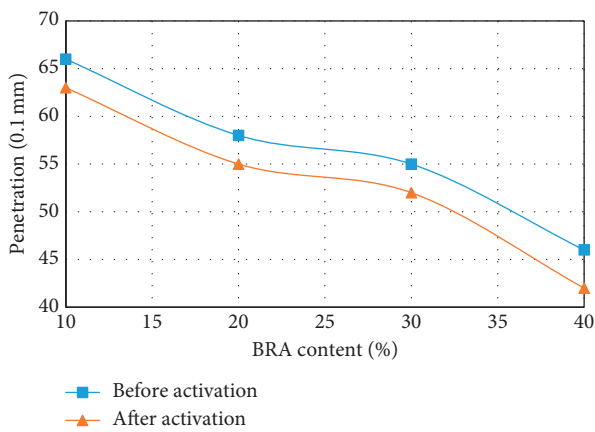


FIGURE 2: Chart of penetration of BRA-modified asphalt with dosage before and after activation.

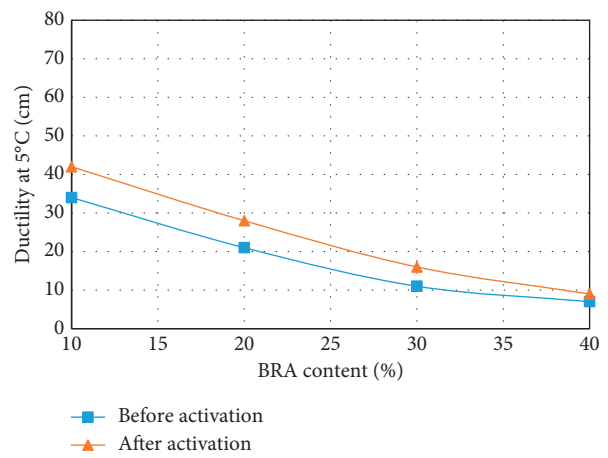


FIGURE 4: Map of ductility at 5°C of BRA-modified asphalt with dosage before and after activation.

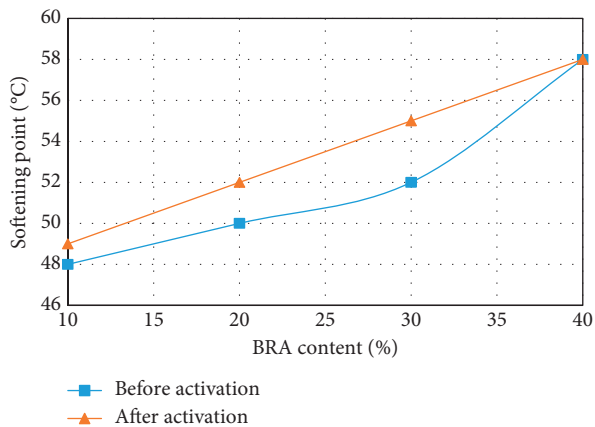


FIGURE 3: Softening point of BRA-modified asphalt before and after activation.

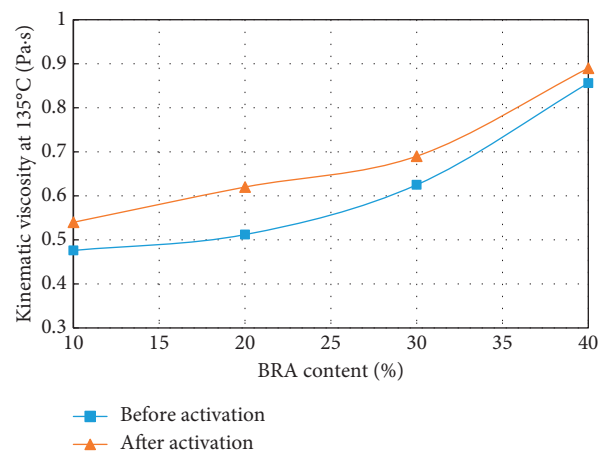


FIGURE 5: Chart of kinematic viscosity at 135°C of BRA-modified asphalt with dosage before and after activation.

activated Buton rock asphalt is more than 30%, the ductility index attenuates seriously. This is due to the ash content of Buton rock asphalt in BRA-modified asphalt. During the ductility test, it is easy to produce stress concentration at

ash particles, which results in low ductility index, indicating that this test method is not suitable for evaluating BRA-modified asphalt.

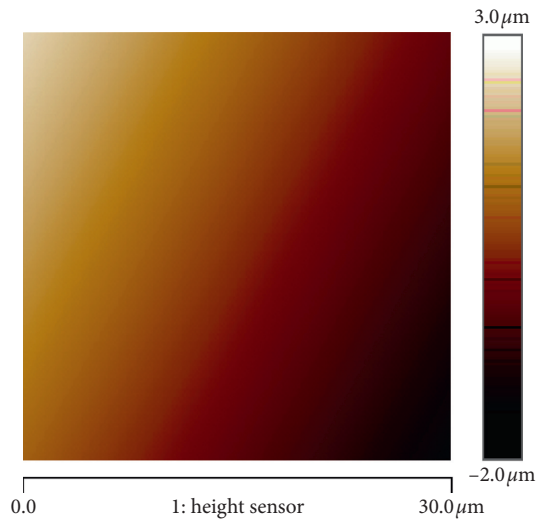


FIGURE 6: Nanomorphology diagram of #70 matrix asphalt.

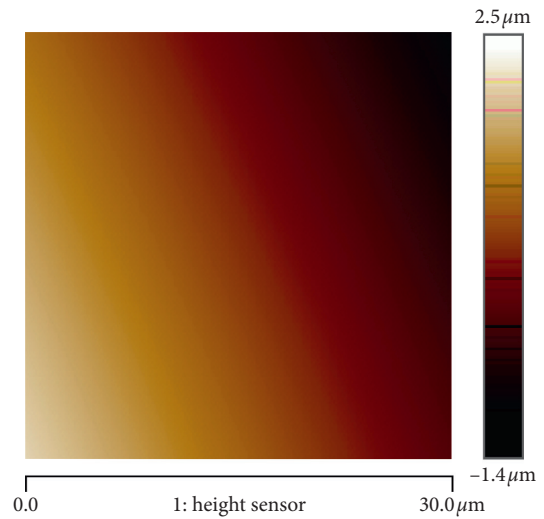


FIGURE 8: Nanomorphology of #70 matrix asphalt + 30% activated Buton rock powder.

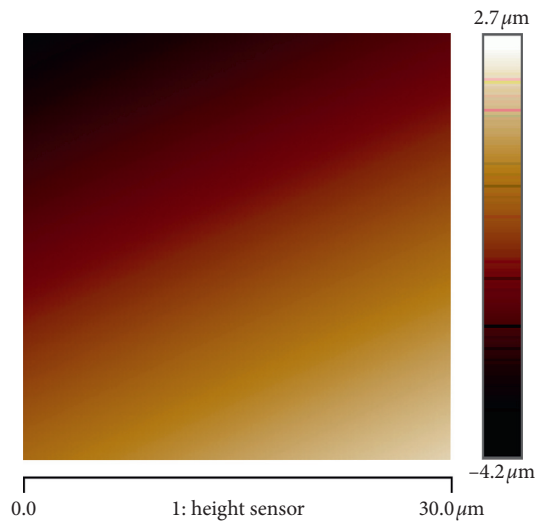


FIGURE 7: Nanomorphology of #70 matrix asphalt + 30% pre-activated Buton rock powder.

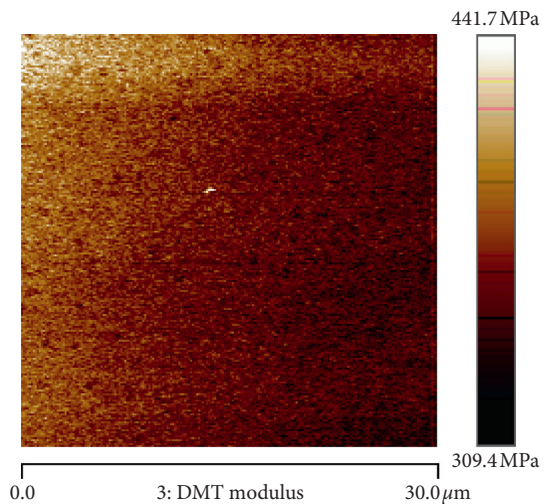


FIGURE 9: DMT modulus diagram of matrix asphalt.

### 3.2. Study on Microstructure of BRA-Modified Asphalt before and after Activation Based on Atomic Force Microscope.

In order to study the effect of activation process on the properties of BRA-modified asphalt from the micropoint of view, in this paper, the nanomorphology of the modified asphalt doped with 30% activated precursor asphalt and activated BRA was observed by atomic force microscopy [19].

The peak force QNM mode is selected for the AFM test. The cantilever end of AFM is RFESPA of Bruker company. Its nominal resonance frequency is 75 Hz, and its nominal elastic constant is 3 N/m (the real elastic constant measured by the “thermal tune” method is 4.3 N/m). The tip material is silicon with a height of 15–20  $\mu\text{m}$  and a nominal tip radius of 8 nm. The peak force set point is 10 nN, the scanning frequency is 0.5 Hz, the scanning angle is  $90^\circ$ , and the scanning area is  $30 \mu\text{m} \times 30 \mu\text{m}$ .

**3.2.1. Nanotopography.** Figures 6–8 show that the nanomorphology of modified asphalt and that of #70 road asphalt have not changed much after adding BRA.

**3.2.2. Nanoadsorption.** Since there is no significant difference between BRA-modified asphalt and #70 road asphalt in nanomorphology, the surface nanoadhesion force of asphalt samples was characterized by the atomic force microscopy (AFM) DMT model [20]. In 1977, Tabor introduced a kind of dimensionless parameter [21], which can be used to distinguish the applicability of JKR and DMT models. The DMT model is suitable for contact with small deformation and large elastic modulus. The DMT model can describe the real force between probe and sample and estimate the adhesion work reasonably. The typical results are shown in Figures 9–11.



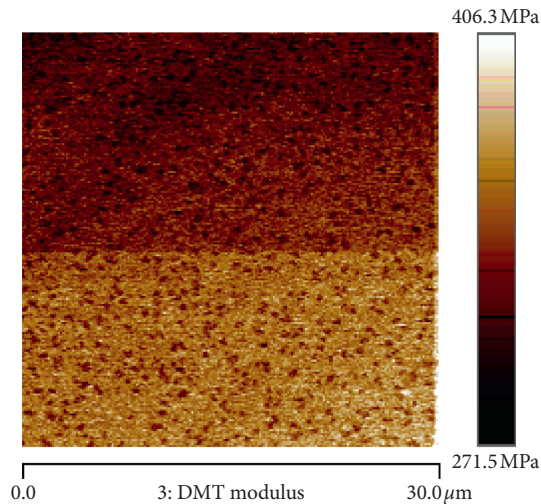


FIGURE 10: DMT modulus diagram of #70 matrix asphalt + 30% preactivated Buton rock powder.

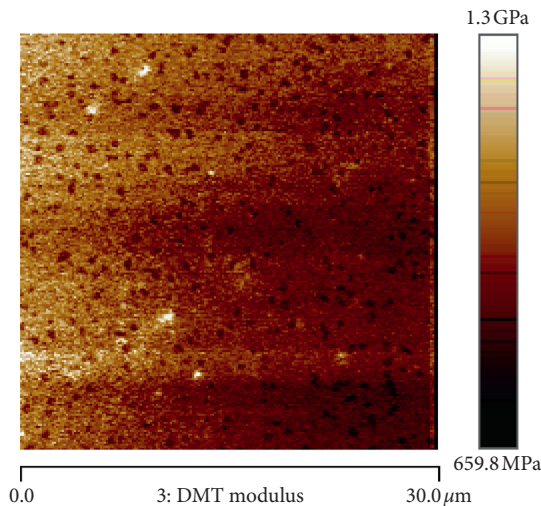


FIGURE 11: DMT modulus diagram of #70 matrix asphalt + 30% activated Buton rock powder.

From Figures 9–11, it can be seen that adding 30% activated Buton rock powder can slightly reduce the surface DMT modulus of base asphalt but adding 30% activated Buton rock powder can significantly improve the surface DMT modulus of base asphalt.

In order to study the overall regularity of different modification effects on asphalt, this part takes the average of the nanoadhesion force of all samples on the area of  $30\ \mu\text{m} \times 30\ \mu\text{m}$ , and the results are shown in Figure 12.

From Figure 12, it can be seen that before 30% activation, Buton rock powder can slightly reduce the DMT modulus of asphalt. However, 30% activated Buton rock powder can significantly improve the DMT modulus of asphalt, and the DMT modulus of modified asphalt is about 2.5 times that of base asphalt. This shows that the viscous degree of activated BRA-modified asphalt has greatly increased, which confirms the macro test results.

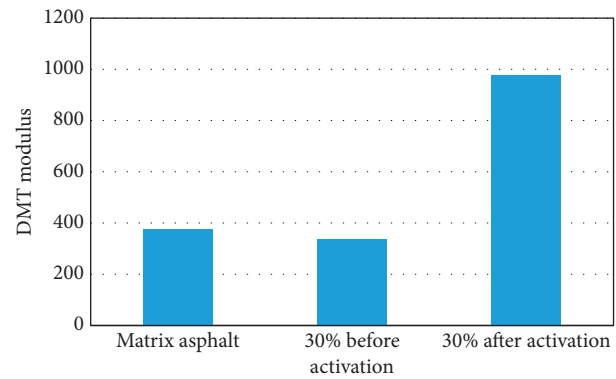


FIGURE 12: Effect of activation on mean modulus of DMT of BRA-modified asphalt.

#### 4. Conclusions

- (1) “Activation” technology activates the resin composition in BRA, and the activated oil is coated with sand grains, which can transform the original rock state asphalt into colloidal state asphalt, which is beneficial to improve the use effect of asphalt.
- (2) Laboratory tests show that the penetration of modified asphalt decreased and softening point, ductility at  $5^\circ\text{C}$ , and kinematic viscosity at  $135^\circ\text{C}$  of the modified asphalt with “activation” process are higher than those without “activation” process, and the trend is more obvious with the increase of the content of the modified asphalt.
- (3) Atomic force microscopy (AFM) was used to test the microproperties of Buton rock asphalt before and after activation. It is found that the DMT modulus of modified asphalt is about 2.5 times that of base asphalt, which indicates that the viscous degree of modified asphalt with activated BRA has been greatly increased and the modification effect is remarkable.

#### Data Availability

The data used to support the findings of this study are included within the article.

#### Conflicts of Interest

The authors declare no conflicts of interest.

#### Authors’ Contributions

Yafei Li and Meng Guo conceived and designed the experiments; Yafei Li performed the experiments; Yafei Li and Xu Liu analyzed the data; Yafei Li contributed reagents/materials/analysis tools; and Meng Guo and Xu Liu wrote the paper.

#### Acknowledgments

This study was supported by the National Natural Science Foundation of China (51808016) and Young Elite Scientists

Sponsorship Program by China Association for Science and Technology (2018QNRC001).


## References

- [1] X. Y. Lu, S. Y. Zhang, and Y. F. Wu, "Effect of Buton rock mineral material on asphalt mixture performance," *Journal of Architectural Materials*, vol. 18, no. 3, pp. 450–457, 2015.
- [2] R. X. Li, *Study on Technical Characteristics of Buton Rock Asphalt Rock Asphalt and its Mixture*, Chang'an University, Xi'an, China, 2010.
- [3] G. Q. Zhou, "Test and research on road performance of Buton rock asphalt and mixture," *Petroleum Asphalt*, vol. 25, no. 4, pp. 40–44, 2011.
- [4] L. Fan, Q. J. Shen, and Y. Y. Zhang, "The influence of natural rock asphalt modification on the performance of asphalt pavement," *Journal of Building Materials*, vol. 10, no. 6, pp. 740–744, 2007.
- [5] R. X. Li, P. W. Hao, C. Wang, and Q. Zhang, "Buton rock asphalt modification mechanism," *Highway Transportation Science and Technology*, vol. 28, no. 12, pp. 16–20, 2011.
- [6] S. T. Liu, Y. S. Yang, J. G. Fang, and Z. Y. Guo, "Experimental study of Buton rock asphalt modified asphalt mixture," *Journal of Tongji University: Natural Science Edition*, no. 3, pp. 351–355, 2007.
- [7] G. Zou and C. Wu, "Evaluation of rheological properties and field applications of Buton rock asphalt," *Journal of Testing and Evaluation*, vol. 43, no. 5, Article ID 20130205, 2015.
- [8] L. P. Liu, J. Z. Qin, and Y. S. Hong, "The influence of manufacturing technology on the high temperature performance of Buton rock asphalt mixture," *Journal of Wuhan University of Technology: Transportation Science and Engineering Edition*, vol. 42, no. 1, pp. 44–47, 2018.
- [9] Y. F. Wu, J. Liao, W. Q. Huang, W. K. Feng, and M. M. Cao, "Buton rock asphalt modified asphalt high temperature performance analysis," *Journal of Chengdu University: Natural Science Edition*, vol. 38, no. 1, pp. 106–110, 2019.
- [10] Y. F. Li, J. Chen, J. Yan, and M. Guo, "Influence of Buton rock asphalt on the physical and mechanical properties of asphalt binder and asphalt mixture," *Advances in Materials Science and Engineering*, p. 7, 2018.
- [11] Y. Tan and M. Guo, "Using surface free energy method to study the cohesion and adhesion of asphalt mastic," *Construction and Building Materials*, vol. 47, pp. 254–260, 2013.
- [12] M. Guo and Y. Tan, "Interaction between asphalt and mineral fillers and its correlation to mastics' viscoelasticity," *International Journal of Pavement Engineering*, pp. 1–10, 2019.
- [13] L. Zhong, Y. Zhang, T. Wang, Y. Ji, P. Norris, and W.-P. Pan, "Optimized methods for preparing activated carbon from rock asphalt using orthogonal experimental design," *Journal of Thermal Analysis and Calorimetry*, vol. 136, no. 5, pp. 1989–1999, 2019.
- [14] X. D. Cha, J. X. Hu, A. H. Liu, and G. Y. Qian, "Experimental analysis of properties of Buton rock asphalt materials," *Journal of Changsha University of Technology: Natural Science Edition*, vol. 14, no. 4, pp. 10–17, 2017.
- [15] Ministry of Transport of the People's Republic of China, *Standard Test Methods of Bitumen and Bituminous Mixture for Highway Engineering*, Ministry of Transport of the People's Republic of China, Beijing, China, 2011.
- [16] Ministry of Transport of the People's Republic of China, *Technical Specifications for Construction of Highway Asphalt Pavements*, Ministry of Transport of the People's Republic of China, Beijing, China, 2004.
- [17] Ministry of Transport of the People's Republic of China, *Modifiers for Asphalt Mixture-Part 5: Natural Asphalt*, Ministry of Transport of the People's Republic of China, Beijing, China, 2014.
- [18] W. T. Huang and G. Y. Xu, "Experimental study on road performance of Buton rock asphalt mixture," *Journal of South China University of Technology: Natural Science Edition*, vol. 40, no. 2, pp. 87–91, 2012.
- [19] J. Yang, M. H. Gong, T. Pauli, J. M. Wei, and X. T. Wang, "Microstructure of asphalt based on atomic force microscopy," *Journal of Petroleum Processing*, vol. 31, no. 4, pp. 959–965, 2015.
- [20] G. Q. Sun, Q. Pang, and D. Q. Sun, "Research progress of asphalt microstructures based on AFM," *Petroleum Asphalt*, no. 4, pp. 18–24, 2016.
- [21] D. Tabor, "Surface forces and surface interactions," *Journal of Colloid and Interface Science*, vol. 58, no. 1, pp. 2–13, 1977.



## Research Article

# Mechanical Characterization and Chemical Identification of Clear Binders for Road Surface Courses

Andrea Grilli <sup>1</sup>, Maurizio Bocci,<sup>2</sup> Amedeo Virgili,<sup>2</sup> and Carla Conti<sup>2</sup>

<sup>1</sup>Università degli Studi della Repubblica di San Marino, via Consiglio dei Sessanta, 99-47890 San Marino, San Marino

<sup>2</sup>Università Politecnica delle Marche, via Brecce Bianche, 1-60131 Ancona, Italy

Correspondence should be addressed to Andrea Grilli; [andrea.grilli@unirmsm.sm](mailto:andrea.grilli@unirmsm.sm)

Received 1 September 2019; Revised 8 December 2019; Accepted 28 December 2019; Published 20 January 2020

Academic Editor: María Criado

Copyright © 2020 Andrea Grilli et al. This is an open access article distributed under the Creative Commons Attribution License, which permits unrestricted use, distribution, and reproduction in any medium, provided the original work is properly cited.

The development of non-black asphalt mixtures for surface courses may play a significant role to improve functional, aesthetic and environmental issues of road pavements. Nowadays, the development of clear binders as substitutes for traditional bitumen in asphalt mixtures, which combine durability and mechanical properties, exalting the color of pavements for a better integration of road networks in urban and environmentally sensitive areas, is undoubtedly a timing challenge. However, the selection and classification of clear binders are often based only on color and standard requirements referred to traditional bitumen that do not describe consistently the binder behavior. A better understanding on clear binder properties is required to guide the aggregate selection and the mix design for surface layer, merging safety, aesthetical and environmental benefits into long lasting pavement. This paper presents a comprehensive experimental program, including empirical tests, infrared spectrum analysis, and rheological testing over a wide range of temperature and frequency, to determine the overall mechanical behavior of three clear binders. Results highlighted that the selected clear binders differ from traditional bitumen in terms of mechanical behavior. Different composition or origin can induce to completely different performance. Moreover, the combination of several testing procedures allowed suggesting specific application methods and uses for the three clear binders.

## 1. Introduction

A new awareness on environmental impact and driver safety has risen more and more interest in non-black asphalt pavements since the color of the road pavement helps in achieving numerous advantages. Indeed, the development of non-black asphalt mixtures may play a significant role to improve functional, aesthetical, and environmental issues for road pavements [1, 2].

Currently, non-black asphalt pavements are intended to satisfy specific functional and safety requirements separating different traffic flows through well-evident pedestrian, bus, or bicycle lanes, or identifying distinctive zones such as intersections, roundabouts, or border of residential areas. Moreover, a non-black asphalt pavement facilitates the integration of the road network in a human context, mitigating and giving an additional contribution to the aesthetical perception of the overall surrounding area. For these

reasons, non-black asphalt pavements also offer favored solutions in historic center, touristic areas, or pathways [3].

Non-black asphalt pavements can be obtained in several ways such as using colored aggregates and pigments to traditional bitumen or clear binders (or a combination of them) in surface treatments and in asphalt mixtures for surface layer [4]. However, after weathering and wearing, the color of aggregates becomes dominant in influencing the aesthetic and durability of pavement color [2]. Therefore, the most effective and durable method appears to be the selection of aggregates, in terms of both physicochemical properties and color, and translucent binders, or so-called “clear binders.”

The transparency of these binders allows the natural color of mineral aggregates to be really exalted over time, along with complying binding and covering performance. An additional paramount potentiality in reducing environmental impact can be obtained when using white aggregate and clear binder. Really, enhanced photometrical characteristics allow energy

consumption for lighting to be significantly reduced with the largest advantages in tunnels [5, 6] and the urban heat island phenomenon to be substantially moderated [7, 8].

In the past, clear binders were mainly used in surface layer mixtures only for pedestrian areas. Nowadays, the improvement of the mechanical performance makes clear binders suitable in trafficked road, too.

Clear binders are special formulations with a yellowish aspect that may contain tackifying resin, dispersing oil, materials of vegetal origin, or polymers [9]. Clear binders can be mainly distinguished in low asphaltene content bitumen, natural binder, and synthetic binder [3, 10]. Though different clear binders offer similar aesthetical impact and mimic the mechanical properties of bitumen, origin and production processes influence their mechanical behavior, durability, and ageing [11]. Therefore, a thorough understanding of clear binder properties over a wide range of temperature and frequency must be considered to address the selection of constituent materials and to deal with the mix design, accurately.

## 2. Objectives

Clear binders are asked to improve the road safety, aesthetic, and environmental impact of pavements, ensuring high mechanical performance to withstand the vehicular traffic. Currently, a lack of standardized methods to classify and to characterize clear binders (they are not polymer modified bitumens, neither paving grade bitumens) makes the selection of clear binders a hazardous and rash procedure, often without matching their specific characteristics with application method and use. A better understanding on clear binder properties is needed to identify specific uses (climatic and traffic conditions) and applications (production, laying and compaction procedures). Future research on a proper mix design method for surface layer mixtures should merge safety aesthetical and environmental benefits into long lasting pavement.

This paper focuses on the chemical identification and mechanical characterization of three clear binders that represent an alternative to traditional bitumen when used in asphalt concrete for surface courses.

In this context, the objectives of this paper are as follows:

- (1) Chemical identification and determination of components in clear binders by Fourier transform infrared spectroscopy (FTIR) testing
- (2) Verification of empirical testing to characterize and to classify clear binders
- (3) Investigation on the viscoelastic behavior of clear binders by means of rheological characterization in a broad range of temperature and frequency
- (4) Recommendation for use/selection of the three clear binders in specific circumstances (traffic loading and climate condition)

## 3. Experimental Program and Testing Procedures

Three yellowish clear binders (so-called K, R, and C) coming from different production processes were selected as the

most representative in the Italian market. The experimental program consisted in three main phases:

- (1) Identification and qualitative analysis of binder components by means of FTIR
- (2) Empirical characterization to classify clear binders using the well-known framework specification for bituminous binders for a preliminary ranking
- (3) Rheological characterization to determine the mechanical properties of clear binders as a function of loading frequency and temperature

In the first phase, FTIR allowed studying the interactions of matter with electromagnetic radiation using electromagnetic waves within a wide, continuous range of frequencies. Fundamental vibrations, mainly stretching and bending of chemical bonds as well as some rotational motions in molecules, were detected in the middle infrared region within the interval of wavenumbers from 4000 to 600  $\text{cm}^{-1}$ . The intensity of signal, passing through the probing sample was measured at each specific wavenumber (wavelength or frequency) by a detector resulting in an interferogram which was immediately transformed into an infrared spectrum by the mathematical function Fourier transform. In this case, spectral data were obtained with a PerkinElmer Spectrum GX1 FT-IR, in transmission mode on NaCl plates. The spectral resolution was 4  $\text{cm}^{-1}$ . Baseline (two-point linear fit), second derivative, Fourier self deconvolution, and low Gaussian character curve fitting procedures were applied. For data handling, Spectrum v.6.3.1 and Grams AI software packages were used.

For the second phase, the empirical characterization of the binders was based on the EN 14023 with regards to the following:

- (i) Penetration value at 25°C complying with EN 1426 to evaluate the consistency of the binders at 25°C
- (ii) Softening point by ring and ball testing in accordance with EN 1427 to evaluate the consistency of the binders at high service temperature and the transition temperature from viscoelastic to viscous behavior
- (iii) Elastic recovery at 25°C complying with EN 13398 to evaluate the behaviour of binders under large deformation
- (iv) Rolling thin film oven test (RTFOT) complying with EN 12607-1 to evaluate the effect of the short-term ageing on the binders in term of mass variation, retained penetration, and increase of softening point
- (v) Viscosity at 100, 135, 160, and 180°C in accordance with EN 13302 to evaluate the consistency of binders at the operative temperatures (storage, pumping, mixing, compacting, and other handling operations)

Moreover, the Ancona stripping test (AST) was used to evaluate potential stripping of a binder-aggregate system [12]. The AST was selected for this preliminary study on the affinity

between clear binders and aggregate. The past experience helped in the interpretation of results (transparent or yellowish color does not facilitate the assessment of the degree of binder coverage on aggregate particles) and sample preparation method. A sample of binder-covered aggregates (60 g of coarse aggregate, passing 10 mm sieve and retained on 6 mm sieve, mixed with 3 g of binder) was placed in a 600 ml beaker with 200 ml of distilled water. The 600 ml beaker was then placed in a 2000 ml beaker containing 600 ml of boiling water for 45 minutes. At the end of this period, the binder-aggregate system was removed from the beaker and cooled at room temperature, and a visual assessment of the stripping percentage was made by three technicians. In this study, the three clear binders were mixed with a siliceous coarse aggregate at the mixing temperature of the specific binder ( $T_{\text{mix}}$ ) as indicated by viscosity testing. The siliceous coarse aggregate was selected having suitable physical properties (Los Angeles coefficient = 17; water absorption = 1.22%; polished stone value = 50; shape index = 10) and luminance ( $69.3 \text{ cd/m}^2$ ) to exalt the aesthetical aspect and photometric characteristics of a surface layer.

In the third phase, the rheological characterization of the clear binders was performed by means of sinusoidal oscillatory tests using a dynamic shear rheometer (DSR). Strain sweep tests were carried out to determine the linear viscoelastic limit and, consequently, a suitable deformation amplitude ( $\gamma = 0.5\%$ ). The frequency sweep with a strain amplitude  $\gamma = 0.5\%$  was conducted to measure the complex modulus  $G^*$ , storage modulus  $G'$ , loss modulus  $G''$ , and the phase angle  $\delta$  over a frequency range from 0.159 to 15.9 Hz (0.159, 0.283, 0.503, 0.894, 1.591, 2.833, 5.029, 8.945, and 15.915 Hz), i.e., from 1 to 100 rad/s, and over a temperature range from 82 to 34°C and from 34 to 4°C (6°C intervals) using the 25 mm plate and the 8 mm plate, respectively (EN 14770: 2012). Although clear binders resulted rheological complex materials, the experimental data measured at different temperatures were superposed onto master curves at a reference temperature ( $T_r = 20^\circ\text{C}$ ) to extend the investigation over a wide range of loading frequency [13]. The data analysis considered the average values from three repetitions for each test.

The obtained results on clear binders were compared with a 70/100 paving grade bitumen (considered as a typical unmodified bitumen) and a styrene butadiene styrene (SBS) modified bitumen PMB 45/80-70 (considered as a typical modified bitumen).

## 4. Analysis of Results

**4.1. Chemical Identification.** When the infrared radiations pass through a sample, some of them are absorbed and others are transmitted. The resulting spectrum represents the molecular absorption or transmission, creating a molecular fingerprint of the sample. Like a fingerprint, no two different molecular structures produce the same infrared spectrum. Figure 1 shows the FTIR spectra for the selected clear binders in comparison with a traditional bitumen (70/100 paving grade bitumen) and a styrene butadiene styrene (SBS) modified bitumen (PMB 45/80-70).

The infrared spectrum of K (light blue line), analogously to a 70/100 traditional bitumen (black line), mainly shows hydrocarbon absorptions like  $\text{CH}_2$  and  $\text{CH}_3$  stretching in the range of  $3000\text{--}2800 \text{ cm}^{-1}$ ,  $\text{CH}_2$  and  $\text{CH}_3$  bending at  $1460$  and  $1376 \text{ cm}^{-1}$ , and a weak band at  $1600 \text{ cm}^{-1}$  due to the presence of aromatic linkages. On the other hand, analogously to a polymer modified bitumen PMB 45/80-70, additional bands at  $969$  and  $699 \text{ cm}^{-1}$  due to the presence of aliphatic  $\text{C}=\text{C}$  double bonds (SBS) can be clearly identified. Moreover, bands at  $1215$  and  $753 \text{ cm}^{-1}$  attributable to  $\text{CH}_2$  out of plane bending deformations can also be highlighted. The data analysis suggests that the origin of K derives from a deasphalted bitumen (low amount of asphaltenes) modified with SBS polymer to perform a satisfactory link with the matrix.

The spectra of C (green line) and R (grey line) can be assigned to hydrocarbon absorptions, like  $\text{CH}_2$  and  $\text{CH}_3$  stretching in the range of  $3000\text{--}2800 \text{ cm}^{-1}$  and  $\text{CH}_2$  and  $\text{CH}_3$  bending at  $1460$  and  $1376 \text{ cm}^{-1}$ . For both binders, high amount of  $\text{CH}_3$  presumes short chains, implying low stiffness at ambient temperature. C and R show a spectrum like an aromatic phthalic polymer (ester,  $\text{CO}$  stretching in the range of  $1740\text{--}1720 \text{ cm}^{-1}$  and  $\text{C-O}$  stretching in the range of  $1170\text{--}1070 \text{ cm}^{-1}$ ), suggesting a synthetic origin. Moreover, the C spectrum deconvolution highlights a band at  $1715 \text{ cm}^{-1}$  that would claim the presence of natural waxes [14].

As regards to polymer modification, the percentage of SBS was evaluated by the ratio between the reference bands at  $1376 \text{ cm}^{-1}$  ( $\text{CH}_3$ , symmetric band) and the characteristic bands at  $969$  and  $699 \text{ cm}^{-1}$  of the unsaturated component [15, 16]. The polymer blend as a modifier for bitumen provides a new route to enhance its rheological properties directly related to service performance. The unsaturation index was calculated as 8.2, 5.0, 4.9, and 2.3 for R, PMB 45/80-70, K, and C, respectively [17].

**4.2. Empirical Characterization.** The most common empirical tests for bitumen characterization were used to classify the selected binders, although results could not necessarily address the same deductions as for traditional bitumen.

The clear binders showed penetration and softening point values of the same magnitude of bituminous binders (Figure 2); hence, bitumen traditional testing may be considered to determine the clear binder consistency at service temperature (from  $25^\circ\text{C}$  to the transition temperature from viscoelastic to viscous behavior).

The selected clear binders are characterized by higher softening point and elastic recovery values than those of paving grade bitumens, due to the contribution of the polymeric modification as highlighted by FTIR.

Binder K showed penetration and elastic recovery values at  $25^\circ\text{C}$  similar to PMB 45/80-70, even if the softening point of K is close to the 70/100 paving grade bitumen [4]. In terms of consistency at service temperature, binder K could be considered as a paving grade bitumen with improved elastic recovery.

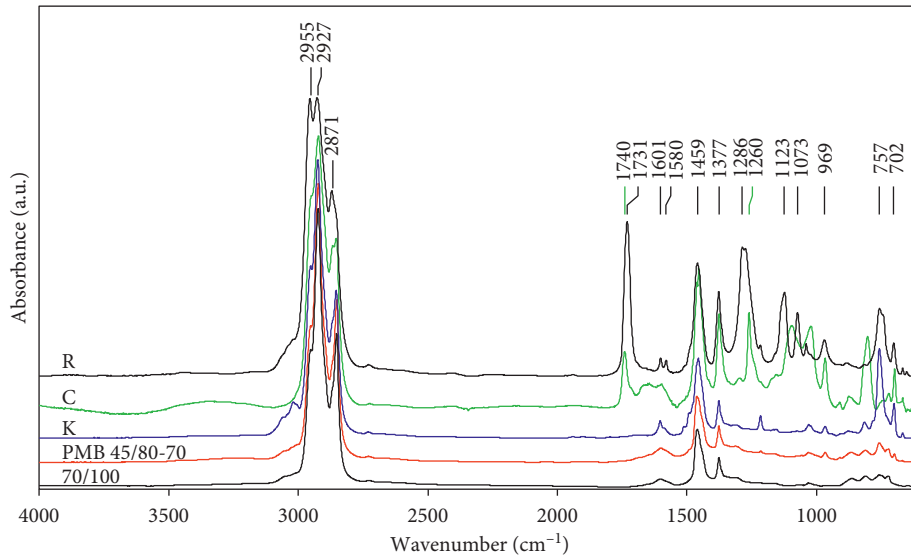


FIGURE 1: FTIR spectra for the selected binders in the range 4000–600  $\text{cm}^{-1}$ .

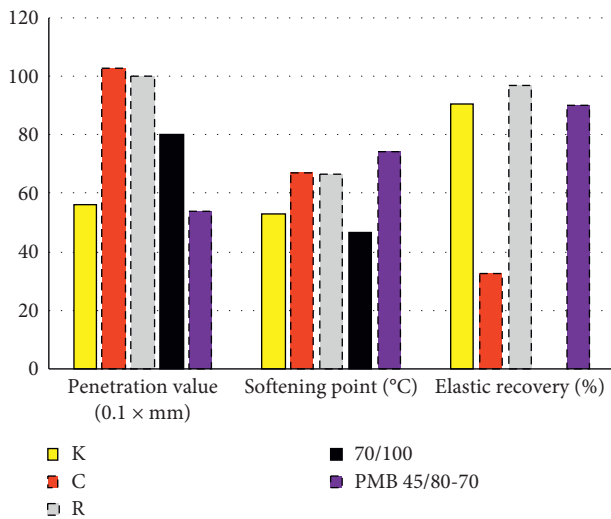


FIGURE 2: Penetration, softening point, and elastic recovery values of tested binders.

Binders C and R have the highest penetration values at 25°C; thus, in terms of consistency at 25°C, binders C and R could be considered softer than the 70/100 paving grade bitumen but with softening point similar to PMB 45/80-70. Moreover, the elastic recovery of binder R is even higher than PMB 45/80-70 confirming the findings from FTIR.

Clear binders showed resistance to short-term ageing process complying with the EN 12591 requirements for their specific grade as shown in Table 1.

The classification method for paving grade bitumens (EN 12591) has been extended to modified binders for road pavements having improved performances. Using the framework specification for polymer modified bitumens (EN 14023), the characteristics for polymer modified bitumens are classified into range of grades suitable for the manufacture of the materials for road construction and

maintenance. Particularly, the designation of polymer modified bitumens comprises the penetration range and the minimum softening point. Following this principle, the nomenclature of K, C, and R should be 45/80-50, 65/105-65, and 65/105-65, respectively.

As far as the elastic recovery is concerned, binder C that showed the lowest elastic recovery value could not be included into a specified class. Note that, as reported by FTIR analysis, binder C had the lowest polymer content.

Dynamic viscosity tests showed that the viscosity values of binder C are similar to those of the 70/100 paving grade bitumen, whereas the other binders showed high viscosity values, closer to those of polymer modified bitumens. As the softening point of binder C is higher than that of a paving grade bitumen, binder C seems to melt quickly from about 60 to 100°C, changing from a modified bitumen-like consistency to a bitumen-like consistency. This behavior appears consistent with the supposition of the presence of natural waxes from FTIR analysis.

Table 2 reports the mixing and compaction temperatures ( $T_{\text{mix}}$  and  $T_{\text{comp}}$ , respectively) obtained by analysing the evolution of viscosity  $\eta$  versus temperature  $T$  using a power law relationship  $\eta = a \cdot T^b$ , where  $a$  and  $b$  are material experimental parameters.

Considering the recommended viscosity ranges for bitumen [4] during mixing and compaction phases of an asphalt concrete (i.e.,  $170 \pm 20$  mPa·s and  $280 \pm 30$  mPa·s, respectively), the binder C has a mixing temperature of about 155°C and a compaction temperature of about 140°C, whereas binders K and R required the highest mixing and compaction temperatures probably due to the high concentration of polymers (Figure 3).

As far as binder stripping concerns, the visual inspection of samples established the following coverage percentages: 75% for binder K, 25% for binder C and 30% for binder R (Figure 4). Therefore, binder K showed the highest affinity with the selected siliceous aggregates. The assessment of the



TABLE 1: Effect of short-term ageing with RTFOT on tested binders.

Binder RTFOT—EN 12607-1	Mass variation		Penetration		Softening point	
	$\Delta m$ (%)		P (mm $\times 10^{-1}$ )	Retained P (%)	R&B ( $^{\circ}\text{C}$ )	$\Delta R\&B$ ( $^{\circ}\text{C}$ )
K	-0.3		46	82	53.4	0
R	-0.8		97	97	68.2	2
C	-0.8		58	56	67.0	0
70/100	-0.7		41	52	58.0	11
PMB 45/80-70	-0.1		37	69	76.2	2

TABLE 2: Mixing and compaction temperatures of selected binders.

Material	$a$	$b$	$T_{\text{mix}}$ ( $^{\circ}\text{C}$ )	$T_{\text{comp}}$ ( $^{\circ}\text{C}$ )
K	$4.0830E+17$	$-6.8072E+00$	182	169
C	$8.0434E+15$	$-6.2605E+00$	153	141
R	$1.2453E+23$	$-9.1289E+00$	193	183
70/100	$2.4879E+18$	$-7.3836E+00$	155	145
PMB				
45/80-70	$7.4602E+22$	$-9.1418E+00$	181	172

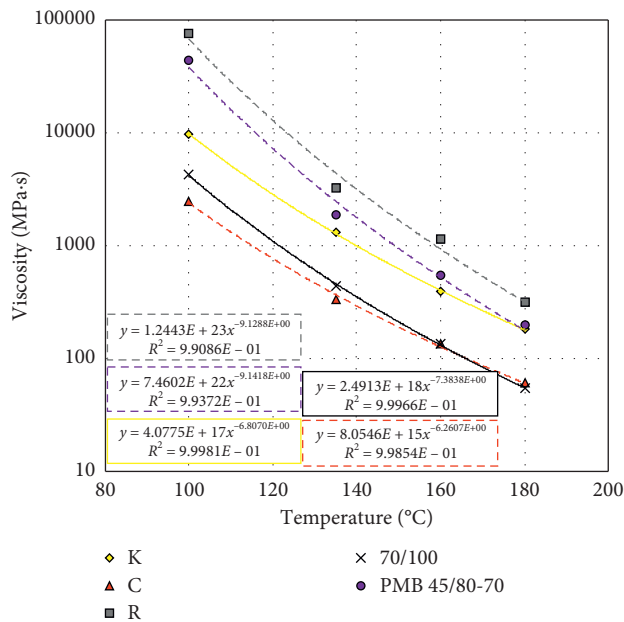


FIGURE 3: Viscosity values at high temperatures of tested binders.

degree of binder coverage on aggregate particles was carried out by drying the samples at room temperature for one day and using a torch to highlight the reflective portion of particles (portion covered by binder).

**4.3. Rheological Characterization.** Master curves of dynamic properties extend the rheological analysis to time and temperature domains. The frequency-temperature superposition principle (FTSP) was applied to allow the identification of continuous rheological master curves in terms of  $G^*$ ,  $\delta$ ,  $G'$ , and  $G''$  [18, 19], in the entire investigated domain of reduced frequencies (from Figures 5–7). The complex modulus master curve at the reference temperature

( $T_r = 20^{\circ}\text{C}$ ) was modelled fitting the experimental data through the equation proposed in NCHRP Report 459 [20] and Williams–Landel–Ferry (WLF) formulation [21]. The shift factors and master curve parameters were simultaneously calculated by a solver, minimizing the sum of squares of differences.

Binder K shows the asymptotical behaviors typical of a paving grade bitumen [22] (Figure 5). At high reduced frequencies, the complex modulus  $|G^*|$  individuates a trend in the logarithmic plot (Figure 5) towards the glassy state limit with the decrease of the phase angle  $\delta$  down to about  $30^{\circ}$ . At low reduced frequencies,  $|G^*|$  master curve shows a constant slope and the phase angle  $\delta$  approaches the limit value of  $90^{\circ}$  achieving the pure viscous flow (Figure 6). However, the intermediate behavior internal to the two asymptotes is mainly characterized by an inflection, between  $10^{-2}$  and  $10^{-4}$  Hz, in complex modulus master curve (Figure 5). In this frequency range, the K behavior deviates if compared to the common trend of a paving grade bitumen [23], showing a simultaneous phase angle (minimum phase angle equal to  $65^{\circ}$ ) and complex modulus decrease with the decrease in reduced frequency (or the increase of temperature). The local minimum of  $\delta$  master curve characterizes bitumens modified by SBS copolymers and binders including the same copolymer [10], identifying the presence of polymer elastic networks or entanglements in the modified binders [23] (Figure 6). The phase angle minimum can be attributed to a hard/soft relaxation for polymer-modified binders [9]. The polymer modification gives an enhanced consistence at high service temperature with higher resistance to non-reversible deformation. Confirming the FTIR results, the continuous development of rheological parameters highlights the good compatibility between the polymer and the binder matrix due to the characteristic absence of asphaltene micelles in binder K, which are traditionally considered as detrimental for bitumen/polymer compatibility [9].

On the contrary, the viscoelastic behavior of binder C and binder R is more complex than a bituminous binder, and it cannot be explained by the uniform transition from elastic response (high reduced frequencies) to viscous response (low reduced frequencies) reducing frequency as for the conventional bitumen [19]. The values of  $\delta$  measured at different temperatures do not overlap to form a unique master curve, implying a thermo-rheologically complex behavior (Figure 6). Therefore, the FTSP could not be used due to the viscous component of the C and R binder response. C and R do not show a unique relaxation mechanism.



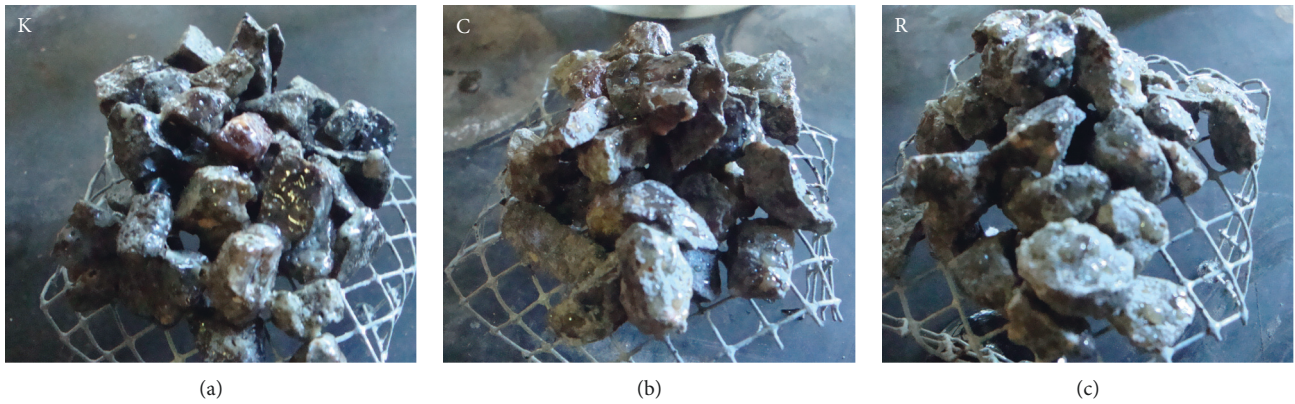


FIGURE 4: Siliceous aggregate and binder systems after AST.

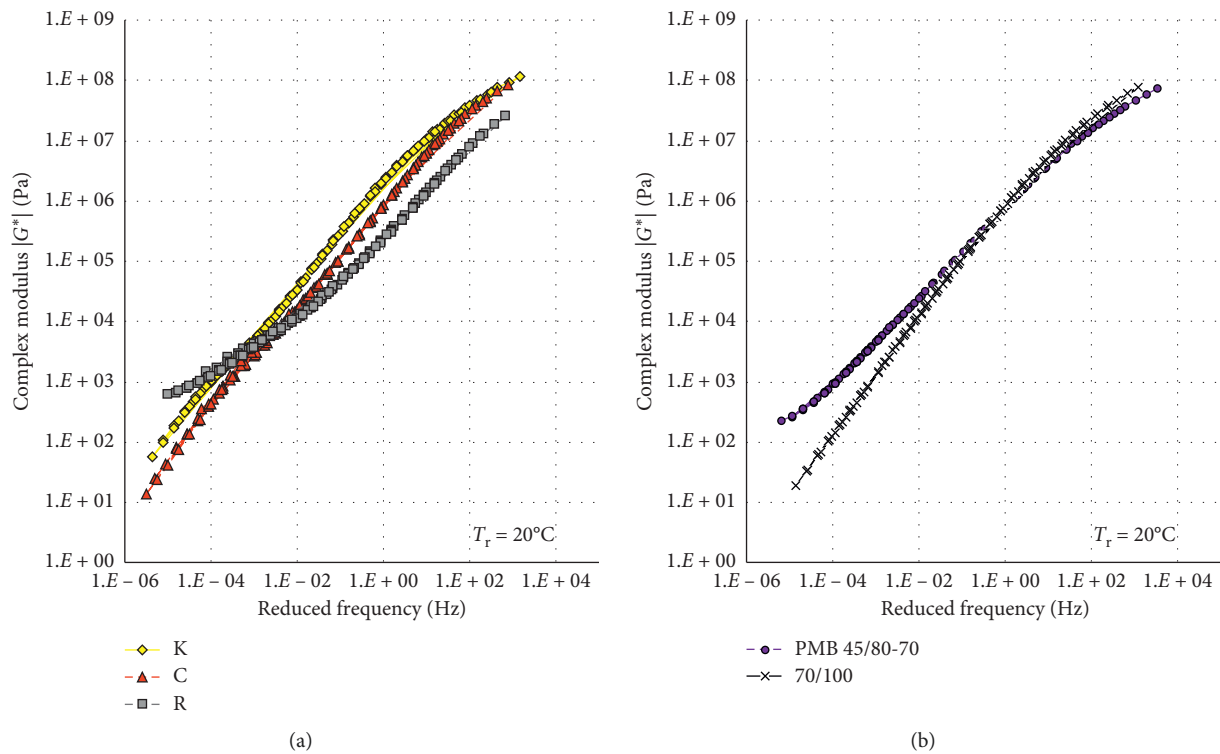


FIGURE 5:  $|G^*|$  master curves for the selected binders in comparison with bituminous binders.

Binder C reaches the pure viscous flow at low reduced frequencies and approaches to the glassy state limit at high reduced frequencies as a paving grade bitumen (Figure 5). Nevertheless, the rheological behavior of the binder C is characterized by an inflection on the  $|G^*|$  master curve and the presence of a discontinuity on  $\delta$  master curve between  $10^{-3}$  and  $10^{-4}$  Hz. In this case, the assumption of thermo-rheological simplicity cannot be properly considered and the FTSP does not apply on the entire time-temperature domain [24]. Specifically, the  $\delta$  master curve can be divided into three regions (Figure 6) [24]. From the highest reduced frequencies to 1 Hz, the rheological properties of binder C follows the common trend of a paving grade bitumen: the

phase angle continuously increases, and the complex modulus decreases as the reduced frequency decreases (or temperature increases). Between 1 Hz and  $10^{-4}$  Hz, the phase angle decays from  $80^\circ$  to  $50^\circ$  and  $|G^*|$  shows a rubbery plateau, highlighting a solid-like behavior or a structured physical network (crystals) into the binder that offers stiffness to the binder. However, the transition to a rubbery state is inhibited by the melting of wax-like materials. Stiffness and elasticity are instantaneously lost when the material turns into a liquid state. Indeed, decreasing frequencies (or increasing temperature) below the discontinuity, the phase angle rises to the limit value of  $90^\circ$ , confirming a liquid state.

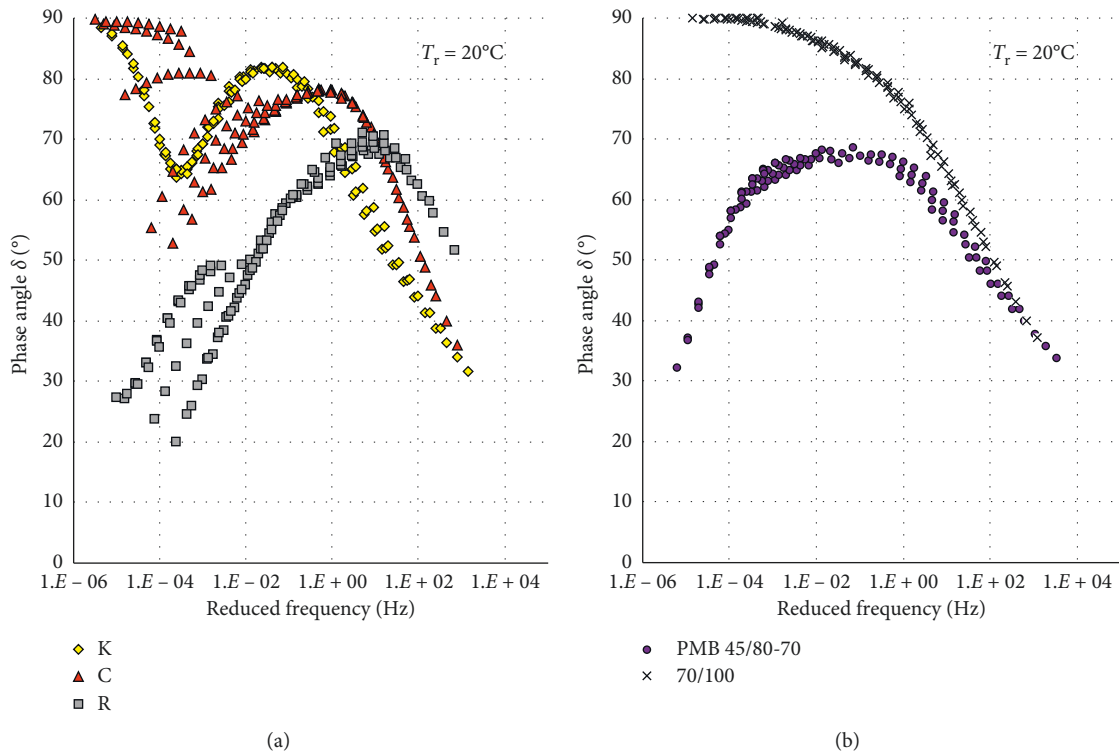


FIGURE 6:  $\delta$  master curves for the selected binders in comparison with bituminous binders.

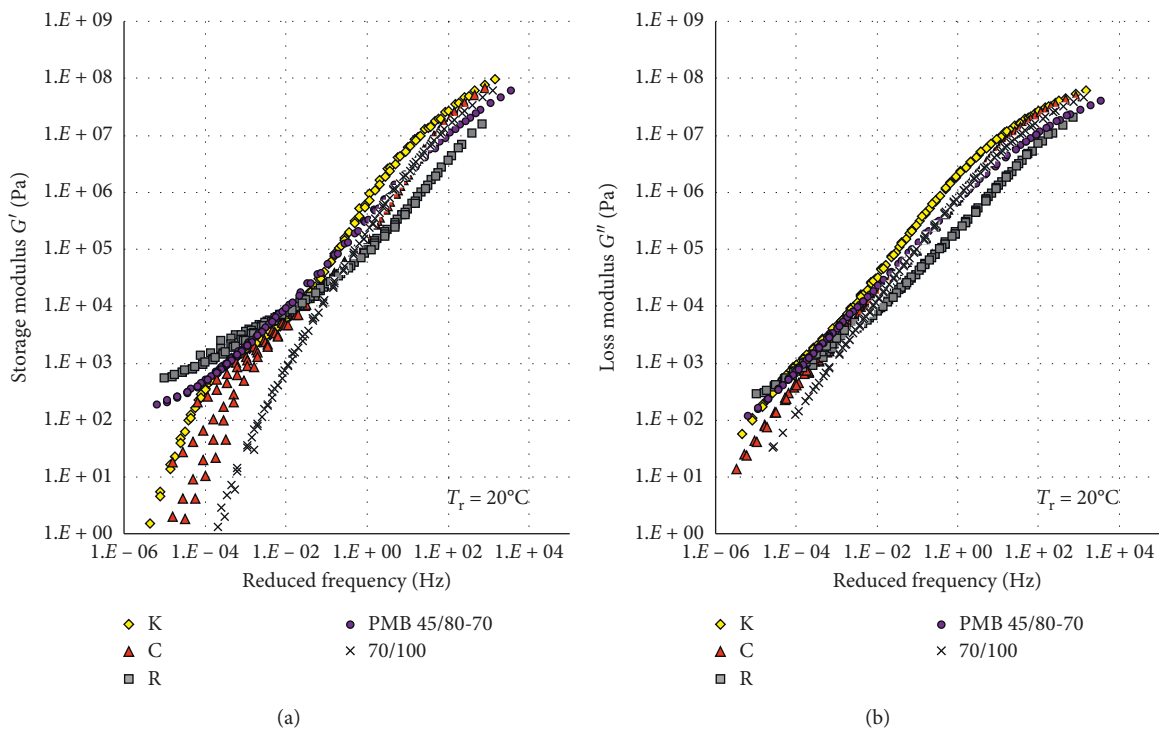


FIGURE 7:  $G'$  and  $G''$  master curves for the selected binders.

Binder R shows an inflection on the  $|G^*|$  master curve and the presence of a discontinuity on  $\delta$  master curve between  $10^{-2}$  and  $10^{-4}$  Hz. At low reduced frequency,  $|G^*|$  master curve tends to a horizontal asymptote with a

rubbery plateau, while  $\delta$  evolves in distinctive branches, highlighting the presence of different solid-like components. Consequently, the FTSP cannot be valid in that frequency range.

Observing the relationship between  $G'$  (storage modulus) and  $G''$  (loss modulus) in Figure 7, it can be asserted that at low frequencies, binder R shows  $G'$  values higher than  $G''$  values. This highlights a high polymer content confirming the FTIR analysis, while binder K reaches the highest storage and loss moduli values at high frequencies, representing a significant resin concentration [13, 18]. At high frequencies, K and C seem to converge at similar glassy modulus values, whereas R keeps the lowest stiffness values.

Considering Figure 7, significant differences among binders occur at intermediate and low frequencies, where the nature of the polymer network is dependent on the properties of the base bitumen (maltenes composition), polymer type and content, and the compatibility of the system [23]. At intermediate frequencies, binder K shows a continuous development of rheological parameters that highlights the good compatibility between the polymer and the binder matrix, whilst binder C shows the melting of wax-like materials with instantaneous decrease in stiffness and elasticity which inhibits the transition to a rubbery state. At low frequencies, binders C and K approach the pure viscous flow, while binder R shows a horizontal asymptote identifying a rubbery plateau. Moreover, binder R appears less susceptible to temperature variations since the master curves evolve in a narrow range in the domain of reduced frequencies.

## 5. Conclusions

Surface courses using clear binder can improve several functional and safety requirements, highlighting specific lanes or areas, harmonizing the integration of the road network in a human context, and mitigating environmental impact. Nevertheless, clear binders have specific properties that differ from straight-run bitumens, significantly. For this reason, the selection and characterization of clear binders must be based on their overall behavior and not only on empirical testing for bitumen characterization.

This paper focuses on the chemical identification and mechanical characterization of three clear binders that can represent an alternative to traditional bitumen. The following conclusions can be drawn:

- (1) FTIR testing suggested different binder origins and important remarks on binder components which resulted consistent to the results from mechanical testing. Particularly, the FTIR analysis pointed out that the origin of K derives from a deasphalted bitumen (low amount of asphaltenes) modified with SBS polymer with effective link between matrix and SBS, whereas C and R show a spectrum like an aromatic phthalic polymer suggesting a synthetic origin. Moreover, the C spectrum deconvolution suggested the presence of waxes.
- (2) Bitumen traditional testing may be considered to determine the clear binder consistency at service temperature (from 25°C to the transition temperature from viscoelastic to viscous behavior) but rheological testing imposed that no prediction can be done at other temperature ranges since the experience on traditional bitumen can address wrong suppositions.
- (3) From empirical testing, it can be asserted that the clear binders could be considered as a paving grade bitumen with improved elastic recovery and softening point. All clear binders comply with the technical requirements on short-term ageing for their specific grade. Dynamic viscosity tests showed that the viscosity values of binder C are close to those of a paving grade bitumen, whereas the other binders showed far higher viscosity values.
- (4) The three tested clear binders are thermo-rheologically complex materials, and the analysis of their behavior needs a specific investigation as testing conditions change.
- (5) Binder K showed the asymptotical behaviors to the glassy state limit or the pure viscous flow and a continuous development of rheological parameters. The local minimum of  $\delta$  master curve identified the presence of polymer elastic networks with good compatibility between the polymer and the binder matrix. On the other hand, C and R binder response in terms of  $\delta$  values highlighted a thermo-rheologically complex behavior. Particularly, C is characterized by the presence of a discontinuity on  $\delta$  master curve at intermediate frequencies due to the melting of wax-like materials and R showed a complex behavior strongly influenced by the presence of different solid-like components which generate a rubbery plateau and a  $\delta$  evolution in distinctive branches at low reduced frequency.
- (6) The obtained results can address specific technical recommendations. Binder K can be considered suitable in a wide range of conditions, while binders C and R appeared rather soft at the service temperatures. C can compromise the durability of pavements under quasistatic traffic loading or in hot and wet weather conditions, whereas binder R showed the best performance at the highest and lowest temperatures.
- (7) The operative temperatures for production and laying of binder C do not change if compared with a paving grade bitumen, whereas binders K and R require higher operative temperatures. Considering the remarkable cost of these binders (about 10 times of a paving grade bitumen), the correct application allows a more sustainable investment.

## 6. List of Standards

- EN 1426: determination of needle penetration (2007).  
 EN 1427: bitumen and bituminous binders; determination of the softening point; ring and ball method (2007).  
 EN 12591: bitumen and bituminous binders; specifications for paving grade bitumens (2009).

EN 12607-1: bitumen and bituminous binders; determination of the resistance to hardening under the influence of heat and air; part 1: RTFOT method (2007).

EN 13302: bitumen and bituminous binders; determination of dynamic viscosity of bituminous binder using a rotating spindle apparatus (2010).

EN 13398: bitumen and bituminous binders; specifications for paving grade bitumens (2010).

EN 14023: bitumen and bituminous binders; framework specification for polymer modified bitumens (2010).

EN 14770: bitumen and bituminous binders; determination of complex shear modulus and phase angle; dynamic shear rheometer (DSR) (2012).

## Data Availability

The data used to support the findings of this study are included within the article.

## Conflicts of Interest

The authors declare that they have no conflicts of interest.

## References

- [1] M. Saint-Jacques and Y. Brosseau, "Coloured bituminous wearing courses in France—overview of uses," in *Proceedings of the 10th International Conference on Asphalt Pavements*, vol. 1, pp. 12–17, ISBN: 978-1-61782-084-7, Quebec City, Canada, August 2006.
- [2] A. Destrée, N. Piérard, and A. Vanelstraete, "Development of a test method to determine the colour durability of coloured bituminous mixtures," *Road Materials and Pavement Design*, vol. 16, no. sup1, pp. 170–186, 2015.
- [3] N. Piérard, J. De Visscher, S. Vansteenkiste, and A. Vanelstraete, "Coloured asphalt pavements: mix design and laboratory performance testing," in *8th RILEM International Symposium on Testing and Characterization of Sustainable and Innovative Bituminous Materials. RILEM Bookseries*, F. Canestrari and M. Partl, Eds., vol. 11, pp. 283–294, Springer, Dordrecht, Netherlands, 2016.
- [4] J. Read and D. Whiteoak, *Shell Bitumen Handbook*, Thomas Telford Publishing, London, UK, 5th edition, 2003.
- [5] M. Bocci, A. Grilli, F. Cardone, and A. Virgili, "Clear asphalt mixture for wearing course in tunnels: experimental application in the Province of Bolzano," *Procedia—Social and Behavioral Sciences*, vol. 53, pp. 115–124, 2012.
- [6] E. Bocci and M. Bocci, "Clear asphalt concrete for energy saving in road tunnels," in *Proceedings of the 12th International Conference on Asphalt Pavements (ISAP)*, vol. 2, pp. 1817–1825, Raleigh, NC, USA, June 2014.
- [7] M. Santamouris, "Using cool pavements as a mitigation strategy to fight urban heat island—a review of the actual developments," *Renewable and Sustainable Energy Reviews*, vol. 26, pp. 224–240, 2013.
- [8] V. Di Maria, M. Rahman, P. Collins, G. Dondi, and C. Sangiorgi, "Urban heat island effect: thermal response of different types of exposed paved surfaces," *International Journal of Pavement Research and Technology*, vol. 6, no. 4, pp. 414–422, 2013.
- [9] D. Lesueur, "The colloidal structure of bitumen: consequences on the rheology and on the mechanisms of bitumen modification," *Advances in Colloid and Interface Science*, vol. 145, no. 1–2, pp. 42–82, 2009.
- [10] F. Merusi and F. Giuliani, "Chromatic and rheological characteristics of clear road binders," *Transportation Research Record: Journal of the Transportation Research Board*, vol. 2293, no. 1, pp. 114–122, 2012.
- [11] K. Plug and A. de Bondt, "Required mechanical properties of a clear binder for coloured asphalt concrete," in *Proceedings of the 16th Asphalt Pavement Engineering and Infrastructure Conference*, Liverpool, UK, February 2017.
- [12] M. Bocci and S. Colagrande, "The adhesiveness of modified road bitumens," in *Proceedings of the 5th Eurobitume Congress*, vol. 1A, Stockholm, Sweden, June 1993.
- [13] F. J. Navarro, P. Partal, F. Martínez-Boza, and C. Gallegos, "Effect of composition and processing on the linear viscoelasticity of synthetic binders," *European Polymer Journal*, vol. 41, no. 6, pp. 1429–1438, 2005.
- [14] H. F. Shurvel, "Spectra-Structure correlation in the mid- and far-infrared," in *Handbook of Vibrational Spectroscopy*, Wiley, Hoboken, NJ, USA, 2006.
- [15] A. Stimilli, G. Ferrotti, C. Conti, G. Tosi, and F. Canestrari, "Chemical and rheological analysis of modified bitumens blended with artificial reclaimed bitumen," *Construction and Building Materials*, vol. 63, pp. 1–10, 2014.
- [16] F. S. Coquet and E. J. Ista, "The determination of SBS, EVA and APP polymers in modified bitumens," in *Polymer Modified Asphalt Binders*, American Society for Testing and Materials, Philadelphia, PA, USA, 1st edition, 1992.
- [17] J. Xu, T. Xia, L. Zhao, B. Yin, and M. Yang, "Correlation between phase separation and rheological behaviour in bitumen/SBS/PE blends," *RSC Advances*, vol. 8, no. 73, pp. 41713–41721, 2018.
- [18] P. Partal, F. Martínez-Boza, B. Conde, and C. Gallegos, "Rheological characterisation of synthetic binders and unmodified bitumens," *Fuel*, vol. 78, no. 1, pp. 1–10, 1999.
- [19] G. D. Airey, M. H. Mohammed, and C. Fichter, "Rheological characteristics of synthetic road binders," *Fuel*, vol. 87, no. 10–11, pp. 1763–1775, 2008.
- [20] H. U. Bahia, D. I. Hanson, M. Zeng, H. Zhai, M. A. Khatri, and R. M. Anderson, "Characterization of modified asphalt binders in superpave mix design," vol. 459, NCHRP Report National Academy Press, Washington, DC, USA, 2001.
- [21] M. L. Williams, R. F. Landel, and J. D. Ferry, "The temperature dependence of relaxation mechanisms in amorphous polymers and other glass-forming liquids," *Journal of the American Chemical Society*, vol. 77, no. 14, pp. 3701–3707, 1955.
- [22] D. A. Anderson, H. U. Bahia, and D. W. Cristensen, "Binder characterization and evaluation—volume 3: physical properties," in *Strategic Highways Research Program. Report Number SHRP-A-369*, National Research Council, Washington, DC, USA, 1st edition, 1994.
- [23] G. D. Airey, "Rheological properties of styrene butadiene styrene polymer modified road bitumens," *Fuel*, vol. 82, no. 14, pp. 1709–1719, 2003.
- [24] M. Pasetto, A. Baliello, G. Giacomello, and E. Pasquini, "Aesthetic and mechanical suitability of a clear synthetic resin as a unconventional binder for road pavements," *Advances in Materials Science and Engineering*, vol. 2019, Article ID 8643608, 15 pages, 2019.



## Research Article

# Effect of Superplasticizer and Wetting Agent on Volumetric and Mechanical Properties of Cold Recycled Mixture with Asphalt Emulsion

Wenting Yang,<sup>1</sup> Jian Ouyang ,<sup>2</sup> Yan Meng,<sup>2</sup> Taixiong Tang,<sup>2</sup> Jijiang Chen,<sup>3</sup> and Baoguo Han<sup>1</sup>

<sup>1</sup>School of Civil Engineering, Dalian University of Technology, Dalian 116024, China

<sup>2</sup>School of Transportation and Logistics, Dalian University of Technology, Dalian 116024, China

<sup>3</sup>Shandong Dashan Road & Bridge Engineering Co. Ltd., Jinan 250101, China

Correspondence should be addressed to Jian Ouyang; [ouyangjian@dlut.edu.cn](mailto:ouyangjian@dlut.edu.cn)

Received 11 September 2019; Revised 8 December 2019; Accepted 17 December 2019; Published 9 January 2020

Academic Editor: Lingxue Kong

Copyright © 2020 Wenting Yang et al. This is an open access article distributed under the Creative Commons Attribution License, which permits unrestricted use, distribution, and reproduction in any medium, provided the original work is properly cited.

Cold recycled mixture with asphalt emulsion (CRME) has gained more appreciation due to its environmental and economical advantages. Surfactant greatly affects the interaction between asphalt emulsion and cement, which can greatly affect the volumetric and mechanical properties of CRME. If the surfactant can greatly improve the volumetric and mechanical properties of CRME, that could be of great attraction. In this study, a polycarboxylate-based superplasticizer and wetting agent (DN500, polymers containing high-pigment groups) were employed to improve the volumetric and mechanical properties of CRME. Results indicate that the addition of superplasticizer and DN500 can reduce the void content of CRME and increase the indirect tensile strength (ITS) and stiffness modulus as well as critical strain energy density (CSED) of CRME. Besides, the failure strain of CRME is also increased by adding superplasticizer and DN500. This phenomenon is probably due to that superplasticizer can decrease the viscosity of cement asphalt emulsion paste (CAEP) and help to form a better asphalt film, and DN500 can moderately decrease the viscosity of CAEP and increase the wetting ability of asphalt emulsion as a wetting agent. CRME with superplasticizer has the best mechanical properties among all CRMEs. Compared to reference CRME, the ITS, stiffness modulus, and CSED of CRME with superplasticizer can increase by 33.7%, 8.0%, and 17.5% at the optimum water content, respectively. It is recommended to improve the volumetric and mechanical properties of CRME by adding superplasticizer.

## 1. Introduction

Asphalt pavement tends to deteriorate gradually during its service life due to traffic load and environment action [1]. As a result, many reclaimed asphalt pavements (RAPs) are produced every year. To minimize nonrenewable fossil fuels and mine resource, recycling of RAP attracts more attention in these years [1, 2]. Nowadays, recycling of RAP has two methods: cold recycling and hot recycling [1]. In cold recycling method, the RAP is first milled and then mixed with asphalt emulsion, water, virgin aggregates, and active additives, such as cement and mineral powder. The

mixture is called as the cold recycled mixture with asphalt emulsion (CRME). Generally, virgin aggregates should be added in order to meet to grading criteria [3, 4]. Compared with the hot recycling, the mixing, laydown, and compaction of CRME can be carried out at the ambient temperature because of the low viscosity of asphalt emulsion. This is beneficial to extend the construction season and construction time. Besides, cold recycling technology (CRT) can also greatly reduce the emission of harmful gases due to no heating required during production [5, 6]. Moreover, CRT can maximize the utilization rate of RAP which can be higher than 70%. It has been proven to be a technically reliable,



environmentally friendly, cost-effective method of strengthening and maintaining a wide range of aged asphalt pavements in different countries [7].

Although the CRT has been widely used in pavement rehabilitation in the world due to its pronounced advantages, there are still some serious challenges in the future application. CRME is normally used in the base and sub-base layers because of its relatively weaker mechanical properties compared to the hot recycled mixture [8]. For instance, the indirect tensile strength (ITS) of CRME is much lower than that of the conventional hot mixture. Pavement scholars and engineers have been trying to use CRME as traditional asphalt layer material in recent years. Therefore, the volumetric and mechanical properties of CRME should be further improved to achieve this ambitious goal.

Many researchers focused on the ITS of CRME in both laboratory and field pavement. Previous studies indicated that the cement could accelerate the breaking of asphalt emulsion and the cement hydration products could enhance the hardness of cement asphalt emulsion paste (CAEP), which increased the ITS of CRME [5, 7, 9, 10]. However, the enhancement effect of cement on CRME is still limited. Besides, the high cement content can decrease the ductility of CRME, thus increasing the risk of cracking. Therefore, the upper cement content in CRME is usually limited to 2%. In addition to the low ITS, some studies showed that the use of CRME ordinarily came out with some problems such as the high void content, stripping, and long curing time [7]. Some voids are formed due to water evaporation during curing so that the void content in the hardened state is very high [11]. Because of the high void content, a large amount of water can easily permeate the interior of the CRME specimen, which affects the adhesive ability of the asphalt emulsion binder and leads to aggregate stripping. It is known that the cement hydration degree and breaking of asphalt emulsion affect the strength of CRME to a great extent [2]. However, the cement hydration and emulsion breaking processes take a long time, so the CRME needs long curing time to achieve the desirable strength. In short, there is a growing need to improve the mechanical properties of CRME to promote the use of RAP [12].

According to the strength theory of the asphalt mixture, the strength of the mixture closely depends on the cohesive force of the asphalt binder and the internal friction resistance provided by aggregate skeleton. Cement can promote cement hydration and breaking of asphalt emulsion to enhance its cohesive force, thus improving the mechanical properties of the asphalt emulsion mixture. However, the high void content reduces the internal friction resistance of aggregate skeleton, so the mechanical properties are also decreased. Factors influencing the volumetric and mechanical properties of CRME were intensively investigated in the past, such as the gradation types, asphalt emulsion content, the additional water content, the cement content and cement types, and filler types [3, 7, 8, 10, 13–20]. These studies are all very meaningful to optimally design the mechanical properties of CRME.

To the best of our knowledge, few studies were conducted to control the interaction between asphalt

emulsion and cement for improving the physical and mechanical properties of CRME, although controlling such interaction is believed to be very important. In the field of grouting cement asphalt emulsion mortar in high-speed railway, the interaction between asphalt emulsion and cement was intensively studied [21–26]. Results indicated that superplasticizer can greatly improve the demulsifying behavior of asphalt emulsion and the rheological properties of fresh cement asphalt emulsion paste (CAEP) [21, 27]. Therefore, the addition of superplasticizer may improve the mechanical properties of CRME. Besides, the mechanical properties of CRME are closely related to whether the CAEP can be well coated on the aggregate surface. It is well known that the wetting agent can reduce the contact angle of aqueous solution. Therefore, it is possible to improve the mechanical and volumetric properties of CRME by adding the superplasticizer and wetting agent.

Based on the above consideration, superplasticizer and wetting agent were added into CRME to improve its mechanical and volumetric properties. The mechanical and volumetric properties of CRME with superplasticizer and wetting agent at different additional water contents are discussed in this paper. Besides, the action mechanism of the wetting agent and superplasticizer is discussed by rheology test. To the best of our knowledge, it is a very meaningful work to improve the mechanical and volumetric properties of CRME.

## 2. Experimental Program

*2.1. Material and Specimen Preparation.* CRME was composed of cationic slow-setting asphalt emulsion, basalt aggregate, RAP, Portland ordinary cement P.O 42.5, and mineral powder. All these materials were obtained from the market. The properties of asphalt emulsion are listed in Table 1 according to the Chinese standard [28]. The cement and mineral powder composition are listed in Tables 2 and 3, respectively. The RAP was obtained from one expressway in Liaoning province in China. Through sieving tests, it was found that the gradation of RAP could not meet the required specification of the Chinese standard [29]. Thus, new aggregates were added to satisfy the gradation requirements. The amounts of new aggregates were 20% by the weight of dry mixture (aggregates and fillers). A uniform dense aggregate gradation for AC-13 was used in this study according to Chinese Technical Specifications [29]. Figure 1 presents the gradation of RAP materials, mix blends, and specification limits. The total amount of fillers (including cement and mineral powder) was 6% by the weight of dry mixture, in which cement accounts for 2% and mineral powder accounts for 4%. The CRMEs are prepared by the following procedure which is shown in Figure 2. Long mixing time can well ensure the uniformity of the mixture. However, the mixing time of asphalt emulsion should be not more than 60 s to avoid the breaking of asphalt emulsion according to the Chinese standard [29]. No significant breaking phenomenon was observed when asphalt emulsion was mixed for 60 s. Thus, the mixing time of every procedure in Figure 2 was chosen as 60 s.

TABLE 1: Properties of asphalt emulsion.

Test of emulsion	Value	Test on residue from distillation	Value
Mean particle size ( $\mu\text{m}$ )	1.52	Residual content (%)	63.4
Residue on sieve 1.18 mm (%)	0	Penetration (25°C, 0.1 mm)	55.1
Storage stability (1 d, 25°C, %)	0.02	Softening point (R & B, °C)	48.8
Storage stability (5 d, 25°C, %)	0.6	Ductility (25°C, mm)	84
Mixing stability with cement, residual (%)	0.75		

TABLE 2: Chemical components of P.O 42.5 cement.

Chemical composition	CaO	SiO <sub>2</sub>	Al <sub>2</sub> O <sub>3</sub>	MgO	SO <sub>3</sub>	Fe <sub>2</sub> O <sub>3</sub>	K <sub>2</sub> O <sub>3</sub>	TiO <sub>2</sub>	Na <sub>2</sub> O
Percentage (% by weight)	62.13	23.45	5.24	2.08	2.05	3.39	0.63	0.07	0.77

TABLE 3: Mineral components of mineral powder.

Mineral composition	C <sub>3</sub> S	C <sub>2</sub> S	C <sub>3</sub> A	C <sub>4</sub> AF
Percentage (% by weight)	46.52	29.57	9.02	8.78

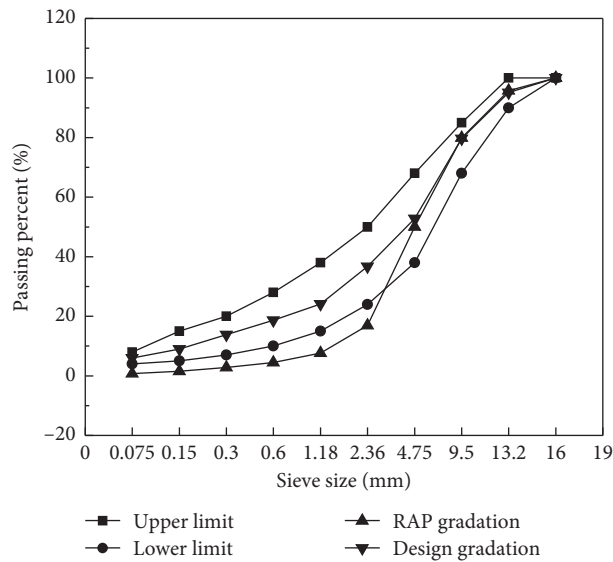


FIGURE 1: Gradation of CRME.

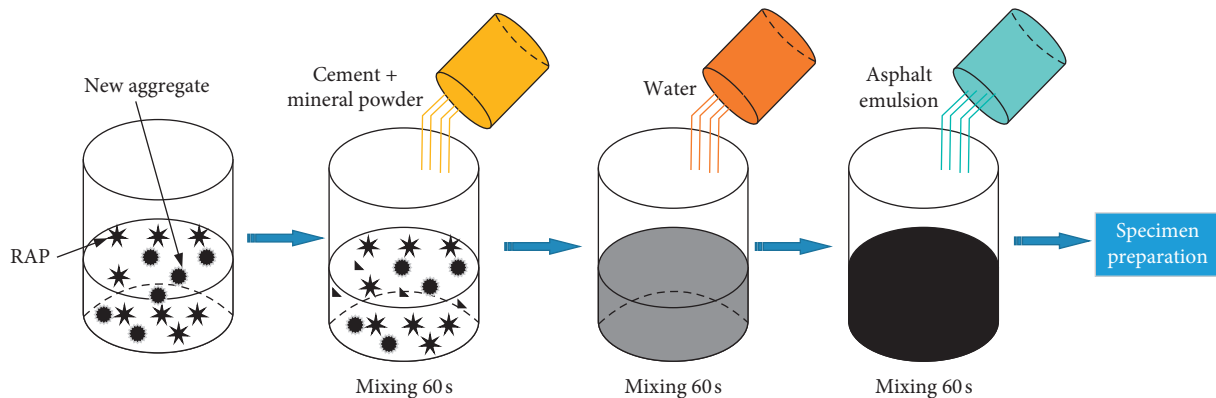


FIGURE 2: Preparation process of the CRME.

There are several methods to determine the optimum asphalt emulsion and the optimum additional water content. However, there is no universally accepted mix design for CRME. In this study, the specimens were firstly prepared with 3% of the asphalt emulsion content (asphalt emulsion to all aggregate ratio by weight). The additional water content was added to the mixture at percentages ranging from 2% to 6% by weight of the total dry mixture at 1% increments. Four specimens were prepared for one mixture. RAP and virgin aggregates were dried in the oven before the experiment. The asphalt emulsion mixture was mixed by the automatic mixing machine for the asphalt mixture and then compacted by applying 75 blows per side with the Marshall hammer. After compaction, the specimens were firstly kept for 24 h at ambient temperature in the molds to finish an initial curing, and then they are extruded and cured in the oven for 3 days at a temperature of 50°C [18]. The initial curing could ensure enough strength to extrude from the molds and the following 3 days curing was to accelerate asphalt emulsion breaking process and cement hydration process to quickly achieve the desirable strength. The optimum additional water content was determined at 3.5% by the weight of dry mixture by using the ITS, void content, and the maximum specific gravity. After obtaining the optimum additional water content, a variable asphalt emulsion content from 2.5% to 5% was used to prepare specimens. The optimum asphalt emulsion content was determined at 3.7% by the same method as the optimum additional water content.

In this study, there are two surfactants used in the CRME. One is polycarboxylic acid-based superplasticizer and the other is wetting agent (DN500, polymers containing high-pigment groups) whose function is to increase the contact angle of liquid (the additional water and asphalt emulsion). In order to determine the optimal dosage of surfactants, different superplasticizers and DN500 dosages were studied, with results listed in Table 4. According to Table 4, the optimum superplasticizer and DN500 dosages are 2% of the weight of cement and 0.5% of total water, respectively. Therefore, reference CRME, CRME with 2% of superplasticizer, and CRME with 0.5% of DN500 were investigated in this study. Meanwhile, the paper studied the experiment about CRME with superplasticizer and DN500, but results showed that the ITS of CRME with superplasticizer (0.95 MPa) was slightly higher than that of CRME with superplasticizer and DN500 (0.86 MPa). Thus, superplasticizer and DN500 were investigated alone in this study. Actually, 0.5% of DN500 in water was recommended by the manufacturer because water can have the best wetting ability at this content. Besides, the optimum superplasticizer content in CRME is higher than that in pure cement paste (normally 1%) perhaps because cement particles only account for 2% of the dry materials in CRME and other solids can also adsorb some superplasticizers. The wetting agent was divided into two parts to be added into the mixture. The first part which accounts for 3/4 was added into asphalt emulsion, and the rest part was added into additional water. In order to study the effect of adding superplasticizer and wetting agent in different additional water contents, the

TABLE 4: Effect of individual addition of different dosages of superplasticizer and DN500 on the ITS of CRME.

Dosages of SP (%)	ITS (MPa)	Dosages of DN500 (%)	ITS (MPa)
0	0.68	0	0.68
1	0.82	0.1	0.70
2	0.95	0.3	0.71
3	0.84	0.5	0.83
4	0.80	0.8	0.82

effect of additional water content ranging from 1% to 5% was investigated in CRME with superplasticizer and wetting agent. It is difficult to fabricate the Marshall specimens with 1% of additional water content for CRME without superplasticizer and wetting agent due to too dry of mixture to be compacted. Therefore, the additional water content ranging from 2% to 6% was tested for reference CRME.

## 2.2. Testing Program

2.2.1. *Void Content Test.* The void content of CRME is calculated according to the following equation [28]:

$$VV = \left(1 - \frac{\rho_s}{\rho_t}\right) \times 100\%, \quad (1)$$

where  $\rho_s$  is the apparent specific gravity of the mixture and  $\rho_t$  is the maximum specific gravity of the mixture. Since the maximum specific gravity of CRME changes with curing time due to water evaporation, the final void content of CRME was studied in this paper. The apparent specific gravity of CRME can be measured by the surface-dry condition method after curing. According to the Chinese standard [28], the maximum specific gravity of CRME can be calculated by

$$\rho_t = \frac{100 + P_a}{P_1/\gamma_1 + P_2/\gamma_2 + \dots + P_n/\gamma_n + P_a/\gamma_a} \times \rho_w, \quad (2)$$

where  $P_a$  is the asphalt aggregate ratio;  $P_1, P_2, \dots, P_n$  are the blending percentage of aggregate of each grade (the aggregate proportion of each grade is 1);  $\gamma_1, \gamma_2, \dots, \gamma_n$  are the specific gravity of aggregate of each grade;  $\gamma_a$  is the specific gravity of bitumen; and  $\rho_w$  is the specific gravity of water.

2.2.2. *Indirect Tensile Strength (ITS) Test.* The ITS test usually determines tensile properties of the asphalt mixture, which can reflect the cracking properties of asphalt pavement [30]. The ITS of CRME is calculated by using the following equation [28]:

$$ITS = \frac{2F_{\max}}{\pi dh}, \quad (3)$$

where ITS is the indirect tensile strength of the specimen;  $F_{\max}$  is the applied load at failure;  $h$  is the thickness of the specimen; and  $d$  is the diameter of the specimen. The specimens were loaded at a deformation rate of 50 mm/min and at a temperature of 15°C.

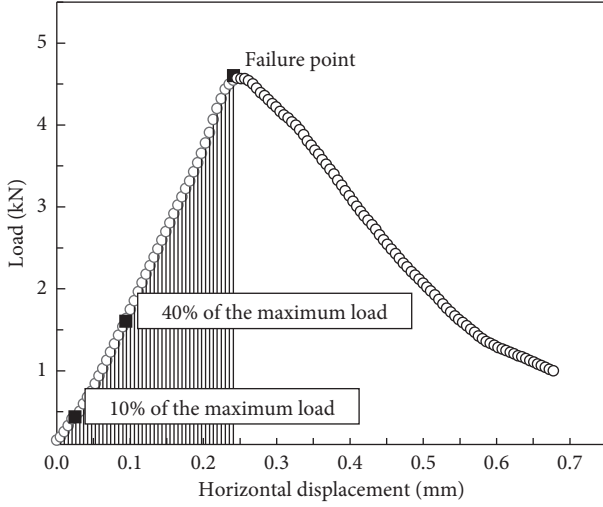


FIGURE 3: Typical curve of force-horizontal displacement.

**2.2.3. Stiffness Modulus Test.** The stiffness modulus is the most important parameter in the mechanical design of asphalt pavement [20]. The stiffness modulus of CRME was calculated by the loading range between 10% and 40% of the maximum load according to the Chinese standard [28] because the load has a good linear relation with displacement in the range. A typical force-displacement curve of CRME is shown in Figure 3, and the stiffness modulus was calculated by the following equation [8, 31]:

$$E = \frac{0.3F_{\max}(4 + \pi\mu - \pi)}{\pi h(u_{40\%} - u_{10\%})}, \quad (4)$$

where  $E$  is the stiffness modulus of the specimen;  $F_{\max}$  is the maximum force achieved during the test;  $h$  is the thickness of the specimen;  $\mu$  is Poisson's ratio of the specimen, and its value is 0.3 according to the Chinese standard [28];  $u_{10\%}$  is the horizontal displacement corresponding to 10% of the failure load; and  $u_{40\%}$  is the horizontal displacement corresponding to 40% of the failure load.

**2.2.4. Failure Strain and Critical Strain Energy Density (CSED) Test.** Failure strain is an index of deformability. A larger failure strain indicates a better deformability. The critical strain energy density (CSED) is based on the stress and strain in the center of the specimen. It can be an indicator of cracking and fatigue resistance [8]. A large CSED indicates a better cracking resistance and a long fatigue life for the mixture. The failure strain of CRME is evaluated by equation (5), and the CSED of CRME is calculated by using the following [8, 31]:

$$\varepsilon = \frac{2u}{d} \cdot \frac{1 + 3\mu}{4 + \pi\mu - \pi}, \quad (5)$$

$$U = \frac{4}{\pi d^2 h} \cdot \frac{1 + 3\mu}{4 + \pi\mu - \pi} \int_u F(u) du, \quad (6)$$

where  $h$  is the thickness of the specimen;  $d$  is the diameter of the specimen;  $u$  is the horizontal displacement; and  $\mu$  is

Poisson's ratio of the specimen, and its value is 0.3 according to the Chinese standard [28].

**2.2.5. Rheology Test.** In this experiment, rheometer shown in Figure 4 was adopted to measure the apparent viscosity under different shear rates at a constant temperature of 20°C. The diameter of the rotor and the inner diameter of the cylinder are 26.659 mm and 28.920 mm. Thus, the thickness of the shear layer is 1.1305 mm. The shear process as shown in Figure 5 was performed in the rheology test. First, a 60 s preshear at 100 s<sup>-1</sup> was intended to create a uniform condition for specimens before testing. Then, specimens were rested for 180 s. Finally, specimens were then sheared with a gradually increasing shear rate from 0 to 100 s<sup>-1</sup> for 100 s. The apparent viscosity of the cement asphalt emulsion paste (CAEP) decreased at first and then increased between 0 and 100 s<sup>-1</sup>, showing that the paste has a minimum apparent viscosity between 0 and 100 s<sup>-1</sup> [32]. The minimum apparent viscosity of the specimen was analyzed in the following section. And the mix proportion list is shown in Table 4. This test was performed thrice for each specimen at least. CAEP was composed of cationic slow-setting asphalt emulsion, Portland ordinary cement P.O 42.5, surfactant (superplasticizer and DN500), and mineral powder. In this study, the mix proportions in Table 5 are to study the effect of water-to-cement (W/C) on CAEP. CAEP had a constant asphalt emulsion-to-cement (AE/C) at 1.75% and a constant mineral powder-to-cement (M/C) at 2%. The dosage of superplasticizer and DN500 was the same as above.

### 3. Results and Discussion

**3.1. The Void Content of CRME with Different Surfactants.** Figure 6 shows the void content of CRME with different surfactants. It can be observed from Figure 6 that the addition of superplasticizer and wetting agent can moderately affect the void content of CRME. The minimum void content is 12.42%, 11.11%, and 11.72% for reference CRME, CRME with DN500, and CRME with superplasticizer, respectively. The void content of CRME can reduce by 5.59% and 10.55% by DN500 and superplasticizer, respectively. Therefore, both addition of DN500 and superplasticizer can be beneficial to the compactibility of CRME. Besides, the corresponding additional water content of CRME at the minimum void content is 3%, 4%, and 4% for reference CRME, CRME with DN500, and CRME with superplasticizer, respectively. The addition of superplasticizer can reduce the water requirement for obtaining the optimum compactibility of CRME. Superplasticizer can sharply reduce the flocculation structure and adsorption ability of cement particles, and also, it can greatly improve the mixing stability of asphalt emulsion with the cement [24, 25]. Thus, more free water can be released during compaction when superplasticizer is added, which is beneficial to the compactibility of CRME. However, it should be noted that the addition of superplasticizer can be harmful to the compactibility of CRME when the additional water content is high. This phenomenon is probably due to that the excess free water released by superplasticizer can





FIGURE 4: Rheometer.

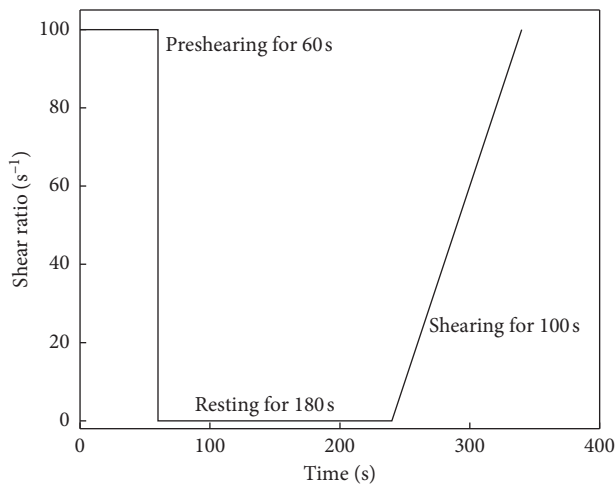


FIGURE 5: Shear rheology method of CAEP.

TABLE 5: Mix proportions of cement bitumen emulsion pastes for rheology test.

Mix	W/C	A/C	M/C
CAEP1	0.4	1.75	2
CAEP2	0.6	1.75	2
CAEP3	0.8	1.75	2

Note: every CAEP includes reference paste, paste with superplasticizer (SP) and paste with DN500.

lead to the high hydrodynamic pressure during compaction. The addition of DN500 does not change the water requirement for obtaining the optimum compactibility of CRME. Thus, its function differs from superplasticizer in improving the compactibility. As a wetting agent, DN500 can increase the wetting ability of fresh cement asphalt emulsion paste (CAEP), thus improving the coating ability of CAEP on aggregate. With more uniform coating state, the compactibility of CRME can be improved. In summary, the superplasticizer and DN500 can reduce the void content of CRME with different action mechanisms.

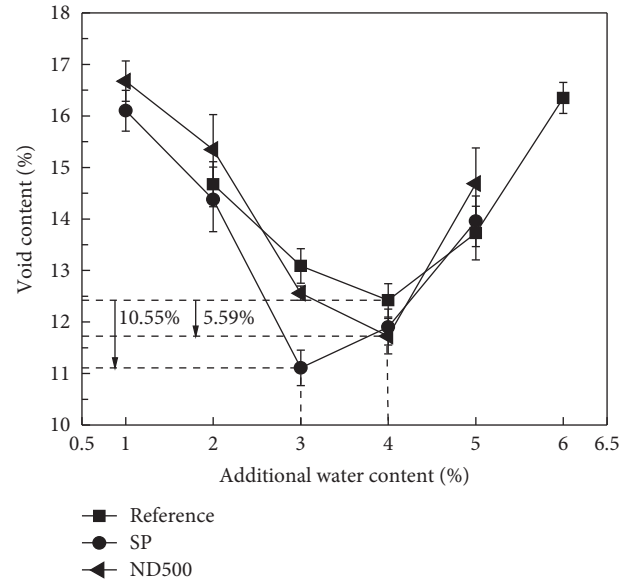


FIGURE 6: The void content of CRME with different surfactants.

3.2. *The ITS of CRME with Different Surfactants.* Figure 7 shows the ITS of CRME with different surfactants. It can be seen from Figure 7 that both addition of superplasticizer and DN500 can increase the maximum ITS of CRME. Certainly, as previously shown in Figure 6, the enhancement effect of superplasticizer and DN500 on CRME is related to the decreased void content of CRME when the two surfactants are added. Besides, this enhancement effect is also related to the improving effect of the two surfactants on the interaction between asphalt emulsion and cement particles. Meanwhile, the fresh mixing state of CRME with 3% of additional water content is shown in Figure 8. It can be seen from Figure 8 that the wetting degree of the mixture is ranked as follows: CAEP with superplasticizer > CAEP with DN500 > reference CAEP. The surfaces of course aggregates are well coated by enough CAEP by adding superplasticizer and DN500. Superplasticizer and DN500 can improve the mixing state of CRME and thus can increase the ITS of CRME. In comparison of Figures 6 and 7, CRME with superplasticizer has an equal void content with reference CRME at 2% of additional water content; however, the ITS of CRME with superplasticizer is much higher than that of reference CRME. Similarly, the ITS of CRME with DN500 is higher than that of reference CRME at 2% of additional water content although the void content of CRME with DN500 is higher than that of reference CRME. Superplasticizer can greatly improve the mixing stability of asphalt emulsion with cement [24, 25] and decrease the viscosity of CAEP [33], which can be beneficial to the coating ability of CAEP on the aggregate surface. As a result, the ITS of CRME can be increased by superplasticizer. Similarly, as a wetting agent, DN500 can greatly increase the wetting ability of asphalt emulsion, which can also increase the strength of CRME. Compared to the maximum ITS of reference CRME, superplasticizer and DN500 can increase the maximum ITS of CRME by 33.7% and 16.7%, respectively. Besides, the price of superplasticizer and DN500 is 1.4 \$/kg and 2.8 \$/kg,



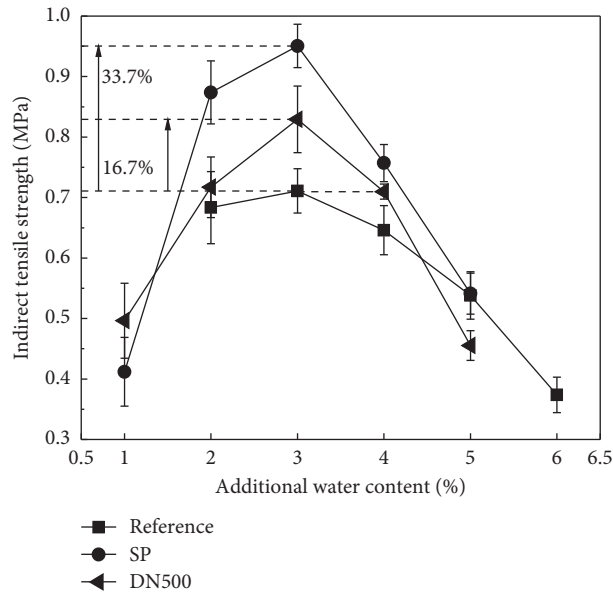


FIGURE 7: The ITS of CRME with different surfactants.

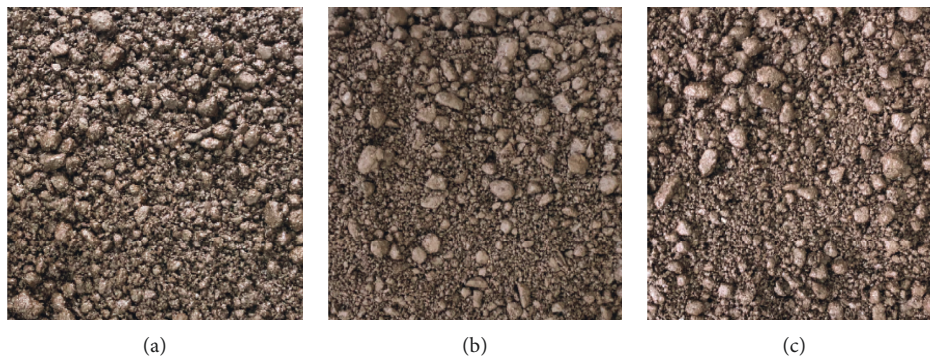


FIGURE 8: Mixing state of CRME with 3% of additional water content. (a) CRME with SP. (b) Reference CRME. (c) CRME with DN500.

respectively. Because superplasticizer and DN500 content is only 2% of cement and 0.5% of total water by weight, the material cost of CRME is only 0.57 \$ and 0.86 \$ per ton with the individual addition of superplasticizer and DN500, respectively. Therefore, the addition of superplasticizer and DN500 nearly does not increase the material cost of CRME. Adding superplasticizer or DN500 into CRME is an efficient and economical way to increase the ITS of CRME.

In comparison of Figures 6 and 7, it is clearly found that the maximum ITS of CRME did not occur at the additional water content of the minimum void content. The corresponding additional water content of the maximum ITS for all CRMEs is 3%. However, the additional water content of CRME at maximum ITS is lower than that at the minimum void content for reference CRME and CRME with DN500. Previous study indicated that the cement asphalt emulsion mixture with maximum ITS had better mechanical properties than that with minimum void content [8]. Thus, the optimum water content of all CRMEs is 3% in this study. The volumetric properties and strength theory of CRME can explain this phenomenon. According to the strength theory

of the asphalt mixture, the strength of the mixture closely depends on the cohesive force of the asphalt binder and the internal friction resistance provided by aggregate skeleton. The internal friction of aggregates decreases with the increasing void content. However, the cohesive force of cement asphalt emulsion paste is highly related to water-to-cement ratio. The hardened cement asphalt emulsion paste becomes looser with the increasing water-to-ratio due to water evaporation [8]. Thus, low water content is beneficial to the hardness and cohesive force of cement asphalt emulsion paste. Because of both effects, the corresponding water content of the maximum ITS is lower than the water content of the minimum air void content.

### 3.3. The Failure Strain of CRME with Different Surfactants.

The failure strain is an indicator of the deformability ability of the asphalt mixture which is related to the cracking resistance of CRME. Figure 9 illustrates the failure strain of CRME with different additional water contents and surfactants. It can be seen from Figure 9 that the failure strain of

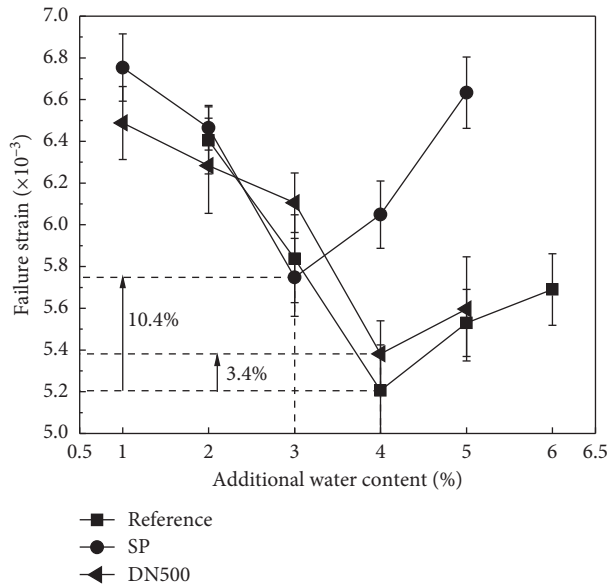


FIGURE 9: The failure strain of CRME with different additional water contents and surfactants.

CRME firstly decreases and then increases with the increasing additional water content. Besides, the failure strain of CRME with superplasticizer and CRME with DN500 is higher than that of reference CRME except for special points. Especially, the minimum failure strain of CRME with superplasticizer can increase by 10.4% compared to the minimum failure strain of reference CRME. A higher failure strain of CRME indicates a better cracking resistance. Therefore, the addition of superplasticizer is greatly beneficial to the cracking resistance of CRME. It should be noted from Figures 6 and 9 that the changing law of failure strain with additional water content is similar to that of void content with additional water content. All CRMEs with lower void content have lower failure strain. This phenomenon was also observed in a previous study with the following probable reason [8]. Voids are beneficial to hinder the propagation path under loading; thus, the increasing void content may increase the failure strain. Besides, a good asphalt film can also increase the deformability of CRME [8]. CRME with superplasticizer and CRME with DN500 have lower void content but higher failure strain than reference CRME, which indicates that the addition of superplasticizer and DN500 are both beneficial to the film formation of asphalt emulsion. As mentioned previously, superplasticizer can greatly improve the mixing stability of asphalt emulsion with cement and DN500 can increase the wetting ability of asphalt emulsion. Both the two surfactants can improve the asphalt film formation. As a result, the deformability of CRME is improved by the two surfactants. Because of the improvement in the asphalt film formation, the failure strain of CRME with superplasticizer at the optimum water content of 3% can be still equal to that of reference CRME.

**3.4. The Stiffness Modulus of CRME with Different Surfactants.** The stiffness modulus of CRME with different additional water contents and surfactants is shown in Figure 10. It is

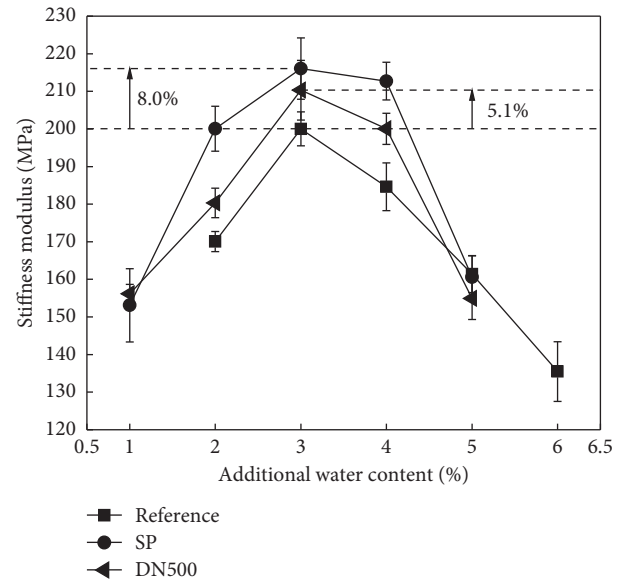


FIGURE 10: The stiffness modulus of CRME with different additional water contents and surfactants.

observed from Figure 10 that the stiffness modulus of CRME firstly increases and then decreases with the increasing additional water content. Besides, the stiffness modulus of CRME with superplasticizer and CRME with DN500 is slightly higher than that of reference CRME. The maximum stiffness modulus of CRME with superplasticizer and CRME with DN500 increased by 8% and 5%, respectively. The stiffness modulus of CRME is mainly related to its strength. In combination of Figures 7 and 10, the relationship between the stiffness modulus and ITS of CRME is obtained, which is shown in Figure 11. It can be observed that a strong correlation exists between ITS and stiffness modulus for all CRMEs, perhaps because all CRMEs have the similar components except the surfactant. The stiffness modulus increases with the increasing ITS. Because the two surfactants can increase the strength of CRME, they can also increase the stiffness modulus of CRME. Compared to the reference CRME, the stiffness modulus of CRME with superplasticizer has a significant increase. A higher stiffness modulus indicates a better deformation resistance. Therefore, the addition of superplasticizer is beneficial to the deformation resistance of CRME.

**3.5. The Critical Strain Energy Density (CSED) of CRME with Different Surfactants.** Although ITS and failure strain are very suitable to characterize the mixture performance in general, they are still not sufficient to reflect the cracking resistance of CBEM because the stiffness modulus of CBEM differs greatly with mix proportion. A more suitable indicator is CSED which has been proved to be a good fatigue cracking indicator of the bitumen mixture [34, 35]. It is also suitable to characterize the fracture behavior of CBEM [36]. The CSED of CRME with different additional water contents and surfactants is shown in Figure 12. It can be seen from Figure 12 that the CSED of CRME firstly increases and then

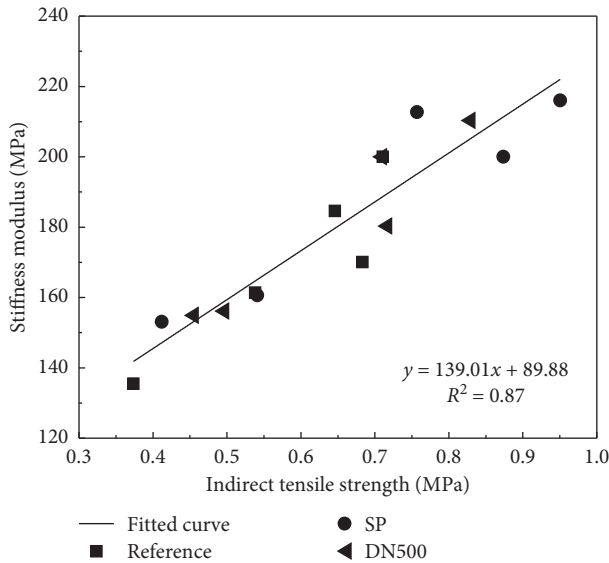


FIGURE 11: Relationship between stiffness modulus and ITS with different surfactants.

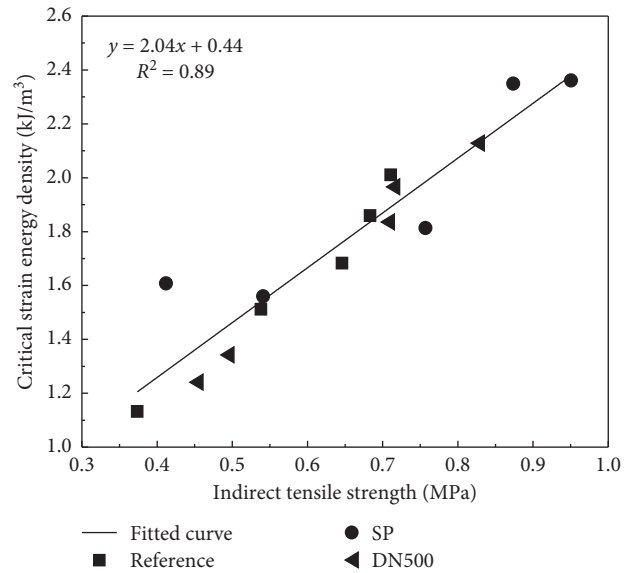


FIGURE 13: Relationship between CSED and ITS with different surfactants.

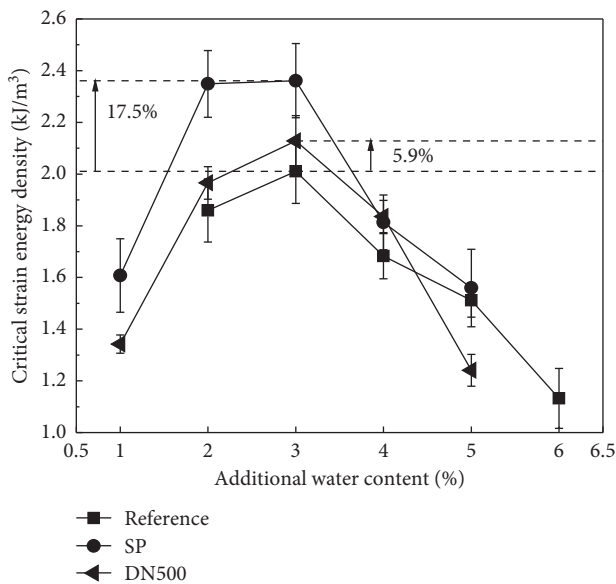


FIGURE 12: The CSED of CRME with different additional water contents and surfactants.

decreases with the increasing additional water content. Besides, the peak CSED of CRME with superplasticizer and DN500 increases by 17.5% and 5.9% compared to that of reference CRME, respectively. The addition of superplasticizer can significantly increase the CSED of CRME with superplasticizer. In comparison combination of Figures 6 and 12, the relationship between the CSED and ITS of CRME is obtained, which is shown in Figure 13. It can be observed from Figure 13 that a strong correlation exists between ITS and CSED for all CRMEs. The CSED increases with the increasing ITS. Because superplasticizer can greatly increase the strength of CRME, it can also increase the CSED of CRME. Since

CSED is an aggregative indicator of the fracture and fatigue cracking resistance, it can be inferred that the fracture and fatigue cracking resistance of CRME can be greatly improved by superplasticizer.

### 3.6. The Apparent Viscosity of CAEP with Different Surfactants.

The apparent viscosity of CAEP can reflect the interaction between asphalt droplets and cement particles. It can also affect the compactibility of CRME and the coating ability of paste on the aggregate surface. Figure 14 shows the apparent viscosity of CAEP with different surfactants. It can be seen from Figure 14 that the apparent viscosity of paste is ranked as follows: CAEP with superplasticizer < CAEP with DN500 < reference CAEP. Superplasticizer can greatly decrease the viscosity of CAEP, which is beneficial to the coating ability of CAEP and the compactibility of CRME. It is reasonable that the addition of superplasticizer can reduce the void content of CRME and improve the mechanical properties of CRME. As a surfactant, DN500 can also moderately decrease the viscosity of CAEP, which is helpful to the compactibility of CRME. Besides, DN500 can improve the coating ability of CAEP as a wetting agent. Therefore, the addition of DN500 can also improve the mechanical properties of CRME.

## 4. Conclusions

This experimental study focused on using the low content level of suitable surfactants to improve the volumetric and mechanical properties of CRME. Based on the results and discussion, the following conclusions can be drawn:

- (1) The addition of superplasticizer can reduce the void content of CRME and greatly increase the ITS of CRME. Meanwhile, the deformability of CRME can also be slightly improved by superplasticizer. This

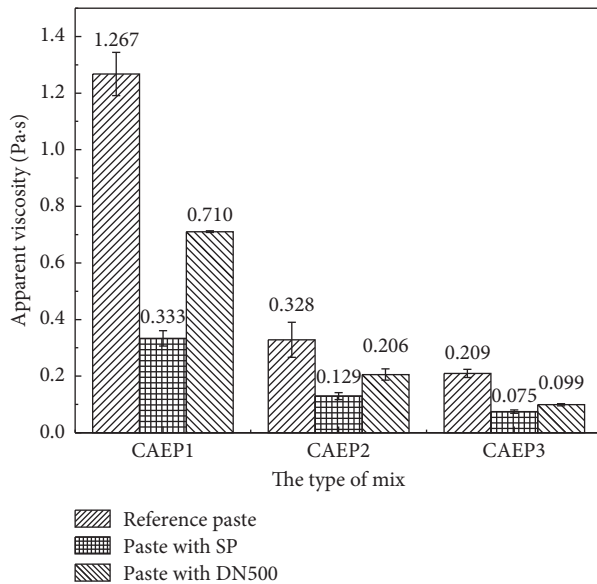


FIGURE 14: The apparent viscosity of CAEP with different surfactants.

phenomenon is probably due to that superplasticizer can decrease the viscosity of CAEP and help to form a better asphalt film.

- (2) The addition of wetting agent (DN500) can also reduce the void content of CRME and increase the ITS of CRME. Meanwhile, the deformability of CRME is not degraded with the increase of strength by adding DN500. This is because DN500 can moderately decrease the viscosity of cement asphalt emulsion paste and increase the wetting ability of asphalt emulsion as a wetting agent.
- (3) The stiffness modulus and CSED of CRME have a linear relationship between the ITS of CRME. Since the addition of superplasticizer can increase the strength of CRME, it can also increase the stiffness modulus and CSED of CRME.
- (4) Since the ITS, failure strain, and CSED are all the indicators of cracking resistance of CRME and the stiffness modulus is the indicator of deformation resistance, the addition of superplasticizer and DN500 is beneficial to the cracking and deformation resistance of CRME. CRME with superplasticizer has the best mechanical properties among all CRMEs. Compared to reference CRME, the ITS, stiffness modulus, and CSED critical strain energy density of CRME with superplasticizer can increase by 33.7%, 8.0%, and 17.5% at the optimum water content, respectively. It is recommended to improve the volumetric and mechanical properties of CRME by adding superplasticizer.

## Data Availability

The data used to support the findings of this study are available from the corresponding author upon request.

## Conflicts of Interest

The authors declare that there are no conflicts of interest regarding the publication of this paper.

## Acknowledgments

The authors thank the research funds from the National Key R&D Program of China (2018YFB1600100) and the National Science Foundation of China (grant no. 51608096).

## References

- [1] J. Lin, T. Wei, J. Hong, Y. Zhao, and J. Liu, "Research on development mechanism of early-stage strength for cold recycled asphalt mixture using emulsion asphalt," *Construction and Building Materials*, vol. 99, pp. 137–142, 2015.
- [2] J. Ouyang, L. Hu, W. Yang, and B. Han, "Strength improvement additives for cement bitumen emulsion mixture," *Construction and Building Materials*, vol. 198, pp. 456–464, 2019.
- [3] A. Stimilli, G. Ferrotti, A. Graziani, and F. Canestrari, "Performance evaluation of a cold-recycled mixture containing high percentage of reclaimed asphalt," *Road Materials and Pavement Design*, vol. 14, no. 1, pp. 149–161, 2013.
- [4] L. Gao, F. Ni, A. Braham, and H. Luo, "Mixed-Mode cracking behavior of cold recycled mixes with emulsion using Arcan configuration," *Construction and Building Materials*, vol. 55, pp. 415–422, 2014.
- [5] A. Modarres and P. Ayar, "Comparing the mechanical properties of cold recycled mixture containing coal waste additive and ordinary Portland cement," *International Journal of Pavement Engineering*, vol. 17, no. 3, pp. 211–224, 2016.
- [6] I. Pérez, L. Medina, and M. Á. del Val, "Mechanical properties and behaviour of in situ materials which are stabilised with bitumen emulsion," *Road Materials and Pavement Design*, vol. 14, no. 2, pp. 221–238, 2013.
- [7] Y. Niazi and M. Jalili, "Effect of Portland cement and lime additives on properties of cold in-place recycled mixtures with asphalt emulsion," *Construction and Building Materials*, vol. 23, no. 3, pp. 1338–1343, 2009.
- [8] J. Ouyang, B. Pan, W. Xu, and L. Hu, "Effect of water content on volumetric and mechanical properties of cement bitumen emulsion mixture," *Journal of Materials in Civil Engineering*, vol. 31, no. 6, Article ID 04019085, 2019.
- [9] X. Li, X. Yin, B. Ma, J. Huang, and J. Li, "Cement-fly ash stabilization of cold in-place recycled (CIR) asphalt pavement mixtures for road bases or subbases," *Journal of Wuhan University of Technology-Materials Science Edition*, vol. 28, no. 2, pp. 298–302, 2013.
- [10] A. Kavussi and A. Modarres, "A model for resilient modulus determination of recycled mixes with bitumen emulsion and cement from ITS testing results," *Construction and Building Materials*, vol. 24, no. 11, pp. 2252–2259, 2010.
- [11] A. Modarres, M. Rahimzadeh, and M. Zarrabi, "Field investigation of pavement rehabilitation utilizing cold in-place recycling," *Resources, Conservation and Recycling*, vol. 83, pp. 112–120, 2014.
- [12] K. Su, Y. Hachiya, and R. Maekawa, "Study on recycled asphalt concrete for use in surface course in airport pavement," *Resources, Conservation and Recycling*, vol. 54, no. 1, pp. 37–44, 2009.
- [13] M. S. Baghini, A. B. Ismail, M. R. B. Karim, F. Shokri, and A. A. Firoozi, "Effects on engineering properties of cement-



- treated road base with slow setting bitumen emulsion,” *International Journal of Pavement Engineering*, vol. 18, no. 3, pp. 202–215, 2017.
- [14] A. Al-Hdabi, H. A. Nageim, F. Ruddock, and L. Seton, “Laboratory studies to investigate the properties of novel cold-rolled asphalt containing cement and waste bottom ash,” *Road Materials and Pavement Design*, vol. 15, no. 1, pp. 78–89, 2014.
- [15] S. Oruc, F. Celik, and M. V. Akpinar, “Effect of cement on emulsified asphalt mixtures,” *Journal of Materials Engineering and Performance*, vol. 16, no. 5, pp. 578–583, 2007.
- [16] M. Bocci, A. Grilli, F. Cardone, and A. Graziani, “A study on the mechanical behaviour of cement-bitumen treated materials,” *Construction and Building Materials*, vol. 25, no. 2, pp. 773–778, 2011.
- [17] X. Fang, A. Garcia, F. Winnefeld, M. N. Partl, and P. Lura, “Impact of rapid-hardening cements on mechanical properties of cement bitumen emulsion asphalt,” *Materials and Structures*, vol. 49, no. 1-2, pp. 487–498, 2016.
- [18] S. Du, “Effect of curing conditions on properties of cement asphalt emulsion mixture,” *Construction and Building Materials*, vol. 164, pp. 84–93, 2018.
- [19] A. Kavussi and A. Modarres, “Laboratory fatigue models for recycled mixes with bitumen emulsion and cement,” *Construction and Building Materials*, vol. 24, no. 10, pp. 1920–1927, 2010.
- [20] M. Ameri and A. Behnood, “Laboratory studies to investigate the properties of CIR mixes containing steel slag as a substitute for virgin aggregates,” *Construction and Building Materials*, vol. 26, no. 1, pp. 475–480, 2012.
- [21] J. Ouyang, Y. Tan, Y. Li, and J. Zhao, “Demulsification process of asphalt emulsion in fresh cement-asphalt emulsion paste,” *Materials and Structures*, vol. 48, no. 12, pp. 3875–3883, 2015.
- [22] S.-G. Hu, T. Wang, F.-Z. Wang, and Z.-C. Liu, “Adsorption behaviour between cement and asphalt emulsion in cement-asphalt mortar,” *Advances in Cement Research*, vol. 21, no. 1, pp. 11–14, 2009.
- [23] X. Fang, A. Garcia-Hernandez, F. Winnefeld, and P. Lura, “Influence of cement on rheology and stability of Rosin emulsified Anionic bitumen emulsion,” *Journal of Materials in Civil Engineering*, vol. 28, no. 5, Article ID 04015199, 2015.
- [24] J. Ouyang, Y. Tan, D. J. Corr, and S. P. Shah, “Investigation on the mixing stability of asphalt emulsion with cement through viscosity,” *Journal of Materials in Civil Engineering*, vol. 28, no. 12, Article ID 04016149, 2016.
- [25] J. Ouyang, L. Hu, H. Li, and B. Han, “Effect of cement on the demulsifying behavior of over-stabilized asphalt emulsion during mixing,” *Construction and Building Materials*, vol. 177, pp. 252–260, 2018.
- [26] J. Ouyang, J. Zhao, and Y. Tan, “Modeling mechanical properties of cement asphalt emulsion mortar with different asphalt to cement ratios and temperatures,” *Journal of Materials in Civil Engineering*, vol. 30, no. 10, Article ID 04018263, 2018.
- [27] J. Ouyang, D. J. Corr, and S. P. Shah, “Factors influencing the rheology of fresh cement asphalt emulsion paste,” *Journal of Materials in Civil Engineering*, vol. 28, no. 11, Article ID 04016140, 2016.
- [28] Ministry of Transport of the People’s Republic of China, *JTJ E02-2011. Standard Test Methods of Bitumen and Bituminous Mixtures for Highway Engineering*, China Communication Press, Beijing, China, 2011.
- [29] Ministry of Transport of the People’s Republic of China, *JTJ F40-2004. Technical Specification for Construction of Highway Asphalt Pavements*, China Communication Press, Beijing, China, 2004.
- [30] T. W. Kennedy, “Practical method of conducting the indirect tensile test,” *The Texas Highway Department*, vol. 53, pp. 10–98, 1972.
- [31] M. Miljković and M. Radenberg, “Characterising the influence of bitumen emulsion on asphalt mixture performance,” *Materials and Structures*, vol. 48, no. 7, pp. 2195–2210, 2015.
- [32] J. Ouyang and Y. Tan, “Rheology of fresh cement asphalt emulsion pastes,” *Construction and Building Materials*, vol. 80, pp. 236–243, 2015.
- [33] J. Ouyang and S. P. Shah, “Factors influencing the structure build-up of fresh cement asphalt emulsion paste,” *Road Materials and Pavement Design*, vol. 19, no. 1, pp. 87–103, 2018.
- [34] H. Wen, X. Li, and S. Bhusal, “Modelling the effects of temperature and loading rate on fatigue properties of hot mixed asphalt,” *International Journal of Pavement Engineering*, vol. 15, no. 1, pp. 51–57, 2014.
- [35] S. Wu, H. Wen, S. Chaney, K. Littleton, and S. Muench, “Evaluation of long-term performance of stone matrix asphalt in Washington state,” *Journal of Performance of Constructed Facilities*, vol. 31, no. 1, Article ID 04016074, 2017.
- [36] M. Miljković and M. Radenberg, “Fracture behaviour of bitumen emulsion mortar mixtures,” *Construction and Building Materials*, vol. 62, pp. 126–134, 2014.



## Research Article

# Material and Structural Properties of Fiber-Reinforced Resin Composites as Thin Overlay for Steel Bridge Deck Pavement

Hui Zhang <sup>1,2</sup>, Chengqi Zhou <sup>2</sup>, Kuan Li <sup>2</sup>, Peiwei Gao <sup>1</sup>, Youqiang Pan <sup>2</sup>  
and Zhixiang Zhang <sup>2</sup>

<sup>1</sup>Nanjing University of Aeronautics and Astronautics, Nanjing, Jiangsu 210016, China

<sup>2</sup>Jiangsu SinoRoad Engineering Research Institute, Nanjing, Jiangsu 211806, China

Correspondence should be addressed to Peiwei Gao; [gpw1963@163.com](mailto:gpw1963@163.com)

Received 28 August 2019; Revised 4 November 2019; Accepted 12 November 2019; Published 18 December 2019

Guest Editor: Jian Ouyang

Copyright © 2019 Hui Zhang et al. This is an open access article distributed under the Creative Commons Attribution License, which permits unrestricted use, distribution, and reproduction in any medium, provided the original work is properly cited.

Fatigue cracks are main damages to steel bridge deck pavement with thermosetting epoxy asphalt. By combining a high-toughness resin material with fiber woven fabrics, this study formed an ultrathin overlay of fiber-reinforced high-toughness resin to improve cracking resistance of pavement. Through theoretical measurement and bending test, this research studied change laws of bending and tensile properties of epoxy asphalt concrete after fiber reinforcement and analyzed bending strength and the maximum failure strain of beams at different temperatures. Moreover, the reinforcing effects of different fibers were discussed. It is found that bending strength, maximum failure strain, and stiffness modulus of the beams with epoxy asphalt are improved after fiber reinforcement. With the decrease of temperature, after fiber reinforcement, the mode of bending failure of the epoxy asphalt mixture (EAM) changes from brittle fracture into shear failure, accompanied with significant yield phenomenon. Furthermore, organic carbon fiber is sensitive to influences of temperature, while glass fiber is least sensitive to temperature.

## 1. Introduction

Steel bridge deck pavement is to pave thin layer structures with thickness of 5~8 cm on the orthotropic plates. Due to flexibility of steel bridge deck, there are extremely high application requirements for pavement materials, mainly including coordinated deformation capacity, waterproofness, high strength, and excellent fatigue performance of steel plates [1–3]. At present, typical pavement schemes, such as epoxy asphalt, gussasphalt, and stone matrix asphalt (SMA), are mainly used [4]. Of them, epoxy asphalt materials with higher antirutting performance at high temperature and bending fatigue performance are universally used in China [5, 6].

Different from thermoplastic asphalt pavement, because epoxy asphalt is a thermosetting material, cracking as shown in Figure 1, a main type of damages mainly occurs in wheel track bands, longitudinal diaphragms of steel box beams, and ends of U-shaped ribs under long-term load [7, 8]. At present, technologies for preventive maintenance of asphalt pavement have been mainly studied, thus proposing some relative

mature schemes, such as fog sealing layer, slurry seal, microsurfacing, and thin overlays. However, at present, there are no mature technologies and materials for timely preventive maintenance of cracks on epoxy asphalt pavement.

The traditional technologies for preventive maintenance of asphalt pavement are mainly based on asphalt materials. Due to limited strength and low bond strength of the materials with epoxy asphalt pavement, peeling and cracking easily appear. The research on the maintenance technology of steel bridge deck pavement started relatively late. There are some researches on cracks, swelling, and patching [9–11] and some achievements in pavement in which the original hot-blended epoxy asphalt is replaced with new cold-blended epoxy resin materials are mainly obtained. However, there are few technologies for preventive maintenance of bridge deck. The authors and other researchers have reported the scheme of preventive maintenance of bridge deck using epoxy resin seal [12, 13]. Because of high requirements for deformation capacity of materials on steel bridge deck pavement, fatigue cracking easily appears when

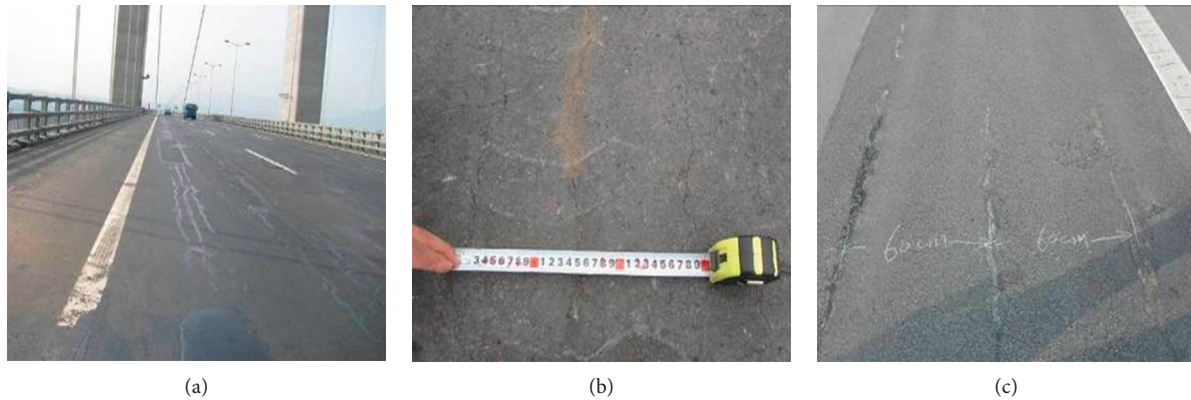


FIGURE 1: Fatigue cracks in epoxy asphalt on steel bridge deck pavement.

using the general scheme of epoxy resin and synchronous surface dressing.

In order to further improve tensile resistance of pavement materials, the research results of the fiber-reinforced asphalt mixture have been reported in many literatures, and the optimal mixing amount and performance mechanisms of the polyester fiber in the asphalt mixture have been proposed [14–16]. As composites emerge, researchers have conducted research and made breakthrough in high-temperature performance, vitrification, and fatigue properties of fiber-reinforced resin materials, which makes it possible for the materials to be applied in engineering of the transportation industry [17–19].

Based on a high-toughness resin material and its combination with fiber woven fabrics, the research prepared an ultrathin overlay of fiber-reinforced high-toughness resin with the thickness of only about 5 mm. The overlay enhanced cracking resistance of the existing epoxy pavement, thus extending service life of steel bridge deck pavement with epoxy asphalt. It is expected to provide supports for research and engineering application of technologies for preventive maintenance of steel bridge deck pavement with epoxy asphalt.

## 2. Materials and Experimental Methods

**2.1. Experimental Materials.** This study used the Bv epoxy asphalt mixture (EAM), which was produced by ChemCo Systems Company in the United States and composed of component A (liquid bisphenol A epoxy resin) and component B (homogeneous compositions comprising petroleum asphalt and curing agent) with the ratio of 100: 518. Special aggregates for steel bridge deck pavement produced by Jiangsu Maodi Group Co., Ltd. and mineral powder manufactured from limestone in Jurong county, Jiangsu province, China, were utilized. The proportion of mineral aggregates, i.e., 1# aggregate (with diameter of 10~13 mm), 2# aggregate (with diameter of 5~10 mm), 3# aggregate (with diameter of 3~5 mm), 4# aggregate (with diameter of 1~3 mm), 5# aggregate (with diameter of 0.075~1 mm), and mineral powder was 2.5%: 22.5%: 21.5%: 22%: 23%: 8.5%. Controlling the resultant gradation according to the median of the gradation range, the results are shown in Table 1. The asphalt-aggregate ratio was 6.5%.

TABLE 1: The aggregate gradation used in this study.

Mesh (mm)	Mass percentage of aggregates passing through meshes (square mesh, mm) (%)					
	13.2	9.5	4.75	2.36	0.6	0.075
Grading requirements	100	95~100	65~85	50~70	28~40	7~14
Resultant gradation	100.0	99.7	75.2	59.3	34.5	11.0
Median of gradation	100.0	97.5	75.0	60.0	34.0	10.5

The used RPF high-toughness epoxy resin was provided by Jiangsu SinoRoad Transportation Science and Technology Co., Ltd., China, and comprised component A (polyurethane-modified epoxy resin) and component B (fatty amine curing agent) with the ratio of 4:1. By referring to the ASTM D638-2014 test method, the tensile strength and elongation of high-toughness resin were measured through tensile test. The tensile strength, elongation at fracture, and tensile elastic modulus were 25.2 MPa, 63.2%, and about 40 MPa, respectively, tested at  $23 \pm 1^\circ\text{C}$  and a stretching rate of 50 mm/min.

In reference to the ASTM D4541-09 test method, bond performance of high-toughness resin and epoxy asphalt concrete was determined through the pull-off test at room temperature of  $23^\circ\text{C}$  and high temperature of  $70^\circ\text{C}$  at a drawing rate of 0.7 MPa/s. The test results are presented in Table 2. At room temperature of  $23^\circ\text{C}$ , the fracture surface in the pull-off test was found at the interface of sealing materials and the mixture, and bond strength of high-toughness resin was 14.65 MPa. When temperature rose to  $70^\circ\text{C}$ , the fracture surface was located in the interior of EAM. The fracture surface in the pull-off test is demonstrated in Figure 2. This indicated that there was a strong bond capacity between high-toughness resin and epoxy asphalt concrete.

The utilized fiber cloth included basalt, glass, and carbon in total. The basalt fiber cloth was manufactured by Jiangsu Tianlong Co. Ltd., China, and represented with BF, while glass fiber cloth was produced by Jiangsu Zhongyitong Company, China, and expressed as GF. Moreover, the carbon fiber cloth was from Zhejiang Haining Company, China, expressed as CF. Performance parameters at room temperature of fiber are presented in Table 3.

TABLE 2: Bond strength of high-toughness resin with epoxy asphalt concrete.

Test temperature (°C)	Pull-off strength (MPa)	Fracture surface
23	14.65	Interface between resin and mixture
70	1.56	Interior of the mixture



FIGURE 2: Fracture interface in pull-off test (70°C).

**2.2. Finite Element Simulation.** By using the finite element software ABAQUS, mechanics simulation was performed on steel bridge deck pavement with fiber-reinforced epoxy resin-modified asphalt (Figure 3). By referring to boundary parameters and the worst load position in literatures [9, 10], the influences of changes of modulus of different fiber-reinforced thin resin layers on mechanical response of the original pavement structure were analyzed. The moduli were 3,000, 5,000, 7,000, 9,000, 11,000, 13,000, 15,000, 17,000, 19,000, and 21,000 MPa. Load was standard axle loading of 100 kN on a single axle with dual tires, and tire pressure was 0.7 MPa. Model parameters are shown in Table 4.

The maximum transverse tensile stress  $\sigma$  and strain  $\epsilon$  were selected as indexes of mechanical analysis. The calculation results are displayed in Figure 4. With the increase of modulus of the thin overlay, the maximum tensile stress and strain of the original epoxy asphalt pavement surface significantly decrease. When modulus of the thin overlay increases to 21,000 MPa, the maximum tensile stress and strain of the original pavement reduce by about 66.2% and 64.3%, respectively, in comparison with the pavement without thin overlay. As modulus of the thin overlay rises, the maximum tensile stress of the thin overlay itself remarkably increases, while the maximum tensile strain significantly decreases. When the modulus of the thin overlay increases from 3,000 to 21,000 MPa, the maximum tensile stress of the thin overlay rises about 212.6% while the maximum tensile strain reduces about 53.7%.

**2.3. Specimen Preparation and Experimental Methods.** By referring to the EN 12697-33-2007 method of specimens prepared by roller compactor, a rutting plate of the EAM was molded. After molding, the plate was placed in an oven to be cured for 4 h at 120°C. After taking it out and cooling to room temperature, the surface of the plate was manually uniformly coated with high-toughness resin by using a brush with coating weight of 0.5 kg/m<sup>2</sup>, and fiber cloth was immediately laid at the same time. After that, high-

toughness resin was smeared on the surface of the fiber cloth again with coating weight of 0.5 kg/m<sup>2</sup>, so as to ensure that the fiber cloth was fully infiltrated in the resin layer. The processes of specimen preparation are shown in Figure 5.

After being cured for 16 h at 23°C, the test plate was cut into prismatic beam specimens with dimensions of 240 ± 2 mm × 30 ± 2 mm × 35 ± 2 mm by using a rock cutting machine. After that, by referring to EN 12697-24-2018, the bending test was conducted on the specimens of the fiber cloth-reinforced epoxy resin-modified asphalt mixture by using the three-point beam (3PB) bending test. The test schematic is shown in Figure 6. By placing one side of fiber resin cloth on the bottom, the maximum bending strength, the maximum fracture strain, and bending stiffness modulus were measured. The test was carried out at room temperature (15°C) and low temperature (−10°C) at loading rate of 50 mm/min.

At present, there are still no specific test methods for evaluating the fatigue resistance of overlay of the fiber-reinforced thin resin. Considering this, the research designed a fatigue test on plates under cyclic loading based on the rutting test, to assess the fatigue resistance of the plate. The test schematic is shown in Figure 7.

The test plates were prepared in the following steps, and the processes of specimen preparation are shown in Figure 8.

- (1) A rutting plate of epoxy asphalt concrete measuring 30 cm long, 30 cm wide, and 2.5 cm thick was molded at first. Then, by using a stone cutting machine, the plate was cut into three plates with the dimensions of 30 cm × 10 cm × 2.5 cm (length × width × thickness), which were then halved to two plates measuring 30 cm long, 5 cm wide, and 2.5 cm thick.
- (2) RPF high-toughness epoxy resin was used to bond the halved specimens into a test plate with the dimensions of 30 cm × 10 cm × 2.5 cm (length × width × thickness), which was then put in the oven to be cured at 60°C for 16 h.
- (3) High-toughness resin was uniformly coated on the surface of the test plate, on which different types of fiber cloth were immediately laid. Then, high-toughness resin was smeared on the surface of the fiber cloth again after the fiber cloth was fully infiltrated in the bottom resin layer and interlaminar bubbles were removed. Then, the plate was placed in the oven to be cured for 16 h at 60°C again.
- (4) After putting the cured plate in the rutting test box for 5 h, metallic supports were placed under two sides of the plate to lift the plate by 20 cm. Then, the fatigue test under wheel rolling was conducted. The loading wheel rolled back and forth along the direction perpendicular to the joint of the plate at the



TABLE 3: Requirements of technical indexes of fiber cloth.

Fiber	Weight (g/m <sup>2</sup> )	Tensile strength (MPa)	Tensile elastic modulus (MPa)	Elongation (%)
CF	300	≥3400	≥2.4 × 10 <sup>5</sup>	≥1.6
GF	450	≥1500	≥0.72 × 10 <sup>5</sup>	≥2.8
BF	300	≥2200	≥1.04 × 10 <sup>5</sup>	≥1.6

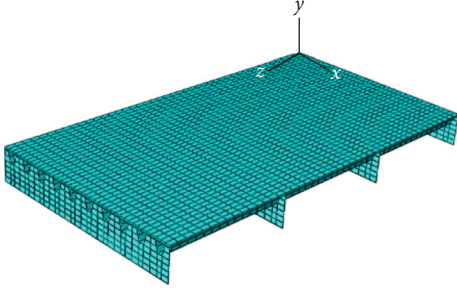


FIGURE 3: Structural model of steel bridge deck pavement.

speed of 42 times per minute at 60 and 75°C. The wheel load used was  $0.7 \pm 0.05$  MPa. The processes of fatigue test are shown in Figure 9.

### 3. Results and Discussion

**3.1. Theoretical Measurement.** Based on the classical theory of fiber composites, it is considered that the single-layer fiber cloth in the fiber-reinforced resin composites studied in this research is continuously and uniformly arranged in the resin matrix and is firmly bonded to the resin matrix. It is assumed that fiber, resin matrix, and fiber cloth-reinforced resin composites have the same tensile strain. Under vertical loading force, the resin matrix completely transfers tensile force  $F$  to fiber through the interface, and the simplified model is displayed in Figure 10.

According to the balance of forces, the following formulas are obtained:

$$\begin{aligned}
 F &= F_f + F_m = \sigma_f \cdot A_f + \sigma_m \cdot A_m, \\
 A_c &= A_f + A_m, \\
 V_f &= \frac{A_f}{A_c}, \\
 V_m &= \frac{A_m}{A_c}, \\
 V_f + V_m &= 1,
 \end{aligned} \tag{1}$$

where  $A_f$ ,  $A_m$ , and  $A_c$  represent the cross-sectional areas of fiber, resin matrix, and fiber cloth-reinforced resin composites, respectively;  $V_f$  and  $V_m$  indicate the volume fractions of fiber and resin matrix, respectively. Moreover,  $\sigma_f$  and  $\sigma_m$  denote the forces applied on fiber and resin matrix, so the average tensile stress on fiber cloth-reinforced composites is shown as follows:

$$\sigma_{cL} = \frac{F}{A_c} = \frac{(\sigma_f \cdot A_f + \sigma_m \cdot A_m)}{A_c} = \sigma_f \cdot V_f + \sigma_m \cdot V_m. \tag{2}$$

In the fiber cloth-reinforced thin resin overlay, the matrix is resin. When fiber cloth and resin matrix are within

the range of elastic deformation, the following formula is obtained in accordance with Hooke's law:

$$\begin{aligned}
 \sigma_f &= E_f \cdot \varepsilon_f, \\
 \sigma_m &= E_m \cdot \varepsilon_m, \\
 \sigma_{cL} &= E_{cL} \cdot \varepsilon_{cL},
 \end{aligned} \tag{3}$$

where  $\varepsilon_f$ ,  $\varepsilon_m$ , and  $\varepsilon_{cL}$  indicate the longitudinal strains of fiber, resin matrix, and fiber cloth-reinforced resin composites, respectively;  $E_f$ ,  $E_m$ , and  $E_{cL}$  represent the elastic moduli of fiber, resin matrix, and composites, respectively. Based on the isostrain assumption  $\varepsilon_f = \varepsilon_m = \varepsilon_{cL}$ , the expression of longitudinal elastic modulus of unidirectional continuous fiber-reinforced composites, that is, the rule of the mixture is demonstrated as follows:

$$E_{cL} = E_f \cdot V_f + E_m \cdot V_m = E_f \cdot V_f + E_m \cdot (1 - V_f). \tag{4}$$

Elastic moduli of CF, BF, and GF are 230, 104, and 72 GPa, respectively, and modulus of the resin matrix is 0.04 GPa. According to formula (4), the relationship between modulus of fiber-reinforced resin composites and fiber content can be obtained as shown in Figure 11. In the experiment, resin content is  $1 \text{ kg/m}^2$ , and weight of fiber is demonstrated in Table 3. In accordance with the ratio of weights of fiber to resin, CF and BF contents are 30% and GF content is 45%. Furthermore, through theoretical calculation, moduli of CF-, BF-, and GF-reinforced resin composites are 69.03, 31.23, and 32.42 GPa, respectively.

Based on formulas (3) and (4), the following formula is obtained:

$$\sigma_{cL} = E_f \cdot \varepsilon_f \cdot V_f + E_m \cdot \varepsilon_m \cdot (1 - V_f). \tag{5}$$

The ratio of load of fiber to resin matrix is presented as follows:

$$\frac{F_f}{F_m} = \frac{E_f \cdot \varepsilon_f \cdot V_f}{[E_m \cdot \varepsilon_m \cdot (1 - V_f)]} = \frac{E_f \cdot V_f}{[E_m \cdot (1 - V_f)]}. \tag{6}$$

In accordance with formula (6), when volume content  $V_f$  of fiber is certain, the larger the ratio of  $E_f/E_m$ , the more the load the fiber bears and the stronger the reinforcing effects are. In theory, because tensile elastic modulus (Table 1) of CF is higher than those of GF and BF, the effects of CF in improving bending and tensile resistance of the composite resin overlay and overall structure of the mixture are the best.

Similarly,  $E'_m$ ,  $E'_f$ , and  $E'_{cL}$  represent the elastic moduli of the matrix of EAM, fiber, and composite structure, respectively;  $V'_m$  and  $V'_f$  indicate the volume fractions of the matrix of EAM and fiber, respectively. Based on bending test of the mixture, tensile elastic modulus of the matrix of EAM in the linear elastic stage is 1,063 MPa, and theoretical moduli of CF-, BF-, and GF-reinforced resin composites are

TABLE 4: Model parameters in finite element simulation.

Structural layer	Length (m) (Z)	Width (m) (X)	Thickness (m) (Y)	Elastic modulus (MPa)	Poisson's ratio
Thin overlay	11.25	6	0.005	—	0.25
Original pavement layer	11.25	6	0.055	2000	0.25
Steel bridge deck	3.75 × 3	6	0.014	210000	0.3
Transverse diaphragm plate	0.01	6	0.84	210000	0.3
U-shaped rib	11.25	0.006	0.28	210000	0.3

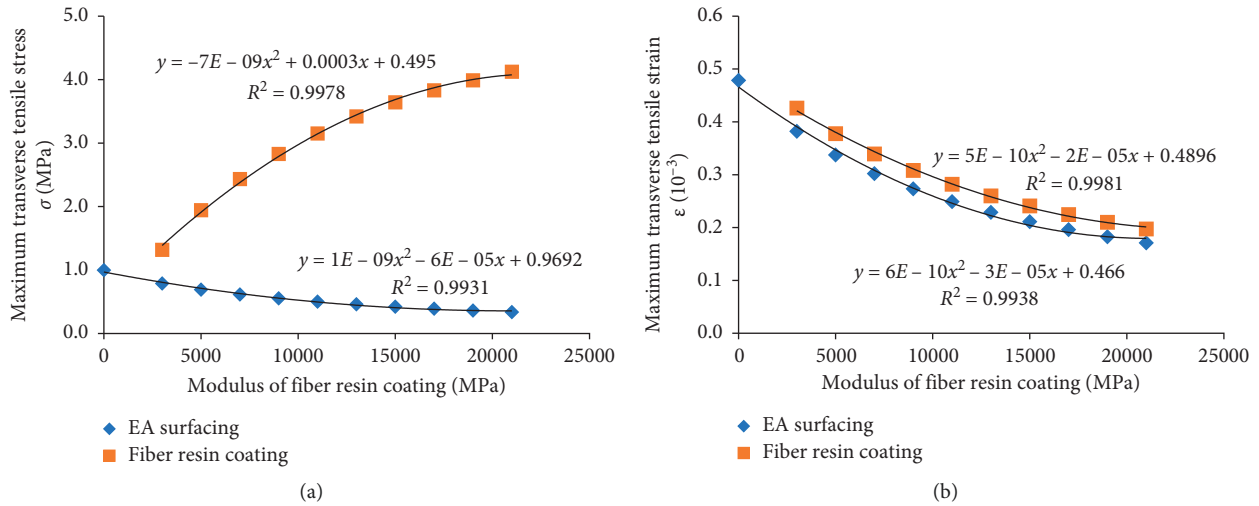


FIGURE 4: Change laws of the maximum tensile stress and strain of the pavement layer with modulus of the thin overlay.

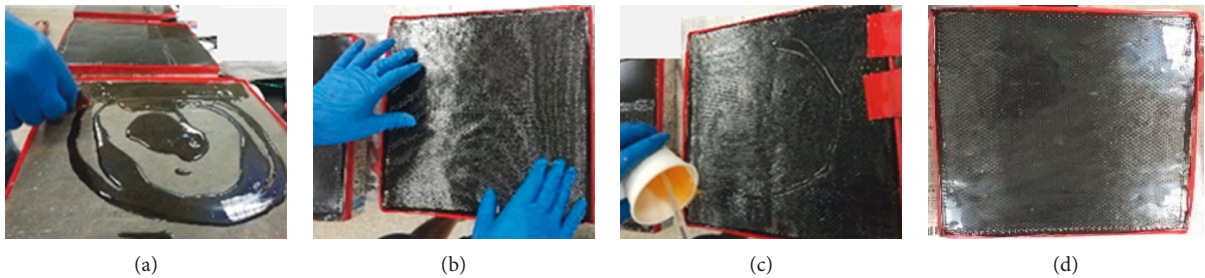


FIGURE 5: Specimen preparation of fiber-reinforced resin composite overlay: (a) blade coating resin on the bottom; (b) laying fiber cloth; (c) brush coating resin on the surface; (d) curing.

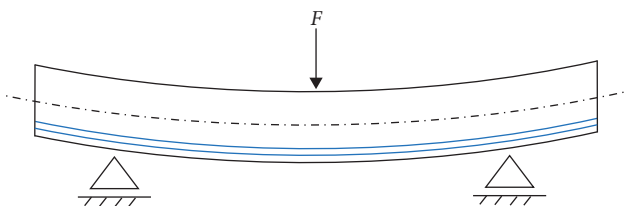


FIGURE 6: Tensile and bending test of the fiber overlay.

69,030, 31,230, and 32,420 MPa, respectively. In accordance with formula (4), theoretical values of tensile elastic moduli of the fiber-reinforced composite structure are shown in Table 5.

### 3.2. Evaluation of Cracking Resistance

3.2.1. Test at Room Temperature. The bending test results at room temperature are shown in Figure 12. The bending

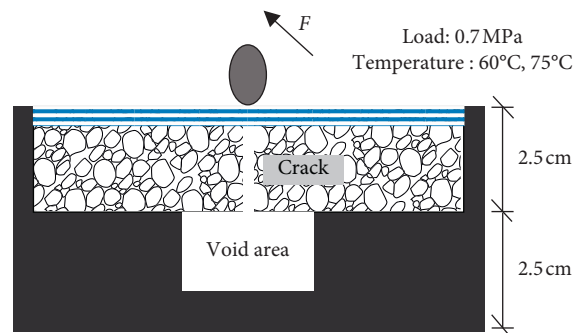


FIGURE 7: Schematic diagram of fatigue test on plates based on rutting.

strength of the EAM beam (blank specimen) is 7.29 MPa at room temperature of 15°C, and the maximum bending strain and bending stiffness in failure are 10,876  $\mu\epsilon$  and



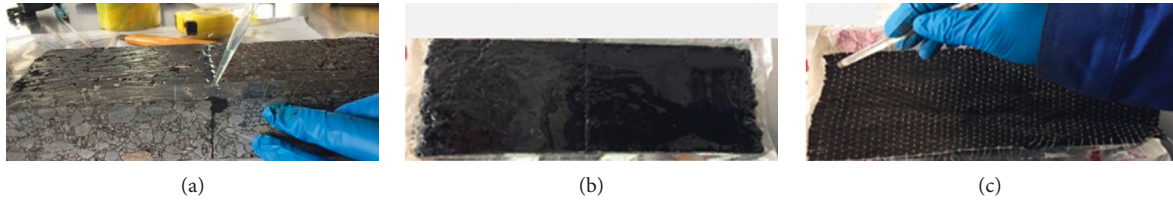


FIGURE 8: Preparation process of the test plate for the fatigue test. (a) Bonding using the high-toughness resin. (b) Smearing the high-toughness resin. (c) Laying CF cloth.

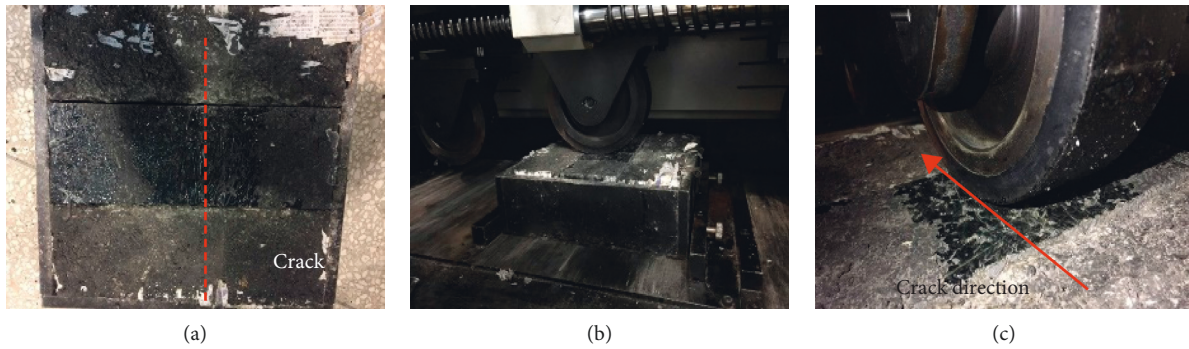


FIGURE 9: Fatigue test on the plate.

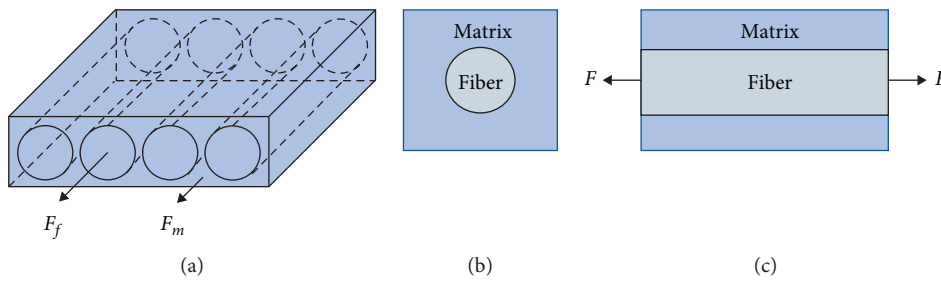


FIGURE 10: Simplified model of unidirectional continuous composites.

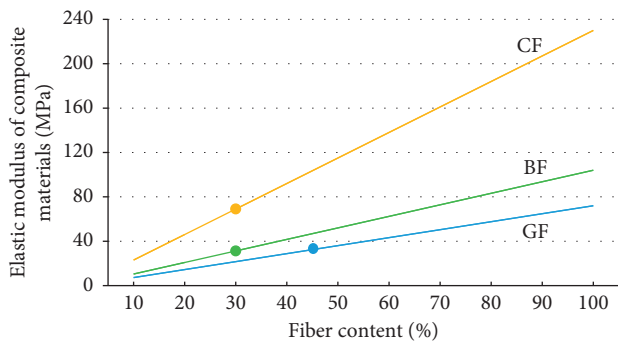


FIGURE 11: Moduli and fiber contents of unidirectional continuous composites.

670 MPa, respectively. After fiber reinforcement, bending strength, maximum bending strain, and bending stiffness of the EAM are improved to some extent. At room temperature of 15°C, the reinforcement amplitude of CF is the highest and bending strength and the maximum bending strain can be improved to 99.62 MPa and

TABLE 5: Tensile elastic moduli of the composite structure through theoretical calculation at room temperature.

No.	Material	Tensile elastic modulus (MPa)
1	EAM beam	1063
2	CF-reinforced beam	4733
3	BF-reinforced beam	2692
4	GF-reinforced beam	2756

50,393  $\mu\epsilon$ . Moreover, bending stiffness in failure can be increased to 1,778 MPa. The reinforcement amplitudes of GF and BF are basically the same and their bending strengths are 41.2 and 42.7 MPa. Furthermore, the maximum bending strains are 28,760 and 32,458  $\mu\epsilon$  and bending stiffness in failure is 1,435 and 1,308 MPa, respectively.

As shown in Figure 13, at room temperature of 15°C, with constant increase of load, bending deflections of the beams linearly rise and shows a good linear elastic trend. The CF-reinforced beam has the highest bending stiffness, followed by GF- and BF-reinforced ones, which all show the

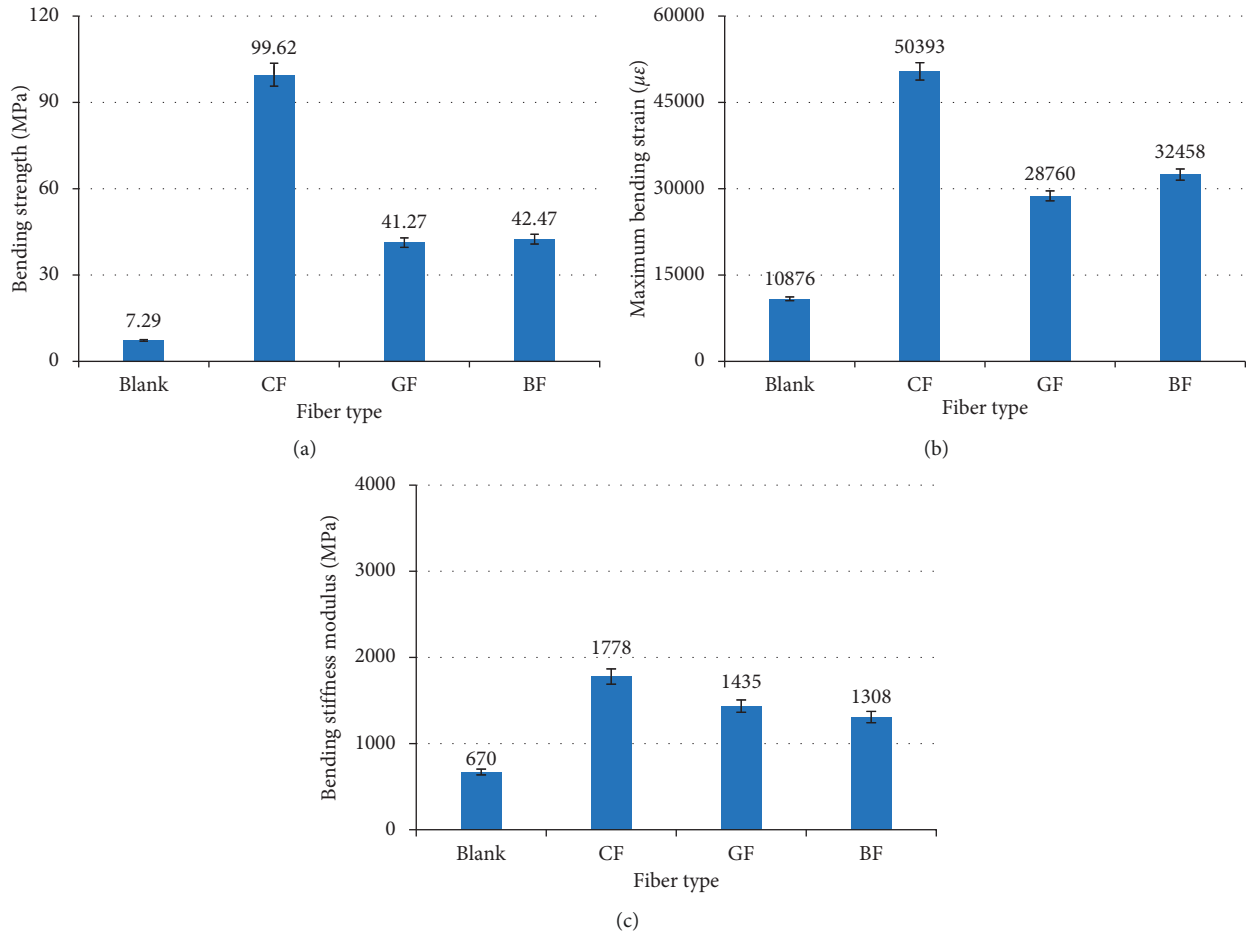


FIGURE 12: Bending test results at room temperature: (a) bending strength at 15°C; (b) the maximum bending strain at 15°C; (c) bending stiffness modulus in failure at 15°C.

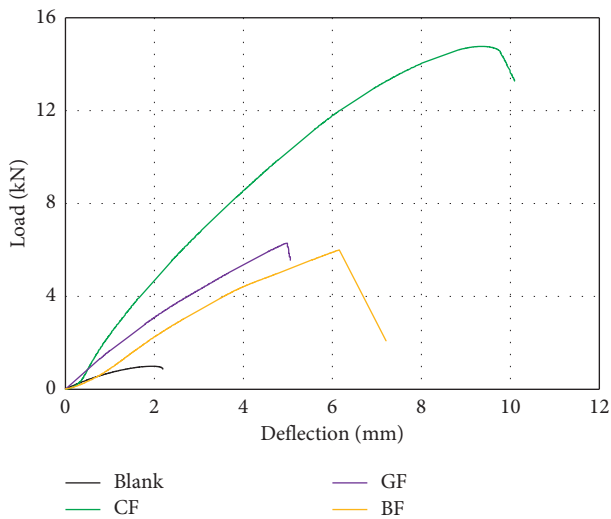


FIGURE 13: Load-deflection curves at 15°C.

typical brittle failure. This law well corresponds to tensile strength and modulus of fiber materials, that is, the higher the tensile strength and elastic modulus of fiber materials for reinforcement, the better the reinforcing effects.

Failure and fracture of the specimens at room temperature of 15°C are shown in Figure 14. The EAM beam (blank specimen), GF-reinforced beam, and BF-reinforced beam all show fracture failure of normal section. The specimen of CF-reinforced beam presents obvious failure phenomenon that the CF-reinforced resin and the epoxy asphalt beam are separated at the bond interface. This indicates that strength and tensile elastic modulus of the CF-reinforced resin composite are much larger than those of the EAM beam, and displacements of them under the same load are inconsistent. With the increase of bending and tensile load, relative slippage occurs on the interface of the CF-reinforced beam, finally resulting in delaminating failure.

3.2.2. *Test at Low Temperature.* The bending test results at low temperature of -10°C are shown in Figure 15; in comparison with the room temperature of 15°C, bending strength of the EAM beam (blank specimen) increases to 15.98 MPa with the decrease of temperature. Moreover, the maximum bending strain reduces to 5,865  $\mu\epsilon$  and bending stiffness in failure rises to 2,724 MPa. After fiber reinforcement, bending strength and the maximum bending strain of EAM increase to some extent.



FIGURE 14: Fracturing behaviors of beam specimens of resin composite overlay reinforced with different fibers at 15°C. (a) Blank. (b) CF. (c) GF. (d) BF.

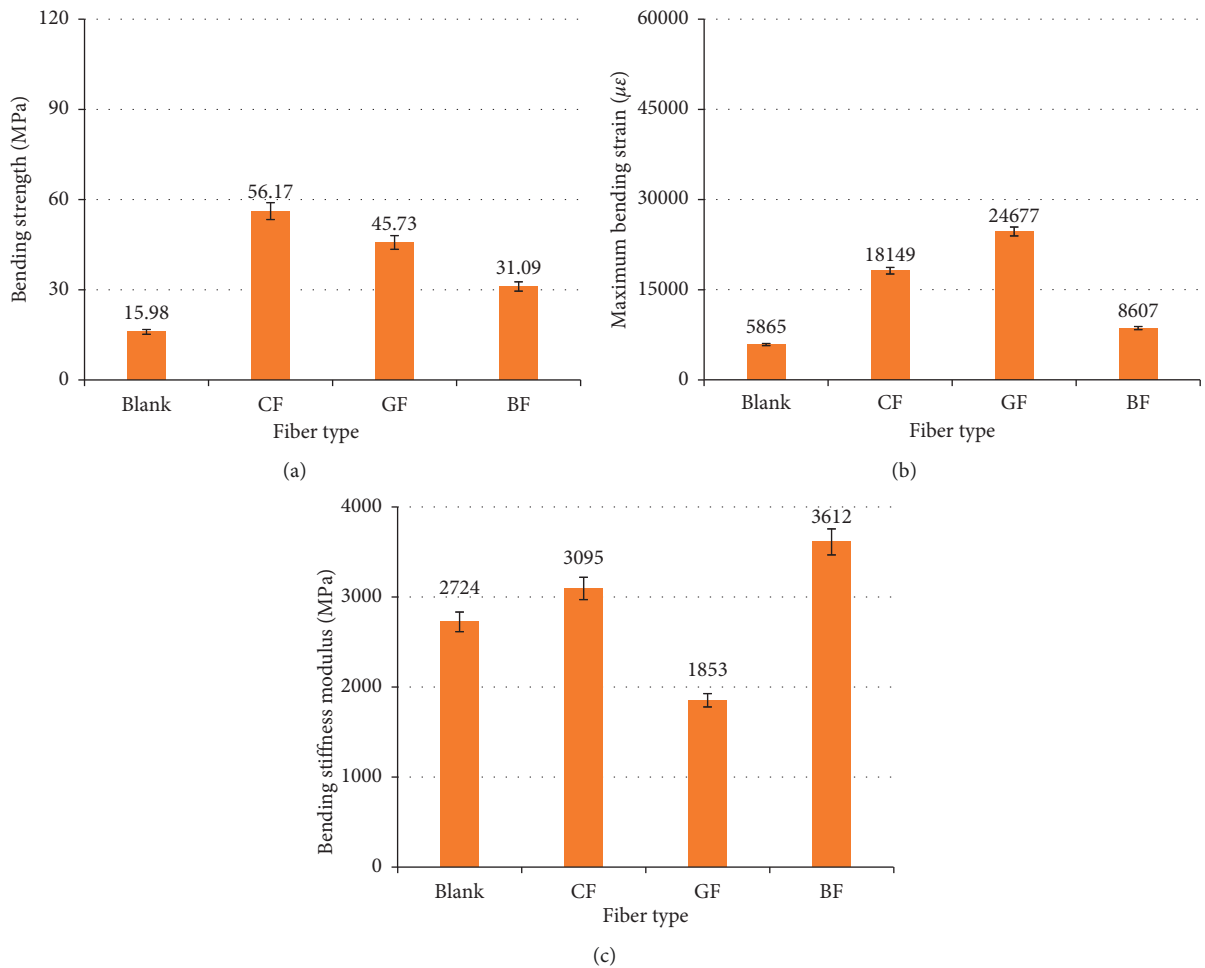
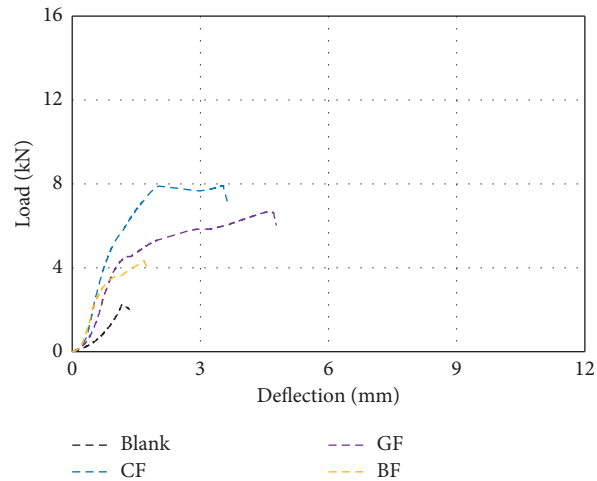


FIGURE 15: Bending test results at low temperature. (a) Bending and tensile strength at  $-10^{\circ}\text{C}$ ; (b) the maximum bending and tensile strain at  $-10^{\circ}\text{C}$ ; (c) bending stiffness modulus at  $-10^{\circ}\text{C}$ .

At low temperature of  $-10^{\circ}\text{C}$ , reinforcing effects of CF are optimal. Bending strength and the maximum bending strain of the CF-reinforced beam are 56.17 MPa and 18,149  $\mu\epsilon$ , respectively, and bending stiffness in failure is 2,724 MPa. For the BF-reinforced beam, bending strength and the maximum bending strain are 31.09 MPa and 8,607  $\mu\epsilon$ , and bending stiffness in failure is 3,612 MPa. In addition, bending strength, maximum bending strain, and bending stiffness in failure of the GF-reinforced beam are 45.73 MPa, 24,677  $\mu\epsilon$ , and 1,853 MPa, respectively.

As shown in Figure 16, at low temperature of  $-10^{\circ}\text{C}$ , as load constantly rises, bending deflections of the beams linearly increase at first. The typical brittle failure is still found on the EAM beam (blank specimen). After fiber reinforcement, when load rises to a certain degree, there is a certain yield phenomenon in the late stage, gradually changing from the initial elastic deformation to plastic deformation until the mixture is finally fractured.

The reason for yield phenomenon at low temperature is generally that shear failure is likely to appear to the materials

FIGURE 16: Load-deflection curves at  $-10^{\circ}\text{C}$ .FIGURE 17: Fracturing behaviors of the beam specimens of resin composite overlays reinforced with different fibers at  $-10^{\circ}\text{C}$ . (a) Blank. (b) CF. (c) GF. (d) BF.

under bending and tensile forces. The fracture surface of the specimens at low temperature of  $-10^{\circ}\text{C}$  is further verified, as shown in Figure 17. The EAM beam (blank specimen) still shows brittle fracture failure. For CF-, GF-, and BF-reinforced beams, the fracture surface shows an angle of  $45^{\circ}$  with load, indicating that tensile strength of the normal section of the materials is very high owing to modulus of fiber largely increasing at low temperature. With the rise of bending and tensile load, shear stress of the oblique section of the materials exceeds the maximum strength, so essentially the materials show shear failure.

**3.2.3. Comparison of Room-Temperature and Low-Temperature Performances.** By analyzing results of different specimens at room temperature and low temperature as shown in Figure 18, the following conclusions are made:

- (1) With the reduction of temperature, obvious brittle phenomenon is found on the EAM beam (blank specimen) and bending stiffness in failure rises from 670 to 2,724 MPa, with increase amplitude of 300%. Bending strength increases from 7.29 to 15.98 MPa, while the maximum bending strain decreases from 10,876 to 5,865  $\mu\epsilon$ .
- (2) Change of performances of the organic CF-reinforced beam is sensitive to temperature, and bending stiffness in failure increases by 74% compared with that at room temperature. Bending strength reduces by 44% from

99.62 to 56.17 MPa and the maximum bending strain decreases to 18,149  $\mu\epsilon$  with amplitude of 64%.

- (3) In comparison with room temperature, bending stiffness of the BF-reinforced beam increases by 176%, while bending strength decreases by 26%. Furthermore, the maximum bending strain reduces by 73% from 32,458 to 8,607  $\mu\epsilon$ .
- (4) For inorganic nonmetal GF-reinforced beam, the change of performance is least sensitive. Bending stiffness rises by 29% compared with that at room temperature, while bending strength increases from 41.27 to 45.73 MPa, with amplitude of 10%. In addition, bending strain reduces by 14% from 28,670 to 24,677  $\mu\epsilon$ .

**3.3. Evaluation of Fatigue Performance.** The results of fatigue tests on the plates are shown in Table 6. Considering that modulus of materials always decreases and cracking resistance of structures declines at high temperatures, the research focuses on testing of fatigue and cracking resistance of the plate at high temperatures. The results of fatigue tests on the plates are consistent with those of static bending tests. The results reveal that

- (1) The EAM beam (blank specimen) is fractured immediately after loading at high temperature of  $60^{\circ}\text{C}$ , while BF-, GF-, and CF-reinforced beams are not damaged, even no cracking appearing at the joints.

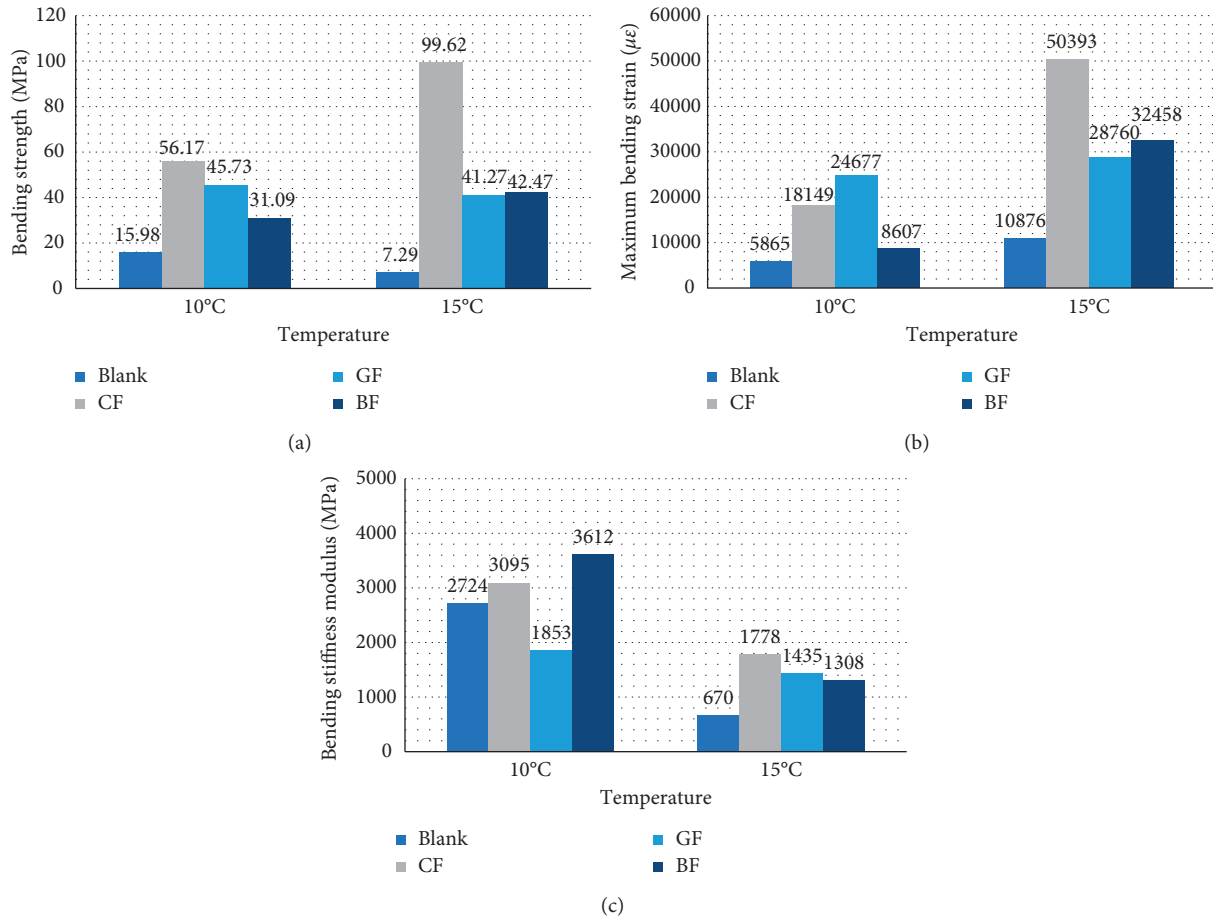


FIGURE 18: Room-temperature and low-temperature performances: (a) bending strength; (b) the maximum failure strain; (c) bending stiffness modulus in failure.

TABLE 6: Fatigue test results of composite structures under wheel rolling at 60 and 75°C.

Fiber type	Temperature (°C)	Test time (h)	Result
EAM beam	60	—	Fracture failure immediately after loading
	75	—	Fracture failure immediately after loading
BF-reinforced beam	60	2	No fracture
	75	1	No fracture and obvious bending at the midspan
GF-reinforced beam	60	2	No fracture
	75	1	Cracking of the mixture
CF-reinforced beam	60	2	No fracture
	75	2	No fracture

(2) As the temperature rises to 75°C, fractures still occur to the EAM beam immediately after loading; the GF-reinforced beam is fractured after loading for 1 h; the BF-reinforced beam presents certain bending after loading for 1 h; while no cracking occurs to the CF-reinforced beam. The fatigue cracking behaviors of the specimens are shown in Figure 19.

#### 4. Application and Effect

The research results have been applied in the pavement and maintenance projects of a series of steel bridge decks, including Zhenjiang–Yangzhou Yangtze River Bridge, the

third Nanjing Yangtze River Bridge, and Suzhou–Nantong Bridge, which are shown in Figures 20 and 21. Double-layer epoxy asphalt of 5.5 cm thick was paved on these steel bridge decks. The construction technologies of the thin overlays mainly involve sandblasting and shot blasting of the original pavement (to enhance the interfacial bonding), smearing of resin, and laying of CF cloth. In addition, to improve the skid resistance, basalt gravels with grain size of 3~5 mm need to be spread on the surface of resin. The structure depth can be as thick as 1.2 mm and the frictional coefficient exceeds 60 BPN. The structural design of the application scheme is displayed in Figure 22. The research results have been applied to the bridges for at least 5 years and still present favorable effects.



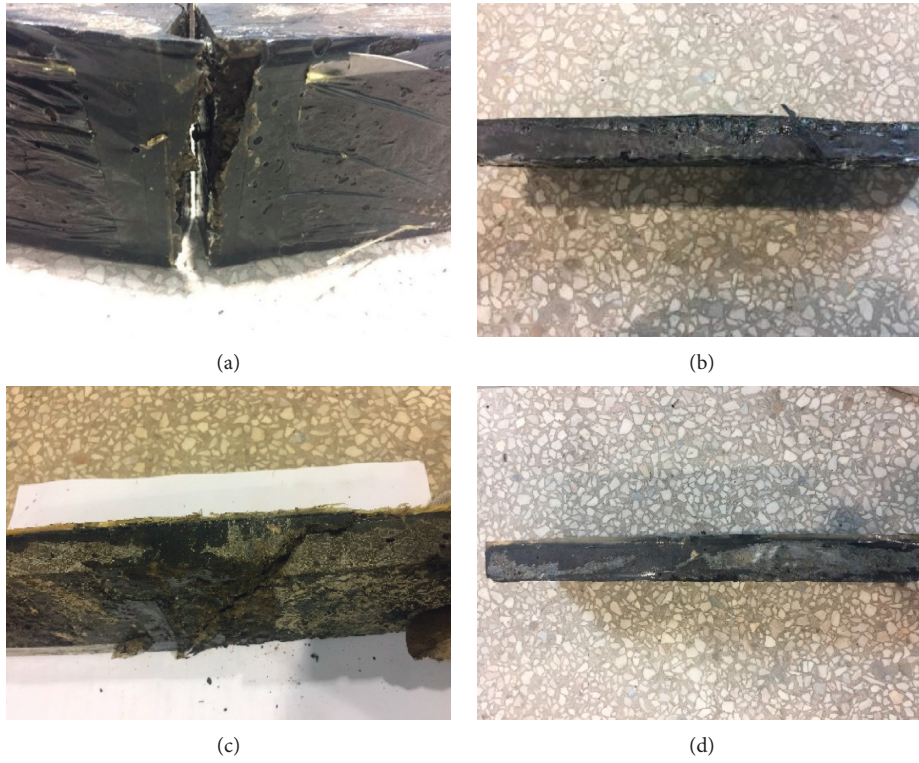


FIGURE 19: Fatigue cracking behaviors of the specimens of resin composite overlays reinforced with different fibers at 75°C. (a) Blank. (b) BF-reinforced beam. (c) GF-reinforced beam. (d) CF-reinforced beam.



FIGURE 20: Continued.





FIGURE 20: Construction technology of the thin overlay of fiber-reinforced resin on the Suzhou–Nantong Bridge.



FIGURE 21: Effects of construction. (a) Zhenjiang–Yangzhou Yangtze River Bridge (2014). (b) The third Nanjing Yangtze River Bridge. (c) Suzhou–Nantong Bridge.

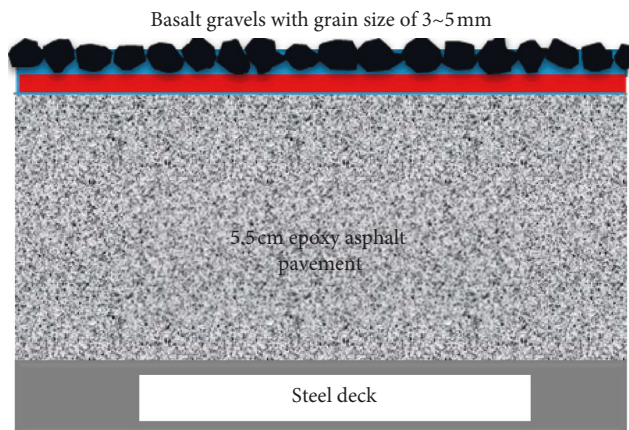


FIGURE 22: Structure of the thin overlay of fiber-reinforced resin.

## 5. Conclusion

Through beam bending test, this study mainly investigated change laws of bending and tensile performances of epoxy asphalt concrete after fiber reinforcement and analyzed bending strength and the maximum failure strain of the beams at different temperatures. Moreover, reinforcing effects of different fibers were discussed. The main conclusions are made as follows:

- (1) After fiber reinforcement, bending strength, maximum failure strain, and stiffness modulus of the EAM beam are improved, which is favorable for cracking resistance in pavement. It provides a theoretical basis manifesting the engineering application value of the thin overlay of fiber-reinforced resin.

- (2) As temperature decreases, the bending and failure mode of fiber-reinforced EAM changes from brittle fracture into shear failure, accompanied with significant yield phenomenon. The result suggests that the thin overlay of fiber-reinforced resin is able to change the brittle failure of the original EAM pavement to yield failure, which makes most of the performance of the pavement materials and exerts practical significance for prolonging the service life.
- (3) By comparing results of CF, GF, and BF, it is found that organic fiber is sensitive to influences of temperature, while GF is least sensitive to temperature.
- (4) By performing fatigue tests on plates, it is found that compared with the original EAM pavement, the CF-reinforced specimen improved the fatigue and cracking resistance at the greatest extent, particularly showing favorable effects at high temperatures.
- (5) To enhance the application value in engineering, a thin overlay structure of CF-reinforced resin and gravel is designed. It can improve fatigue performance and skid resistance of the pavement. The earliest application of the design has been in service for 8 years, still showing favorable effects.

### Data Availability

The data used to support the findings of this study have not been made available.

### Conflicts of Interest

The authors declare that there are no conflicts of interest.

### Acknowledgments

The authors would like to acknowledge the Jiangsu Natural Science Foundation (Youth Fund) (BK20180113), the Jiangsu Natural Science Foundation (Surface Project) (BK20181112), the High-Level Talent Project Funding Scheme of Jiangsu (XCL-CXTD-007), the Post-Doctoral Fund of China (2018M630559), and the Fundamental Research Nantong Metro Group Co., Ltd. for their financial support in this project.

### References

- [1] M. S. G. Cullimore, I. D. Flett, and J. W. Smith, "Flexure of steel bridge deck plate with asphalt surfacing," *IABSE Periodical*, vol. 1, pp. 58–83, 1983.
- [2] T. O. Medani, "Asphalt surfacing applied to orthotropic steel bridge decks," Report 7-01-127-1, Delft University of Technology, Delft, Netherlands, 2001.
- [3] V. S. Gopalratnam, J. W. Baldwin, B. A. Hartnagel, and R. A. Rigdon, "Evaluation of wearing surface systems for orthotropic steel plate bridge decks," Report 89-2, Missouri Highway Transportation Dept, University of Missouri, Columbia, MI, USA, 1989.
- [4] European Asphalt Pavement Association, *Asphalt Pavements on Bridge Decks*, European Asphalt Pavement Association, Brussels, Belgium, 2013.
- [5] W. Huang, Z. Qian, G. Chen, and J. Yang, "Epoxy asphalt concrete paving on the deck of long-span steel bridges," *Chinese Science Bulletin*, vol. 48, no. 21, pp. 2391–2394, 2003.
- [6] W. Huang, Z. Qian, and G. Cheng, "Application of epoxy asphalt concrete to pavement of long span steel bridge deck," *Journal of Southeast University (Natural Science Edition)*, vol. 32, no. 5, pp. 783–787, 2002, in Chinese.
- [7] Z.-D. Qian, L. I. Zhi, and C.-H. Chen, "Fracture criterion for mode I crack of epoxy asphalt concrete paving course of steel deck bridge pavement," *China Journal of Highway and Transport*, vol. 21, no. 5, pp. 33–38, 2008.
- [8] T. J. Chen, *Research on Crack Behavior of Long-Span Steel Bridge Deck Epoxy Asphalt Pavement*, Southeast University, Nanjing, China, 2006.
- [9] H. Zhang, Y. Pan, and C. Yin, "Research on cracking mechanism and repair techniques of epoxy asphalt on steel bridge deck pavement," in *Proceedings of the 2016 TRB Annual Meeting*, pp. 16–3539, Washington, DC, USA, January 2016.
- [10] H. Zhang, Y. Pan, and D. Yu, "Study on the properties of rapidly repairing materials in steel bridge deck pavement based on cold-blended modified resin," *Modern Transportation Technology*, vol. 1, no. 12, pp. 7–8, 2005.
- [11] H. Zong, *Technique Research on Diseases Restoration for Epoxy Asphalt Concrete Paved on Steel Deck Bridge*, Southeast University, Nanjing, China, 2005.
- [12] H. Zhang, G. Shan, and Y. Pan, "Thin overlay technology for cold-blended modified resin in steel bridge deck pavement with epoxy asphalt," *Transportation Science & Technology*, vol. 2, pp. 169–172, 2016.
- [13] Transportation Research Board of the National Academies, "Long-Term Performance of Polymer Concrete for Bridge Decks," NCHRP SYNTHESIS 423, Transportation Research Board of the National Academies, Washington, DC, USA, 2011.
- [14] Transportation Research Board of the National Academies, "Fiber additives in asphalt mixtures," NCHRP Synthesis 475, Transportation Research Board of the National Academies, Washington, DC, USA, 2015.
- [15] J. Feng, *Reinforcing Mechanisms and Properties of Fiber Asphalt Mixture*, Southeast University, Nanjing, China, 2006.
- [16] Y. Sun, M. Zhang, and L. Wang, "Analysis of viscoelastic damages of crack resistance of fiber reinforced asphalt concrete pavement," *Highway*, vol. 58, no. 8, pp. 174–178, 2013.
- [17] B. Burks, J. Middleton, D. Armentrout, and M. Kumosa, "Effect of excessive bending on residual tensile strength of hybrid composite rods," *Composite Materials Science and Technology*, vol. 70, no. 10, pp. 1490–1496, 2010.
- [18] C. Atas and A. Dogan, "An experimental investigation on the repeated impact response of glass/epoxy composites subjected to thermal ageing," *Composites Part B: Engineering*, vol. 75, pp. 127–134, 2015.
- [19] M. Zhang, B. Sun, and B. Gu, "Accelerated thermal ageing of epoxy resin and 3-D carbon fiber/epoxy braided composites," *Composites Part A: Applied Science and Manufacturing*, vol. 85, pp. 163–171, 2016.

## Research Article

# Investigation of the Performance of the Ecofriendly Fiber-Reinforced Asphalt Mixture as a Sustainable Pavement Material

Bowen Guan <sup>1</sup>, Jianan Liu <sup>1</sup>, Jiayu Wu,<sup>1</sup> Jingyi Liu,<sup>1</sup> Haitao Tian,<sup>1</sup> Tengbin Huang,<sup>1</sup> Chengcheng Liu,<sup>1</sup> and Tao Ren<sup>2</sup>

<sup>1</sup>School of Material Science and Engineering, Chang'an University, Xi'an, Shaanxi 710064, China

<sup>2</sup>The 2nd Engineering Co. Ltd. of China Railway 17 Bureau Group Corporation, Xi'an, Shaanxi 710064, China

Correspondence should be addressed to Jianan Liu; liujn1996@163.com

Received 3 August 2019; Accepted 28 September 2019; Published 13 December 2019

Guest Editor: Andrea Grilli

Copyright © 2019 Bowen Guan et al. This is an open access article distributed under the Creative Commons Attribution License, which permits unrestricted use, distribution, and reproduction in any medium, provided the original work is properly cited.

This article presents a study to evaluate the performance of the ecofriendly calcium sulfate whisker fiber- (CSWF-) reinforced asphalt mixture as a sustainable pavement material. Asphalt mixtures containing 0.2 wt.%, 0.4 wt.%, 0.6 wt.%, and 0.8 wt.% of the CSWF were designed by the Marshall method. Asphalt mixtures without fiber were also prepared as control samples. The Marshall test, wheel-tracking test, low-temperature bending test, water sensitivity test, and fatigue test were conducted to evaluate the performance of the CSWF asphalt mixture. And the mechanism of fiber reinforcement was discussed. The results showed that the CSWF could improve the high-temperature stability and low-temperature crack resistance of the asphalt mixture. Water stability of asphalt mixtures in the presence of the CSWF was also improved. When the CSWF content was 0.4 wt.% of the total mixture, the performance of the asphalt mixture is the best. Compared with the conventional asphalt mixture, the CSWF asphalt mixture not only utilized power plant waste effectively to preserve ecosystems but also improved the performance of the pavement, which is suggested to be used in sustainable pavement construction and rehabilitation.

## 1. Introduction

Pavement plays a significant role in the transportation network affecting economic and social development of the country. At present, there are about billions of kilometers of pavement in the world [1]. These pavements enhance the social productivity and improve people's quality of life. However, pavement construction and rehabilitation consume a large number of materials derived from nonrenewable natural resources, which will destroy the environment. Meanwhile, due to the combined effects of repeated traffic loadings and the environment's influence such as rain, sunlight, and chemicals, the asphalt pavement begins to deteriorate significantly and needs to be rehabilitated after three to five years of service [2, 3]. Repeated rehabilitation of the pavement will also destroy the environment. Therefore, it

is necessary to construct sustainable pavements. According to the definition of the Federal Highway Administration (FHWA), sustainable pavement should meet three requirements: meeting performance standards, utilizing resources effectively, and preserving the ecosystem [4]. A large number of studies have shown that the addition of ecofriendly fibers is an effective method to preserve ecosystems and improve the long-term performance of pavements [5–11]. In addition, some studies have found that green technologies hold promise in developing more sustainable pavements [1, 12]. Guan et al. found that the combination of 0.4 wt.% brucite fiber produced from the brucite tailings can effectively improve the strength and toughness of the fiber-reinforced asphalt mixture [13]. Nsengiyumva et al. found that the addition of the corn husk fiber could not only enhance the cracking resistance of HMA but also improve the cracking



resistance of cold-mix asphalt (CMA) [14]. Stempihar et al. found that fiber-reinforced asphalt concrete can be used as a sustainable paving material for airfields [15].

As a novel kind of ecofriendly fiber, the calcium sulfate whisker fiber (CSWF) is made from flue gas desulfurized gypsum which is the byproduct produced by limestone-gypsum wet flue gas desulfurization in thermal power plants [16]. The CSWF is widely used as a reinforced material and is also commonly applied to surface modification, polymer materials, papermaking technology, friction materials, and other aspects [17–21]. Yang et al. assessed the mechanical property of clay aerogel with the CSWF content, and the CSWF/clay aerogel composite was found to effectively form a dense “honeycomb” structure, increasing the modulus and consequently resulting in a high mechanical strength of composite materials [22]. Wang et al. evaluated the impact of the CSWF on the reinforced effect in silicone rubber composites and concluded that the CSWF was beneficial to the development of tensile strength and elongation of room-temperature-vulcanized silicone rubber/CSWF composites [23]. Xing et al. studied the effect and mechanism of the calcium carbonate whisker on the asphalt binder and found that the addition of the calcium carbonate whisker can improve the softening point of asphalt and decrease its penetration and ductility [24]. From these researches, it is found that, due to the high strength, large specific surface area, and high-temperature resistance, the CSWF can improve the performance of the matrix material effectively. The performance of the asphalt mixture may be improved by the addition of the CSWF. However, few studies reported this. In China, the deposit of flue gas desulfurization gypsum is up to billions of tons and amounts up to more than 50 million tons per year [25]. To utilize this power plant waste effectively and improve the performance of the pavement, the utilization of the CSWF in the asphalt mixture as a sustainable pavement material in the asphalt pavement may be a promising way.

In this paper, the performance of the ecofriendly CSWF-reinforced asphalt mixture as a sustainable pavement material was investigated. The performance of the CSWF asphalt mixture was evaluated by the Marshall test, wheel-tracking test, three-point bending test, fatigue test, and water sensitivity test under harsh environment. According to the test results above, the optimum content of the CSWF in the asphalt mixture was determined to satisfy the optimum performance of the asphalt mixture. Meanwhile, the mechanism of the CSWF-modified asphalt mixture was also discussed.

## 2. Materials and Methods

**2.1. Materials.** In this study, base asphalt 90# according to the American Society of Testing Materials (ASTM) was used as the binder. Its properties are shown in Table 1. Physical properties of the calcium sulfate whisker fiber are provided by the manufacturer, which are shown in Table 2. It can be seen from Table 2 that the calcium sulfate whisker has good thermal stability and high tensile strength. The morphology of the CSWF was captured by using an SEM. Figure 1(a) presents the appearance of the CSWF. And Figures 1(b),

TABLE 1: Technical indicators of the asphalt binder.

Test properties	Unit	Test results	Test basis
Penetration (25°C, 100 g, 5 s)	0.1 mm	86.4	ASTM D5-97
Softening point	°C	47.0	ASTM D36-06
Ductility (15°C, 5 cm/min)	cm	182	ASTM D113-99
Wax content	%	1.74	ASTM D3344-90
Specific gravity	—	1.030	ASTM D70-76
Flash point	°C	304	ASTM D92-02
RTFOT (163°C, 75 min)			
Mass change	%	0.15	ASTM D2872-04
Penetration ratio (25°C)	%	60.5	ASTM D5-97
Ductility (10°C)	cm	10.1	ASTM D113-99

TABLE 2: Main characteristics of the CSWF.

Characteristics	Unit	Test results
Diameter	$\mu\text{m}$	2–4
Length	$\mu\text{m}$	40–60
Length/diameter ratio (mean)	—	16
Tensile strength	MPa	2050
Melt temperature	°C	1450

1(c), and 1(d) show the micrograph of the CSWF at various scales from 50  $\mu\text{m}$  to 5  $\mu\text{m}$ . The CSWF exhibited a white fluffy powdery appearance with obvious edges and corners on the surface that promotes mixture resistance to several pavement distresses. Industrial sodium sulfate ( $\text{Na}_2\text{SO}_4$ ) was used in the test, and the content of sodium sulfate was more than 99%. SK-90# matrix asphalt is used in this paper, and the coarse aggregate is the crushed basalt mineral, with a density of 2.86  $\text{g}/\text{cm}^3$ . The fine aggregate was obtained from crushed basalt and mechanical sand, with a density of 2.83  $\text{g}/\text{cm}^3$ . The mineral filler is of limestone type, with a density of 2.73  $\text{g}/\text{cm}^3$ . And more than 95% of the filling size is less than 75  $\mu\text{m}$ .

**2.2. Sample Preparation.** Gradation is the AC-13 asphalt mixture, and the designed gradation is shown in Table 3. The samples of the asphalt mixture with 0%, 0.2%, 0.4%, 0.6%, and 0.8% CSWF contents were prepared in accordance with the Chinese standard JTG E20-2011 [24]. To achieve good fiber dispersion, the CSWF and aggregate were mixed in a rotary mixer at 600 RPM for 90 seconds before the asphalt and mineral filler were added.

**2.3. Scanning Electron Microscopy (SEM) Analyses.** The microstructures of the CSWF and CSWF-reinforced asphalt mixture were examined by a scanning electron microscope (SEM).

**2.4. Marshall Test.** According to the content of different CSWFs, the optimum asphalt content (OAC), bulk specific gravity, air void volume (VV), voids in mineral aggregates (VMA), and Marshall stability (MS) of different asphalt mixtures were obtained by the Marshall test. All tests were



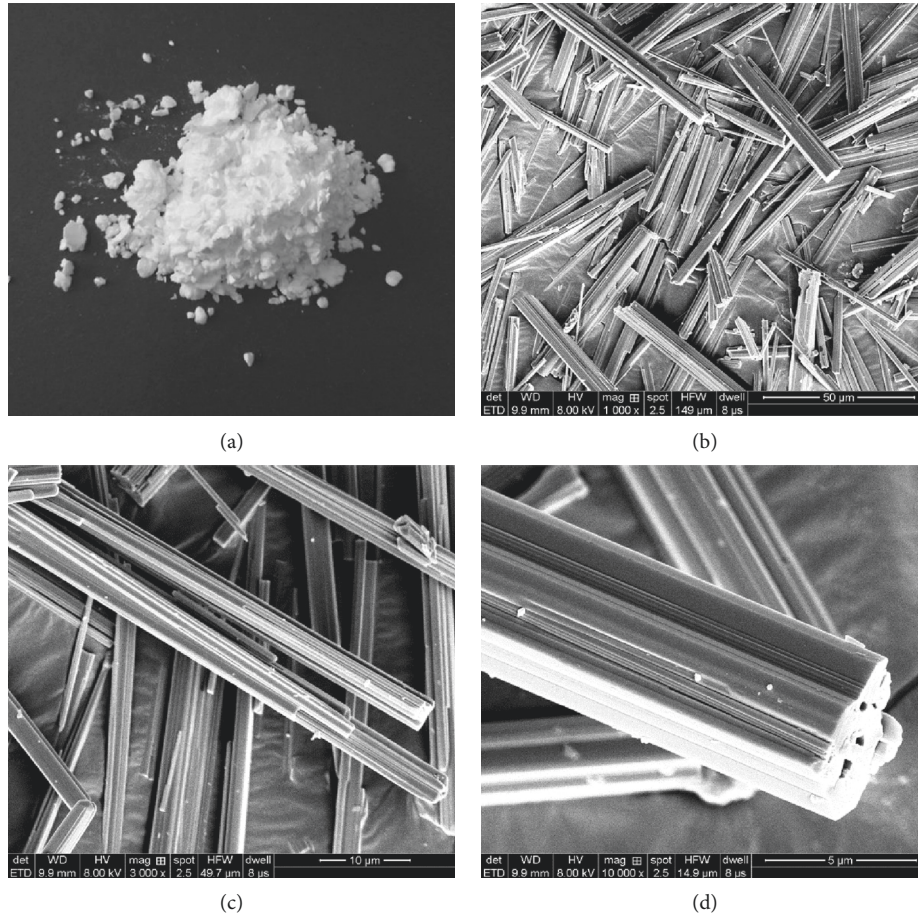


FIGURE 1: SEM micrographs of the CSWF: (a) appearance; (b) magnification: 1000 times; (c) magnification: 3000 times; (d) magnification: 10000 times.

TABLE 3: Mineral gradation of AC-13 mixture design.

Sieve size (mm)	Percent of aggregate passing for a given sieve size									
	16	13.2	9.5	4.75	2.36	1.18	0.6	0.3	0.15	0.075
Percent passing	100	96	77	49.8	35	25	22	14	11	7

conducted following the method T0709 in JTG E20-2011 [23].

**2.5. Wheel-Tracking Test.** The wheel-tracking test was conducted in terms of JTG E20-2011 (T0719) [26]. The loose asphalt mixture was compacted into a few  $300 \times 300 \times 50$  mm slabs. These slabs were placed in the testing chamber at  $60^\circ\text{C}$  for 6 h. Then, a solid rubber tire moved back and forward on the slab surface with the travel distance of  $230 \pm 10$  mm. The test load was 0.7 MPa, and the test wheel-rolling speed was  $42 \pm 1$  cycles/min. The DS (times/mm) can be calculated by equation (1). Each asphalt mixture with different CSWF contents was repeatedly tested four times to acquire a reliable measure of the DS of the test specimen.

$$DS = \frac{(t_2 - t_1) \times N}{d_2 - d_1} \times C_1 \times C_2 = \frac{42 \times 15}{d_{60} - d_{45}}, \quad (1)$$

where  $t_1$  and  $t_2$  are time corresponding to 45 min and 60 min, respectively;  $N$  is the wheel-traveling speed, and  $N = 42$  cycles/min in this paper;  $d_1$  and  $d_2$  are the rutting depth recorded at  $t_1$  and  $t_2$ , respectively; and  $C_1$  and  $C_2$  are parameters and taken as 1 in this paper.

**2.6. Low-Temperature Cracking Test.** The three-point bending test was conducted in accordance with the Chinese standard JTG E20-2011 (T0715) [26] to evaluate the effect of the CSWF on the low-temperature cracking performance of the asphalt mixture. The span length was 200 mm. The midpoint of the beam was stressed, and the load was applied at a speed of 50 mm/min. The loose asphalt mixture was compacted into a  $300 \times 300 \times 50$  mm slab and sawed into a beam ( $250 \times 30 \times 35$  mm) such that each span length is 200 mm. The test temperature was  $-10^\circ\text{C}$ . Five parallel samples were used in this test.

$$R_B = \frac{3 \times L \times P_B}{2 \times b \times h^2},$$

$$\varepsilon_B = \frac{6 \times h \times d}{L^2}, \quad (2)$$

$$\varepsilon_B = \frac{6 \times h \times d}{L^2},$$

where  $R_B$  is the maximum bending stress (MPa);  $\varepsilon_B$  is the flexural strain ( $\mu\varepsilon$ );  $b$  is the width of the cross section (mm);  $h$  is the height of the cross section (mm);  $d$  is the midspan deflection at failure (mm);  $L$  is the span of the beam (mm); and  $P_B$  is the maximum load (N).

**2.7. Freeze-Thaw Split Test.** The freeze-thaw split test was conducted in accordance with the Chinese standard JTG E20-2011 (T0729) [26] to evaluate the effect of the CSWF-reinforced asphalt mixture on the water sensitivity performance. Marshall specimens were divided into two groups. The control group tested the splitting strength at 25°C with a loading rate of 50 mm/min, marked as  $R_{T1}$ . The second group tested the splitting strength under freeze-thaw cycles at a temperature between -18°C (16 h) and 60°C (24 h), marked as  $R_{T2}$ . Both conditioned and unconditioned specimens were put in a water bath at 25°C for at least 2 h. Finally, the specimens were loaded until failure, and the tensile strength ratio (TSR) was calculated using equations (3)–(5). Five parallel samples were used in this test.

$$R_{T1} = \frac{0.006287P_{T1}}{h_1}, \quad (3)$$

$$R_{T2} = \frac{0.006287P_{T2}}{h_2}, \quad (4)$$

$$\text{TSR} = \frac{\bar{R}_{T2}}{\bar{R}_{T1}} \times 100, \quad (5)$$

where TSR is the tensile strength ratio (%);  $R_{T1}$  is the average tensile strength (MPa) of the unconditioned specimen;  $R_{T2}$  is the average tensile strength (MPa) of the conditioned specimen;  $P_{T1}$  is the maximum value of the test load for the test pieces in the first group (N); and  $P_{T2}$  is the maximum value of the test load for the test pieces in the second group (N).

**2.8. Four-Point Bending Fatigue Test.** The fatigue life of the asphalt mixture was measured by a four-point bending fatigue test in JTG E20-2011(T0739) [26]. The four-point bending fatigue test is loaded in a partial sinusoidal loading with load-to-stress ratios of 0.1, 0.2, 0.3, and 0.4. The loose asphalt mixture was rolled into a square billet with a size of 400 × 300 × 75 mm and sawed into a beam (380 × 50 × 63 mm) at 25°C. Five parallel samples were used in this test.

**2.9. Vacuum Immersion Attack Test.** The vacuum immersion attack test of 10% (by weight of the total solution) sulfate concentration was improved by referring to the Chinese

standard JTG E20-2011 (T0709-2011) [26]. The effect of sulfate attack on the CSWF-reinforced asphalt mixture was simulated by soaking Marshall specimens in 10% sodium sulfate solution. The Marshall stability of the control asphalt mixture and CSWF-reinforced asphalt mixture was tested. The specimens were put into a vacuum dryer with vacuum about 97.3 kPa for 15 min. Then, under the action of negative pressure, the sodium sulfate solution with a mass fraction of 10% was put into the dryer and all specimens were immersed in the sodium sulfate solution (the submergence height was no less than 20 mm). After 15 min, normal pressure was restored. Marshall specimens of the CSWF-reinforced asphalt mixture and Marshall specimens of the control asphalt mixture were tested for Marshall stability every 24 h after 48 h of immersion in sodium sulfate solution. The effect of water sensitivity of the CSWF-reinforced asphalt mixture under sulfate attack was studied, and the feasibility of using the CSWF-reinforced asphalt mixture in the sulfate environment was discussed. Three parallel samples were used in this test.

**2.10. Sulfate-Freeze-Thaw Cycle Test.** Marshall specimens (24 specimens) were formed by compaction (50 times for each side) with 0.4 wt.% CSWF, which were divided into 6 groups with 4 samples in each group. Referring to the freeze-thaw split test, the specimens were soaked for 10 h in 10% sodium sulfate instead of water. Marshall specimens without freeze-thaw cycle were tested for splitting tensile strength after 72 h of curing. The other five groups were first placed in a plastic bag containing 10% sodium sulfate solution and kept at -18°C for 16 h. Then, they were removed from the bag and immersed in a water bath at 60°C for 6 h. Five groups of specimens and control group were immersed in a water bath at 25°C for 2 h and tested. The 24 Marshall specimens were subjected to 0–5 freeze-thaw cycles, respectively, and the appearance changes of samples after freeze-thaw cycles were observed. Through the above experiments, the influence of salt-freeze-thaw cycle coupling on the water stability of the common asphalt mixture and CSWF-reinforced asphalt mixture was studied. Four parallel samples were used in this test.

**2.11. Sulfate-Wet-Dry Cycle Test.** The sulfate-wet-dry cycle was similar to the sulfate-freeze-thaw cycle. The Marshall specimens were immersed in 10% sodium sulfate solution and kept at 30°C for 12 h and oven-dried at 40°C for 12 h. After each sulfate-wet-dry cycle, four specimens were taken out to test the splitting strength, and the relevant test results were recorded. According to the results, the durability of the CSWF-reinforced asphalt mixture under sulfate-wet-dry cycles was analyzed. Three parallel samples were used in this test.

### 3. Results and Discussion

**3.1. Marshall Index.** Figures 2 to 6 show CSWF-reinforced asphalt mixture parameters, including the optimum asphalt content (OAC), bulk specific gravity, VV, VMA, and

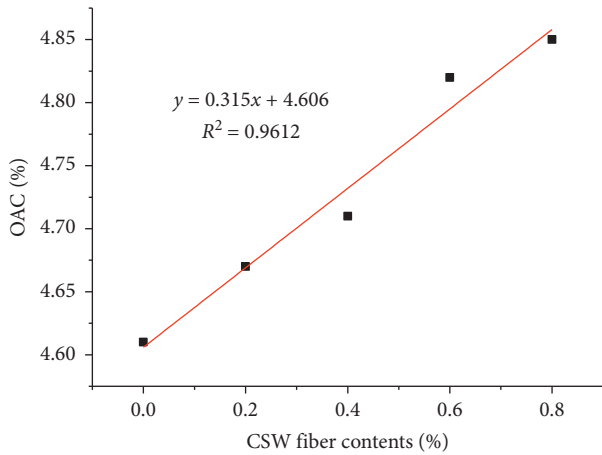


FIGURE 2: Change in the OAC for different CSWF contents.

Marshall stability (MS) of each mixture. With the CSWF content increase, the OAC increased from 4.61% to 4.85%. The main reason for this phenomenon was that the fiber increased the internal specific surface area and absorbed part of the free asphalt, so the asphalt content of the mixture increased.

Figure 3 shows the bulk specific gravity of the asphalt mixture with different CSWF contents. All of the bulk specific gravity values were between 2.48 and 2.56. With the CSWF content increase, the bulk specific gravity of the CSWF-reinforced asphalt mixture gradually decreased.

Figure 4 shows that the value of VV increased with the increase of the CSWF content. The data show a positive correlation between VV and CSWF content. This increase occurred probably due to the increase of CSWF surface area that absorbed more free asphalt.

Figure 5 reveals that, for different asphalt mixtures, the VMA also increase with the increasing content of the CSWF.

MS results are shown in Figure 6. Compared to those of the control group, the MS results of the test groups were improved by almost 7.4%, 21.7%, 16.2%, and 8.5%. Generally, the MS is an indicator to evaluate the anticracking ability. A larger MS value means a better anticracking ability. Maximum MS values were obtained when 0.40 wt.% CSWF was added.

**3.2. High-Temperature Stability.** Figure 7 displays the dynamic stability of the fiber-reinforced asphalt mixture with different CSWF contents. Ordinarily, a higher DS value means a preferable antirutting performance. When the CSWF content is less than 0.8 wt.%, the DS of the asphalt mixture with the CSWF goes up significantly, indicating that the high-temperature stability of the asphalt mixture can be improved. From Figure 7, it can be seen that dynamic stability of the asphalt mixture increased with the increase of the CSWF content. Compared with that of the nonfiber asphalt mixture, dynamic stability of the 0.4 wt.% content of the CSWF-reinforced asphalt mixture increased by 45.3%. Because the fiber absorbs the asphalt, the free asphalt content was reduced and the bonding strength was increased.

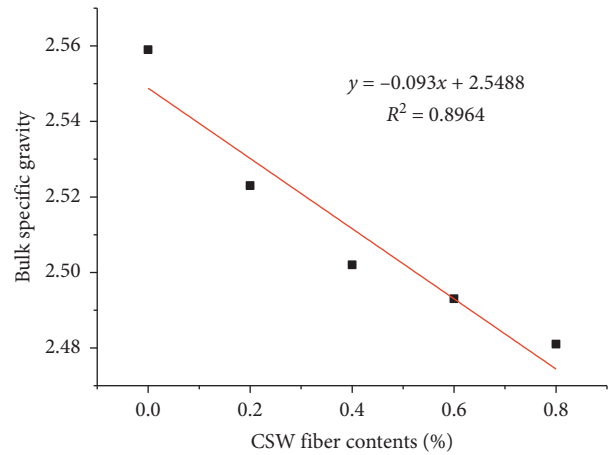


FIGURE 3: Change in bulk specific gravity for different CSWF contents.

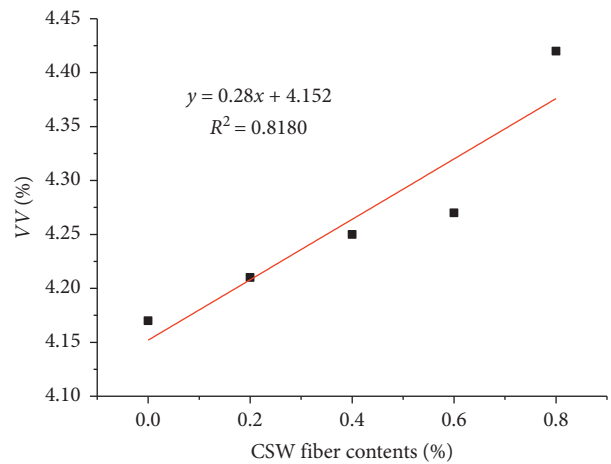


FIGURE 4: Change in VV for different CSWF contents.

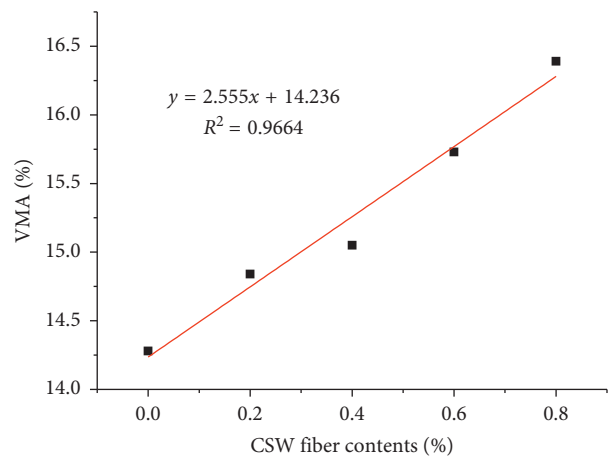


FIGURE 5: Change in VMA for different CSWF contents.

Figure 8 shows the micrograph of CSWF-reinforced asphalt. The fibers are evenly dispersed throughout the asphalt, increasing its mechanical strength. It is indicated that the



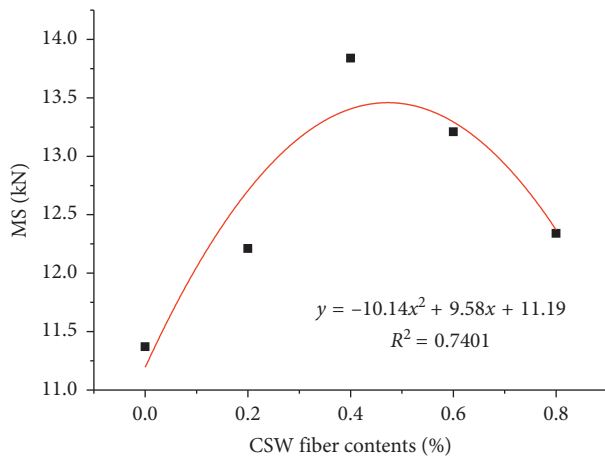


FIGURE 6: Change in MS for different CSWF contents.

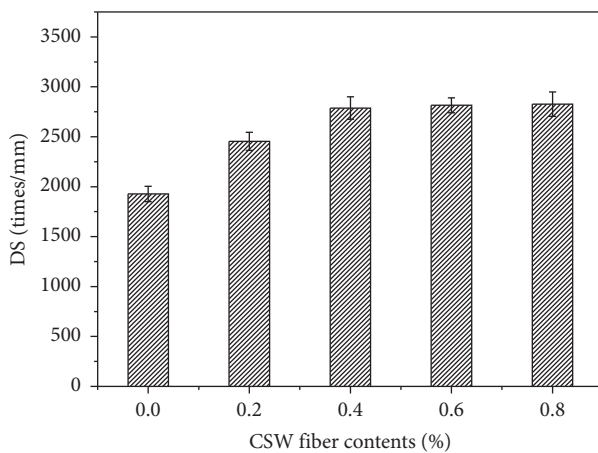


FIGURE 7: Change in DS for different CSWF contents.

CSWF formed a mesh structure in the asphalt mixture, with asphalt and CSWF having a good absorption and adhesion ability. In addition, the CSWF has the function of bridge connections, which could strengthen the weak area of the interface between the aggregate and the asphalt.

**3.3. Low-Temperature Stability.** The low-temperature bending test was conducted under  $-10^{\circ}\text{C}$ . The result is elaborated in Figures 9–11. From Figures 9–11, it can be summarized that there is good parabolic curve fitting among the fiber-reinforced asphalt mixtures with different CSWF contents and the bending tensile strength, the maximum tensile strain, and the bending stiffness modulus. The bending tensile strength and tensile strain rose first and then came down with the CSWF content increase. It is indicated that the excessive content of the fiber would result in poor low-temperature stability of the asphalt mixture due to its uneven dispersion. Therefore, when the content of the CSWF reached a certain figure, the resistance of the mixture to the low-temperature crack will decrease. Furthermore, the bending tensile strength and tensile strain showed good performance at 0.4 wt.% CSWF content. The decrease of the

bending stiffness modulus indicated that the CSWF could improve toughness and strong crack resistance of the asphalt mixture at low temperatures. Compared with that of the control asphalt mixture, the anticracking ability at low temperatures of the 0.4 wt.% content of the CSWF-reinforced asphalt mixture increased by 17.0%. The reason for this phenomenon is also attributed to the morphology effect of the CSWF with its needle-like granules. In addition, the CSWF has the function of bridge connections, which strengthens the weak area of the interface between the aggregate and the asphalt. The main reason for the above phenomenon is that the CSWF forms a special layered structure between the aggregate and the asphalt, which plays a key role in bridge connection and enhances the bonding effect with aggregates. Under the action of fibers, asphalt has higher stress recovery and ductility recovery, so as to improve the self-healing ability of the asphalt mixture [27, 28].

**3.4. Water Sensitivity.** Figure 12 shows the results of water sensitivity for five different types of asphalt mixtures. As shown in Figure 12, the freeze-thaw split strength of the CSWF-reinforced asphalt mixture increases from 0.2 wt.% to 0.8 wt.% compared to that of the control asphalt mixture. CSWF can improve the splitting tensile strength and water sensitivity of the asphalt mixture before and after freeze-thaw cycling. When the CSWF content is less than 0.4 wt.%, the splitting tensile strength significantly increased. From Figure 12, it is obvious to see that when the whisker content is about 0.4 wt.%, the tensile strength ratio of the freeze-thaw split is highest and then declines as the CSWF content increases. It is indicated that the optimum content of the CSWF was 0.4 wt.%. At the optimum content, the freeze-thaw splitting tensile strength of the CSWF-reinforced asphalt mixture increased by 12% and 28% compared with that of the control asphalt mixture and asphalt mixture without whisker addition after freeze-thaw cycles, respectively. The main reason for this phenomenon is that the fiber absorbed and assimilated on bitumen. During the freeze-thaw cycle, the CSWF increased the roughness of the interface that made the asphalt film thick and enhanced the interface bonding ability. This is the reason why the CSWF-reinforced asphalt mixture exhibited higher values for TSR and had good resistance to water damage.

**3.5. Fatigue Performance Evaluation.** Fatigue tests were carried out on the asphalt mixture mixed with and without CSWF. At the same stress ratio, the fatigue frequency and increase range of the asphalt mixture with the CSWF were calculated. The test data and results are shown in Figure 13. It can be seen from Figure 13 that, under the same stress ratio loading, the fatigue times of the asphalt mixture with the CSWF are all higher than those without CSWF. When the stress ratio was 0.1, the fatigue life of the CSWF-reinforced asphalt mixture increased by 7.2%, and when the stress ratio was 0.3, the fatigue life increased by 54.2%. These data show that the effect of CSWF addition on the fatigue frequency of the asphalt mixture was not obvious when the stress level was low. With the increase of stress ratio, the

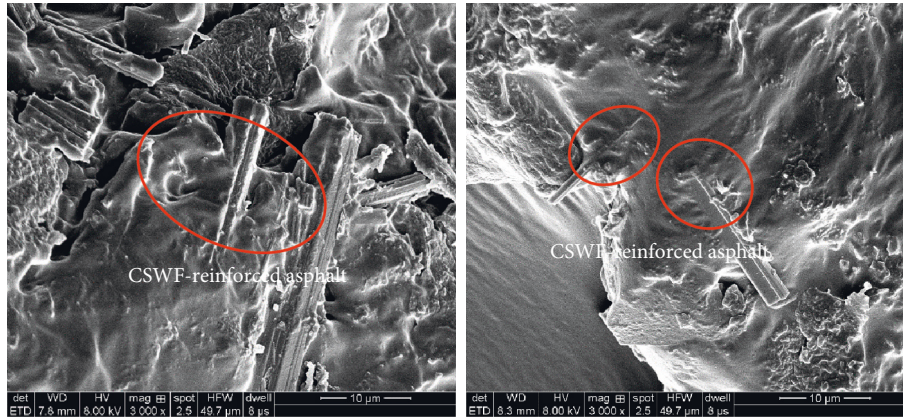


FIGURE 8: SEM micrographs of CSWF-reinforced asphalt.

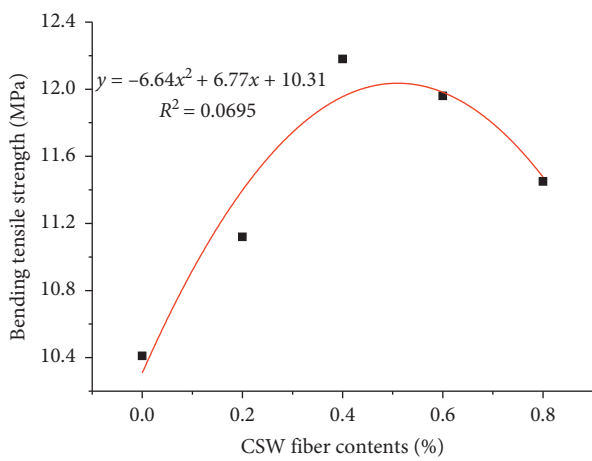


FIGURE 9: Bending tensile strength for different CSWF contents.

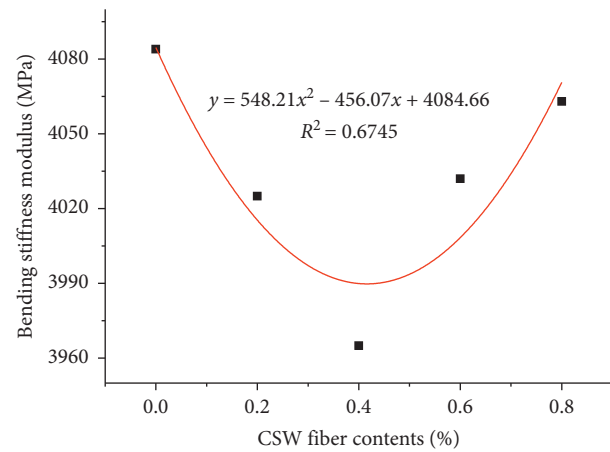


FIGURE 11: Bending stiffness modulus for different CSWF contents.

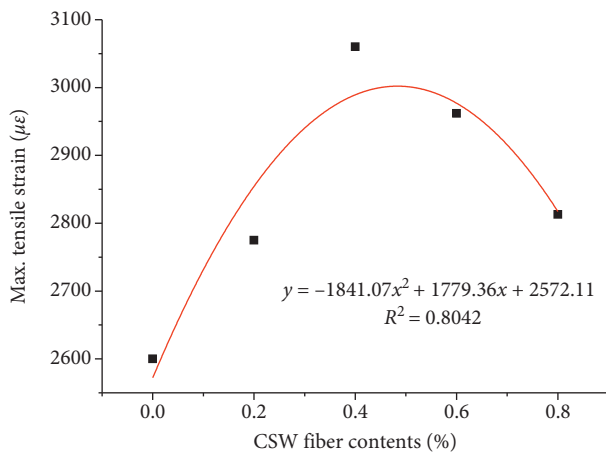


FIGURE 10: Maximum tensile strain for different CSWF contents.

CSWF improved the fatigue resistance of the asphalt mixture significantly, and the fatigue life of the fiber-modified asphalt mixture had been greatly improved. The addition of the CSWF could improve the fatigue life of the asphalt mixture and the fiber-modified asphalt mixture under the constantly changing stress state as well as extend the service life of the asphalt mixture.

**3.6. Water Sensitivity in Sulfate Environment.** MS test results of various asphalt mixtures after sulfate attack are shown in Figure 14. After 48 h immersion in the Marshall test, the Marshall stability of the control sample was 10.47 kN and that of the CSWF-reinforced asphalt mixture was 10.58 kN. The MS of the control sample decreased 19.5% and 51.6% when soaked in sodium sulfate for 2 d and 8 d compared with 2 d immersion in water, respectively. However, the MS of the CSWF-reinforced asphalt mixture decreased 17.7% and 40.9% in 2 d and 8 d under sulfate attack compared with 2 d immersion in water, respectively. It is indicated that the performance of the asphalt mixture in the salt attack environment declined more seriously than that in the water environment, and the CSWF has certain enhancement effect on sulfate attack resistance of the asphalt mixture. And the CSWF can enhance the anti-sulfate attack ability of the asphalt mixture.

**3.7. Water Sensitivity under Salt-Freeze-Thaw Cycles.** The test data of freeze-thaw splitting tensile strength and freeze-thaw splitting tensile strength ratio without freeze-thaw cycles and each freeze-thaw cycle are shown in Figure 15. It can be seen that, under the action of salt-freeze-thaw cycles, the tensile strength of freeze-thaw cracking of the two mixtures



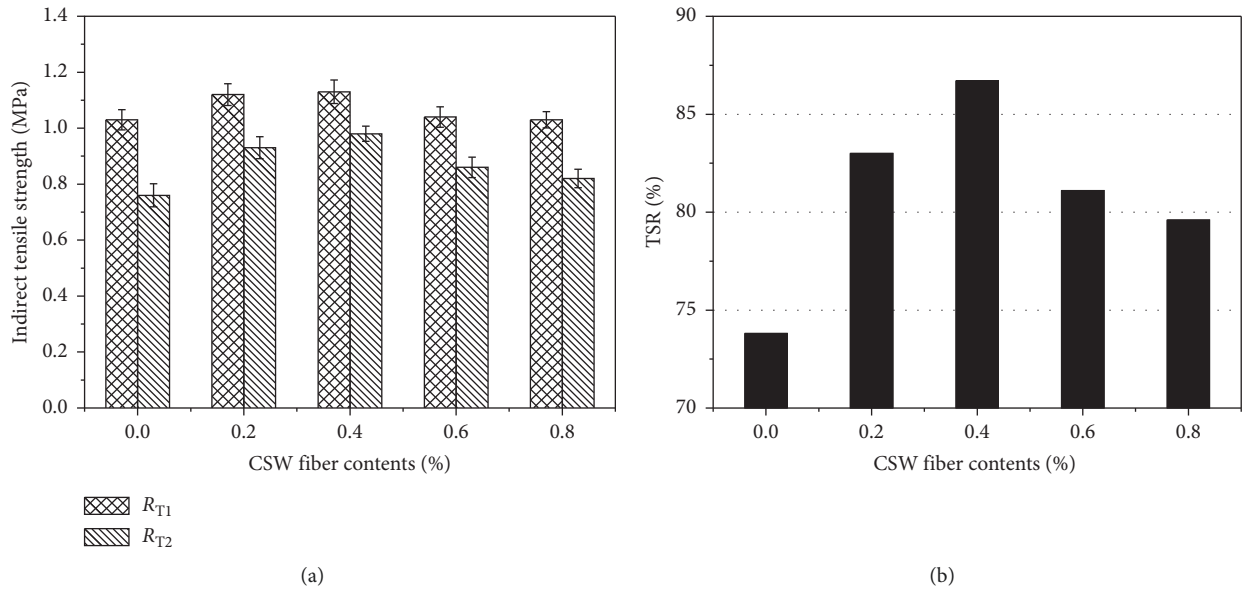


FIGURE 12: Water sensitivity of different CSWF contents: (a) residual strength; (b) TSR.

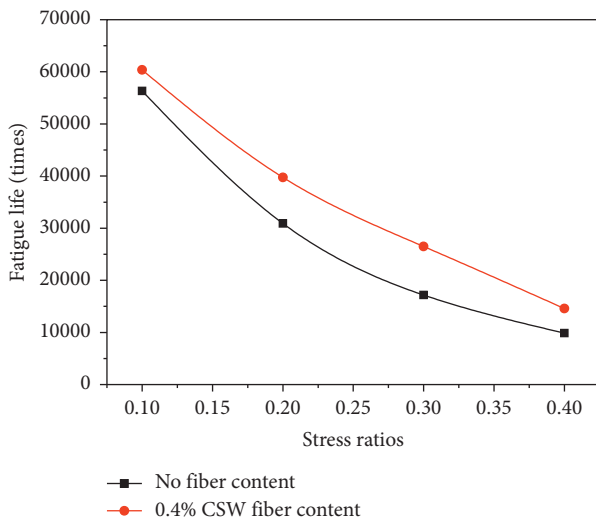


FIGURE 13: Fatigue life of the mixture under different stress ratios.

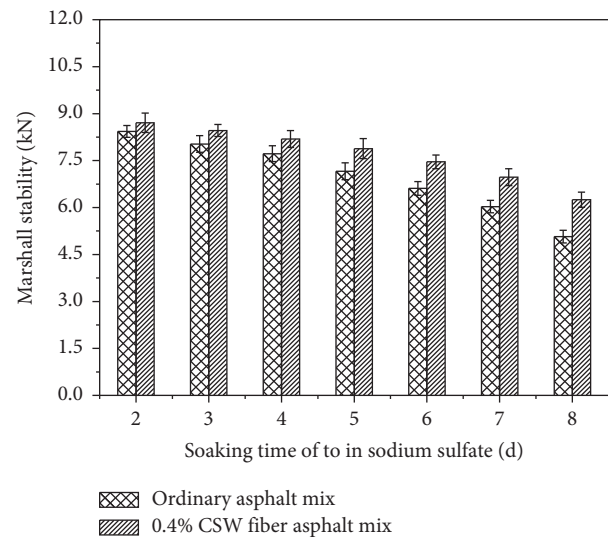


FIGURE 14: Marshall stability of the mix under the sodium sulfate solution attack.

decreased significantly. After 5 salt-freeze-thaw cycles, the tensile strength of freeze-thaw splitting of the ordinary asphalt mixture decreased to 0.30 MPa, and tensile strength of the 0.4 wt.% content of the CSWF-reinforced asphalt mixture also went down to 0.47 MPa. The tensile strength ratios of freeze-thaw cracking were 27% and 39.8%, respectively. It is indicated that the addition of the CSWF could effectively improve the sulfate attack resistance and freeze-thaw cycle resistance of the asphalt mixture.

**3.8. Water Sensitivity under Salt-Wet-Dry Cycles.** It can be seen from Figure 16 that the splitting strength of both mixtures decreased under the continuous action of the salt-wet-dry cycle. The addition of the CSWF could improve the sulfate attack resistance and wet-dry cycle resistance of the

asphalt mixture. This is similar to what happens in the salt-freeze-thaw cycle, but not as intense as in that cycle.

**3.9. Comparison with Different Fiber-Reinforced Asphalt Mixtures.** Table 4 shows physical properties of different fibers. Table 5 shows the results of high-temperature stability, low-temperature stability, water sensitivity, and fatigue performance under different types and the optimum content of the fiber. Compared with that of the control group, the DS of 0.4 wt.% CSWF-reinforced asphalt mixture increased by 44.6%, the low-temperature crack resistance increased by 17%, and the TSR increased by 17.4%. As can be seen from Table 5, compared with that of other fiber-reinforced asphalt mixtures, the road performance of the

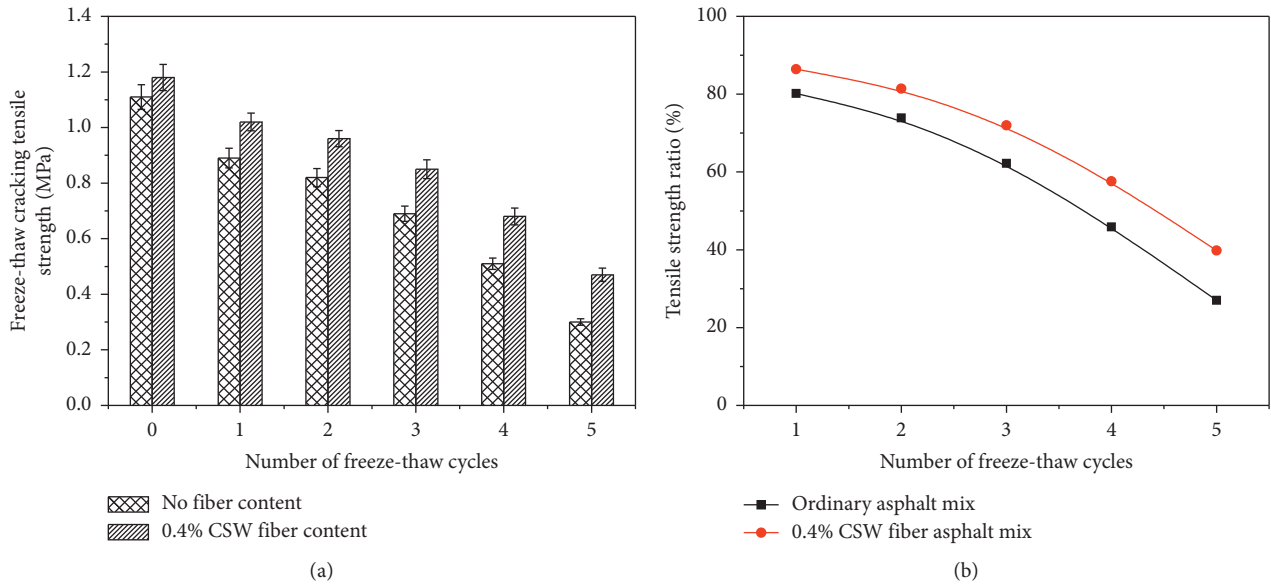


FIGURE 15: Variation curves of tensile strength ratio of freeze-thaw cracking with the number of sulfate-freeze-thaw cycles: (a) tensile strength of freeze-thaw cracking; (b) tensile strength ratio of freeze-thaw cracking.

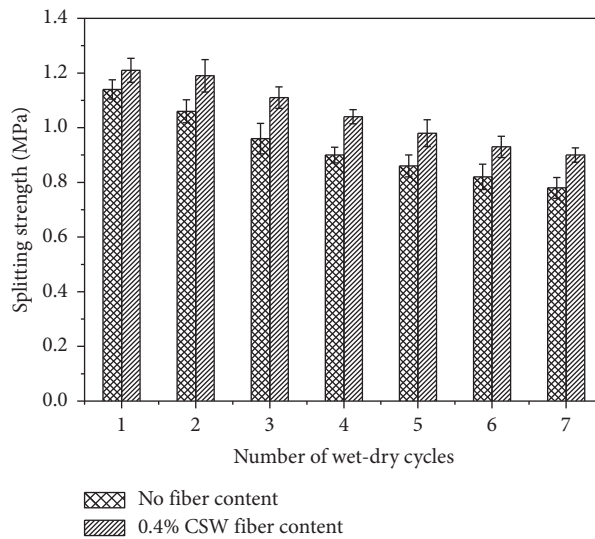


FIGURE 16: Variation curves of splitting strength with the number of sulfate-wet-dry cycles.

TABLE 4: Physical properties of different fibers.

Fiber type	Properties					Reference
	Diameter (mm)	Length (mm)	Length/diameter ratio	Tensile strength (MPa)	Melt temperature (°C)	
CSWF	0.003	0.05	16	2050	>1400	This paper
Brucite fiber	0.02	0.5	25	932	>400	[13]
Lignin fiber	0.045	1.1	24	—	—	[29]
Glass fiber	12	—	—	3250	>1500	[30]
Basalt fiber	0.013	6	460	3200	—	[8]
Polyester fiber	0.02	6	300	531	—	[29]
Polyacrylonitrile fiber	0.013	5	385	>910	—	[29]

TABLE 5: Improvement of asphalt mixture performance by addition of different fibers.

Types of fibers	Optimum fiber content (%)	Dynamic stability (times/mm)	Improvement of asphalt mixture performance				Fatigue life		Reference
			Max. bending stress (MPa) (%)	Max. tensile strain ( $\mu\epsilon$ ) (%)	TSR (%)	Stress ratio	Number of fatigue life cycles (%)		
CSWF	0.4	+44.16	+17.0	+13.9%	86.7	0.3	+54.2%	This paper	
Brucite fiber	0.4	+53.8	+23.4	+13.0%	87.5	0.3	+18.3%	[13]	
Lignin fiber	0.35	+8.4	+11.7	+6.0%	68.0	0.3	+68.1%	[29]	
Diatomite + glass fiber	0.2 + 0.3	+77.4	+9.6	+26.2%	—	0.4	+114.3%	[30]	
Basalt fiber	0.4	+82.5	+22.5	—	93.0	—	—	[8]	
Polyester fiber	0.35	+19.5	+8.1	+4.0%	77.5	0.3	+59.8%	[29]	
Polyacrylonitrile fiber	0.35	+32.5	+6.4	+2.0%	75.5	0.3	+130.0%	[29]	

CSWF-reinforced asphalt mixture is not significantly improved, but the enhancement effect is relatively balanced. As can be seen from Figure 5, the CSWF is a single crystal fiber which has a small diameter and length compared with other fibers but has a high tensile strength. The efficiency of a fiber-reinforced composite depends on the fiber/matrix interface stress transfer capability. Because of the small particle size of the CSWF, the mechanical property enhancement effect of the asphalt mixture is poor. However, under various harsh environments, the CSWF with needle-like granules and small particle size forms embedding and anchoring in the mixture, consequently increasing the mechanical bonding force between the asphalt and the aggregate.

#### 4. Conclusions

This study investigated the performance of the ecofriendly calcium sulfate whisker fiber- (CSWF-) reinforced asphalt mixture as a sustainable pavement material. Conclusions were summarized as follows:

- (1) With the increase of the CSWF content, the anti-rutting performance, low-temperature crack resistance, and durability of the asphalt mixture were improved significantly.
- (2) According to the analysis of road performance results, the optimal content of the CSWF is 0.4 wt.%. Under the 0.4 wt.% content of the CSWF, DS, bending tensile strength, and TSR increased by 44.6%, 17.0%, and 17.4% compared with those of the control sample, respectively.
- (3) Durability damage of the asphalt mixture is caused by infiltration and expansion pressure generated in the process of sulfate crystallization-dissolution. The CSWF-reinforced asphalt mixture has better resistance to cracking strength degradation under the coupling action of salt-freeze-thaw cycles and salt-dry-wet cycles.
- (4) Compared with the conventional asphalt mixture, the CSWF asphalt mixture not only utilized power plant waste effectively to preserve ecosystems but also improved the performance of the pavement,

which is suggested to be used in sustainable pavement construction and rehabilitation.

#### Data Availability

The data used to support the findings of this study are included within the article.

#### Conflicts of Interest

The authors declare that they have no conflicts of interest.

#### Acknowledgments

The authors wish to thank the financial support from the Program of China Scholarships Council (No. 201806565048), the Program of Traffic Innovation Management Consulting Research Project of Yunnan Province (No. 2019304), the China Postdoctoral Science Foundation (No. 2019M653520), the Natural Science Foundation of Jiangxi Province (20192BBG70064), and the Fundamental Research Funds for the Central Universities, CHD (Nos. 300102319102, 300102319202, and 3001102319501).

#### References

- [1] W. J. Sun, G. Lu, C. Ye et al., "The state of the art: application of green technology in sustainable pavement," *Advances in Materials Science and Engineering*, vol. 2018, Article ID 9760464, 19 pages, 2018.
- [2] D. V. Thanh and C. P. Feng, "Study on Marshall and Rutting test of SMA at abnormally high temperature," *Construction and Building Materials*, vol. 47, pp. 1337–1341, 2013.
- [3] S. Tayfur, H. Ozen, and A. Aksoy, "Investigation of rutting performance of asphalt mixtures containing polymer modifiers," *Construction and Building Materials*, vol. 21, no. 2, pp. 328–337, 2007.
- [4] American Association of State Highway and Transportation Officials (AASHTO), *Transportation and Sustainability Best Practices Background, Sustainability Peer Exchange—Center for Environmental Excellence*, American Association of State Highway and Transportation Officials, Washington, DC, USA, 2009.

- [5] H. K. Shanbara, F. Ruddock, and W. Atherton, "A laboratory study of high-performance cold mix asphalt mixtures reinforced with natural and synthetic fibres," *Construction and Building Materials*, vol. 172, pp. 166–175, 2018.
- [6] Q. Xue, L. Liu, and Y. J. Chen, "Study on the action effect of pavement straw composite fiber material in asphalt mixture," *Construction and Building Materials*, vol. 43, pp. 293–299, 2013.
- [7] T. Takaikaew, P. Tepsriha, S. Horpibulsuk, M. Hoy, K. E. Kaloush, and A. Arulrajah, "Performance of fiber-reinforced asphalt concretes with various asphalt binders in Thailand," *Journal of Materials in Civil Engineering*, vol. 30, no. 8, Article ID 04018193, 2018.
- [8] Y. C. Cheng, W. Wang, Y. Gong, S. Wang, S. Yang, and X. Sun, "Comparative study on the damage characteristics of asphalt mixtures reinforced with an eco-friendly basalt fiber under freeze-thaw cycles," *Materials*, vol. 11, no. 12, p. 2488, 2018.
- [9] O. S. Abiola, W. K. Kupolati, E. R. Sadiku, and J. M. Ndambuki, "Utilisation of natural fibre as modifier in bituminous mixes: a review," *Construction and Building Materials*, vol. 54, pp. 305–312, 2014.
- [10] S. Serin, N. Morova, M. Saltan, and S. Terzi, "Investigation of usability of steel fibers in asphalt concrete mixtures," *Construction and Building Materials*, vol. 36, pp. 238–244, 2012.
- [11] D. Luo, A. Khater, Y. Yue et al., "The performance of asphalt mixtures modified with lignin fiber and glass fiber: a review," *Construction and Building Materials*, vol. 209, pp. 377–387, 2019.
- [12] R. He, X. Huang, J. Zhang, Y. Geng, and H. Guo, "Preparation and evaluation of exhaust-purifying cement concrete employing titanium dioxide," *Materials*, vol. 12, no. 13, p. 2182, 2019.
- [13] B. W. Guan, R. Xiong, R. He, S. Chen, and D. Ding, "Investigation of usability of brucite fiber in asphalt mixture," *International Journal of Pavement Research and Technology*, vol. 7, no. 3, pp. 193–202, 2014.
- [14] G. M. Nsengiyumva, K. Santosh, Y.-R. Kim, H. Xu, and Y. Yang, *New Mixture Additives for Sustainable Bituminous Pavements*, Nebraska Transportation Center, Lincoln, NE, USA, 2018.
- [15] J. J. Stempihar, M. I. Souliman, and K. E. Kaloush, "Fiber-reinforced asphalt concrete as sustainable paving material for airfields transportation research record," *Journal of the Transportation Research Board*, vol. 2266, no. 1, pp. 60–68, 2012.
- [16] X. Wang, L. Wang, Y. Wang et al., "Calcium sulfate hemihydrate whiskers obtained from flue gas desulfurization gypsum and used for the adsorption removal of lead," *Crystals*, vol. 7, no. 9, p. 270, 2017.
- [17] H. Fan, X. Song, Y. Xu, and J. Yu, "Insights into the modification for improving the surface property of calcium sulfate whisker: experimental and DFT simulation study," *Applied Surface Science*, vol. 478, pp. 594–600, 2019.
- [18] W. J. Yuan, J. Cui, Y. Cai, and S. Xu, "A novel surface modification for calcium sulfate whisker used for reinforcement of poly(vinyl chloride)," *Journal of Polymer Research*, vol. 22, no. 9, p. 173, 2015.
- [19] X. Feng, Y. Zhang, G. Wang, M. Miao, and L. Shi, "Dual-surface modification of calcium sulfate whisker with sodium hexametaphosphate/silica and use as new water-resistant reinforcing fillers in papermaking," *Powder Technology*, vol. 271, pp. 1–6, 2015.
- [20] W. Yuan, J. Cui, and S. Xu, "Mechanical properties and interfacial interaction of modified calcium sulfate whisker/poly(vinyl chloride) composites," *Journal of Materials Science & Technology*, vol. 32, no. 12, pp. 1352–1360, 2016.
- [21] J. Wang, K. Yang, and S. Lu, "Preparation and characteristic of novel silicone rubber composites based on organophilic calcium sulfate whisker," *High Performance Polymers*, vol. 23, no. 2, pp. 141–150, 2011.
- [22] L. Yang, Y. Lu, F. He, H. Wu, T. Xu, and M. Xiao, "Preparation and characterization of clay aerogel composites reinforced by calcium sulfate whisker," *Journal of Nanoscience and Nanotechnology*, vol. 18, no. 11, pp. 7896–7901, 2018.
- [23] J. C. Wang, X. C. Pan, Y. Xue, and S. J. Cang, "Studies on the application properties of calcium sulfate whisker in silicone rubber composites," *Journal of Elastomers & Plastics*, vol. 44, no. 1, pp. 55–66, 2011.
- [24] X. Y. Xing, J. Pei, R. Li, and X. Tan, "Effect and mechanism of calcium carbonate whisker on asphalt binder Materials," *Research Express*, vol. 6, no. 5, Article ID 055306, 2019.
- [25] H. J. Sun, D. Tan, T. Peng, and Y. Liang, "Preparation of calcium sulfate whisker by atmospheric acidification method from flue gas desulfurization gypsum," *Procedia Environmental Sciences*, vol. 31, pp. 621–626, 2016.
- [26] JTG E20-2011, *Standard Test Methods of Bitumen and Bituminous Mixtures for Highway Engineering*, China Communications Press, Beijing, China, 2011.
- [27] B. A. Shu, S. Wu, L. Dong et al., "Synthesis and properties of microwave and crack responsive fibers encapsulating rejuvenator for bitumen self-healing," *Materials Research Express*, vol. 6, no. 8, Article ID 085306, 2019.
- [28] B. A. Shu, S. Wu, L. Dong et al., "Microfluidic synthesis of polymeric fibers containing rejuvenating agent for asphalt self-healing," *Construction and Building Materials*, vol. 219, pp. 176–183, 2019.
- [29] Q. Xu, H. Chen, and J. A. Prozzi, "Performance of fiber reinforced asphalt concrete under environmental temperature and water effects," *Construction and Building Materials*, vol. 24, no. 10, pp. 2003–2010, 2010.
- [30] Q. L. Guo, L. Li, Y. Cheng, Y. Jiao, and C. Xu, "Laboratory evaluation on performance of diatomite and glass fiber compound modified asphalt mixture," *Materials & Design*, vol. 66, pp. 51–59, 2015.